Faculté d'Ingénierie Biologique,
Agronomique et Environnementale
Earth and Life Institute
Université catholique de Louvain (UCL)

Weathering of powdered volcanic rocks: laboratory and modelling studies for assessing rates and environmental impacts

Carlos Francisco Aragón Tobar

Thèse présentée en vue de l'obtention du grade de Docteur en Sciences agronomiques et ingénierie biologique

17 th April, 2019

Promoteur:

Prof. Pierre Delmelle, UCL/ELI/ELIE, Belgium

Membres du jury:

Prof. Bruno Henry de Frahan (Président), UCL/ELI/ELIA, Belgium
Prof. Sophie Opfergelt (Secrétaire), UCL/ELI/ELIE, Belgium
Prof. Yves Goddéris, Géosciences Environnement Toulouse, OMP, France
Prof. Lei Chou, ULB/BGeoSys, Belgium

Aragón-Tobar, C.F. (2019) *Weathering of powdered volcanic rocks: laboratory and modelling studies for assessing rates and environmental impacts*. Thèse présentée en vue de l'obtention du grade de Docteur en Sciences agronomiques et ingénierie biologique. Université catholique de Louvain.

SUPERVISOR:

Prof. Pierre Delmelle, UCL/ELI/ELIE, Belgium

MEMBERS OF THE EXAMINING BOARD:

Prof. Bruno Henry de Frahan (chairperson), UCL/ELI/ELIA, Belgium
Prof. Sophie Opfergelt (secretary), UCL/ELI/ELIE, Belgium
Prof. Yves Goddéris, Géosciences Environnement Toulouse, OMP, France
Prof. Lei Chou, ULB/BGeoSys, Belgium

LOCATION:

Louvain-la-Neuve

PUBLIC DEFENSE:

17th April 2019

This PhD thesis was supported by the “Top World Universities” program funded by the government of Ecuador through the Secretarial of Higher Education, Science, Technology and Innovation SENECYT under grant agreement No. 003-CIBAE-2014 (2014-2018) and by the “Programme de mobilité 2018-2019” of Université catholique de Louvain (UCLouvain) funded through L’Académie de recherche et d’enseignement supérieur (ARES).

“Dove c’è una grande volontà non posssono esserci grandi difficoltà”

“Where the willingness is great, the difficulties cannot be great”

Niccolò Machiavelli, Il Principe

Acknowledgements

It has been a long trip since I started my PhD thesis on April 2014. Along this path, there has been so many people that have supported and encouraged me in so different ways that this single page will remain meagre to express all my gratitude towards them.

To my supervisor, Prof. Pierre Delmelle, who took the risk of working with an Ecuadorian student that he barely knew. Thanks for taking me under your wing. It has been a priceless experience having you as a mentor through the ups and downs of the experimental science. Merci beaucoup Pierre pour tout votre soutien inconditionnel pendant tous ces cinq ans de travail, merci de m'avoir accueilli dans le laboratoire des Sols.

To all the members of the examining board who contributed to the accomplishment of this thesis: Prof. Bruno Henry de Frahan, Prof. Sophie Opfergelt, Prof. Yves Goddéris and Prof. Lei Chou. The outstanding scientific perspective provided by all of you improved the quality of the work presented in this thesis. Thanks to Prof. Yves Goddéris who welcomed me at the Geosciens Environnement Toulouse GET and taught me, with passion and patience, about the WITCH model. Thanks to the optimism of Prof. Sophie Opfergelt which inspired me to always keep moving forward. To Prof. Phillippe Sonnet who helped me during my upgrade meeting. To Prof. Jacques Schott at GET who with his vast experience introduced to me the exciting world of the dissolution rates of silicates. To Prof. Johnathan Castro and Dr. Pablo Forte who welcomed me in the Institut für Geowissenchaften at the University of Mainz.

Muchas gracias a mi familia, que siempre estuvo a mi lado por sus interminables oraciones y apoyo durante este tiempo en el extranjero. A mi señora bonita, Elena, a babacim Carlos, a mi querida Lau, a mi carisimo Enriquito. A mi numerosa familia Aragón Duque y Tobar Rosas en Ecuador, Estados Unidos y Alemania. Thank you especially to my dear auntie Delita for her endless generosity towards me. Danke an meine deutsche Familie für ihre bedingungslose Unterstützung, für ihren großzügigen Empfang während dieser Zeit. Zu meiner lieben Cousine Lizi.

A la gente en Ecuador que hizo todo esto posible, al Departamento de Metalurgia Extractiva de la Escuela Politécnica Nacional. A mis profesores y amigos del DEMEX, Ernesto de la Torre, Alicia Guevara, Evelyn Criollo, seño Verito, Kleverito, Dianita.... Gracias mi querida "inge" Alice por brindarme esta oportunidad la cual me cambió la vida.

Merci beaucoup à tous les membres du laboratoire de Sols (ELIE) qui ont toujours su me donner une place au sein du laboratoire depuis que je suis arrivé. À Françoise Hauwen qui a été un ange pendant ce temps, merci pour vos soupes mais surtout pour votre immense affection et générosité. À Anne Iserentant qui ne m'a pas seulement ouvert les portes du laboratoire mais aussi les portes de sa maison pour me recevoir dans sa famille. À Claudine Givron, qui a été toujours souriante pour m'aider. Aux membres du laboratoire qui m'ont aidé avec la construction du réacteur, Bernard Douxfils, Jacques De Thier et Frédéric Laurent pour les longues journées de travail au GERU et dans la salle climatique.

Thanks to all the wonderful team of talented young researchers that I had the honor of encountering at the Soils Laboratory. Starting by all my office mates, with whom I spent unforgettable moments of joy and excitement, Marie Detiene, (the first one welcoming me at the airport), Yolanda Ameijeiras (& Celso Lorenzo, mis ñaños españoles), Marie-Liesse Vermiere (Lya), Gabriela Ruiz (Gaby), Catherine Hirst (Cathy-Cathy), Elisabeth Mauclet and Charles Vander Linden. As well to those who with their daily work enlarged science and inspired me: Brieuc Hardy, Rawaa Ammar (أختي الحبيبة), Zimin Li, Michelle Quimbo, Marlon Calispa, Noa Ligot, Mathilde Paque, Aubry Vandeuren (Aubrito), Benoît Pereira, Boris Hanesse, Clairia Kankurize, François Gaspard, Arthur Monhonbal, Fidèle Barhebwa. Inga Tarasenko (Спасибо моим дорогим русским друзьям Инге и Алексу. Я никогда не забуду мое прекрасное время в Москве с вами). Thanks to Elena Maters who inspired and encouraged me during these years, starting by sharing the climatic room during our dissolution experiments and then your experience as an outstanding young researcher which has enriched my perspective about pursuing a career in sciences.

To my dear family in faith in Louvain la Neuve. Eliana Manangón (Ely-chan), gracias por tu bondad, por estar siempre presente en todos los buenos y malos momentos vividos en LLN. To Agnieszka Goj, moja droga Aga, dziękuję za niekończące się spotkania, modlitwy, wyjazdy, pobieranie próbek o czwartej nad ranem. Bez Ciebie nigdy bym nie skończył tego doktoratu. Dziękuję mojej polskiej rodzinie. To Marce Daniluk for her kind technical support. To my dear friends from the ecuadorian-latino comunity in Louvain-la-Neuve, Isaac Meza, Nathalie de la Torre, Anilu Barrera, María Himelda Robalino, Deysi Yungan, Diana Andrade, Gabriela Bidegain, Yenni Velazquez, Walter Florez, Andrea Guardia, Camila Carvallo. To the wonderfull friends I made in LLN, to Eva Pospisilova (Evicka), for the happy shared moments with pancakes, cokctails and other Czech delicacies. To Cyrille Doss and his enriched life experience. To my friends from the Rosary group: Egle Kivytaite, Louise Giovaninetti, Jorge Fraile, Fabian Bald, Marinho Bertanha. To my friend of international adventures, Asher de Saadeleer, thanks for being an example of courage. To my dear friend Juliane Duchesne, thanks for the

long chats about life. Merci à notre „nonita", Anne-Marie, qui a été toujours présente avec ses prières. To the Dominicains at Lovain la Neuve (Zbigniew Krysiewicz, Patrick Gillard) and Alexis Pidault who provided me not only with a place to stay but also enlightened my path with their life phylosophy.

To my friends from Ecuador who stayed with me during these years: Julia Jimenez (July), Katty Cabezas, Cristina Pavón, Darío Pavón, Gaby Mora, Anita Alvarez, María José Lovato, Erika Solano, Dianita Celi, Nancy Correa, Iván Zúñiga, Carito Cruz, Sebastián Suarez, Verónica Jara, Adriana Arguero.

Finally, to those who I do not mention here but shared with me a kind smile, chat or any sign of tenderness when I needed the most the encouragement to finish this PhD.

To those who will feel identified with this scientific work or with my life experienced as a foreign student abroad.

Abstract

Continental weathering of extrusive magmatic rocks, including pyroclastic materials (i.e. volcanic ash), is an essential component of the global geochemical cycles of key elements such as C and Si. However, we still lack an in-depth quantitative understanding of the controlling factors. In particular, the role of rock crystallinity and chemical composition in dictating dissolution and hence, weathering rates, remain unclear. In this PhD research, we determined experimentally the dissolution rates of polycrystalline magmatic rocks, spanning a range of representative chemical compositions and mineralogies.

The rock dissolution rates were measured at steady sate and far-from equilibrium using a homemade fluidized bed reactor (Chapter 3). The experiments were carried out in alkaline and acidic pH conditions at 20-25 °C. We first document the formation of a micrometric leached layer at the surface of a basaltic ash subjected to dissolution in the pH range 2-11 (Chapter 4). The composition of this layer varies between a Si and Al-rich endmembers, depending on the reactive solution pH and highlights that dissolution is incongruent. The potential influence of the degree of crystallinity on dissolution rates was assessed by comparing the behaviour a low-Si (basalt) and high-Si (dacite) rocks with their glassy (non-crystalline) counterparts (Chapter 5). Our results show that in the case of the basaltic composition, the crystalline rock was less reactive compared to the glass, but the opposite was true for the dacite. Finally, we argue that the dissolution rates of andesite, dacite and rhyolite polycrystalline rocks can be approximated based on the dissolution kinetics of their major constituents, i.e. silicate glass and plagioclases ± pyroxenes (Chapter 6).

The last part of this PhD is a modelling exercise. We applied a mechanistic box model (WITCH) to simulate the weathering of a modern-day, continent-scale rhyolitic ash deposit and to assess its effects on atmospheric CO_2 consumption and weathering fluxes. WITCH relies largely on laboratory kinetics laws to describe chemical weathering in the natural environment. We simulated the weathering of an ash deposit (with variable thicknesses) representative of a supereruption of Yellowstone volcano, USA, and which covers much of North America. The calculations were performed for weathering periods ranging from 0.1 up to 10,000 years. The model results reveal the importance of the ash deposit thickness and drainage conditions in dictating the spatial distribution of the Si and base cation fluxes generated through weathering. They also highlight that the emplacement and subsequent weathering of a continent-size deposit of rhyolitic ash strongly enhances the

continental flux of dissolved Si to the ocean for several thousands of years. However, in contrast with basaltic lavas, chemical weathering of the rhyolitic deposit has a minor influence on the concentration of atmospheric CO_2. This reflects the low contents of calcium/magnesium silicate minerals in the silicic ash material. We further infer that the dissolution rate values for the rhyolitic ash as deciphered from the model outputs are in good agreement with those obtained experimentally. Overall, this PhD research provides new insights into the dissolution rates of polycrystalline magmatic rocks. It also demonstrates the potential of large-scale volcanic explosive eruptions to enhance the weathering flux of Si on the millennial timescale.

Table of Contents

List of Tables

List of Figures

PART I
OVERVIEW

CHAPTER 1 General Introduction

1.1. CONTEXT

Weathering is one of the major geologic processes in the rock cycle that shapes Earth's surface and alters rock materials, converting all kinds of rocks into sediment, eventually forming soils. Rock weathering occurs in response to the interaction of the lithosphere with the atmosphere, hydrosphere, and biosphere (Keller, 1957). Weathering includes both physical and chemical processes. Chemical weathering occurs when the minerals in a rock are chemically altered or dissolved. Chemical weathering of silicate minerals results from the differences in the thermodynamic conditions that existed at the time of the mineral formation and that of ambient conditions at the Earth's surface (White and Brantley, 1995).

The importance of chemical weathering of terrestrial rocks for the rock cycles and key biogeochemical cycles (e.g., C and Si) has long been recognized (e.g., White and Brantley, 1995). Chemical weathering has also gained recognition in environmental studies related to water quality, watershed acidification, nutrient cycling, and the feedback between chemical weathering and climate. The atmospheric CO_2 consumption by chemical weathering of Ca- Mg silicate rocks has a direct link with global climate at the geological timescale (Berner, 1995). This has been highlighted in laboratory experiments (e.g., Pronost et al., 2011), field test (e.g., Gislason et al., 2009; Matter et al., 2011) and geochemical modelling (e.g., Beaulieu et al., 2012, Goddéris et al., 2013).

Most silicate rocks on Earth are magmatic rocks, either intrusive or extrusive. According to several studies, weathering of basalt rocks account for around 20% of the global CO_2 drawdown (Gaillardet et al., 1999; Hartmann et al., 2009). Understandably, numerous laboratory, field and modelling studies focus on unravelling the mechanisms of weathering and quantifying its rate in different environmental conditions. These investigations focus largely on the weathering of silicate minerals and glass (i.e. representing the portion of magma that did not crystallize upon cooling) taken separately (Palandri et al., 2004; Gislason and Oelkers, 2003; Wolff-Boenisch et al., 2004 and references therein). In comparison, much less is known regarding the weathering of polycrystalline silicate rocks that are comprised of minerals embedded in a glassy matrix.

This PhD is concerned with the chemical weathering of magmatic polycrystalline rocks formed when a magma erupts from a subaerial volcano. Here, such rocks will be simply referred as to "volcanic rocks". Rapid magma cooling at the Earth's surface produces volcanic rocks spanning a broad range of crystallinities, from glassy to finely grained crystalline textures. One further

distinguishes the non-fragmentary (lavas) from fragmentary (pyroclastic) volcanic rocks, the latter resulting from the violent breaking of magma during an explosive volcanic eruption. Volcanic ash corresponds to a pyroclastic rock material <2 mm in diameter (Grozinger et al., 2007).

The PhD research draws on two approaches: (i) experimental determinations of dissolution rates for volcanic rocks in aqueous solutions at various pH conditions and at room temperature and (ii) simulation of the weathering of a continent-scale ash deposit over different timescales using a geochemical model. These approaches seek to enlarge the current understanding of the weathering of volcanic rocks and of their potential geochemical implications.

The first part of the PhD thesis relates to the measurement of dissolution rates of volcanic rocks with compositions representative of those found for terrestrial volcanic eruptions. The experiments are conducted in the laboratory using a fluidized-bed reactor built in our laboratory. The design of this equipment was inspired from the work of Chou and Wollast (1984). The second part of the thesis focuses on the application of a geochemical box model named WITCH (Goddéris et al., 2006) to simulate mineral weathering following the regional deposition of ash from a hypothetical modern day large-scale volcanic eruption (i.e. a so-called supereruption). The WITCH model incorporates laboratory-derived rate laws to describe chemical weathering in the natural environment quantitatively.

1.2. AIMS AND OBJECTIVES

The present PhD research presents the results of experimental and modelling studies aimed at improving our knowledge of the chemical weathering of volcanic rocks. The specific research objectives are:

i. To develop and use a fluidized-bed reactor to measure the far-from equilibrium, steady state dissolution rates of powdered volcanic rocks at different acidity conditions.
ii. To describe the dissolution behavior of a basaltic ash at acidic and alkaline pH values using the fluidized-bed reactor.
iii. To assess the effect of crystallinity on the dissolution rates of volcanic rocks with different chemical compositions.
iv. To test the hypothesis that the dissolution rates of a crystalline volcanic rock can be approximated by considering the dissolution rates of its main constituents taken individually.
v. To quantify the impact of a continent-size ash deposit on chemical weathering fluxes and atmospheric CO_2 consumption at different timescales using the geochemical model WITCH.

1.3. THESIS OUTLINE

Part I of the thesis provides an overview of the research topic and of the methods involved in the experimental work. **Chapter 2** presents the background related to the main properties of volcanic rocks. This is followed by a general description of chemical weathering and chemical weathering rate of silicates. **Chapter 3** describes the main analytical and experimental techniques. This includes the techniques applied for characterizing the volcanic rock samples as well those used to measure the composition of aqueous solutions generated during the dissolution experiments. Chapter 3 also details the features of the fluidized-bed reactor that we built.

Part II of the thesis comprises four data chapters. The first three relates to the experimental determinations of the dissolution rates of volcanic rocks, including polycrystalline rock, ash and glass, using the fluidized-bed reactor at room temperature (20–25 °C). **Chapter 4** presents the results obtained for a basaltic ash subjected to dissolution at pH values of 2, 3, 5, 8, 10 and 11. C**hapter 5** compares the experimental dissolutions rates measured for crystalline volcanic rocks of basaltic, dacitic and rhyolitic composition at pH 4 with those obtained for their glassy counterparts. **Chapter 6** reports the dissolution rates of a basalt, andesite, dacite and rhyolite polycrystalline rocks at pH 2, 3 and 5 and discusses these in light of the dissolution rates of the individual rocks' constituents as available from the scientific literature. The fourth chapter **(**C**hapter 7)** of **Part II** starts with a brief description of the geochemical model WITCH. It then describes the results generated by applying WITCH to simulate the weathering of a continent-size ash deposit resulting from a modern-day eruption of Yellowstone volcano, USA.

The final part of the thesis document **Part III** is **Chapter 8**, which highlights the key contributions made by this study.

Figure 1.1. sketches the context of the PhD research and shows the articulation of the thesis chapters

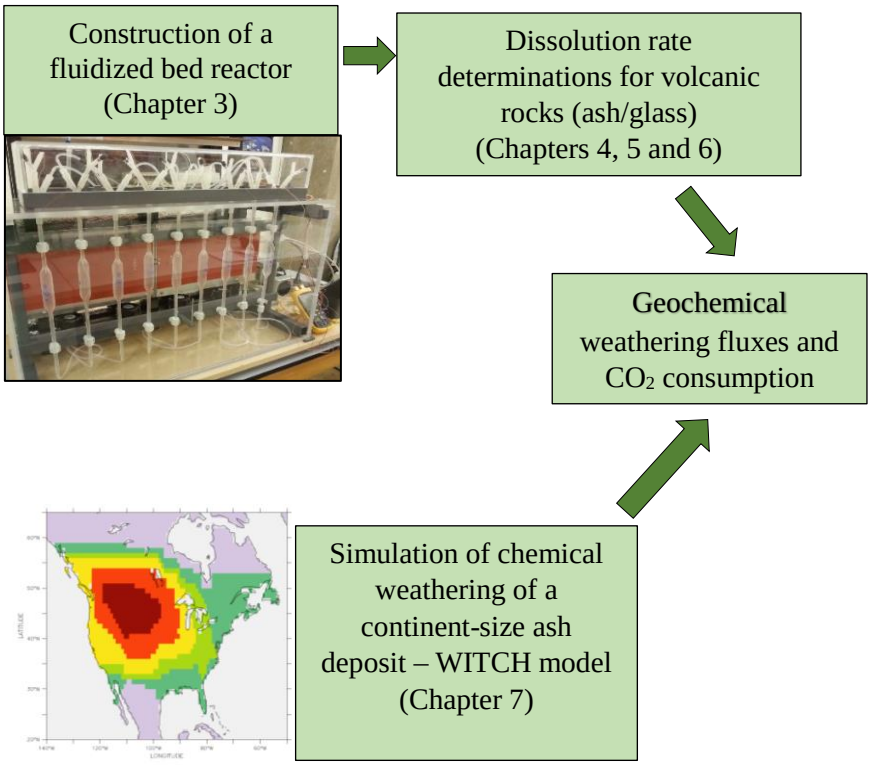

Figure 1.1. Illustration of the context of the PhD research and articulation of the thesis chapters.

References

Beaulieu, E., Goddéris, Y., Donnadieu, Y., Labat, D. and Roelandt, C. (2012) High sensitivity of the continental-weathering carbon dioxide sink to future climate change. Nature climate change. Vol.2. pp. 346-349.

Berner, R.A. (1995) Chemical weathering and Its Effect on Atmospheric CO_2 and Climate. In Chemical Weathering Rates of Silicate Minerals. Eds. White, A.F & Brantley S.L. Reviews in Mineralogy. Volume 31. pp. 575-583.

Chou, L. and Wollast, R. (1984) Study of weathering of albite at room temperature and pressure with a fluidized bed reactor. Geochimica et Cosmochimica Acta Vol 48. 2205-2217.

Dessert, C., Dupré, B., François, L.M., Schott, J., Gaillardet, J., Chakrapani G. and Bajpai S. (2001) Erosion of Deccan Traps determined by river geochemistry: impact on the global climate and the $^{87}Sr/^{86}Sr$ ratio of seawater. Earth and Planetary Science Letters 188, pp 459-474.

Gaillardet, J., Dupré, B., Louvat, P., Allègre, C.J. (1999) Global silicate weathering and CO_2 consumption rates deduced from the chemistry of large rivers. Chem.Geol. 159, 3-30.

Gislason, S.R., Oelkers, E.H., Eiriksdottir, E.S., Kardjilov, M.I., Gisladottir, G., Sigfusson, B., Snorrason, A., Elefsen, S., Hardardottir, J., Torssander, P., Oskarsson, N. (2009) Direct evidence of the feedback between climate and weathering. Earth And Planetary Science Letters 277(1-2):213-222.

Gislason, S.R., Oelkers, E.H. (2003). Mechanism, rates, and consequences of basaltic glass dissolution: II. An experimental study of the dissolution rates of basaltic glass as a function of pH and temperature. Geochimica et Cosmochimica Acta, 67 (20), 3817-3832.

Goddéris, Y., Brantley, S.L., François, L.M., Schott, J., Pollard, D., Déqué, M. and Dury M. (2013) Rates of consumption of atmospheric CO_2 through the weathering of loess during the next 100yr of climate change. Biogeosciences, 10, 135-148.

Goddéris, Y., François, L., Probst, A., Schott, J., Moncoulon D. Labat, D. and Viville D. (2006) Modelling weathering processes at the catchment scale : The WITCH numerical model. Geochimica et Cosmochimica Acta 70, 1128-1147.

Grotzinger, J., Jordan, T.J., Press, F. and Siever R. (2007) Understanding Earth. Fifth Edition. Chapter 4 Igneous Rocks.

Hartmann, J., Jansen, N., Dürr, H.H., Kempe, S., Köhler, P. (2009) Global CO_2- consumption by chemical weathering: What is the contribution of highly active weathering regions? Global and Planetary Change 69. Pp. 185-194.

Keller, W.D. (1957) The Principles of Chemical Weathering. An Integrated Review of the Principles of Chemical Weathering as Taken from the Literature, and the Relation of Weathering to Certain Aspects of Geology, Pedology and Civilization. Lucas Brother Publisher. Columbia, Missouri. pp.5, 9, 21, 54, 57.

Matter, J.M., Broecker, W.S., Gislason, S.R., Gunnlaugsson, E., Oelkers, E.H., Stute, M., Sigurdardóttir, H., Stefansson, A., Alfreðsson, H.A., Aradóttir, E.S., Axelsson, G., Sigfússon, B., Wolff-Boenisch, D., (2011) The CarbFix Pilot Project – storing carbon dioxide in basalt. Energy Procedia 4, 5579–5585.

Palandri J.L. and Kharaka Y.K. (2004) A compilation of rate parameters of water-mineral interaction kinetics for application to geochemical modeling. U.S. Geological Survey. Open file report 2004-1068.

Pronost, J., Beaudoin, G., Tremblay, J., Larachi, F., Duchesne, J., Hébert, R., Constantin, M., 2011. Carbon sequestration kinetic and storage capacity of ultramafic mining waste. Environ. Sci. Technol. 45, 9413–9420.

White A.F & Brantley S.L. (1995) Chemical weathering rates of silicate minerals: an overview. In Chemical Weathering Rates of Silicate Minerals. Eds. White, A.F & Brantley S.L. Reviews in Mineralogy. Volume 31. pp. 1-22.

Wolff-Boenisch, D., Gislason S. R., Oelkers, E. and Putnis, C.V. (2004) The dissolution rates of natural glasses as a function of their composition at pH 4 and 10.6 and temperatures from 25 to 74°C. Geochimica et Cosmochimica Acta, Vol.68, No. 23, pp 4843-4858.

CHAPTER 2 State of the art

2.1. OVERVIEW OF VOLCANIC ROCKS

Volcanic rocks (or extrusive igneous rocks) are formed at or very near the Earth's surface when magma, including dissolved volatiles such as H_2O, CO_2, SO_2, HCl, etc. are discharged at the surface during an effusive or explosive eruption (Hyndman, 1985; Grozinger et al., 2007). Volcanic rocks are found in nature as *lavas* or *pyroclasts* (Hyndman, 1985; Grozinger et al., 2007). *Lava* corresponds to a magma which has solidified at the Earth's surface. It is the typical product of effusive eruptions. *Pyroclasts* are broken pieces of magma ejected violently during an explosive eruption. The fragments may be individual crystals, glass and/or rock fragments. The various types of pyroclasts are mainly distinguished by their size. *Bombs* and *blocks* have a mean diameter exceeding 64 mm. Pyroclasts of any shape with a mean diameter of 64 mm to 2 mm are defined as *lapilli*. Pyroclasts with a mean diameter less than 2 mm are *ash grains* being further divided into *coarse ash* (2 mm to 1/16 mm) and *fine ash* (less than 1/16 mm) (Le Maitre et al., 2002). Pyroclast deposits may be consolidated or not. The different types of volcanic rocks are shown in Figure 2.1.

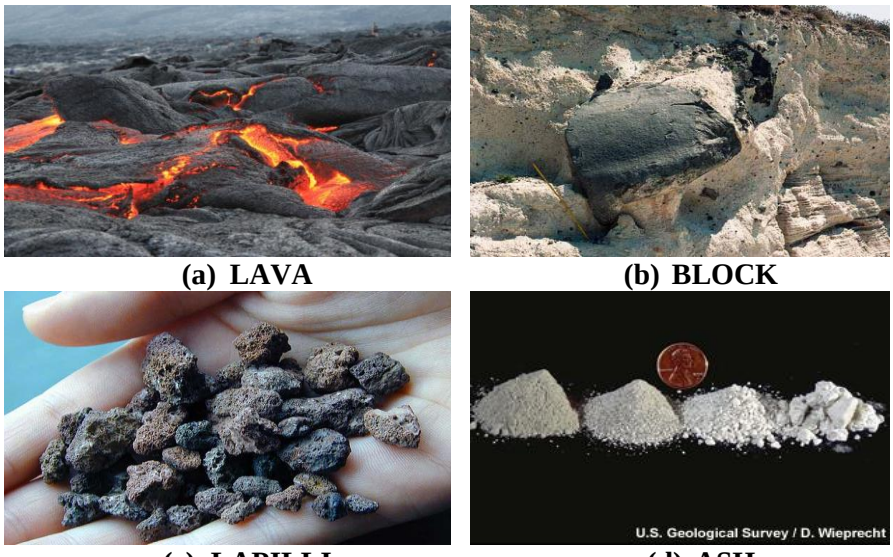

(a) LAVA **(b) BLOCK**

(c) LAPILLI **(d) ASH**

Figure 2.1. Different kinds of volcanic rocks: (a) A view of lava flowing from Kilauea (Hawai) (Photo: Russel McLendon); (b) Large ballistically ejected block on Santorini (Greece) (Photo: VolcanoDiscovery); (c) Lapilli from Vesuvius (Photo: J. Alean); (d) Volcanic ash (U.S. Geological Survey Photo: D.E. Wieprecht).

2.1.1. Texture

Volcanic rocks display three types of texture: glassy, interlocking and fragmental (Fig. 2.2). The rock's texture reflects the rate at which it cooled and therefore the environment in which it formed. A glassy texture is represented by rock made of a solid mass of glass, or of tiny crystals surrounded by glass. Volcanic rocks that consist of mineral crystals that intergrow when the melt solidifies, and thus fit together like pieces of a jigsaw puzzle, have an interlocking texture, and are called crystalline volcanic rocks. Depending on the size of the crystals, crystalline volcanic rocks are further subdivided into phaneritic, aphanitic and porphyritic (Fig. 2.3). Phaneritic rocks have crystals large enough to be identified with the naked eye. In contrast, aphanitic rocks have crystals too small to be identified with the naked eye. Porphyritic rocks have larger crystals surrounded by mass of fine crystals. In a porphyritic rock, the larger crystals are called phenocrysts, whereas the mass of finer crystals is called groundmass.

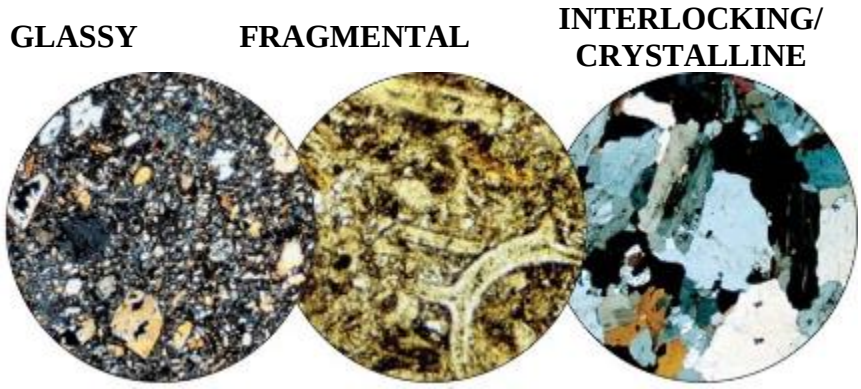

Figure 2.2. Photomicrographs of thin sections reveal the different textures of igneous rocks.
Taken from Khattak (2016).

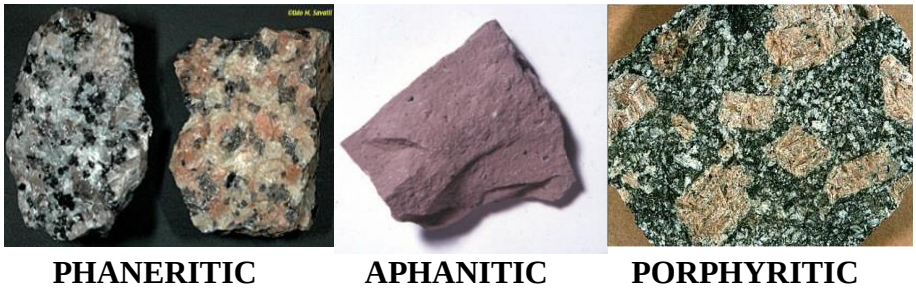

Figure 2.3. Texture of crystalline volcanic rocks.
Taken from Eifert (2011).

2.1.2. Chemical composition

The chemical composition of a volcanic rock relates to that of its source magma. It reflects the original source of the magma and the way in which the magma evolved before finally solidifying. The different compositional classes are distinguished on the basis of silica content: basalt (45< SiO_2 < 52 wt. %), andesite (52 < SiO_2 < 63 wt. %), dacite and rhyolites (63 wt. % < SiO_2). A more detailed classification is obtained by plotting the alkali element (Na + K) contents as a function of the SiO_2 content using the so-called Total Alkali Silica (TAS) diagram (Gill, 2010; Fig. 2.4).

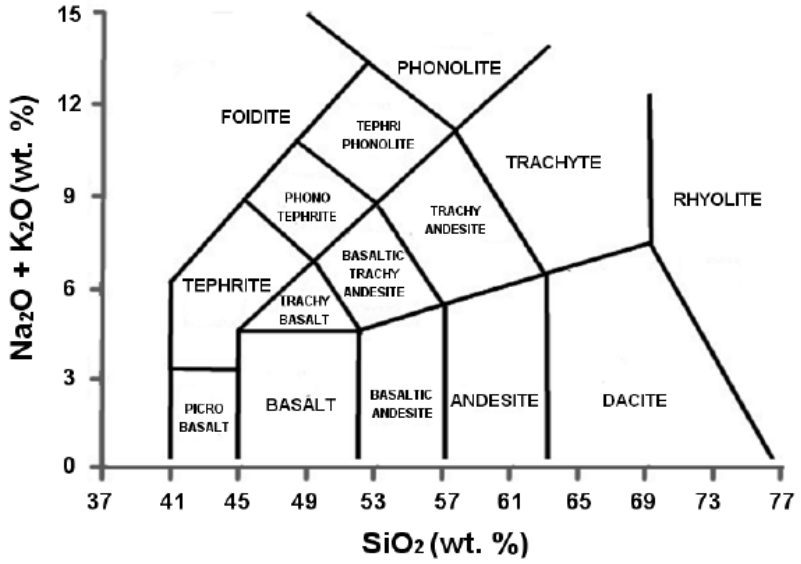

Figure 2.4. Total Alkali Silica diagram used for classifying volcanic rocks. *Taken from Le Maitre et al. (2002).*

2.1.3. Mineralogy

Glass

Volcanic rocks show various degrees of crystallinity. In most cases, the crystals are entrapped in a glassy groundmass. Volcanic glass corresponds to the magma portion that did not crystallize during cooling and solidification. Glass is an amorphous material consisting of a random network of Si tetrahedra connected by bridging oxygens (Si-O-Si) (Mysen and Richet, 2005). The tetrahedral is the basic structural unit of silicate glasses. The

tetrahedral have a well-defined geometry and are linked to each other through their corners in a manner similar to the connection between tetrahedral in crystalline SiO_2 (Henderson et al., 2006). Beyond adjacent tetrahedral, the medium or intermediate- range structure contains rings of tetrahedral and other interconnected units whose exact structures are not well understood (Henderson et al., 2006). Trivalent Al or Fe can substitute tetravalent Si in the network if a cation is present nearby to compensate for the charge difference (Mysen and Richet, 2005).

Silicon, O, Al and Fe are referred to as glass forming elements (GFEs). Monovalent and divalent cations (Na^+, K^+, Ca^{2+}, Mg^{2+}, Fe^{2+}) may act either as charge compensators or network modifiers (GMEs) (Scholze, 1990; Oelkers and Gislason, 2001). The network formers act as the centers of glass polyhedral units (tetrahedral). The oxygen species linking the polyhedral units are called bridging oxygen (BO) and these not linking the polyhedra are called non-bridging oxygen (NOB). Modifiers and additives create non-bridging oxygen species to maintain charge neutrality in a glass structure (Henderson et al., 2006; Mahapatra and Lu, 2010). A schematic of glass structure showing network former (Si), network intermediates (Al and Fe), network modifiers (Na, K, Ca, Mg), network additives (minor components: Mn, Ti, Sr, Zr….), and bridging and non-bridging oxygen species is given in Figure 2.5.

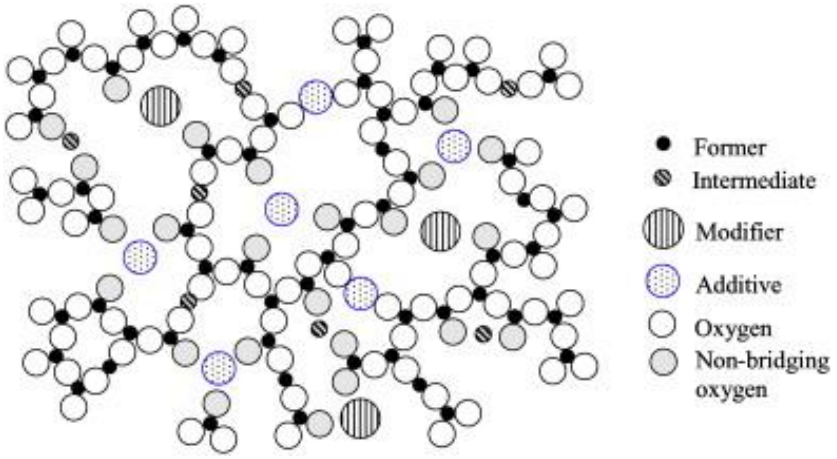

Figure 2.5. Schematic illustration of the aluminosilicate glass network.
Taken from Mahapatra and Lu (2010).

Because of its amorphous structure, glass is not restricted to specific stoichiometries, as crystalline minerals are. This means that glass has a wider range of possible compositions. In order to better describe the glass structure, the network connectivity (NC) (polymerization state/connectedness) has been defined, as the average number of bridging oxygen (BO) atoms bound to a network-forming cation, generally Si. Thus, high values of NC typically indicate a well-connected glass network, which is not prone to dissolution. Lower values indicate a fragmented, disconnected network that has many reactive sites and is prone to dissolution (Liebau, 1985; Hill, 1996; Criscenti et al., 2005; Wolff-Boenish et al., 2006; Christie et al., 2016).

Minerals

The minerals found in volcanic rocks have crystallized in the source magma. They consist dominantly of silicate minerals. As new crystals form during magma crystallization, they extract certain chemicals preferentially from the melt. As a result, the chemical composition of the remaining melt progressively changes as the magma cools. In a cooling mafic (low-SiO_2) magma, olivine and calcium-rich plagioclase form first. The Ca-plagioclase reacts with the melt to form more plagioclase, but the newer plagioclase contains more Na. Meanwhile, some olivine crystals react with the remaining melt to produce pyroxene, which may encase olivine crystals or even replace them. However, some of the olivine and Ca-plagioclase crystals settle out of the melt, taking Fe, Mg, and Ca atoms with them. As the melt continues to cool, plagioclase continues to form, with later-formed plagioclase having progressively more Na than earlier-formed plagioclase. Pyroxene crystals react with melt to form amphibole, and then amphibole reacts with the remaining melt to form biotite. At temperatures of between 650 ºC and 850 ºC, only about 10% melt remains, and this melt has a high silica content. At this stage, the final melt freezes, yielding felsic minerals such as quartz, K-feldspar, and muscovite. The specific sequence of mineral-producing reactions that take place in a cooling, initially mafic, magma is known as Bowen's reaction series. Besides the silicate minerals, Fe-Ti oxide minerals such as Ti-magnetite and ilmenite also crystallize in most magmas (Hyndman, 1985; Grozinger et al., 2007; Gill, 2010). Table 2.1 provides the chemical formula of minerals commonly found in volcanic rocks (Nakagawa and Ohba, 2002).

Table 2.1. Common minerals found in volcanic rocks.

Group	Mineral	End Member	Chemical Formula
Olivine	Olivine	Forstelite	Mg_2SiO_4
		Fayalite	$Fe^{2+}{}_2SiO_4$
Feldspar	Plagioclase	Anorthite	$CaAl_2Si_2O_8$
		Albite	$NaAlSi_3O_8$
	Alkali feldspar	Potassium feldspar	$KAlSi_3O_8$
Pyroxene	Orthopyroxene	Enstatite	$MgSiO_3$
	Clinopyroxene	Ferrosilite	$Fe^{2+}SiO_3$
		Wollastonite	$CaSiO_3$
Amphibole	Hornblende	Actinolite	$Ca_2(Mg,Fe^{2+})_5Si_8O_{22}(OH)_2$
		Edenite	$NaCa_2(Mg,Fe^{2+})_5AlSi_7O_{22}(OH)_2$
		Pargasite	$NaCa_2(Mg,Fe^{2+})_4Al_3Si_6O_{22}(OH)_2$
		Tschermakite	$Ca_2(Mg,Fe^{2+})_3Al_3Si_6O_{22}(OH)_2$
	Cummingtonite		$(Mg,Fe^{2+})_7Si_8O_{22}(OH)_2$
Mica	Biotite	Annite	$K_2Fe^{2+}{}_6Al_2Si_6O_{20}(OH)_4$
		Siderophyllite	$K_2Fe^{2+}{}_5Al_4Si_5O_{20}(OH)_4$
		Phlogopite	$K_2Mg_6Al_2Si_6O_{20}(OH)_4$
		Eastonite	$K_2Mg^{2+}{}_5Al_4Si_5O_{20}(OH)_4$
Spinel	Titanomagnetite	Magnetite	$Fe^{2+}Fe^{3+}{}_2O_4$
		Ulvospinel	$Fe_{2+2}TiO_4$
	Ilmenite		$Fe^{2+}TiO_3$

Figure 2.6 portrays how the mineral assemblages in volcanic rocks (intrusive/coarse-grained: granite, diorite, gabbro and periodotite; extrusive/fine-grained: rhyolite, andesite and basalt) change with chemical composition. The vertical axis shows the mineral composition of a given rock as percentage of its volume. The horizontal axis is a scale of silica content by weight (Grozinger et al., 2007).

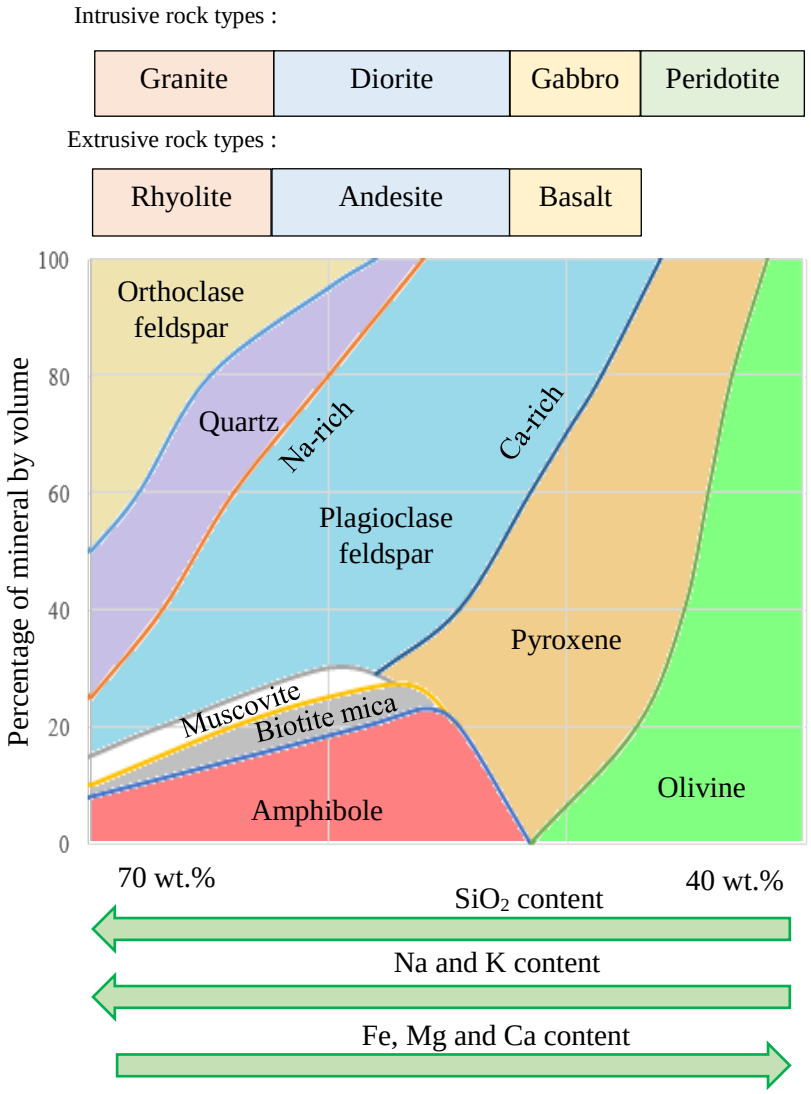

Figure 2.6. Classification model of igneous rocks. The vertical axis shows the mineral composition of a given rock as a percentage of its volume. The horizontal axis is a scale of silica content by weight.
Adapted from Grozinger et al. (2007).

2.2. VOLCANIC ASH AND ENVIRONMENTAL EFFECT OF TEPHRA DEPOSITION

2.2.1. Overview of volcanic activity

Volcanic eruptions represent fluxes of matter and energy from the interior to the surface of the Earth (Sigurdsson, 2015). Volcanism occurs when magmas and dissolved volatile species are extruded from pipes or cracks as lava or when they explode to produce pyroclastic materials. Magma (molten rock inside the Earth) rises buoyantly to the surface because, as a fluid, it is less dense that surrounding rock. (Grozinger et al., 2007). Dissolved volatile species found in molten magma include water (H_2O), carbon dioxide (CO_2), sulphur dioxide (SO_2), hydrogen sulphide (H_2S), hydrochloric acid (HCl) and possible hydrofluoric acid (HF) (Sigurdsson, 2015).

Volcanic eruptions can produce localized phenomena (Figure 2.7), such as pyroclastic flows/pyroclastic density currents (fast moving current of hot gas and volcanic matter) and lahars (mudflow composed of pyroclastic material, rock debris and water), which are the most destructive and dangerous (Auker et al., 2013). However, the most frequent, and often widespread, volcanic hazard is tephra, occurring in more than 90% of all eruptions (Newhall and Hobllitt, 2002). Tephra comprises fragments of rock produced when magma or vent materials are explosively disintegrated during an eruption. Larger tephra (blocks or bombs) follow ballistic trajectories and pose a local threat (usually < 5 km). Smaller diameter tephra, comprising lapilli and ash are convected upwards within the eruption column and dispersed away from the volcano by winds or buoyancy forces (Loughlin et al., 2015). Ash particles can be carried hundred or even thousands of kilometres away from the source falling out of suspension over large multi-national areas to form ash falls (Scasso et al., 1994). Ash fall are the volcanic hazard with the greatest potential to directly or indirectly after the largest number of people worldwide (Simkin et al., 2001, Witham, 2005).

2.2.1.2. Sizes of volcanic eruptions

Volcanic eruption is usually measured by magnitude and/or intensity (Pyle, 2015). The magnitude of an eruption is defined as total erupted mass (kg), while intensity is defined as the rate of eruption, or mass flux (kg per second). Magnitude, *M*, is defined as the base 10 log of the mass erupted in kilograms minus 7. Magnitudes range over 9 orders of magnitude with magnitude 9 eruptions being the largest (e.g. the largest Holocene eruption being magnitude 7.4 as pointed by Brown et al., 2014). The range of intensities is very large, from a few kg s^{-1} to a billion kg s^{-1} in exceptional rare events (Loughlin et al., 2015).

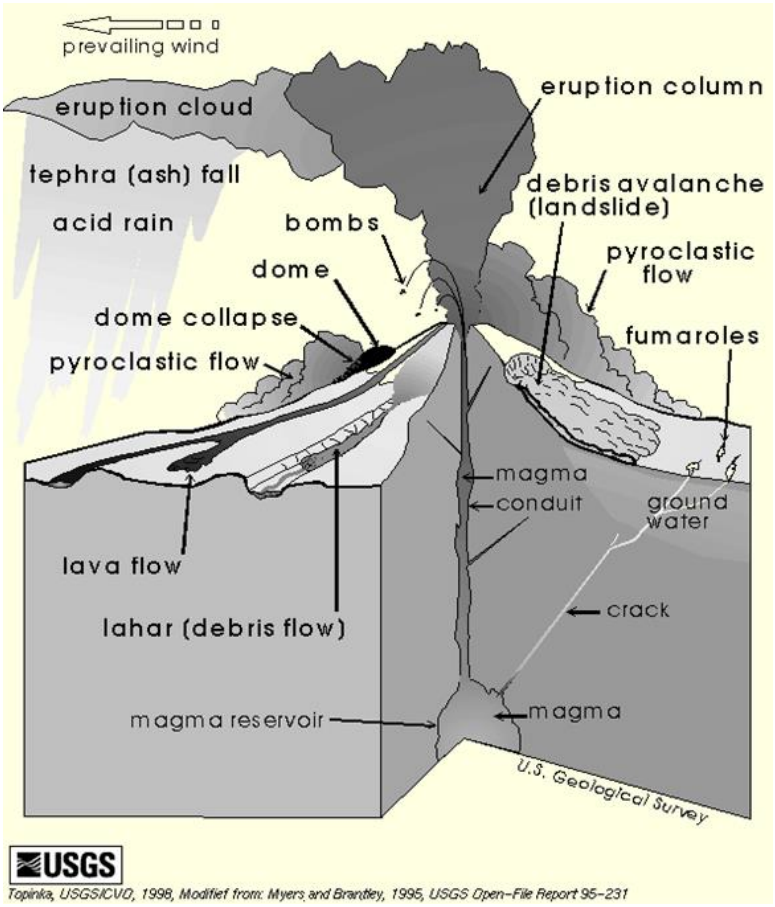

Figure 2.7. Schematic representation of the main volcanic hazards associated to volcanic eruptions.

Taken from 1995 U.S. Geological Survey Open-File Report 96-231.

The amount of material in an eruption can be also described in terms of volume of material. Volume is normally described in two ways: (a) DRE (dense rock equivalent) is an estimate of the pre-eruption volume of erupted magma (densities range from ~ 2.2-2.8 x 10^3 kg m^{-3}) and for explosive eruptions (b) the volume of pyroclastic material emitted (density averages roughly ~10^3 kg m^{-3}). The volume of pyroclastic material deposit at Earth'surface, commonly used to characterize explosive eruptions, is thus two or three times greater than that of the magma necessary to form the material due to the difference in density (Miller and Wark, 2008).

In order to compare the size of different types of eruptions, a magnitude scale is commonly used. For instance, the *Volcanic Explosive Index (VEI)* comprises a scale from 0 to 8 (Table 2.2). VEI is approximately equivalent to the magnitude (M), which is based on a logarithmic scale of mass. The VEI is based on the volume of material erupted during an explosive eruption (which can be estimated based on fieldwork after an eruption) and also the height of the eruptive column of ash (Newhall and Self, 1982).

Table 2.2. Volcanic explosivity index (VEI).
Modified after Newhall and Self (1982).

VEI	Ejected volume (km^3)	Frequency on Earth	Example
0	$> 10^{-6}$	daily	Kilauea, Hawaii
1	$> 10^{-5}$	daily	Stromboly, Italy
2	$> 10^{-3}$	weekly	Galeras, Colombia, 1993
3	$> 10^{-2}$	Yearly	Nevado del Ruiz, Colombia, 1985
4	$> 10^{-1}$	~every 10 a	Soufrière Hills, West Indies, 1995
5	> 1	~every 50 a	Mount St. Helens, USA, 1980
6	>10	~every 100 a	Pinatubo, Philippines, 1991
7	>100	~ every 1000 a	Tambora, Indonesia, 1815
8	>1000	~every 10,000 a - 100,000 a	Supereruptions: Toba, 74 ka

2.2.2. Volcanic ash physical and chemical properties

Volcanic ash is defined as the solid material < 2 mm in diameter produced by eruptive processes including magma fragmentation during volatile exsolution and bubble bursting, erosion of the conduit wall and vent, and collision and abrasion of larger pyroclasts (Fischer and Schmincke, 1984; Heiken and Wohletz, 1992). The bulk chemical composition of volcanic ash reflects that of the source of magma consists primarily of the major crustal elements silicon (Si), aluminium (Al), iron (Fe), magnesium (Mg), calcium (Ca), sodium (Na), potassium (K) and titanium (Ti). The ash comprises a mixture of glass and mineral components. (Heiken and Wohletz, 1992).

The magma composition influences indirectly ash physical properties via its effect on melt viscosity. The more silica-rich, crystal-rich, metal-poor and volatile poor the magma, the higher its viscosity and therefore its

fragmentation energy, resulting in the production of finer ash (Mysen and Richet, 2005). The composition and viscosity of the source magma also influences ash properties such as density (Shipley and Sarna-Wojcicki, 1983) and shape (e.g., spherical, elongate, bubble wall shards) (Heiken and Wohletz, 1992).

2.2.3. Environmental effects of tephra (ash) emission-deposition

Volcanic eruptions can produce a number of hazards that vary widely in their spatial distribution and in the impacts they can have for society (Loughlin et al., 2015). Tephra deposition can affect large areas and cause significant damage to natural and agricultural ecosystems. Among the tephra receiving environments, vegetation and soil systems are of high importance as their damage may result in lower agricultural potential of the affected areas due to the decreased net productivity, loss of crops, water contamination (Ayris and Delmelle, 2012).

The intensity and duration of the environmental impacts of tephra are governed by a combination of factors, such as time of the year (e.g. harvest season or planting season), the residence time of tephra deposit in terrestrial ecosystems, the physico-chemical characteristics of the tephra deposit (e.g. deposit thickness, chemical reactivity) and environmental receptor characteristics (Ayris and Delmelle, 2012).

2.2.3.1. Tephra emission in the atmosphere

Airbone tephra may influence the atmosphere's physical properties. If present in vast quantities, tephra in the stratosphere may be accompanied by increased reflection of solar radiation back to space (Mass and Robock, 1982). A continent-size ash deposit with a high albedo would induce changes in the energy budget of the atmosphere, as simulated by Jones et al. (2007). Tephra in the atmosphere could also serve as cloud condensation nuclei (CCN) (Lathem et al. 2011). Under certain conditions, the efficiency of tephra to initiate ice nucleation is though comparable to or greater than that of other natural mineral dust materials (Steinke et al., 2011). Similar to airborne mineral dust particles (Usher et al., 2003), tephra emissions may also temporarily affect the chemical composition of the atmosphere by interacting with significant trace gases including SO_2, O_3, NO_x and organic compounds (Maters et al., 2016).

2.2.3.2. Tephra deposition on vegetation

Tephra deposition affects vegetation through both physical and chemical processes. Tephra deposition on leaves may result in the localized death of

leaf tissues caused by the abrasiveness of tephra to the plants. Besides, cementation of the surface tephra layer may serve as a barrier for seed emergence (Wilson et al., 2011). From the chemical perspective, tephra on foliage when in contact with water may damage plants due to the release of soluble compounds (e.g. halide salts), as it was suggested after the eruption of Mt. St. Helens (Cook et al., 1981). Tephra deposition on soil may indirectly affect vegetation via releases of elements and consequent plant uptake (Cronin et al., 1997).

2.2.3.3. Tephra deposition on soil

The direct effect of tephra deposition on soil can manifest in a soil albedo change, which increase (dark-colored) or decrease (light-colored) soil temperature, which may in turn cause heat stress in roots (Smith et al., 2010; Cook et al., 1981). A tephra deposit on soil can also affect water and gas exchanges between soil and atmosphere. For instance, tephra can enhance water conservation in soils (Tejedor et al., 2003). Besides, tephra cementation can further impact water infiltration rate (Leavesley et al., 1989). Thus, crusts formed in tephra deposits may diminish water storage in the underlying soil, cause runoff and hence erosion (Jones et al., 2017).

Fresh tephra deposits on soil may release acidic compounds upon exposure to rainwater. This may result in a transient drop in pH of the soil. Tephra leaching could be accompanied by the release of toxic concentrations of Al in the soil solution along with some exchangeable cations (Ca, Mg, K and Na) (Dahlgren, 2008). Another effect impact of tephra on soils is contamination with fluoride (Weinstein and Davison, 2004). A tephra deposit on soil can also bring positive effects to nutrient poor soils by releasing key agronomically useful elements such as P, S, Ca, Na, K, Mg, Se and in small amounts B, Co, Cu and Zn (Cronin et al., 1998).

2.2.3.4. Tephra deposition on ice/snow surfaces

A tephra deposit can significantly reduce snow or ice albedo in the visible wavelengths, thereby affecting the snow or ice surface energy budget. Generally, a thin layer of tephra will be conductive to enhance snow or ice ablation rates due to increase absorption of solar energy and heat transfer into the ice or snow (Brock et al., 2007; Ayris and Delmelle, 2012).

2.2.3.5. Tephra deposition on aquatic systems

The entrance of tephra into water bodies may instigate a range of physical effect, shaping river or lake morphology and having detrimental impact on phytoplankton and larger plants (Ayris and Delmelle, 2012). Tephra deposition into lakes and rivers after an eruption will cause transient increases

in turbidity. High turbidity reduces light penetration and hence may impact on photosynthetic activity (Grobbelaar, 1985).

Changes in the composition of rivers from the draining of catchments affected by tephra fallout have been also noticed in some studies (Lee, 1996; Klein, 1984; Cushing and Smith, 1982, Flaathen and Gislason, 2007). Thus, tephra exposure to rain or snow in catchment areas may alter river water chemistry for a period of hours, days or weeks. Additionaly, when deposited in water bodies, tephra can be a direct source of nutrient for phytoplankton (Eicher and Rounsefell, 1957; Lotter et al., 1995; Telford et al., 2004). In addition, tephra deposits over lake bottom sediments may create an impermeable barrier; this impedes nutrient exchange across the water-sediment interface (Barker et al., 2000; Telford et al., 2004).

It is also recognized the potential role of tephra in supplying Fe to Fe-limited regions of the ocean (Dugge et al., 2007, 2010; Jones and Gislason, 2008, Olgun et al., 2011). It has been also proposed that frequent explosive eruption from silicic large igneous provinces may have been responsible for climate forcing by ocean Fe fertilization throughout Earth's history (Cather et al., 2009). While the presence of soluble elements in tephra can be beneficial for the aqueous biota, it may also have detrimental effects. Duggen et al. (2007) and Jones and Gislason (2008) pointed out that heavily loading of tephra in water bodies with low concentrations of organic ligands, such as open ocean surface waters and fresh water, could exceed the toxicity threshold of free Cu. Other soluble elements present in tephra, including Al, As, Ba, Cd, Co, F, Mn, Ni, Pb and Zn, could be also considered as potential inhibitors of biological growth in aquatic environments (Brand et al., 1983, 1986; Chakraborty et al., 2010).

2.3. CHEMICAL WEATHERING

Weathering is the response of the lithosphere with the atmosphere, hydrosphere, and biosphere (Keller, 1957). Weathering is one of the major geologic processes in the rock cycle that shapes Earth's surface and alters rock materials, converting all kinds of rocks into sediment and forming soils (Grozinger et al., 2007). There are two types of weathering: physical and chemical weathering. *Physical weathering* takes place when solid rock is fragmented by mechanical processes that do not change its chemical composition. *Chemical weathering* occurs when the minerals in a rock are chemically altered or dissolved. Chemical weathering of silicate minerals results from the differences in the thermodynamic conditions that existed at the time of the mineral formation and that of ambient conditions at the Earth's surface (White and Brantley, 1995).

The importance of chemical weathering has long been recognized in relation to the Earth's ecosystems and interactions with biology, hydrology and climate (White and Brantley, 1995). Chemical weathering has gained recognition in environmental studies related to water quality, watershed acidification, nutrient cycling, and the feedback between chemical weathering and global CO_2 budgets and global warming (White and Brantley, 1995).

During the weathering of silicate and carbonate minerals atmospheric CO_2 is taken up and converted to dissolved bicarbonate (HCO_3^-), which is then transferred to the ocean via river transport (Berner, 1995). The HCO_3^-, after delivery to the oceans by rivers, can be stored there or removed from the oceans in the forms of carbonate minerals or organic matter in sediments (CO_2 is fixed to form biomass in the oceans, organic matter in sediments is the residue of organic life which is buried in the ocean) (Berner, 1995). Typical (simplified) chemical weathering reactions of carbonate and silicate minerals, including the possible precipitation reactions in the ocean are shown below (Hartmann et al., 2009).

Carbonate

$$CaCO_3 + CO_2 \downarrow + H_2O \rightarrow Ca^{2+} + 2HCO_3^- \rightarrow CaCO_3 \downarrow + CO_2 \uparrow + H_2O \quad [2.1]$$

(No net-sink of consumed atmospheric CO_2)

Olivine

$$Mg_2SiO_3 + 4CO_2 \downarrow + 4\,H_2O \rightarrow 2\,Mg^{2+} + 4HCO_3^- + H_4SiO_4$$
$$\rightarrow 2\,MgCO_3 \downarrow + SiO_2 \downarrow + 2CO_2 \uparrow + 4H_2O \quad [2.2]$$

(Net sink <50% of consumed atmospheric CO_2 due to other processes such as alteration of the oceanic crust, etc.)

Albite

$$2Na\,Al\,Si_3O_8 + 2CO_2 \downarrow + 11H_2O$$
$$\rightarrow Al_2Si_2O_5(OH)_4 + 2\,Na^+ + 2HCO_3^- + 4H_4SiO_4$$
$$\rightarrow Al_2Si_2O_5(OH)_4 + 2\,Na^+ + 2HCO_3^- + 4SiO_2 \downarrow + 8\,H_2O \quad [2.3]$$

(Net sink of consumed atmospheric CO_2 <100% due to other processes such as reverse weathering or evaporite precipitation)

As observed from Equations [2.1], [2.2] and [2.3], atmospheric carbon is consumed during the dissolution reaction itself (Berner, 1995). However, the weathering of silicates, and not carbonates, exerts a major long-term control on atmospheric CO_2 (Berner, 1995). In contrast to the weathering of Ca- and Mg- carbonates (Eq. [2.1]), the weathering of Ca- and Mg- silicates (equations [2.2] and [2.3]) results in the net removal of CO_2 from the atmosphere (Berner, 1995). Because carbonate dissolution is not a geologic long-term sink (since carbonate precipitation in the oceans returns the consumed CO_2 relatively rapidly) accurate understanding of silicate to carbonate weathering proportion and its spatial distribution is essential, when discussing CO_2 as a climate factor (Lenton and Britton, 2006).

Sodium and K added to the oceans by silicate weathering are not removed as carbonates by reaction analogous to those illustrated by Equations [2.2] and [2.3] above, because of the great solubility of Na- and K- carbonate minerals (Berner, 1995). Sodium and K added by silicate weathering are removed by silicate formation (reverse weathering or basalt-seawater reaction) in the oceans with the return of CO_2, originally consumed by continental weathering to the atmosphere (Berner, 1995).

The atmospheric CO_2 consumption by chemical weathering of Ca-, Mg-silicate rocks has a direct link with global climate (Berner, 1995) as demonstrated by laboratory experiments (Pronost et al., 2011), field test (Matter et al., 2011) and geochemical modelling (Beaulieu et al., 2012, Goddéris et al., 2013).

Hartmann et al. (2009) calculated that the global CO_2-consumption by chemical weathering is ~237 Mt C a^{-1}. Silicate weathering accounts for 63% of the global CO_2-consumption. Previous studies indicate similar values for the consumption of atmospheric/soil CO_2 by weathering, i.e. between 258 and 288 Mt C a^{-1} (granitoids and carbonates) (Gaillardet et al., 1999; Amiotte-Suchet et al., 2003). Gaillardet et al. (1999) suggested that basalt weathering alone accounts for as much as 30 to 35% of CO_2 by silicate weathering.

Hartmann et al. (2009) estimated the spatial distribution of rock weathering (Figure 2.8). Hotspots correspond to areas where weathering rates are > 10 times higher than the global average (2 t C km^{-2} a^{-1}). Warm and high runoff areas are named hyperactive areas, which feature weathering rates 5 to 10 times greater than global average rates. Only ~9% of the global exorheic area (where water constantly flows out under all climatic circumstances) is responsible for about ~50% of CO_2- consumption by chemical weathering (or if hotspots and hyperactive areas are considered: ~3.4% of exorheic surface area correspond to ~28% of the global CO_2 consumption). The contribution of endorheic areas (limited drainage) to the global CO_2-consumption is minor (~3.7 Mt C a^{-1}).

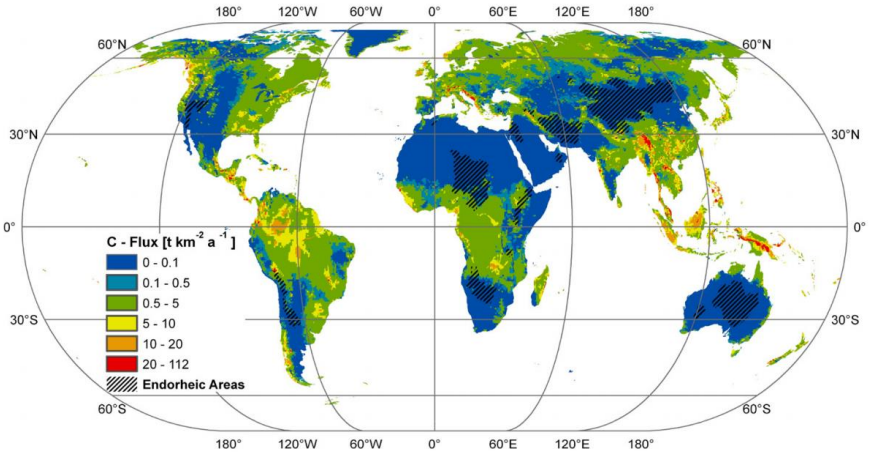

Figure 2.8. Global distribution of CO_2-consumption by chemical weathering. Note the global average for exorheic areas is ~ 2t C km^{-2} a^{-1}.
Taken from Hartmann et al. (2009).

It is important to highlight that Hartmann's map (Figure 2.8) was obtained using a high-resolution model for global CO_2-consumption by chemical weathering. This model was calibrated with data mainly from Japan and evaluated with regional literature. This modelling approach entails some

limitations. In fact, as pointed by Hartmann et al. (2009), future models should be calibrated region by region, incorporating local to regional data on geochemical composition for distinguished lithological classes, as well as weathering and diagenetic history (specifically for sediment classes). Additionally, future global dynamic carbon models need to recognize changes in the spatial correlation between runoff and lithology.

Chemical weathering of silicates is promoted by dissolved protons in water; dissolved CO_2 (to form carbonic acid, H_2CO_3) being the most common source of acidity. Other sources of acidity include sulfur dioxide and nitrogen gases emitted form volcanoes and coastal marshes, but its effect compared to CO_2 in chemical weathering of silicates remains limited on the global scale (Grozinger et al., 2007). Other sources of acidic ground water include a range of organic acids secreted during the life cycle of organism such as lichens, bacteria, filamentous algae and cyanobacteria (Huddart and Stott, 2010). It is also important to recognize the impact of humans in producing acidic rainfall from air pollution in urban areas (Huddart and Stott, 2010). Additionally, during the oxidation of sulfides, like pyrite, sulfuric acid is generated, which eventually dissolves rock forming materials (Chigira and Oyama, 2000).

Carbonic acid (H_2CO_3) is a weak acid formed when atmospheric CO_2 dissolves in rain water. Although rainwater contains only a relatively small amount of dissolved H_2CO_3 (0.0006 g L^{-1}), that amount is enough to weather feldspars and dissolve rocks over long periods of time (Grozinger et al., 2007).

Chemical weathering processes by which rock-forming minerals may be attacked (damage or weakening of the mineral network), altered (replacement or exchange of new species) or transformed (generation of new species) include: solution (dissolution or chelation), hydrolysis, hydration, isomorphous replacement and oxidation/reduction reactions (Huddart and Stott, 2010). The removal of metal ions by solution or hydrolysis, the addition or removal of water, and the substitution of one ion by another all have the potential not only to weaken or stress the rock-forming minerals but to change its properties, such as its solubility (Huddart and Stott, 2010). They can transform a mineral by removal and substitution to create a new, secondary mineral (Huddart and Stott, 2010). Therefore, three basic products of chemical weathering can be recognized: (a) a residual framework of minerals resistant to weathering; (b) secondary clay minerals formed by transformation of primary silicate minerals; (c) the loss of minerals and both cations and anions in solution (Huddart and Stott, 2010).

2.3.1. Controls on the intensity of chemical weathering

Several factors control the intensity of chemical weathering, either intrinsic to the particular rock (susceptibility of the minerals) or extrinsic, for example including the influence of rainfall and temperature.

Intrinsic factors encompass the presence of discontinuities and mineral susceptibility. Chemical weathering is enhanced by the presence of discontinuities within the rock since they allow the penetration of air and water (Huddart and Stott, 2010). Mineral susceptibility can be expressed through the Bowen's reactions series (Fig. 2.9).

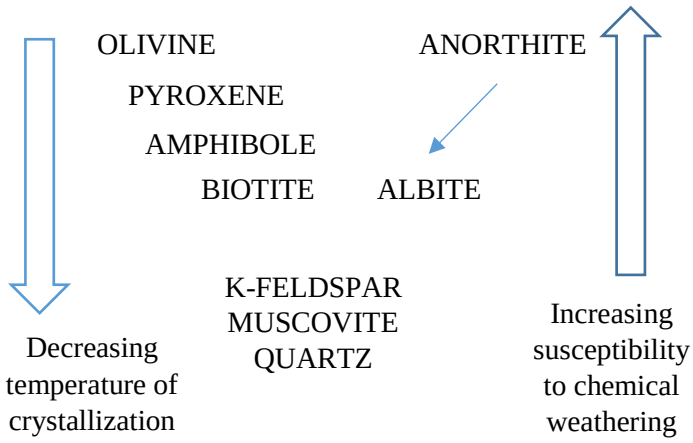

Figure 2.9. Bowen's reactions series and mineral susceptibility to chemical weathering.
Taken from Huddart and Stott (2010).

Mineral susceptibility to weathering has also been linked with the relative stability of different cations. The general mobility sequence is calcium ≥ sodium ≥ magnesium ≥ silica ≥ aluminum ≥ potassium ≥ iron ≥ titanium. The concentrations of these cations in a particular mineral may help to determine its stability to weathering (Huddart and Stott, 2010).

Extrinsic factors refer to the environment conditions that impact chemical weathering. These include climate, vegetation and topography which drive variations in temperature, water dynamics and water chemistry (Huddart and Stott, 2010). As illustrated in Figure 2.10, the environmental factors can be divided between thermodynamic and kinetic factors, which combined with the nature of the parental material, the organic activity, the topography and the climate affect in different ways the weathering rate of minerals and rocks in natural environments (Curtis, 1976; Huddart and Stott, 2010).

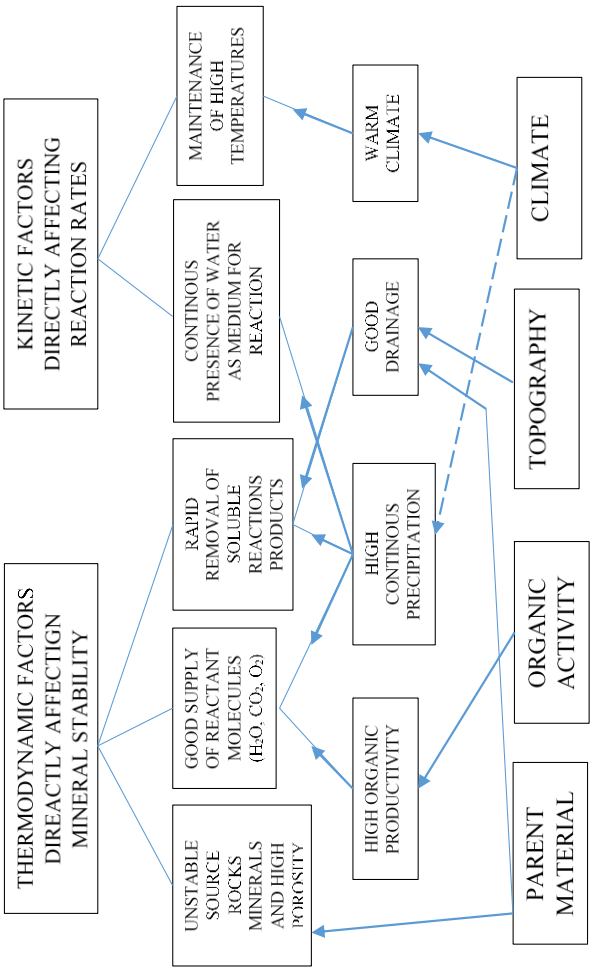

Figure 2.10. Extrinsic factor affecting chemical weathering of minerals. *Taken from Huddart and Stott, 2010 and Curtis (1976).*

2.3.2. Measuring weathering rates

Weathering studies are being conducted over a wider range of geochemical environments and geographic localities (White and Brantley, 1995). Efforts have also been made to characterize global weathering flux rates more accurately and to develop global weathering models (White and Brantley, 1995). Natural weathering can be characterized by changes in microscopic surface morphologies of mineral grains, by solid and solute changes in soil profiles, from solutes fluxes in small watersheds and large river basins and by continental and global-scale element cycles (White, 2011).

Chemical weathering is characterized in either qualitative or quantitative terms (White, 2011). Qualitative approaches entail comparing the relative weathering of different minerals or the weathering of the same mineral in different environments (White, 2011). The second approach focuses on the determination of weathering rates that quantitatively describe silicate mineral and rock weathering (White, 2011). Thus, the rates obtained are related to reaction mechanisms and can be used as predictive tools in estimating how weathering will behave under various environmental conditions (White, 2011).

The **weathering rate** *R (mol* m^{-2} s^{-1}*)* of a primary silicate mineral is commonly defined by the relationship (White, 2011):

$$R = \frac{\Delta M}{S\,t} \qquad [2.4]$$

where ΔM (mol) is the mass change due to weathering, S (m^2) is the total surface area involved and t (s) is the duration of the reaction (White, 2011). Thus, weathering rate is equivalent to a **chemical flux** (*mol* m^{-2} s^{-1}; White, 2011). Weathering rates can be element, or mineral specific. Weathering rates based on geographic and volumetric surface areas are referred to as **weathering fluxes**, and weathering based on specific surface areas are referred to as mineral specific **weathering rates** (White, 2011). Examples of element-based rates are those reported for annual stream or river discharge, and normalized to the watershed area (White, 2011). **Watershed fluxes** are commonly defined as the sum of rock-derived base cations solubilized per unit area of geographic surface and per unit of time, being equivalent to **chemical denudation** (Bluth and Kump, 1994; White and Blum, 1995). This approach commonly involves comparing changes between initial and final solution concentrations in a known volume of water (White, 2011). The calculation of mineral weathering rates based on solute concentrations is complicated by the fact that individual solution species are commonly produce by more than one weathering reaction. Thus, it is assumed that weathering products are characterized by specific geochemical end-members representing lithologies (e.g., carbonate or silicates).

Silicate weathering fluxes based on mineral flux data in the literature are less common than element-base data (White, 2011). More data are available for plagioclase feldspar than other mineral phases, which partly reflects the more common occurrence of the former in crystalline rocks. Weathering rates of other silicates are more difficult to determine from elemental fluxes because their major components are commonly derived from more than one mineral (White, 2011).

2.3.3. Measuring chemical weathering rates in natural systems (catchments and river chemistry)

The determination of weathering rates by solute budgets requires the measurement of the inputs to a catchment from the atmosphere and the output from the catchment, usually in the form of surface runoff (Drever and Clow, 1995). The difference between the flux in and the flux out for each element represents the generation (or removal) of the element by processes within the catchment. Chemical weathering is not the only process affecting solute budgets. Uptake by plants and cation exchange may significantly influence element fluxes (Drever and Clow, 1995). Assuming that the time-scale is long enough that changes in water storage can be ignored, Drever and Clow (1995) used Eq. [2.5] to illustrate the main solute budgets.

$$\begin{aligned} solutes\ in\ outflow = {} & solutes\ from\ atmosphere \\ & + solutes\ from\ weathering \\ & \pm solutes\ from\ change\ in\ biomass \\ & \pm change\ in\ exchange\ pool \\ & - precipitation\ in\ secondary\ minerals \end{aligned} \quad [2.5]$$

There is not simple direct way of measuring the contribution of chemical weathering to the solutes measured at the output of a catchment. The most common approach is to assign values to (or simply ignore) the biomass change and ion exchange terms in Eq. [2.5] and determine the weathering term by difference (Drever and Clow, 1995). For instance, in catchments where bedrock weathers rapidly, the weathering term is much larger than the other two. Where atmospheric deposition has not been affected significantly by pollution, neglecting the ion exchange term should not introduce much error, and in catchments that are largely unvegetated, the biomass term should be negligible.

An alternative approach is to consider the budget of an element that is not significantly affected by ion exchange or biomass uptake, such as sodium or silicon (Stauffer and Wittchen, 1991; White and Blum, 1995). If the flux of sodium from weathering is known (output- atmospheric input), and the stoichiometry of weathering is known, then the fluxes of the other cations, notably Ca^{2+} and Mg^{2+}, can be calculated by multiplying the sodium flux by the appropriate stoichiometric ratio (Drever and Clow, 1995). However, in coastal areas with low weathering rates, the flux of Na from weathering may be small compared to the flux from the atmosphere, and in general there is no easy way of measuring the stoichiometry of weathering. Silica can be used instead of sodium. The advantage is that the input-output budget of silica can

be established with more certainty than that of sodium. The disadvantage is that silica is partially retained in secondary minerals such as kaolinite and smectite and may be affected by adsorption-desorption reaction and plant uptake. Further, when silicon enters into the oceans it is partly taken up by diatoms, which use silicon as an essential nutrient for their growth (Struyf et al., 2009).

Several researches have used Sr isotopes to characterize the relative contribution of cation exchange and weathering in the output budgets of catchments (Aberg et al., 1989; Miller et al., 1993). If it is assumed that Ca^{2+} behaves exactly as Sr^{2+}, then the Ca^{2+} in the outflow can be assigned to the two sources in the same ratio as for Sr (Drever and Clow, 1995). Another approach to establish a long term weathering budget for a catchment is to measure the accumulation of soil and the change in composition that occurs as bedrock is converted to soil (White, 1995). Table 2.3 contains a tabulation of weathering rates for the common silicate minerals based on average watershed fluxes and geographic areas (White, 2011).

Table 2.3. Weathering rates for selected silicate minerals based on average annual watershed discharge.
Taken from White (2011).

Watershed	**Rate (mol ha^{-1} yr^{-1})**	**References**
Plagioclase		
Emerald Lake, CA, USA	44	Williams et al. (1993)
Loch Vale Watershed, CO, USA	86	Mast et al. (1990)
Gigndal Watershed, Norway	100	Frogner (1990)
Lapptrasket Basin, Sweeden	148	Andersson-Calles and Erisckssson (1979)
Rio Parana, Brazil	174	Benedetti et al. (1994)
Plastic Lake, Canada	185	Kirkwood and Nesbitt (1991)

Table 2.3 (continued). Weathering rates for selected silicate minerals based on average annual watershed discharge.
Taken from White (2011).

Watershed	Rate (mol ha^{-1} yr^{-1})	References
K-feldspar		
Pond Branch, MD, USA	11	Cleaves et al. (1970)
Silver Creek, ID, USA	44	Clayton (1986)
Plastic Lake, Canada	69	Kirkwood and Nesbitt (1991)
Biotite		
Lapptrasket Basin, Sweeden	3	Andersson-Calles and Erisckssson (1979)
Loch Vale Watershed, CO, USA	26	Mast et al. (1990)
Hornblende		
Lapptrasket Basin, Sweeden	2	Andersson-Calles and Erisckssson (1979)
Plastic Lake, Canada	8	Kirkwood and Nesbitt (1991)
Emerald Lake, CA, USA	24	Williams et al. (1993)

2.3.4. Weathering rates of aluminosilicates

Weathering rates of aluminosilicates have been extensively quantified in the latest years, either for silicate minerals or for natural and synthetic glasses. The rate equations reported for dissolution rates of minerals are usually used as input data in geochemical modelling codes to assess the temporal evolution of fluids during water-rock interaction both in natural systems and in industrial processes (Goddéris et al., 2009).

Weathering rates depend on factors such as the mineralogy of the rocks exposed, the reactive surface area of these minerals, the supply of water, its residence time in the soil and initial pH, the abundance of organic acids, and the temperature of the solutions in contact (Kump et al., 2000), additional factor already mentioned by Keller (1957) include oxygen and other gases in the system, the macro and micro flora and fauna present, wetting and drying of colloids and salts in the rocks, and land topography.

The weathering rates of common silicates are presented in Table 2.4.

Table 2.4. BET surface area-normalized weathering rates of common silicates.

Taken from White (2011).

Weathering environment	**Log rate (mol m^{-2} s^{-1})**	**References**
Plagioclase		
Davis Run saprolite, VA, USA	-16.4	White et al. (2001)
Panola bedrock, GA, USA	-15.7	White et al. (2001)
Modesto Soil, Merced, CA, USA	-15.1	White et al. (1996)
Trnavka River watershed, Czech	-14.0	Paces (1986)
Gardsjon watershed soil, Sweden	-13.1	Sverdrup (1990)
Loch Vale Nano-Catchment, CO, USA	-12.8	Clow and Drever (1996)
K-feldspar		
Davis Run Saprolite, VA, USA	-16.8	White et al. (2001)
Upper Modesto Soil, Merced, CA, USA	-15.3	White et al. (1996)
Loch Vale Nano-Catchment, CO, USA	-13.8	Clow and Drever (1996)
Gardsjon watershed soil, Sweden	-13.3	Sverdrup (1990)
Hornblende		
Chine Hat Soil, Merced CA, USA	-17.0	White et al. (1996)
Riverbank Soil, Merced, CA, USA	-16.0	White et al. (1996)
Lower Modesto Soil, Merced, CA, USA	-15.7	White et al. (1996)
Lake Gardsjon, Sweden	-13.6	Sverdrup (1990)
Biotite		
Panola, GA, USA	-16.5	White (2002)
Rio Icacos, Puerto Rico	-15.4	White (2002)
Loch Vale Nano-Catchment, CO, USA	-14.1	Clow and Drever (1996)
Quartz		
Rio Icacos, Puerto Rico	-15.1	White (2002)

2.4. MINERAL DISSOLUTION RATES

The quantification of chemical weathering rates is not an easy task and therefore, a great effort is devoted to measuring chemical kinetics in well-controlled systems and developing theoretical models to express the rate and mechanism of mineral reaction (White and Brantley, 1995). A rate equation that expresses mineral weathering must be compatible both with experimental observation and with fundamental concepts of chemical kinetics, whether at the atomic, reactor, soil, bedrock, watershed or global scale (Lasaga, 1995). A rate equation properly parametrized for a well-understood and carefully controlled system, will be useful in extrapolating to other systems (White and Brantley, 1995).

On one hand it is believed that careful measurement of laboratory dissolution kinetics, surface complexation, and mineral surface areas will yield predictive models for mineral weathering at a variety of scales from atomic surface to the global (White and Brantley, 1995). On the other hand, it has been also pointed that natural weathering kinetics will never be fully quantified or easily predicted, but it is known as well that the attempt at quantification is a useful process by which understanding emerges (White and Brantley, 1995; Lasaga, 1995).

The transition state theory (TST) combined with the surface complexation approach (SC) have been used to describe mineral dissolution over wide ranges of solution composition, chemical affinity, and temperature (Schott et al., 2012).

2.4.1. Transition State Theory (TST)

The TST (Eyring, 1935) assumes that (i) in order to reach products, the reactants need to overcome an energy barrier (activated complex), and (ii) direct and reversible attachment of reactants at mineral surface sites governs the dissolution/precipitation. This theory is used to describe the mineral dissolution/precipitation kinetics near equilibrium (Schott et al., 2012).

The TST focuses on the activated complex and assumes that the reaction rate is equal to the product of two terms, the concentration of the activated complex and the frequency with which these complexes cross the energy barrier (Schott et al., 2009).

$$r_+ = k\,[AB^*] \qquad [2.6]$$

where r_+ is the forward reaction rate, *k* refers to a rate constant and *[AB*]* represents the concentration of the activated species.

The reaction rate constant can be expressed in term of the thermodynamic functions for the formation of the activated complex. It is assumed that the activated complex is the same for the forward and backward reaction (Lasaga 1981). Thus, the reaction rate constant is expressed by:

$$r = r_+ \,(1 - e^{\Delta G/\sigma RT}) = \, r_+ \,(1 - e^{A/\sigma RT}) \qquad [2.7]$$

where *ΔG* represents the Gibbs free energy difference between reactants and products, *A* is the chemical affinity of the elementary reaction, and *R* and *T* denote the gas constant and absolute temperature. *ΔG* and *A* both are normalized to one mole of the elementary reaction. The chemical affinity of an overall reaction is related to the chemical affinity of the elementary reaction by a stoichiometric coefficient (σ), equal to the number of moles of activated complex required to transform one mole of reactant (Schott et al. 2009).

The forward rate can be expressed as:

$$r_+ = \, k_+ \, \prod_i a_i^{ni} \qquad [2.8]$$

where k_+, is a rate constant, and a_i and n_i stand for the activity of the *ith* species involved in the activated complex (or its precursor) formation reaction and the reactions order with respect to this species, respectively. Eq. [2.8] accounts, for example, for the proton and organic ligand promoted dissolution of aluminosilicates or the inhibition of their dissolution by aqueous aluminum (Schott and Oelkers, 1995; Oelkers and Schott, 1998).

TST-derived rate laws such as shown in Equation [2.8] are usually implemented in geochemical modelling codes describing water-rock interaction. The key to using the TST to describe dissolution rates as a function of solution composition is identification of the stoichiometry and reactions forming activated complexes from the reactants. Insight into these surface complexes can be obtained from the surface complexation approach (SC) (Schott et al., 2009).

2.4.2. Surface complexation approach (SC)

The formation of activated complexes from the reactants is important in the context of the TST. It has been suggested that the activated complex for the dissolution and precipitation reaction has the same stoichiometry as the surface complexes that form on mineral surfaces (Schott et al., 2009). In the absence of water, the surface of a metal oxide is characterized by the presence of low-coordinated metals, giving rise to Lewis acidity. In aqueous solution, water molecules coordinate to these metal centers and dissociative chemisorption occurs with formation, depending on solution pH, of positively, negatively charged and neutral hydroxyl groups that can be exchanged with the ligands present in solution (Schott et al., 2009).

When placed in an aqueous solution the coordinative environment of metals at the mineral-water interface can be changed by formation of inner or outer sphere complexes which promote surface dissolution by polarizing and/or weakening interatomic bonds in the vicinity of the central metal and thus facilitating its detachment into solution (Schott et al., 2009).

A schematic representation of the surface of a metal oxide is presented in Figure 2.11. This shows the possible interactions with water according as described above (Schott et al., 2009).

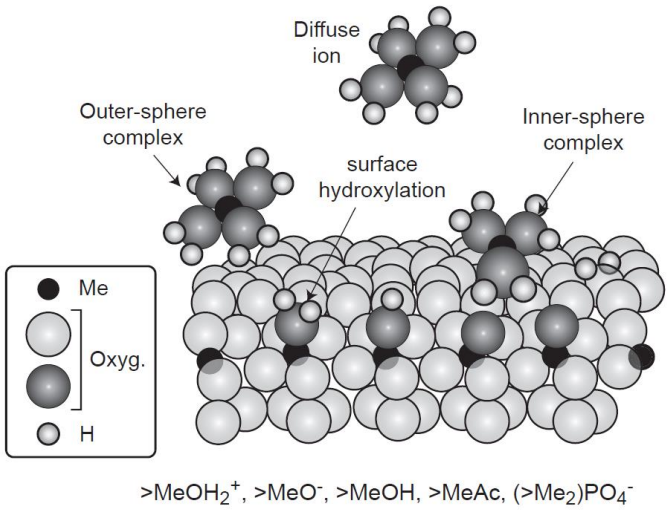

Figure 2.11. Representation of the surface of a metal oxide in the presence of water.
Taken from Schott et al. (2009).

The surface species present at the mineral-fluid interface can be viewed, within the TST, as the precursor of the activated complex (Stumm et al., 1983). The precursor has the same stoichiometry and its concentration is proportional to that of the activated complex (Wieland et al., 1988). The following rate laws can be written to describe proton- (Eq. [2.9]), hydroxyl- (Eq. [2.10]) and ligand- (Eq. [2.11]) promoted dissolution, by analogy with reactions derived from TST (Schott et al., 2009).

$$r_{+,H} = k_H \{> MeOH_2^+\}^{n_H} \quad [2.9]$$

$$r_{+,OH} = k_{OH} \{> MeO^-\}^{n_{OH}} \quad [2.10]$$

$$r_{+,L} = k_L \{> MeL\}^{n_L} \quad [2.11]$$

where the k_i (k_H, $k_{OH,}$ k_L) are the rate constants, {>MeX} stands for the concentration of the various rates controlling surface precursor complexes, and n_i (n_H, $n_{OH,}$ n_L) represents the reaction order with respect to the subscripted complex (Schott et al., 2009).

2.4.3. The SCM/TST description of the kinetics of dissolution of oxide minerals

The dissolution of single oxide minerals requires breaking only one type of bond. The far from equilibrium dissolution rate for simple oxides can be described from the sum of parallel elementary reactions occurring at metal centers (Schott et al., 2009).

$$r_{+,H} = k_H \{> MeOH_2^+\}^{n_H} + k_{OH} \{> MeO^-\}^{n_{OH}} + k_L \{> MeL\}^{n_L} + k_{H2O} \quad [2.12]$$

where n_H and n_{OH} are the reaction orders of proton- and hydroxyl-promoted dissolution. The rate of the ligand-promoted dissolution is generally assumed to be proportional to the ligand surface concentration $> MeL$ so, n_L is usually assumed to be equal to one. Most mineral dissolution experiments have been performed in diluted solutions in which water concentration is roughly constant. Therefore, the impact of water activity on mineral oxide dissolution kinetics, as incorporated in the final term of Equation [2.12], is poorly known (Schott et al., 2009).

2.4.4. Dissolution mechanism and rates of multi-oxides minerals

The dissolution of mixed oxide minerals, including many major rock forming silicates, requires the breaking of more than one type of metal-oxygen bond. The dissolution mechanism of multi-oxide minerals and glasses can involve sorption reactions, as well as exchange reaction between protons and constituting metals that are not essential to maintaining the mineral structure (Schott et al., 2009). These reactions are demonstrated, for instance, by the formation of metal depleted leached layers during the dissolution process.

These exchange reactions arise in multioxides because metal-oxygen bonds break at very different rates depending on their relative strength. This relative bond strength is also reflected in the rate of exchange of water molecules in the coordination sphere of the corresponding aqueous ions. Thus, multioxide mineral structure and composition have a strong impact on the extent of the non-stoichiometric release of elements and the thickness of formed leached layers (Schott et al., 2009).

By comparing the relative rates for breaking metal-oxygen bonds and the structure of multi-oxide silicates, Oelkers (2001) proposed a dissolution mechanism for the major multi-oxide silicates including aluminosilicates, basic silicates, and natural glasses. An example is found in Figure 2.12.

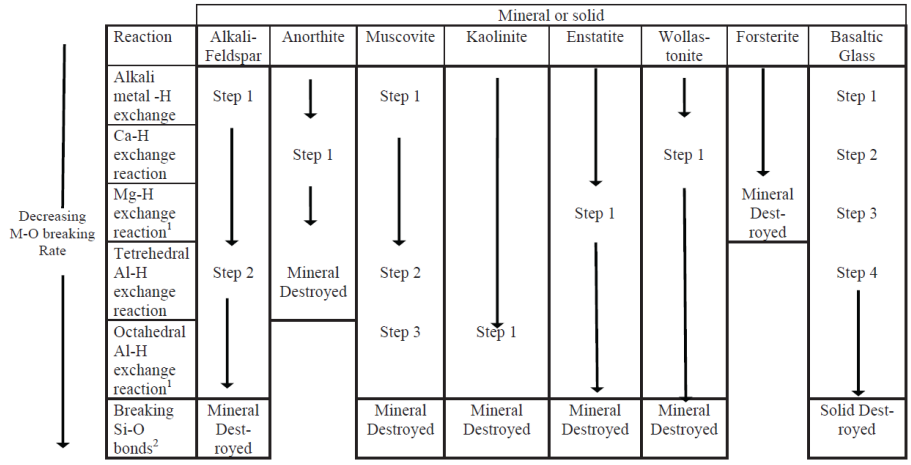

Figure 2.12 Summary of dissolution mechanism of some minerals and basaltic glass at acidic conditions.
Taken from Oelkers (2001).

In general, at acidic conditions, monovalent metal-oxygen bonds break more rapidly than divalent metal-oxygen bonds, which break faster than Si-O bonds. Dissolution is initiated by the removal of the metal having the fastest breaking metal-oxygen bonds. The removal of metals from the silicate structure is coupled to the addition of protons into the mineral structure (Oelkers et al., 2009).

2.4.5. Aluminosilicate minerals and glass dissolution rates

Equilibrium vs. far from equilibrium

In a classic sense (Pitzer and Brewer, 1961; Denbigh, 1971), a system is in **equilibrium** when it occupies a specific region of space within which there is no spontaneous tendency for change to occur (Bethke, 2008). Thus, all possible chemical reactions are in equilibrium. For example, Figure 2.13 shows the rates of kaolinite (and albite) dissolution-precipitation at 150 °C and pH=2, illustrating the equilibrium definition.

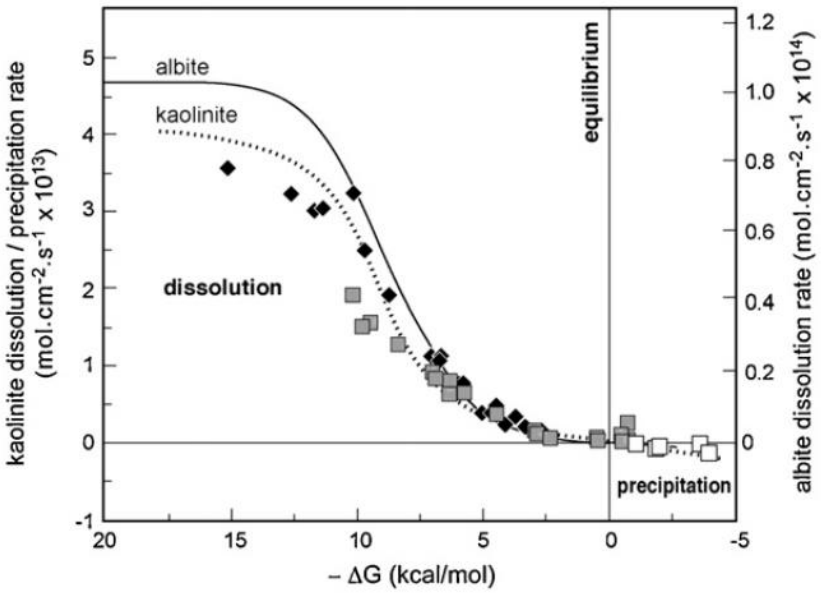

Figure 2.13. Kaolinite dissolution/precipitation rates at 150 °C and pH = 2 *(Devidal et al., 1997)* and albite dissolution rates at 150 °C and pH = 9.2 *(Hellmann and Tisserand, 2006)* as a function of the Gibbs free energy of the mineral dissociation reaction.
Taken from Schott et al. (2012).

In contrast, in a **far from equilibrium** system, one or more reactions proceed toward equilibrium at rates that are vanishingly small on the time scale of interest (Bethke, 2008). For example, Figure 2.14 shows the variation of dissolution rates of albite under far from equilibrium conditions (reactions to precipitate this mineral have not progressed to equilibrium), until the far from equilibrium dissolution rate at steady state is reached.

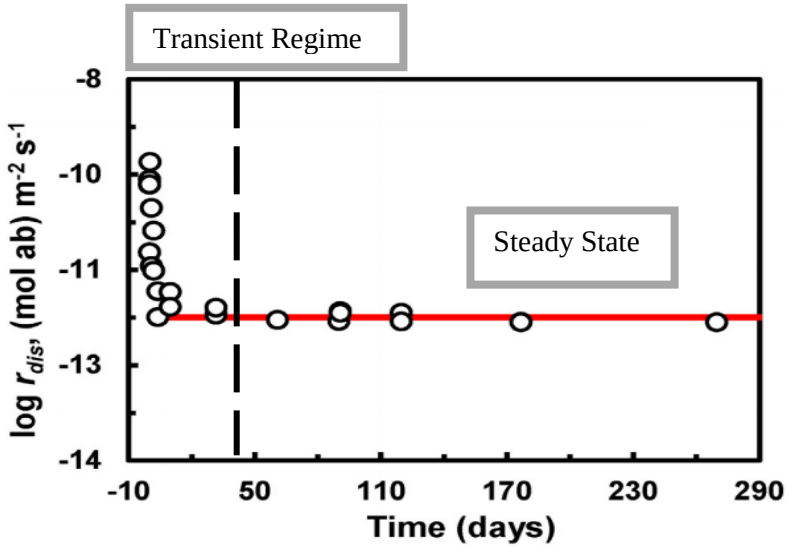

Figure 2.14. Albite dissolution rates at 22 °C and pH 3.
Adapted from Zhu et al. (2016).

Far-from equilibrium dissolution rates

The term **dissolution rate** in the present study refers to the steady-state temporal metal release rate divided by the stoichiometric number of moles of this metal in each mole of dissolving mineral or glass. **Steady state** is defined as conditions where dissolution rates are time independent and where dissolution is stoichiometric (Oelkers, 2001).

In this study, for the experimental determination of the steady-state dissolution rate associated to volcanic material (rock/glass), we applied the approach followed by Oelkers (2001), Oelkers et al. (2001), Wolff-Boenisch et al. (2004) and Declerq et al. (2013) through the application of the transition state theory and the surface complexation approach.

Removal of the metals with the fastest breaking metal-oxygen bond by proton exchange reaction marks the start of the dissolution. Dissolution continues by

the successive removal of metals in the order of the relative rates for breaking their corresponding metal-oxygen bonds, until the mineral or glass structure is destroyed (Guy and Schott, 1989).

The formation of an Al and Si-rich surface of constant thickness that leads to long-term stoichiometric dissolution has been already described (Schott et al., 2009). This leached layer is formed as a result of the rapid exchange of protons for alkali and alkaline-earth metals near the glass surface (Guy and Schott, 1989). The rate limiting step of natural aluminosilicate glass dissolution is the destruction of this Si- and Al- rich surface layer. Inside this layer Al-O bonds are weaker compared with their Si-O counterparts, leading to the formation of partially detached Si tetrahedral. For numerous Al silicates, the removal of the partially detached Si from the leached layer constitutes the rate limited step (Oelkers, 2001; Oelkers and Gislason, 2001; Gislason and Oelkers, 2003; Wolff-Boenisch et al., 2004).

According to Oelkers (2001) partially detached Si are formed from the removal of adjacent Al atoms:

$$> (Si-O)_n - Al + 3H^+ \rightarrow n\left(> Si - O - H_{\frac{3}{n}}\right) + Al^{3+} \quad [2.13]$$

Where >Si-O-$H_{3/n}$ represents a partially detached Si whereas >$(Si\text{-}O)_n$-Al represents fully attached Si groups near the glass surface. The law of mass for the reaction is:

$$K_1 = \frac{a_{Al^{3+}}\, X^n_{>Si-O-H_{3/n}}}{a^3_{H^+}\, X_{>(Si-O)n-Al}} \quad [2.14]$$

Where K_1 corresponds to the equilibrium constant of the reaction, a_i denotes the activity of the *ith* aqueous species, *n* refers to the number of partially detached Si created by the removal of one Al atom from the surface, and X_i stands for the mole fraction of the surface species.

If it is assumed that the surface has retained most of its Al, i.e. $X_{>(Si\text{-}O)n\text{-}Al} \approx 1$, reorganizing Eq.2.14 gives:

$$X^n_{>Si-O-H_{\frac{3}{n}}} = \left(K_1 \frac{a^3_{H^+}}{a_{Al^{3+}}}\right)^{1/n} \quad [2.15]$$

Using the TST (Eyring, 1935; Lasaga, 1981), the far-from-equilibrium dissolution rate, r_+, is proportional to the concentration of these partially detached Si near the surface (Oelkers et al., 1994; Shott and Oelkers, 1995; Schott et al., 2009).

$$r_+ = k_+ X_{>Si-O-H_{3/n}} = k'_+ \left(\frac{a^3_{H^+}}{a_{Al^{3+}}}\right)^{1/n} \quad [2.16]$$

Where k_+ refers to a rate constant and $k'_+ = k_+ K_1^{1/n}$

In this study, Eq. [2.16] will be used to describe the measured dissolution rates of volcanic rocks/glass at different pH conditions.

2.5. LABORATORY DISSOLUTION STUDIES TO QUANTIFY CHEMICAL WEATHERING OF ALUMINOSILICATES

Over the last few decades, considerable experimental effort has been made to quantify the weathering rates of silicate minerals (Brantley, 2003, and references therein) and glass (e.g. Oelkers and Gislason, 2001; Gislason and Oelkers, 2003; Wolff-Boenisch et al., 2004; Stockmann et al., 2008). In order to quantify chemical weathering rates of aluminosilicates, laboratory experiments have been conducted on a plethora of minerals and glasses under controlled conditions of temperature, pH, and solution composition (Schott et al., 1981; Cygan et al., 1989; Oelkers and Gisalson, 2001, Declerq et al., 2013). Experiments have been run using different reactor designs such as batch, continuously stirred, plug flow and fluidized bed (Chou and Wollast, 1984, Wolff-Boenisch et al., 2004, Gudbrandsson et al., 2014, Ostertag-Henning et al., 2014) (see Chapter 3).

Si-O tetrahedra are the building blocks of silica minerals and glasses. Within minerals, Si-O tethrahedra form a regular, geometrically repeating pattern, over a large scale of unit cells (Doremus, 1994). In contrast, the Si-O tethahedra in glass do not exhibit the large scale regularity of minerals. The difference in polymerization between a 'crystalline' mineral and an 'amorphous' glass lies in the degree of long-range order of Si-O tethrahedra in the structure. Owing to rapid quenching, the glass exhibits less polymerization and less ordering of Si-O bonds than the minerals, making it less resistant to dissolution reactions (Wolff-Boenisch et al., 2006).

Regarding the dissolution of pure minerals, Palandri et al. (2004) have compiled kinetics parameters for over 70 minerals, including for all the major classes of silicates. Those rate parameters are for surface controlled reactions at conditions that are far from equilibrium, mainly pure minerals. The plagioclase feldspars have been studied extensively at acid conditions (e.g. Chou and Wollast, 1984; Blum and Lasaga, 1991; Brantley and Stilling, 1996; Ganor et al., 2005; Hellmann et al., 2010). Dissolution rates of pyroxene have also been extensively studied in the laboratory (e.g. Schott and Berner, 1985, Brantley and Chen, 1995, Stockmann et al., 2008; Zakaznova-Herzog et al., 2008). Dissolution rates of olivines has been also reported (e.g. Grandstaff, 1977; Wasklewicz et al., 1993; Chen and Brantley, 2000; Hanchen et al., 2006; Daval et al., 2011).

Dissolution studies for complex plagioclase solid solutions/exsolutions are less frequent, although we could mention the study of Gudbrandsson et al. (2014). This study presented an attempt to determine experimentally the dissolution rates of plagioclase (ranging in composition from An2 to An89) as a function of their composition using mixed-flow reactor techniques. Thus, it

was determined an equation describing plagioclase dissolution rates ($r_{si,BET}$ mol cm^{-2} s^{-1}) as a function of mineral composition and aqueous fluid compositions found at 22 °C and pH<6.

$$\log r_{Si,BET} = (0.004An\% + 0.05) \times log\left(\frac{a_{H^+}^3}{a_{Al^{3+}}}\right) + 0.033\, An\% - 14.77 \quad [2.17]$$

An% (percent anorthite in the plagioclase solid solution)

In terms of glass dissolution, it could be mentioned the work done on basaltic and borosilicate glasses using flow through systems (e.g. Guy and Schott, 1989; Oelkers and Gislason, 2001; Gislason and Oelkers, 2003) and rhyolitic volcanic glasses (Yokoyama and Banfield, 2002, Declerq et al., 2013). Some natural glass dissolution studies were performed in either high ionic strength/seawater solutions or at high temperatures, and many were carried out in closed system batch reactors (Crovisier et al., 1982, Crovisier et al., 2003). To overcome problems of formation of secondary phases, other studies have been performed in mixed flow reactors estimating far-from equilibrium dissolution rates (e.g Oelkers and Gislason, 2001; Gislason and Oelkers, 2003).

Some glass dissolution studies were aimed at the potential utility as nuclear host of basaltic and borosilicate glasses (Techer et al. 2000; Crovisier et al. 2003; Rajmohan et al., 2010). Other aimed to understand the dissolution mechanism through the leaching of siliceous glass (Fiore et al. 1999; Wolff-Boenisch et al. 2004). There are also studies of glass leaching behavior in order to understand the role of glass in natural process (Cailleteau et al., 2008). Dissolution studies focused as well in the determination of leaching rates from natural systems (tephra/tuff/glass/andisols) (Shoji et al., 1993; Dahlgren et al., 1999; Shikazono et al., 2004) and in the comparison with laboratory dissolution experiments (Hochella and Banfield, 1995; Yokoyama and Banfield, 2002).

Regarding dissolution studies of volcanic glass, we could mention the study of Wolff-Boenisch et al. (2004, 2006). Wolff-Boenish et al. (2004), using 17 volcanic glasses from Icelandic volcanic eruptions of the last 3,200 years, generated an equation to describe the variation of far-from-equilibrium natural glass dissolution rates as a function of glass composition at the low temperatures typical of Earth surface environments. Based on dissolution rate measurements obtained at pH 4 and 25 °C for natural glasses varying in composition from basalt to rhyolite, Wolff-Boenisch et al. (2004) established a quantitative relationship linking $r_{Si,geo}$ (mol m^{-2} s^{-1}) to the glass silica content:

$$\log r_{Si,geo} = -0.03 \times [SiO_2\ (wt.\%)] - 7.58 \quad [2.18]$$

The study conducted by Wolff-Boenisch et al. (2006) illustrated the effect of crystallinity on dissolution kinetics as a function of chemical composition for natural glasses and silicate minerals. They conclude that natural silicate glass dissolution rates were significantly faster than their silicate mineral counterparts only when they were Si-rich. Si-poor glasses and minerals (e.g., of ultrabasic composition) exhibit similar dissolution rates as crystallinity has little effect on Si polymerization in these solids.

As it has been presented, there is a plethora of dissolution studies performed on individual minerals and glasses, while the studies focused on polycrystalline and poly-mineral rocks are less frequent among dissolution studies. Accounting for multi-mineral rock dissolution studies, we could mention the work done on a metabasalt (actinolite and chlorite) by Critelli et al. (2014), on serpentinite (antigorite and magnetite) by Critelli et al. (2015), on a multi-mineral sediment (quartz, smectite, plagioclase and K-feldspar) by Beckingham et al. (2016, 2017), on carbonate rich shale (calcite, illite, quartz) by Deng et al. (2017), on carbonate rock (calcite and dolomite) by Levenson et al. (2017), on organic rich shale (calcite, quartz, kaolinite) by Kreisserman and Emmanuel (2018).

2.6. MODELLING WEATHERING PROCESS AT LARGE SCALE THROUGH NUMERICAL MODELS

Geochemical models are especially important in weathering process research, not because they produce results of their own right, but because they allow complex and non-linear systems to be investigated and data from such systems to be interpreted. With models, the interaction of several simultaneous process in a single experiment can be studied. Models serve to test the synthesized understanding of a system, based on mathematical representation of its subsystems and the proposed coupling subsystems. In addition, models predict what will happen in the future, based on the capability to explain how and why weathering process at large scale have worked in the past (Sverdrup and Warfinge, 1995).

A main challenge for the accurate description of continental weathering is to identify the main factors controlling chemical weathering and to quantify their effect in given environments and at various geometric and time scales. Therefore, a critical step is the building of a numerical model describing the large-scale (watershed-scale) weathering of silicate rocks, based on a

description of the weathering processes as mechanistic as possible (including dissolution of primary and secondary minerals and precipitation of secondary minerals and coupled to hydrological processes) (Goddéris et al., 2006).

The level of complexity dictates the parameters that must be measured for the system. As models attempt to simulate systems at larger scales, model typically incorporate parameters measurable at the scale of interest, and ignore or lump other parameters that are measured at lower scales. For example, a mass balance mode of a watershed is typically normalized per unit land area, whereas a mass balance model of dissolution in a chemical reactor is typically normalized per unite area of mineral surface (White and Brantley, 1995).

By the time models reach the scale of global or continental weathering, weathering is analyzed as a system of equations describing fluxes, normalized by subaerial land area, between major reservoirs. This systems approach, while unable to reproduce exact rates or elucidate fundamentals mechanism, yields insight into the sensitivity of the global system to changes in the significant variables.

Mechanistic models already exist that work at the square-meter-scale in natural environments and are capable of describing weathering process down to approximately the root depth. For instant, kinetic models such as the KINDIS code (Madé et al., 1994) have been used in an attempt at describing mineral dissolution in natural environment (Probst et al., 2000). Among those models, the pioneering and most complete one is the SAFE model developed by Sverdrup and Warfinge (1995) that has been tested and validated for many locations and has been upscaled in several countries to create regional weathering maps (Goddéris et al., 2006).

These mechanistic models have been used to described weathering processes and fluxes at the watershed scale (Goddéris et al., 2006, 2009), to interpret mineral and aqueous species profiles in weathering regoliths (Brantley and White, 2009; Goddéris et al., 2010; Maher et al., 2009), to quantify reactive transport of CO_2 injected in deep saline aquifers (Daval et al., 2010; Knauss et al., 2005; White et al., 2005; Xu et al., 2005), and to predict the response of a large artic watershed to future climate change (Beaulieu et al., 2012). These models are based on a rigorous description of the reactive transport occurring in the critical zone taking into account the effect of water drainage (Schott et al., 2012).

Goddéris et al. (2006) proposed a mechanistic numerical model of silicate weathering operating at the catchment scale, named WITCH. In chapter 8, the application of this model in our study is shown along with the model description.

2.7. IMPORTANCE OF ROCK REACTIVE SURFACE AREA FOR THE QUANTIFICATION OF CHEMICAL WEATHERING

Currently there is not protocol for determining the mineral reactive surface area. Therefore, it is often estimated using one of many specific surface area (SSA) or effective surface area approximations (Brantley et al., 2008; Bourg et al., 2015; Beckingham et al., 2016). Specific surface area approximations include geometric surface areas and laboratory measured BET surface. Effective surface areas account for the distribution of reactive sites on mineral surfaces, surface roughness, or mineral accessibility (Beckingham et al. 2016). In reactive transport simulations, variations in mineral reactive surfaces areas result not only in discrepancies in mineral reaction rates, but porosity evolution as well (Gaus et al., 2008; Atchley et al., 2014).

Some minerals have been found to dissolve and precipitate in nature at different rates than they do in laboratory experiments (Bethke, 2008). Such discrepancies have been commonly attributed to difficulties in representing the surface area of minerals in natural samples (e.g., Aagard and Helgeson, 1982). In the laboratory, the mineral is fresh and any surface coatings have been removed. The same mineral in the field, however, may be shielded with oxides, hydroxides and/or organic coatings. Natural samples may be occluded by contact with other materials, including reactions products, organic matter, and other grains. In addition, the aged surface of the natural sample is probably smoother than the laboratory material and hence contains fewer kinks and sharp edges, which are highly reactive (Bethke, 2008).

It has been argued that surface area estimates do not accurately reflect the real surface area available for the weathering reaction. In nature, field systems rarely have uniformly sized particles. Thus, some mineral surfaces may be inaccessible due to disconnected pores, cementation or clay coatings (e.g., Ganor et al., 2005; Béarat et al., 2006; Peters, 2009; Crandell et al., 2012; Landrot et al., 2012, Nishiyama and Yokohama, 2013; Waldmann et al., 2014). In these systems, therefore, mineral abundance alone may not accurately reflect the accessibility of mineral surfaces to reactive fluids and the effect of transport limitations needs to be considered (Van Cappellen, 1995; Brantley et al., 2008; Scislewski and Zuddas, 2010; Salehikhoo and Li, 2015, Jung and Navarre-Sitchler, 2018).

For most of the minerals, the abundance is greater than the corresponding accessibility. In other words, mineral abundance overestimates mineral accessibility. For clay minerals, however, mineral abundance underestimates mineral accessibility. This is expected given that clay minerals often occur as a grain coating (Peters, 2009, Beckigham et al., 2017). For instance, in sandstone samples backscattered electron imaging has revealed clay coatings

on grain surfaces which limit accessibility to other mineral surfaces (Peters, 2009; Waldmann et al., 2014; Lai et al., 2015).

In addition, studies of grain dissolution in rocks should take into account the heterogeneity of the surface reactivity inherent to the crystal structure and randomness of the dissolution process itself, differences in reactivity for various crystal faces and effects of grain edges/boundaries (Fischer et al., 2014, Fischer and Luttge, 2017). Moreover, existing estimates of reactive surface area do not account for the possibility that reactive surface area may evolve during reaction due to dissolution of armoring/altered layer (White and Peterson, 1990; Anbeek, 1993; Luquot and Gouze, 2009; Noiriel et al., 2009; Scislewski and Zuddas, 2010; Gouze and Luquot, 2011, Beckigham et al., 2017).

2.8. MODELLING STRATEGY TO SCALE FROM LABORATORY REACTORS TO APPLICATION AT LARGER SCALES

In early dissolution studies (Lasaga, 1984), it was assumed that the results of laboratory experiments could be applied directly to the natural systems. Transferring the laboratory results to field situations, however, has proved to be more challenging. There is no certainty that the reaction or reaction mechanism studied in laboratory will predominate in nature. For instance, some laboratory experiments are conducted under conditions in which the fluid is far from equilibrium with the mineral, although reactions in nature proceed over a broad range of saturation states across which the laboratory result may not apply (Bethke, 2008). Additionally, whereas most laboratory experiments have been conducted in largely abiotic experiments, the action of bacteria or plant-driven fungal may influence reactions rates in nature (e.g., Chapelle, 2001; Bonneville et al., 2009).

To scale from chemical reactors to watersheds, models usually assume weathering occurs predominantly at the soil grain surface, which is typical estimated from geometric surface area based upon acreage of land, soil porosity, and grain geometric (White, 1995). However as pointed out by some authors (e.g., Hochella and Banfield, 1995), weathering could also occur along internal porosity of grains and microcracks in bedrock. Thus, the question of scaling from the laboratory to the watershed becomes a problem of deciding which flow path contributes the predominant flux of the component of interest to the overall mass balance (White and Brantley, 1995).

A practical consideration in reaction modelling is choosing the extent to which reaction kinetics should be integrated into the calculations. The database required to support the calculation has to include rate laws for every possible reaction mechanism for each mineral. Even unstable minerals that can be neglected in equilibrium models would have to be included in the dataset, since they could form in a kinetic model (Bethke, 2008).

The modelling has to trace a number of reactions occurring at broadly different rates. For each calculation, it is needed to set initial conditions, requiring knowledge of hydrologic factors (flow rates, residence times, etc.) and biological interactions which in natural environments are not always fully quantified. A well-known strategy for conceptualizing kinetic reaction paths is to divide mineral reactions into three groups. The first group contains the reactions that proceed quickly over the time span of the calculation. We can safely assume that these minerals remain in equilibrium with the fluid. A second group consist of minerals that react negligibly over the calculation and hence may be ignored or suppressed. The reactions for the remaining minerals fall in the third group, for which we need to account for reactions kinetics. (Bethke, 2008).

Nowadays, quantification of mineral weathering rates in field systems have to rely upon numerical models which couple fluid advection, diffusion, chemical reaction and biological interactions. Such numerical models evaluate the relative flux contribution from dissolution along internal porosity, along micro- and macro-pores, and along fractures considering the possible interactions with the biota (i.e. vegetation, fungi, etc.). Codes which attempt to couple fluid flow and reaction have become available only in recent years (Goddéris et al., 2006, 2009; Brantley and White, 2009; Goddéris et al., 2010; Maher et al., 2009; Beaulieu et al., 2012).

Although full parameterization of such geochemical models seems to remain impossible on any spatially extensive scale, the continuous collection of both field and laboratory measurements try to provide the "best" inputs for the basic physical, chemical and biological variables in the systems of interest. In this way, the main challenge is still to design and implement laboratory and field experiments which carefully extract one variable at a time to isolate and compare with the coupled numerical models (White and Brantley, 1995).

References

Aagaard, P. and Helgeson, H.C. (1982) Thermodynamic and kinetic constraints on reaction rates among mineral and aqueous solutions, I. Theoretical considerations. American Journal of Science 282. 237-285.

Aberg, G., Jacks, G., Hamilton, P.J. (1989) Weathering rates and $^{87}Sr/^{86}Sr$ ratios: an isotopic approach. J Hydrol 109. pp. 65-78.

Amiotte-Suchet, P., Probst, J.L., Ludwig, W. (2003) Worldwide distribution of continental rock lithology: implications for the atmospheric/soil CO_2 uptake by continental weathering and alkalinity river transport to the oceans. Global Biogeochemical Cycles 17 (2), GB1038.

Anbeek, C. (1992) Surface roughness of mineral and implications for dissolution studies. Geochim. Cosmochim. Acta 56, 1461-1469.

Andersson-Calles, U.M. and Ericksson, E. (1979) Mass balance of dissolved inorganic substances in three representative basins in Sweden. Nordic Hydrol. 28. pp.99-114.

Aomine, S. and Wada, K. (1962) Differential weathering of volcanic ash and pumice, resulting in formation of hydated halloysite. The American Mineralogist, Vol. 47. 1024-1048.

Atchley, A.L., Navarre-Sitchler, A.K. and Maxwell, R.M. (2014) The effects of physical and geochemical heterogeneities on hydro-geochemical transport and effective reaction rates. J. Contam. Hydrol. 165, 53-64.

Auker, M., Sparks, R., Siebert, L., Crosweller, H. and Ewert, J. (2013) A statistical analysis of the global historical volcanic fatalities record. Journal of Applied Volcanology. 2:2. 1-24.

Ayris, P.M. and Delmelle, P. (2012) The immediate environmental effects of tephra emissions. Bull Volcanol 74: 1905-1936.

Barker, P., Telford, R., Merdaci, O., Williamson, D., Taieb, M., Vincens, A., Gilbert, E. (2000) The sensitivity of a Tanzanian crater lake to catastrophic tephra input and four millennia of climate change. Holocene: 10(3): 301-310.

Béarat, H., McKelvy, M.J., Chizmeshya, A.V.G., Gomley, D., Nunez, R., Carpenter, R.W., Squires, K., and Wolf, G.H. (2006) Carbon sequestration via aqueous olivine mineral carbonation: role of passivating layer formation. Environ. Sci. Technol;40, 4802-4808.

Beaulieu, E., Goddéris, Y., Donnadieu, Y., Labat, D. and Roelandt, C. (2012) High sensitivity of the continental-weathering carbon dioxide sink to future climate change. Nature climate change. Vol.2. pp. 346-349.

Beckingham, L.E., Steefel, C.I., Swift, A.M., Voltolini, M., Yang, L., Sheets, J.M., Cole, D.R., Kneafsey, T.J., Mitnick, E.H., Zhang, S., Gautier, L., Ajo-Franklin, J.B., DePaolo, D.J., Mito, S. and Xue, Z. (2017) Evaluation of accessible mineral surface areas for improved prediction of mineral reaction rates in porous media. Geochimica et Cosmochimica Acta 205: 31-49.

Beckingham, L.E., Mitnick, E.H., Steefel, C.I., Zhang, S., Voltolini, M., Swift, A.M., Yang, L., Cole, D.R., Sheets, J.M., Ajo-Franklin, J.B., DePaolo, D.J., Mito, S., Xue, Z. (2016) Evaluation of mineral reactive surface area estimates for prediction of reactivity of a multi-mineral sediment. Geochimica et Cosmochimia Acta 188: 310-329.

Benedetti, M. F., Menard, O., Noack, Y., Caralho, A. And Nahon, D. (1994) Water-rock interactions in tropical catchments: field rates of weathering and biomass impact. Chem. Geol. 118. pp. 203-220.

Berner, R.A. (1995) Chemical weathering and Its Effect on Atmospheric CO_2 and Climate. In Chemical Weathering Rates of Silicate Minerals. Eds. White, A.F & Brantley S.L. Reviews in Mineralogy. Volume 31. pp. 575-583.

Bethke, C.M. (2008) Geochemical and biogeochemical reaction modeling. 2nd Edition. Cambrigde University Press. New York. pp. 9-10, 236-242.

Blum, A.E., Lasaga, A.C., (1991). The Role of Surface Speciation in the Dissolution of Albite. Geochimica et Cosmochimica Acta, 55(8): 2193-2201.

Bluth G.S. and Kump L.R. (1994) Lithologic and climatic controls on river chemistry. Geochim. Cosmochim. Acta 58. Pp. 2341-2359.

Bonneville, S., Smits, M.M., Brown, A., Harrington, J., Leake, J.R., Brydson, R., Benning, L.G. (2009) Plant-driven fungal weathering: Early stages of mineral alteration at the nanometer scale. Geological Society of America. V.37.7. pp. 615-618.

Bourgh, I.C., Beckingham, L.E. and DePaolo, D.J. (2015) The nanoscale basis of CO_2 trapping for geologic storage. Environ. Sci. Technol. 49, 10265-10284.

Brand, L.E., Sunda, W.G., Guillard, R.R.L. (1983) Limitation of marine phytoplankton reproductive rates by zinc, manganese, and iron. Limnol Oceanogr 28(6):1182–1198.

Brand, L.E., Sunda, W.G., Guillard, R.R.L. (1986) Reduction of marine phytoplankton reproduction rates by copper and cadmium. J Exp Mar Biol Ecol 96(3):225–250.

Brantley, S.L., White, A.F. (2009) Approaches to modeling weathered regolith. Rev. Min. Geochem. 70. 435-484.

Brantley, S.L., Kubicki, J.D. and White, A.F. (eds.) (2008) Kinetics of Water-Rock Interaction. Springer, New York, NY.

Brantley, S.L., (2003) Reaction Kinetics of Primary Rock-forming Minerals under Ambient Conditions. In: Editors-in-Chief: Heinrich, D.H., Karl, K.T. (Eds.), Treatise on Geochemistry. Pergamon, Oxford, pp. 73-117.

Brantley, S.L., Stillings, L., (1996) Feldspar dissolution at 25 °C and low pH. American Journal of Science, 296(2): 101-127.

Brantley, S.L., Chen, Y., (1995) Chemical weathering rates of pyroxenes and amphiboles, Chemical Weathering Rates of Silicate Minerals. Reviews in Mineralogy, pp. 119-172.

Brock, B., Rivera, A., Casassa, G., Bown, F., Acunn, C (2007) The surface energy balance of an active ice-covered volcano: Villarica Volcano, southern Chile: Ann Glaciol 45(1): 104-114.

Brown, S.K., Crosweller, H.S., Sparks, R.S.J., Cottrell, E., Deligne, N.I., Ortiz Guerrero, N., Hobbs, L., Kiyosugi, K., Loughlin, s.C., siebert, L., Takarada, S. (2014) Characterization of the Quaternary eruption record: analysis of the Large Magnitude Explosive Volcanic Eruptions (LaMEVE) database. Journal of Applied Volcanology, 3:5. pp.22.

Cailleteau, C., Angeil, F., Deveux F., Gin S., Jestin J., Jollivet P. and Spalla O. (2008) Insight into silicate-glass corrosion mechanisms. Nat. Mater. 7, 978–983.

Cather S.M., Dunbar, N.W., McDowell, F.W., McIntosh, W.C., Scholle, P.A. (2009) Climate forcing by iron fertilization from repeated ignimbrite eruptions: the icehouse–silicic large igneous province (SLIP) hypothesis. Geosphere 5(3):315–324.

Chakraborty, P., Raghunadh Babu, P.V., Acharyya, T., Bandyopadhyay, D. (2010) Stress and toxicity of biologically important transition metals (Co, Ni, Cu and Zn) on phytoplankton in a tropical freshwater system: an investigation with pigment analysis by HPLC. Chemosphere 80 (5):548–553.

Chapelle, F.H. (2001) Ground-Water Microbiology and Geochemistry. 2nd ed. Wiley. New York.

Chen, Y., Brantley, S.L., (2000) Dissolution of forsteritic olivine at 65 °C and 2 < pH < 5. Chemical Geology, 165(3-4): 267-281.

Chigira, M. and Oyama, T. (2000) Mechanism and effect of chemical weathering of sedimentary rocks. Developments in Geotechnical Engineering. Vol 84. pp. 267-278.

Christie, J.K., Ainsworth, R.I., de Leeuw, N.H. (2016) Investigating structural features which control the dissolution of bioactive phosphate glasses: Beyond the network connectity. Journal of Non-Crystalline Solids 432. 31-34.

Clayton, J.L. (1986) An estimate of plagioclase weathering rate in the Idaho batholith based upon geochemical transport rates. In Rates of Chemical Weathering of Rocks and Minerals (eds. S. Coleman and D. Dethier). Academic Press, Orlando, pp. 453-446.

Cleaves, A.T., Godfrey, A.E. and Bricker, O.P. (1970) Geochemical balance of small watershed and its geomorphic implications. Geol. Soc. Am. Bull. 81. pp.3015-3032.

Clow, D.W. and Drever, J.I. (1996) Weathering rates as a function of flow through an alpine soil. Chemical Geology 132. pp. 131-141.

Cook, R.J., Barron, J.C., Papendick, R.I., Williams, G.J. (1981) Impact on agriculture of the Mount St. Helens eruptions: Sciene 211.4477. pp. 16-22.

Crandell, L.E., Peters, C.A., Um, W., Jones, K.W. and Lindquist, W.B. (2012) Changes in the pore network structure of Hanford sediment after reaction with caustic tank waste. J. Contam. Hydrol. 131, 89-99.

Criscenty, L.J.; Kubicki, J.D., Brantley, S.L. (2005) Silicate Glass and Mineral Dissolution: Calculated Reactions Paths and Activation Energies for Hydrolysis of a Q^3 Si by H_3O^+ Using Ab Initio Methods. J. Phys. Chem. A 110, 198-206.

Critelli, T., Marini L., Schott J., Mavromatis V., Apollaro, C., Rinder, T., De Rosa, R., Oelkers, E.H., (2015) Dissolution rate of antigorite from a whole-rock experimental study of serpentinite dissolution from 2 < pH < 9 at 25°C: Implications for carbon mitigation via enhanced serpentinite weathering. Applied Geochemistry 61 (2015) 259–271.

Critelli, T., Marini, L., Schott, J., Mavromatis, V., Apollaro, C., Rinder, T., De Rosa, R., Oelkers, E.H., (2014). Dissolution rates of actinolite and chlorite

from a whole-rock experimental study of metabasalt dissolution from 2 ≤ pH ≤ 12 at 25°C. Chem. Geol. 390, 100–108.

Cronin S.J., Hedlye, M.J., Neall, V.E., Smith, R.G., (1998) Agronomic impact of tephra fallout from the 1995 and 1996 Ruapehu Volcano eruptions, New Zealand. Environmental Geology 34.1. pp. 21-30.

Cronin, S.J., Hedlye, M.J., Smith, R.G., Neall, V.E. (1997) Impact of Ruapehu ash fall on soil and pasture nutrient status 1. October 1995 eruptions. New Zeland Journal of Agricultural Research 40.3. pp. 271-291.

Crovisier, J.L., Advocat, T., Dussossoy, J-L. (2003) Nature and role of natural alteration gels formed on the surface of ancient volcanic glasses (Natural analogs of waste containment glasses) Journal of Nuclear Materials 321. pp. 91-109.

Crovisier, J.L., Thomassin, J.H., Juteau, T., Eberhart, J.C., Touray, J.C., Baillif, P. (1982) Experimental seawater-basaltic glass interaction at 50°C: Study of early developed phases by electron microscopy and X-ray photoelectron spectrometry. Geochimica et Cosmochimica Acta Vol. 47. pp. 377-387.

Curtis, C.D. (1976) Stability of minerals in surface weathering reactions: A general thermochemical approach. Earth Surface Processes 1(1): 63-70.

Cushing, C.E. and Smith, S.D. (1982) Effects of Mount St. Helens ashfall on lotic algae and caddislies. J. Freshw Ecol 1(5). pp. 527-538.

Cygan, R.T., Casey, W.H., Boslough, M.B., Westrich, H.R., Carr, M.J., Holdren, Jr., G.R. (1989) Dissolution kinetics of experimentally shocked silicate minerals. Chem. Geol. 78, 229-244.

Dahlgren, R.A. (2008) Acid deposition effects on soils. In: Encyclopedia of Soil Science. Springer, 2008, pp. 2-7.

Dahlgren R.A., Ugolini F.C. and Casey W.H. (1999) Field weathering rates of Mt. St. Helens tephra. Geochim. Cosmochim. Acta 63, 587-598.

Daval, D., Sissmann, O., Menguy, N., Saldi, G.D., Guyot, F., Martinez, I., Corvisier, J., Garcia, B., Machouk, I., Knauss, K.G., Hellmann, R., (2011) Influence of amorphous silica layer formation on the dissolution rate of olivine at 90 °C and elevated pCO_2. Chemical Geology, 284(1–2): 193-209.

Daval, D., Hellmann, R., Corvisier, J., Tisserand, D., Martinez, I., Guyot, F. (2010) Dissolution kinetics of diopside as a function of solution saturation state: macroscopic measurements and implications for modeling of geological storage of CO_2. Geochim. Cosmochim. Acta 74. 2615-2633.

Declerq, J., Diedrich, T., Perrot, M., Gislason, S.R., Oelkers, E.H. (2013) Experimental determination of rhyolitic glass dissolution rates at 40-200°C and 2<pH<10.1. Geochimica et Cosmochimica Acta 100. 251-263.

Denbigh, K. (1971) The principles of Chemical Equilibrium. 3rd Edition. Cambridge University Press.

Deng, H., Voltolini, M., Molins, S., Steefel, C., DePaolo, D., Ajo-Franklin, J., Yang, L. (2017) Alteration and Erosion of Rock Matrix Bordering a Carbonate-Rich Shale Fracture. Environ. Sci. Technol. 51: 8861-8868.

Dessert, C., Dupré, B., François, L.M., Schott, J., Gaillardet, J., Chakrapani, G. and Bajpai, S. (2001) Erosion of Deccan Traps determined by river geochemistry: impact on the global climate and the 87Sr/86Sr ratio of seawater. Earth and Planetary Science Letter 188. pp. 459-474.

Devidal, J.L., Schott, J., Dandurand, J.L. (1997) An experimental study of kaolinite dissolution and precipitation kinetics as a function of chemical affinity and solution composition at 150 °C, 40 bars, and pH 2,6, 8, and 7.8. Geochim. Cosmochim. Acta 61. 5165-5186.

Díaz, F., Jimenez, C.C., Tejedor, M. (2004) Influence of the thickness and grain size of tephra mulch on soil wáter evaporation. Agricultural Water Management 74. 47-55.

Drever, J. I. and Clow, D.W. (1995) Weathering rates in catchments. In Chemical Weathering Rates of Silicate Minerals. Eds. White, A.F & Brantley S.L. Reviews in Mineralogy. Volume 31. pp. 463-483.

Doremus, R.H. (1994) Glass Science. Wiley, New York.

Duggen, S., Olgun, N., Croot, P., Hoffman, L., Dietze, H., Teschner, C. (2010) The role of airborne volcanic ash for the surface ocean biogeochemical iron-cycle: a review. Biogeosciences Discussions 6:6441–6489.

Duggen, S., Croot, P., Schacht, U., Hoffman, L. (2007) Subduction zone volcanic ash can fertilize the surface ocean and stimulate phytoplankton growth: evidence from biogeochemical experiments andsatellite data. Geophys Res Lett 34(L01612).

Eicher, G.J., Rounsefell, G.A. (1957) Effects of lake fertilization by volcanic activity on abundance of salmon. Limnol Oceanogr 2(2): 70-76.

Eifert T.L. (2011, October 15) Sedimentary Rock Textures. Geology for Today. Retrieved from http://www.geologyfortoday.com/rock-textures.html

Eyring, H. (1935) The activated complex in chemical reactions. J. Chem. Phys. 3. 107-115.

Flaathen, T.K. and Gislason, S.R. (2007) The effect of volcanic eruptions on the chemistry of surface water: the 1991 and 2000 eruptions of Mt. Hekla, Iceland: J Volcanol Geotherm Res 164(4): 293-316.

Fiore, S., Huertas, F. J., Tazaki, K., Huertas F. and Linares J. (1999) A low temperature experimental alteration of a rhyolitic obsidian. Eur. J. Mineral. 11, 455–469.

Fischer, C. and Luttge, A. (2017) Beyond the conventional understanding of water-rock reactivity. Earth and Planetary Science Letters 457: 100-105.

Fischer, C., Kurganskaya, I., Schäfer, T., Lüttge, A. (2014) Variability of crystal surface reactivity: What do we know? Applied Geochemistry 43. 132-157.

Fisher R.V. and Schmincke, H.U. (1984) Pyroclastic Rocks. Springer-Verlag, Berlin, Chapter 1, pp. 472.

Frogner, T. (1990) The effect of acid deposition on cation fluxes in artificially acidified catchments in western Norway. Geochim. Cosmochim. Acta 54. Pp. 769-780.

Gaillardet, J., Dupré, B., Louvat, P., Allègre, C.J. (1999) Global silicate weathering and CO_2 consumption rates deduced from the chemistry of large rivers. Chem.Geol. 159, 3-30.

Ganor, J., Roueff, E., Erel, Y., Blum, J.D., (2005) The dissolution kinetics of a granite and its minerals - Implications for comparison between laboratory and field dissolution rates. Geochimica Et Cosmochimica Acta, 69(3): 607-621.

Gaus, I., Audigane, P., André, L., Lions, J., Jacquemet, N., Durst, P., Czernichowski-Lauriol, I. (2008) Geochemical and solute transport modelling for CO_2 storage, what to expect from it? Int. J. Greenh. Gas Con 2, 605-625.

Gill, R. (2010) Igneous rocks and Processes. A practical guide. Wiley-Blackwell. UK. Chapter 1. An introduction to magmas and magmatic rocks.

Gislason, S.R., Oelkers, E.H. (2003). Mechanism, rates, and consequences of basaltic glass dissolution: II. An experimental study of the dissolution rates of basaltic glass as a function of pH and temperature. Geochimica et Cosmochimica Acta, 67 (20), 3817-3832.

Goddéris, Y., Brantley, S.L., François, L.M., Schott, J., Pollard, D., Déqué, M. and Dury M. (2013) Rates of consumption of atmospheric CO_2 through the

weathering of loess during the next 100yr of climate change. Biogeosciences, 10, 135-148.

Goddéris, Y., William, J.Z., Schott, J., Pollard, D., Brantley, S.L. (2010) Time evolution of the mineralogical composition of Mississippi Valley loess over the last 10 kyr: climate and geochemical modeling. Geochim. Cosmochim. Acta 74. 6357-6374.

Goddéris, Y., Roelandt, C., Schott, J., Pierret, M.C., François, L.M. (2009) Towards an Integrated Model of Weathering, Climate, and Biospheric Processes. Reviews in Mineralogy & Geochemistry. Vol.70 pp. 411-434.

Godderis Y., François L., Probst A., Schott J., Moncoulon D., et al. (2006) Modelling weathering processes at the catchment scale: The WITCH numerical model. Geochimica et Cosmochimica Acta, Elsevier, 70, pp.1128-1147.

Gouze, P. and Luquot, L. (2011) X-ray microtomography characterization of porosity, permeability and reactive surface changes during dissolution. J. Contam. Hydrol. 120-121, 45-55.

Grandstaff, D.E., (1977) Some kinetics of forsterite olivine dissolution. Transactions-American Geophysical Union, 58(6): 539-539.

Grobbelaar, J.U. (1985) Phytoplankton productivity in turbid waters. J Plankton Res 7 (5). 653-663.

Grotzinger, J., Jordan, T.J., Press, F. and Siever R. (2007) Understanding Earth. Fifth Edition. Chapter 4 Igneous Rocks. p. 78-83. Chapter 5 Sedimentation p.102. Chapter 16 Weathering, erosion, and mass wasting p.371-391.

Gudbrandsson S., Wolff-Boenisch D., Gislason S.R. and Oelkers E.H. (2014) Experimental determination of plagioclase dissolution rates as a function of its composition and pH at 22°C. Geochimica et Cosmochimica Acta 139 (2014) 154–172.

Guy, C. and Schott, J. (1989) Multisite surface reaction versus transport control during the hydrolysis of a complex oxide. Chemical Geology, 78, 181-204.

Hanchen, M., Prigiobbe, V., Storti, G., Seward, T.M., Mazzotti, M., (2006) Dissolution kinetics of fosteritic olivine at 90-150 °C including effects of the presence of CO_2. Geochimica et Cosmochimica Acta, 70(17): 4403-4416.

Hartmann, J., Jansen, N., Dürr, H.H., Kempe, S., Köhler, P. (2009) Global CO_2- consumption by chemical weathering: What is the contribution of highly active weathering regions? Global and Planetary Change 69. Pp. 185-194.

Hayes, S.K., Montgomery, D.R., Newhall, C.G. (2001) Fluvial sediment transport and deposition following the 1991 eruption of Mount Pinatubo. Geomorphology 45, pp. 211-224.

Hellmann, R., Tisserand, D. (2006) Dissolution kinetics as a function of the Gibbs free energy of reaction: an experimental study based on albite feldspar. Geochim. Cosmochim. Acta 70. 364-383.

Henderson, G.S., Calas, G. and Stebbins, J.F. (2006) Silicate Glasses and Melts. Elements, Vol.2, pp. 269-273.

Heiken, G. and Wohletz, K. (1992) Volcanic Ash. University of California Press, London, p.246.

Hellmann, R., Daval, D., Tisserand, D., (2010) The dependence of albite feldspar dissolution kinetics on fluid saturation state at acid and basic pH: Progress towards a universal relation. Comptes Rendus Geoscience, 342(7): 676-684.

Hill, R. (1996) An alternative view of the degradation of bioglass. Journal of materials science letters 15. 1122-1125.

Hochella, M.F. and Banfield, J.F. (1995) Chemical weathering of silicates in nature: A microscopic perspective with theoretical considerations. In: White, A.F. and Brantley, S.L. (eds.) Chemical weathering rates of silicate minerals. 31. Mineralogical Society of America. Washington DC. 353-406.

Huddart, D. and Stott, T. (2010) Earth Environments. Past, Present and Future. Willey-Blackwell. UK. pp. 251-267.

Hyndman, D.W. (1985) Petrology of Igneous and Metamorphic Rock. Second Edition. McGraw-Hill Book Company. International series in the Earth & Planetary Sciences. Chapter 3. Classification and characteristics of Igneous Rocks. chapter 3.

Iles, C.E., Hegerl, G.C., Schurer, A.P., Zhang, X. (2013) The effect of volcanic eruptions on global precipitation. Journal of Geophysical research: atmospheres, vol. 118, pp. 8770-8786.

Jerran, D. and Petford, N. (2011) The Field Description of Igneous Rocks. The geological field guides series. Second edition. Chapter 1 Introduction and occurrence.

Jones, R., Thomas, R.E., Peakall, J., Manville, V. (2017) Rainfall-runoff properties of tephra: Simulated effects of grain-size and antecedent rainfall. Geomorphology 282. pp. 39-51.

Jones, M.T., Gislason, S.R. (2008) Rapid releases of metal salts and nutrients following the deposition of volcanic ash into aqueous environments. Geochim Cosmochim Acta 72(15):3661–3680.

Jones, M.T., Hembury, D.J., Palmer, M.R., Tonge B., Darling, W.G, Loughlin, S.C. (2011) The weathering and elemental fluxes from active volcanoes to the oceans: a Monserrat case study. Bull Volcanol 73. 207-222.

Jones, M.T., Stephen, R., Sparks, J., Valdes P.J. (2007) The climate impact of supervolcanic ash blankets. Clim Dyn 29:553–564.

Jung, H., Navarre-Sitchler, A. (2018) Physical heterogeneity control on effective mineral dissolution rates. Geochimica et Cosmochimica Acta 227. 246-263.

Knauss, K.G., Johnson, J.W., Steefel, C.I. (2005) Evaluation of the impact of CO_2, co-contaminant gas, aqueous fluid and reservoir rock interactions on the geological sequestration of CO_2. Chem. Geol. 217. 339-350.

Keller, G. (2005 a) Biotic effects of impacts and volcanism. Earth and Planetary Science Letters 215. 249-264.

Keller, G. (2005 b) Impacts, volcanism and mass extinction: random coincidence or cause and effect? Australian Journal of Earth Sciences 52 (725-757).

Keller, W.D. (1957) The Principles of Chemical Weathering. An Integrated Review of the Principles of Chemical Weathering as Taken from the Literature, and the Relation of Weathering to Certain Aspects of Geology, Pedology and Civilization. Lucas Brother Publisher. Columbia, Missouri. pp.5, 9, 21, 54, 57.

Khattak O. (2016, March 6) How do you describe an Igneous Rock. Retrieved from http://geologylearn.blogspot.com/2016/03/how-do-you-describe igneous-rock.html

Kirkwood, D.E. and Nesbitt, H.W. (1991) Formation and evolution of soils from an acidified watershed: Plastic Lake, Ontario, Canada. Geochimica et Cosmochimica Acta, Vol. 55. Issue 5. pp. 1295-1308.

Kreisserman Y. and Emmanuel, S. (2018) Release of Particulate Iron Sulfide during Shale-Fluid Interaction. Environ. Sci. Technol. 52, 638-643.

Kump, L.R., Brantley, S.L. and Arthur, M.A. (2000) Chemical weathering, atmospheric CO_2, and climate. Annu. Rev. Earth Planet. Sci. 28:611–67.

Lai, P., Moulton, K. and Krevor, S. (2015) Pore-scale heterogeneity in the mineral distribution and reactive surface area of porous rocks. Chem. Geol. 411, 260-273.

Landrot, G., Ajo-Franklin, J.B., Yang, L., Cabrini, S. and Steefel, C.I. (2012) Measurement of accessible reactive surface area in a sandstone, whit application to CO_2 mineralization. Chem. Geol. 318-319, 113-125.

Lasaga, A.C. (1995) Fundamental approaches in describing mineral dissolution and precipitation rates. In Chemical Weathering Rates of Silicate Minerals. Eds. White, A.F & Brantley S.L. Reviews in Mineralogy. Volume 31. pp. 23-86.

Lasaga, A.C. (1984) Transition state theory. In Lasaga, A.C., Kirkpatrick, R.J. (eds.) Kinetics of Geochemical Processes. Rev Mineral 8:1-68.

Lasaga, A.C. (1981) Transition State Theory. Rev Mineral 8. 135-169.

Lathem, T.L., Kumar, P., Nenes, A, Dufek, J., Sokolik, I.N., Trail, M., Russell, A. (2011) Hygroscopic properties of volcanic ash. Geophys Res Lett 38 (L118082).

Leavesley, G.H., Lusby, G.C., Lichty, R.W. (1989) Infiltration and erosion characteristics of selected tephra deposits from the 1980 eruption of Mount St. Helens, Washington, USA. Hydrological sciences journal. 34.3. pp. 339-353.

Lee, D.B. (1996) Effects of the eruptions of Mount St. Helens on physical, chemical and biological characteristics of surface water, ground water, and precipitation in the Western United States. In: US Geological Survey Water-Supply Paper 2438.

Lenton, T.M., Britton, C. (2006) Enhanced carbonate and silicate weathering accelerates recovery from fossil fuel CO_2 perturbations. Global Biogeochemical Cycles 20 (3). GB3009.

Levenson, Y., Ryb, U., Emmanuel, S. (2017) Comparison on field and laboratory weathering rates in carbonate rocks from an Eastern Mediterranean drainage basin. Earth Planet. Sc. Lett., 465, 176-183.

Le Bas, M.J. and Streckeisen, A.L. (1991) The IUGS systematics of igneous rocks. Journal of the Geological Society, London, vol. 148, pp. 825-833.

Le Maitre, R.W. (Ed), Streckeisen A., Zanettin, B., Le Bas, M.J., Bonin, B., Bateman, P., Bellieni, G. Dudek, A., Efremova, S., Keller, J., Lameyre, J.,

Sabine, P.A., Schmid, R., Sorensen, H. and Woolley, A.R. (2002) Igneous Rocks. A classification and Glossary of Terms. Cambridge University Press. Chapter 2. Classification and nomenclature.

Liebau, F. (1985) Structural Chemistry of Silicates; Springer-Verlag: Berlin.

Lotter, A.F., Birks, H.J.B., Zolitschka, B. (1995) Late-Glacial pollen and diatom changes in response to two different environmental pertubations: volcanic eruptions and Younger Dryas cooling. J Palolimnol 14(1): 23-47.

Loughlin, S.C., Vye-Brown, R.S.J., Sparks, S.K., Brown, J., Barclay, E., Calder, E., Cottrell, G., Jolly, J-C., Komorowski, C., Mandeville, C., Newhall, J., Palma, S., Potter, S. and Valentine, G. (2015) An introduction to global volcanic hazard and risk. In: Global Volcanic Hazards and Risk. Loughlin. S.C., Sparks, S., Brown, S., Jenkins, S. and Vye-Brown, C. (eds). DOI 10.1017/CBO9781316276273.

Luquot, L. and Gouze, P; (2009) Experimental determination of porosity and permeability changes induced by injection of CO_2 into carbonate rocks. Chem. Geol. 265, 148-159.

Madé, B., Clément, A., Fritz, B. (1994) Modeling mineral/solution interactions: the thermodynamic and kinetic code KINDISP. Computers and Geoscienes 20(9). 1347-1363.

Mahapatra, M.K.; Lu, K. (2010) Glass-based seals for solid oxide fuel and eletrolizer cells – A review. Materials Science and Engineering R 67. 65-85.

Maher, K., Steefel, C.I., White, A.F., Stonestrom, D.A. (2009) The role of reaction affinity and secondary minerals in regulation chemical weathering rates at the Santa Cruz Soil Chronosequence California. Geochim. Cosmochim. Acta 73. 2804-2831.

Mass, C., Robock, A. (1982) The short-term influence of the Mount St. Helens volcanic eruption on surface temperature in the Nortwest United States. Mon Weather Rev 110: 614-619.

Mast, M.A., Drever, J.I., Baron, J. (1990) Chemical Weathering in the Loch Vale Watershed, Rocky Mountain National Park, Colorado. Water Resources Research, Vol. 26. No.12. pp. 2971-2978.

Maters, E.C., Delmelle, P., Rossi, M.J., Ayris, P.M., Bernard, A. (2016) Controls on the surface chemical reactivity of volcanic ash investigated with probe gases. Earth and Planetary Science Letters 450. pp. 254-262.

Matter, J.M., Broecker, W.S., Gislason, S.R., Gunnlaugsson, E., Oelkers, E.H., Stute, M., Sigurdardóttir, H., Stefansson, A., Alfreðsson, H.A.,

Aradóttir, E.S., Axelsson, G., Sigfússon, B., Wolff-Boenisch, D., (2011) The CarbFix Pilot Project – storing carbon dioxide in basalt. Energy Procedia 4, 5579–5585.

Miller, C.F. and Wark, D.A. (2008) Supervolcanoes and their explosive supereruptions. Elements. Vol.4. pp. 11-16.

Miller, E.K., Blum, J.D., Friedland, A.J. (1993) Determination of soil exchangeable-cation loss and weathering rates using Sr isotopes. Nature 362/ 438-441.

Mysen, B.O. and Richet, P; (2005) Silicate Glasses and Melts: Properties and Structure. Elsevier, London, pp. 544.

Nakagawa, M. and Ohba, T. (2002) Minerals in Volcanic Ash 1: Primary Minerals and Volcanic Glass. Global Environmental Research, 6, 41-51.

Newhall, C. G. and Hoblitt, R.P. (2002) Constructing event trees for volcanic crises. Bulletin of Volcanology. 64. 3-20.

Newhall, C.G. and Self S. (1982) The volcanic explosive index (VEI): An estimate of explosive magnitude for historical volcanism. Journal of Geophysical Research 87: 1231-1238.

Nishiyama, N., and Yokoyama, T. (2013) Does the reactive surface are of sandstone depend on water saturation? - The role of reactive-transport in water film. Geochim. Cosmochim. Acta 122, 153-169.

Noiriel, C., Luquot, L., Madé, B., Raimbault, L., Gouze, P. and van der Lee, J ; (2009) Changes in reactive surface area during limestone dissolution: an experimental and modelling study. Chem. Geol. 265, 160-170.

Oelkers, E.H. (2001) General kinetic description of multioxide silicate mineral and glass dissolution. Geochmica et Cosmochimica Acta, Vol 65, No.21, pp. 3703-3719.

Oelkers, E.H. and Gislasson, S.R. (2001) The mechanism, rates and consequences of basaltic glass dissolution: I. An experimental study of the dissolution rates of basaltic glass as a function of aqueous Al, Si, and oxalic acid concentrations at 25°C and pH=3 and 22. Geochimica et Cosmochimica Acta, 65, 3671-3681.

Oelkers, E.H., Schott, J. (1998) Does organic acid adsorption affect alkali feldspar dissolution rates, Chem. Geo. 151, 235-245.

Oelkers, E.H., Schott, J., Devidal, J.L. (1994). The effect of aluminum, pH, and chemical affinity on the rates of aluminosilicate dissolution reactions. Geochim. Cosmochim. Acta, 58 (9), 2011-2024.

Olgun, N., Duggen, S., Croot, P.L., Delmelle, P., Dietze, H., Schacht, U., Óskarsson, N., Siebe, C., Auer, A., Garbe-Schönberg, D. (2011) Surface ocean iron fertilization: The role of airborne volcanic ash from subduction zone and hot spot volcanoes and related iron fluxes into the Pacific Ocean. Global Biogeochem Cycles 25(4):GB4001.

Ostertat-Henning, C., Risse, A., Thomas, B., Rosenbauer, R., Rochelle, C., Purser, G. . . . Truche, L. (2014) GaMin'11-an international inter-laboratory comparison for geochemical CO_2- saline fluid- mineral interaction experiments. Energy Procedia 63. 5538-5543.

Paces, T. (1986) Rates of weathering and erosion derived from mass balance in small drainage basins. In: Rates of Chemical Weathering of Rocks and Minerals (S.M. Colman and D.P. Dethier eds), pp. 531 – 550.

Palandri J.L. and Kharaka Y.K. (2004) A compilation of rate parameters of water-mineral interaction kinetics for application to geochemical modeling. U.S. Geological Survey. Open file report 2004-1068.

Peters, C.A. (2009) Accessibilities of reactive minerals in consolidated sedimentary rock: an imaging study of three sandstones. Chem. Geol. 265; 198-208.

Pitzer, K.S. and Brewer, L. (1961) Revised edition of Thermodynamics, by Lewis G.N. and Randall, M. 2nd Edition. MacGraw-Hill, New York.

Probst, A., El Gh'Mari, A., Aubert, D., Fritz, B., Mc Nutt, R. (2000) Stronium as a tracer of weathering processes in a silicate catchment polluted by acid atmospheric inputs, Strengbach, France. Chem. Geol. 170. 203-219.

Pronost, J., Beaudoin, G., Tremblay, J., Larachi, F., Duchesne, J., Hébert, R., Constantin, M., 2011. Carbon sequestration kinetic and storage capacity of ultramafic mining waste. Environ. Sci. Technol. 45, 9413–9420.

Pyle, D. (2015) Sizes of volcanic eruptions. In: Sigurdsson, H., Houghton, B., McNutt, S., Rymer, H. and Stix. J. (eds.) The Encyclopedia of Volcanoes. Second ed. Academic Press. London.

Rajmohan, N., Fruger, P. and Gin, S. (2010) Composition effects on synthetic glass alteration mechanism: Part 1. Experiments. Chem. Geol. 279, 106–119.

Robock, A. (2000) Volcanic eruptions and climate. Reviews of Geophysics, 38,2. pp. 191-219.

Salehikhoo, F. and Li, L; (2015) The role of magnesite spatial distribution patterns in determining dissolution rates: when do they matter? Geochim. Cosmochim. Acta 155, 107-121.

Scasso, R., Corbella, H. and Tiberi, P. (1994) Sedimentological analysis of the tephra from the 12-15 August 1991 eruption of Hudson volcano. Bulletin of Volcanology. 56. 121-132.

Scholwe, H. (1990) Glass. Nature, Structure and Properties. Springer-Verlag, London, pp.454.

Schott, J., Oelkers, E.H., Bénézeth, P., Goddéris, Y., François, L. (2012) Can accurate kinetic laws be created to describe chemical weathering? C. R. Geoscience 344 (2012) 568–585.

Schott, J., Pokrovsky, O.S. and Oelkers, E.H. (2009) The link between mineral dissolution/precipitation kinetics and solution chemistry. Reviews in Mineralogy & Geochemistry. Vol 70 pp. 207-258, 2009.

Schott, J., Oelkers, E.H. (1995). Dissolution and Crystallization Rates of Silicate Minerals as a function of Chemical Affinity. Pure and Applied Chemistry, 67 (6), 903-910.

Schott, J., Berner, R.A., (1985) Dissolution mechanisms of pyroxenes and olivines during weathering, The chemistry of weathering. Springer, pp. 35-53.

Schott, J., Berner, R.A. and Sjöberg E.L. (1981) Mechanism of pyroxene and amphibole weathering. I. Experimental studies of iron-free minerals. Geochim. Cosmochim. Acta 45, pp 2123-2135.

Scislewski, A. and Zuddas, P. (2010) Estimation of reactive mineral surface area during water-rock interaction using fluid chemical data. Geochim. Cosmochim. Acta 74, 6996-7007.

Shikazono, N., Takino, A. and Ohtani, H. (2004) An estimate of dissolution rate constanta of volcanic glass in volcanic ash soil from the Mt. Fuji area, central Japan. Geochemical Journal, vol. 39, 185-196.

Shipley, S. and Sarna-Wojcicki, A.M. (1983) Distribution, thickness, and mass of late Pleistocene and Holocene tephra from major volcanoes in the northwestern United States: A preliminary assessment of hazards from volcanic ejecta to nuclear reactors in the Pacific Northwest. United States Geological Survey Miscellaneous Field Studies Map MF-1435, pp.1-27.

Shoji, S., Dahlgren, R., Nanzyo, M. (1993) Genesis of Volcanic Ash Soils. In: Shoji, S., Nanzyo, M. and Dahlgren, R., Eds., Volcanic Ash Soils—Genesis, Properties and Utilization, Developments in Soil Science, Elsevier, Amsterdam. Chapter 3.

Sigurdsson, H., Houghton, B., McNutt, S.R., Rymer, H. and Stix, J. (Eds.) (2015) Encyclopedia of Volcanoes, Second Edition. Academic Press, London, pp. 1421.

Simkin, T., Siebert, L. and Blong, R. (2001) Disasters: Volcano fatalities-lessons from the historial record. Science. 291.

Smith, A.M., Coupland, G., Dolan, L., Harberd, N., Jones, J., Martin, C., Sablowski, R., Amey, A. (2010) Plant biology: New York: Garland Science.

Stauffer, R.E. and Wittchen, BD. (1991) Effect of silicate weathering on water chemistry in forested, upland, felsic terrane of the USA. Geochim Cosmochim Acta 55: 3253-3271.

Steinke, I., Möhler, O.M., Kiselev, A., Niemand, M., Staathoff, H., Schnaiter, M., Skrotzki, J., Hoose, C., Leisner, T. (2011) Ice nucleation properties of fine ash particles from the Eyjafjallajökull eruption in April 2010. Atmos Chem Phys Discuss 11. 17665-17698.

Stockmann, G., Wolff-Boenisch, D., Gislason, S.R., Oelkers, E.H., (2008) Dissolution of diopside and basaltic glass: the effect of carbonate coating. Mineralogical Magazine, 72(1): 135-139.

Struy, E., Smis, A., Van Damme, S., Meire, P., Conley, D.J. (2009) The Global Biogeochemical Silicon Cycle. Silicon 1:207-213.

Stumm, W., Furrer, G., Kunz, B. (1983) The role of surface coordination in precipitation and dissolution of mineral phase. Chroat Chem. Acta58: 593-611.

Sverdrup, H. and Warfvinge, P. (1995) Estimating field weathering rates using laboratory kinetics. In Chemical Weathering Rates of Silicate Minerals. Eds. White, A.F & Brantley S.L. Reviews in Mineralogy. Volume 31. Pp. 485-541.

Sverdrup, H.U. (1990) The Kinetics of Base Cation Release due to Chemical Weathering. Lund University, Lund.

Techer, I., Advocat, T., Lancelot, J., Liotard, J. (2000) Basaltic glass: alteration mechanism and analogy with nuclear waste glasses. Journal of Nuclear Materials 282. 40-46.

Tejedor, M., Jiménez, C.C., Díaz, F. (2003) Use of volcanic mulch to rehabilitate saline-sodic soils. Soil Science Society of America Journal 67.6. pp. 1856-1861.

Telford, R., Barker, P., Metcalfe, S., Newton, A. (2004) Lacustrine responses to tephra deposition: examples from Mexico. Quat Sci Rev 23 (23-24): 2337-2353.

Usher, C.R., Michael, A.E., Grassian, V.H. (2003) Reactions on mineral dust: Chem Rev 103 (12): 4883-4939.

Van Cappellen, P. (1995) Reactive surface area control of the dissolution kinetics of biogenic silica in deep-sea sediments. Chemical Geology 132: 125-130.

Waldmann, S., Busch, A., van Ojik, K., and Gaupp R. (2014) Importance of mineral surface areas in Rotliegend sandstones for modeling CO_2-water-rock interactions. Chem. Geol; 378-379, 89-109.

Wasklewicz, T., Dorn, R.I., Clark, S., Hetrick, J., Pope, G., Liu, T., Krinsley, D.H., Dixon, J., Moore, R.B., Clark, J. (1993) Olivine does not necessarily weather 1st. Singapore Journal of Tropical Geography, 14(1): 72-80.

Weinstein, L.H. and Davison, A. (2004) Flourides in the environment: effects on plants and animals: CABI.

White, A.F. (2011) Natural Weathering Rates of Silicate Minerals. US Geological Survey. In: Geochemistry of Earth Surface Systems form the treatise on Geochemistry. Eds. Holland, H.D. and Turekian, K.K. Academic Press. First edition. pp. 205-235.

White, S.P., Allis, R.G., Moore, J., Chidsey, T., Morgan, C., Gwynn, W., Adams, M. (2005) Simulation of reactive transport of injected CO_2 on the Colorado Plateau, Utah, USA. Chem. Geol. 217. 387-405.

White, A.F., Blum, A.E., Schulz, M.S., Huntington, T.G., Peters, N.E. and Stonenstrom, D.A. (2002) Chemical weathering of the Panola Granite: Solute and regolith elemental fluxes and the weathering rate of biotite. In Water-Rock Interactions, Ore Deposits, and Environmental Geochemistry. The Geochemical Society, Special Publication No.7. Eds. Hellmann, R. and Wood, S.A. pp. 37-59.

White, A.F., Bullen, T.D., Schulz, M.S., Blum, A.E., Huntington, T.G. and Peters, N.E. (2001) Differential rates of feldspar weathering in granitic regoliths. Geochimica et Cosmochimica Acta, Vol. 65. No.6. pp. 847-869.

White, A.F., Blum, A.E., Schulz, M.S., Bullen, T.D., Harden, J.W. and Peterson, M.L. (1996) Chemical weathering rates of a soil chronosequence on granitic alluvium: I. Quantification of mineralogical and surface area changes

and calculation of primary silicate reaction rates. Geochimica et Cosmochimica Acta, Vol.60. No.14. pp. 2533-2550.

White, A.F. (1995) Chemical weathering rates of silicate minerals in soils. In Chemical Weathering Rates of Silicate Minerals. Eds. White, A.F & Brantley S.L. Reviews in Mineralogy. Volume 31. pp. 407-461.

White A.F. and Blum, A.E. (1995) Effects of climate on chemical weathering rates in watersheds: Geochimica et Cosmochimca Acta, 59, pp 9776-9782.

White A.F & Brantley S.L. (1995) Chemical weathering rates of silicate minerals: an overview. In Chemical Weathering Rates of Silicate Minerals. Eds. White, A.F & Brantley S.L. Reviews in Mineralogy. Volume 31. pp. 1-22.

White A. F. and Peterson M.L. (1990) Role of reactive-surface-area characterization in geochemical kinetic models. In Chemical Modeling of Aqueous Systems II. American Chemical Society, 461-475.

Wieland, E., Werhli, B., Stumm, W. (1988) The coordination chemistry of weathering: III. A generalization of t the dissolution rates of minerals. Geochim Cosmochim Acta 52. 1969-1981.

Williams, M.W., Brown, A.D., Melack, J.M. (1993) Geochemical and hydrologic controls on the composition of surface water in a high elevation basin. Sierra Nevada, California. Limnology and Oceanography. Vol 38. 775-797.

Wilson, T., Cole, J., Cronin, S., Stewart, C., and Johnston, D. (2011) Impacts on agriculture following the 1991 eruption of Vulcan Hudson, Patagonia: lessons for recovery. Natural Hazards 57.2. pp. 185-212.

Wolff-Boenisch, D., Gislason, S.R., Oelkers, E.H. (2006) The effect of crystallinity on dissolution rates and CO2 consumption capacity of silicates. Geochimica et Cosmochimica Acta 70. 858-870.

Wolff-Boenisch, D., Gislason S. R., Oelkers, E. and Putnis, C.V. (2004) The dissolution rates of natural glasses as a function of their composition at pH 4 and 10.6 and temperatures from 25 to 74°C. Geochimica et Cosmochimica Acta, Vol.68, No. 23, pp 4843-4858.

Xu, T., Apps, J.A., Pruess, K. (2005) Mineral sequestration of carbon dioxide in sandstone-shale system. Chem. Geol. 217. 295-318.

Yokoyama, T. and Banfield, J.F. (2002) Direct determination of the rates of rhyolite dissolution and clay formation over 52,000 years and comparison

with laboratory measurements. Geochimica et Cosmochimica Acta, Vol. 66, No. 15, pp. 2665-2681.

Zakaznova-Herzog, V.P., Nesbitt, H.W., Bancroft, G.M., Tse, J.S., (2008) Characterization of leached layers on olivine and pyroxenes using high-resolution XPS and density functional calculations. Geochimica Et Cosmochimica Acta, 72(1): 69-86.

Zhu, C., Liu, Z., Zhang, Y., Wang, C., Scheafer, A., Lu, P., Zhang, G.B. Georg, R., Yuan H.L., Rimstidt, J.D. (2016) Measuring silicate mineral dissolution rates using Si isotope doping. Chem. Geol., http://dx.doi.org/10.1016/j.chemgeo.2016.02.027

CHAPTER 3 Analytical and Experimental Techniques

3.1. ORIGIN OF THE VOLCANIC POWDERED ROCKS AND GLASS SAMPLES USED IN THIS STUDY

Eight samples of volcanic rock-glass-ash from seven volcanos around South America (Tungurahua-Ecuador-2006, Guagua Pichincha-Ecuador-1999 and Puyehue-Chile-2013), Europe (Katla-Iceland-934, Mt. Etna-Italy-2002, 2013 and Lipari-Italy-729) and Asia (Mt. Unzen-Japan-1991) were selected. The samples fall within the range of compositions typically produced in volcanic eruptions, i.e. from basalt to rhyolite (Hyndman, 1985; Hall, 1996). Table 3.1 provides details on the studied volcanic rock and glass samples. Photographs of the natural samples prior to treatment are shown in Figure 3.1. Figure 3.2 is a map with the locations of the volcanoes from where the samples were collected.

Table 3.1. Description of the volcanic rock-glass samples used in this study.

Type of sample	Volcano	Place and year of the eruption	Used in chapter
BASALTIC SAMPLES			
Ash	Mt. Etna	Italy-Sicily-2013	4
Rock	Mt. Etna	Italy-Sicily-2002	5
Rock	Katla	Iceland-934	6
ANDESITIC SAMPLE			
Rock	Tungurahua	Ecuador-2006	6
DACITIC SAMPLES			
Rock	Mt. Unzen	Japan-1991	5
Rock	Guagua Pichincha	Ecuador-1999	6
RHYOLITIC SAMPLES			
Obsidian	Lipari	Italy-729	5
Rock	Puyehue	Chile-2013	6

BASALTIC SAMPLES

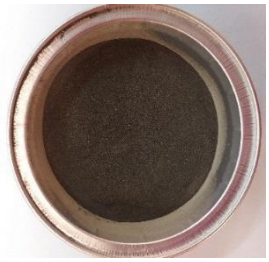

Etna ash

Etna rock

Katla rock

ANDESITIC SAMPLE

Tungurahua rock

DACITIC SAMPLES

Unzen rock

Guagua Pichincha rock

RHYOLITIC SAMPLES

Lipari obsidian

Puyehue rock

Figure 3.1. Photographs of the volcanic rock samples used in this study.

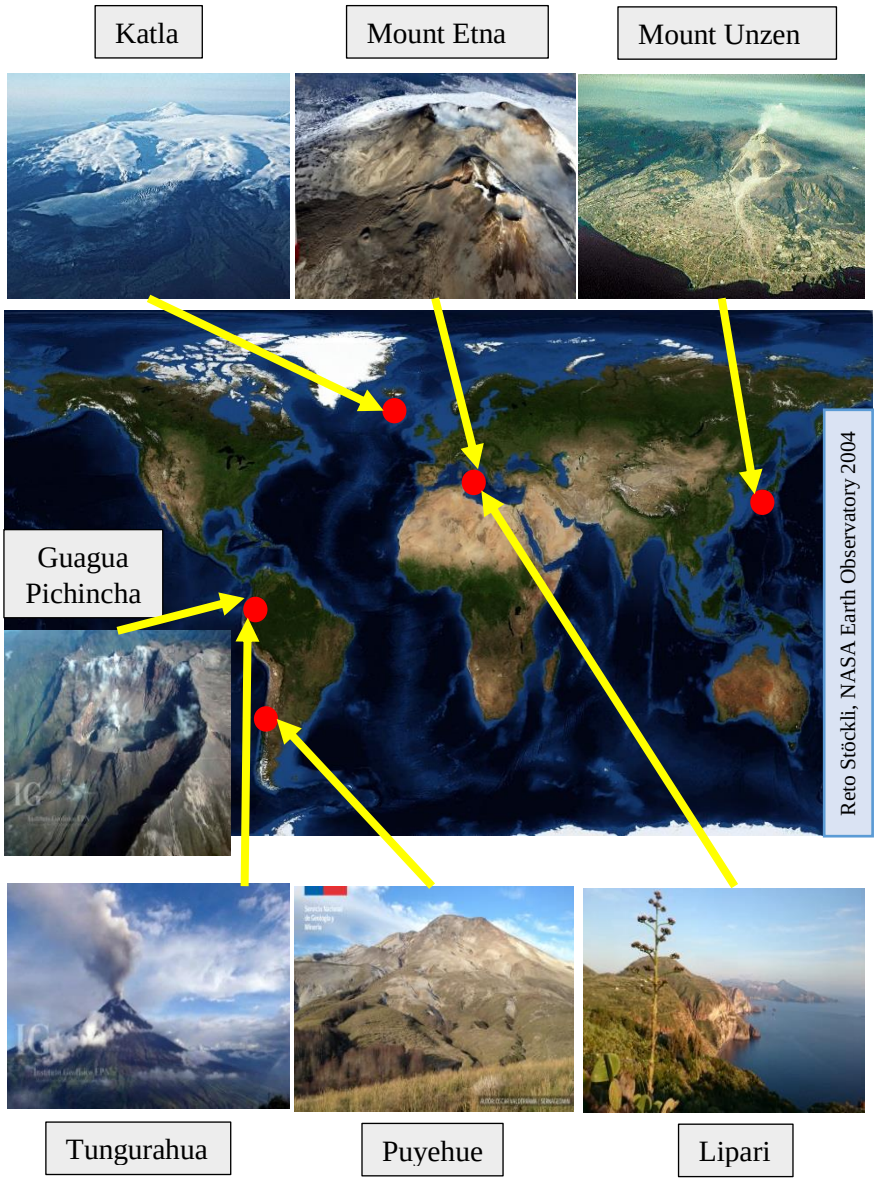

Figure 3.2. Map showing the locations of the volcanoes from which the rock-glass-ash materials used in this study originate. Katla (Photo: O. Sigurdsson, Iceland GeoSurvey); Mt. Etna (Photo: M. Neri, INGVvulcani); Mt. Unzen (Photo: USGS Cascades Volcano Observatory); Guagua Pichincha (Photo: P. Mothes, Instituto Geofísico EPN); Tungurahua (Photo: S. Hidalgo, Instituto Geofísico EPN); Puyehue (Photo: O. Valderrama, SENARGEOMIN); Lipari (Photo: G. De Astis, INGVvulcani).

3.2. PARTICLE SIZE DISTRIBUTION BY LASER DIFFRACTION

Particle size distribution of the ash/rock/glass powder was determined by laser diffraction (COULTER LS 100Q, UCLouvain). A suspension consisting of distillated water and ash-glass-rock (< 0.5 g.) was prepared and passed through the analyzer. The presence of aggregates was verified exposing the suspension to ultrasonic irradiation for 1 minute. The results with and without ultrasonic destabilization were statistical compared. Fraunhofer diffraction equation (Jacquinot, 1957) was used to obtain the volumetric percentage for each laser beam (ISO 13320:2009). Statistical calculations such as standard deviation and variance were available. The most common approach for expressing laser diffraction results was reported by the D10, D50, and D90. The D50 is the size in microns that splits the distribution with half above and half below this diameter. Using the same convention, the D90 describes the diameter where ninety percent of the distribution has a smaller particle size and ten percent has a larger particle size. The D10 diameter has ten percent smaller and ninety percent larger. A three point specification featuring the D10, D50 and D90 will be considered complete and appropriate for most particulate materials (HORIBA, 2012).

3.3. SPECIFIC GRAVITY

Specific gravity was measured according to the method described in ISO 1183-1:2012 and by Funk and Dinger (1993) using a 5 mL glass pycnometer (specific gravity bottle 4.9038 ± 0.01 mL [BLAUBRAND NS10/19], UCLouvain). Ash-glass-rock density was determined based on the displacement of milliQ water (density = 998.2071 kg m^{-3} at 20°C) when a defined amount of sample (0.2 g.) is added. The pycnometer was then filled with water with and without ash-glass-rock. The weight of the displaced liquid was determined based on the difference between those terms, and hence its specific gravity, applying the Eq. [3.1].

$$\rho_{sample} = \frac{w_{sample}}{V_{pic} - \frac{w_{Water\ displaced}}{\rho_{water\ 20°C}}} \quad [3.1]$$

Where ρ_{sample} is the density of the volcanic ash-glass-rock sample (kg m^{-3}), w_{sample} is the weight of the sample placed in the pycnometer (kg). $w_{Water\ displaced}$ is the difference reported between the amount of water required to fill the pycnometer (kg) when an amount of volcanic ash-glass-rock (w_{sample}) is added (kg). V_{pic} is the normalized volume for the specific gravity bottle (m^3) and $\rho_{water\ 20°C}$ corresponds to the density of milliQ water at given temperature (kg m^{-3}).

3.4. SPECIFIC SURFACE AREA ANALYSIS

3.4.1. Geometric specific surface area

The geometric specific surface area is calculated using the equation Eq. [3.2] given by Brantley et al., (1999) and it was computed on the basis of their particle size distribution, as follows:

$$A_{geo} = \frac{6}{\rho * d_{eff}} \quad [3.2]$$

Where A_{geo} is the geometric surface area ($m^2\ g^{-1}$), ρ is the ash-glass-rock density (expressed as $g\ m^{-3}$) and d_{eff} is the effective particle diameter (m). The number 6 is based on the assumption that grains have a regular and smooth spherical shape. Assuming a homogeneous particle distribution, d_{eff} can be obtained from (Tester et al., 1994).

$$d_{eff} = \frac{d_{max} - d_{min}}{ln\left(\frac{d_{max}}{d_{min}}\right)} \quad [3.3]$$

Where *dmax* [m] and *dmin* [m] refer to the maximum and minimum beam for each particle fraction in the distribution size obtained in the laser diffraction spectroscopy.

Particle size distribution can be also used to calculate the d_{eff} value by dividing the size distribution into a finite amount of bins and assuming equivalent spherical diameters of particles that correspond to the mean size of each bin (Cepuritis et al., 2017):

$$d_{eff} = \sum_{i=dmin}^{dmax} x_i \frac{d_{i+1} - d_i}{ln\left(\frac{d_{i+1}}{d_i}\right)} \quad [3.4]$$

where x_i refers to the volumetric fraction of particles within each size bin d_i and d_{max} and d_{min} refer to the maximum and minimum size bin measured by laser diffraction spectroscopy, corresponding to x_{dmax}=0.99 and x_{dmin}=0.01 respectively.

Some limitations of the method to estimate the effective diameter using Eq. [3.3] (used in some dissolution studies, e.g. Wolff-Boenisch et al., 2004), include for instance that the effective diameter (d_{eff}=78 μm in the study of Wolff-Boenisch et al., 2004) of the powders could be reached by several size distributions (see Figure 3.3).

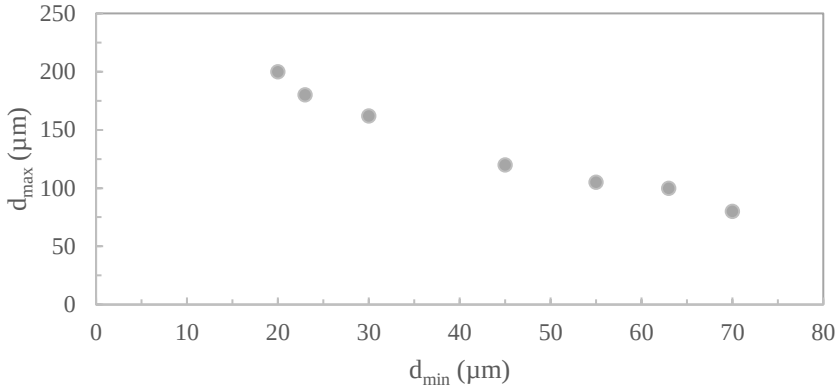

Figure 3.3. D_{max} vs D_{min} of the powdered material necessary to reach an effective diameter of 78 µm, which will produce the same geometric area A_{geo} applying Eq. [3.2] and Eq. [3.3].

Additionally, for an effective diameter comprised between 50-100 µm and using typical values of rock's density (ranging from 2.3 g cm^{-3} for a rhyolite to 3 g cm^{-3} for a basalt) the A_{geo} will be always comprised between 0.02 and 0.04 m^2 g^{-1}, with little influence of the particle size distribution (see Figure 3.4). Therefore, we could affirm that the A_{geo} does not make a good distinction among powdered samples of different reactivity while the samples presented similar average particle diameter and density.

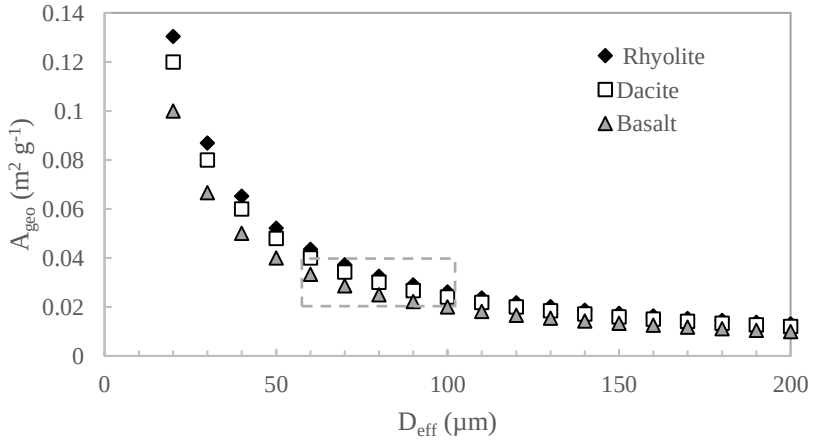

Figure 3.4. Variation of the geometric surface area in function of the effective diameter (µm) for three typical rocks (Basalt ρ= 3 g cm^{-3} Dacite ρ= 2.5 g cm^{-3} Rhyolite ρ= 2.3 g cm^{-3}).

3.4.2. Specific surface area (Brunauer, Emmet and Teller)

Specific surface area was evaluated by gas adsorption (krypton) (UCLouvain, Géosciences Environnement Toulouse and Institut de Science de Matériaux de Mulhouse) according to Brunauer, Emmett und Teller (Brunauer et al., 1938) as described in the standard ISO 9277:2010. Specific surface area SSA_{BET} (m^2 g^{-1}) was defined as the ratio between the absolute surface area of the volcanic material (ash, glass, rock) and its mass (sample weight: 0.5 g in this study).

The BET method involves the determination of the amount of the gas required to cover the external and the accessible internal pore surfaces of a solid with a complete monolayer of nitrogen or krypton. The monolayer capacity was calculated from the adsorption isotherm (Ermeling, 2014).

The BET equation is as follows:

$$\frac{1}{\left\{V\left[\left(\frac{P_o}{P}\right)-1\right]\right\}} = \left[\frac{(C-1)}{V_m\,C}\;x\;\left(\frac{P}{P_o}\right)+\frac{1}{(V_m\,C)}\right] \qquad [3.5]$$

Where

P partial vapor pressure of adsorbate gas in equilibrium with the surface at 77.4 K (196°C), (Pa)

P_o saturated pressure of adsorbate gas, (Pa)

V volume of gas adsorbed at standard temperature and pressure (273.15 K and 1.013 x 10^5 Pa) (mL)

V_m volume of gas adsorbed at standard temperature and pressure to produce an apparent monolayer on the sample surface [mL]

C BET constant, dimensionless constant that is related to the enthalpy of adsorption of the adsorbate gas on the powder sample

As it was mentioned by Hiemenz and Rajagopalan (1997), a linear plot of $1/\left\{W\left[\left(\frac{P_o}{P}\right)-1\right]\right\}$ at varing (P/Po) is used to derived V_m and C from the intercept and slope of the straight line. Once V_m was obtained, it was expressed in number of gas molecules, and then taking account the cross sectional area of the absorbed gas molecule, the sample surface area was obtained.

Approximately 300 mg of sample were degassed for at least two hours at 150 °C prior to analysis. For each volcanic sample (ash, rock, glass), a five point krypton adsorption isotherm at 77 K (-196 °C) was obtained using a Micromeritics ASAP 2000 instrument. It is also possible to obtain the adsorption isotherm using Nitrogen gas instead of Krypton gas, but as it has been pointed by the American Society for Testing and Materials (2015), nitrogen gas is favoured for analysis of powdered materials with low specific surface areas (<1 m^2 g^{-1}). The error on the BET analytical measurements was estimated between 0.5 and 2%.

Roughness factor. As it has been established by Wolff-Boenish et al. (2004), the ratio between BET and geometric surface area (A_{BET}/A_{geo}) will be referred as roughness factor.

3.5. BULK COMPOSITION

3.5.1. Alkaline Fusion and Inductively Coupled Plasma Atomic Emission Spectroscopy

Inductively coupled plasma atomic emission spectroscopy (ICAP 6000 Series/Emission Spectrometer, UCLouvain) was used to determine the weight percent oxide of the bulk samples, i.e. major elements composition (SiO_2, Al_2O_3, Fe_2O_3, MgO, CaO, Na_2O, K_2O) and trace elements composition (TiO_2, P_2O_5, MnO, SO_4, SrO, BaO, ZrO, ZnO, CuO).

Alkaline fusion was required to dissolve the sample, 0.1 g of volcanic material (ash, glass, rock) were mixed with 1.6 g of Lithium Metaborate ($LiBO_2$ 99.9% ALDRICH) and 0.4 g of Lithium Tetraborate ($B_4Li_2O_7$ 99% Fluka) on graphite crucibles (Chao and Sanzolone, 1992). The fusion was done at 1000°C for 10 minutes. The oxide phase obtained was digested on an acid bath (50 mL of HNO_3 at 80 °C) with magnetic stirring. The resulting solution was diluted with MilliQ water until 100 mL before sending it to analytical detection.

Additional dissolutions of 1:10 and 1:2 (dissolved sample: Milli-Q water) were needed depending on the element. Besides, a reference matrix containing the elements to be analyzed was prepared using certificate standards (CertiPUR® ICP Standard MERCK). This matrix was used to validate the accuracy of the technique applied. The detection limit was 10 µg $L^{-1}$for Si, Na, K and S, 4 µg L^{-1} for Mn, 3 µg L^{-1} for Fe, 2 µg L^{-1} for Al, 1.5 µg L^{-1} for Mg and 0.8 µg L^{-1} for Ca. The error on the ICP-AES analytical measurements was estimated about 1.5% (>50 ppb) and 0.5% (50-200 ppb).

3.6. MINERALOGICAL CHARACTERIZATION BY X-RAY DIFFRACTION

Samples of different volcanic material (glass, rock, ash) were pulverized using an agate mortar and pestle. The powder obtained (>40μm) were spread over a plastic sample holder and place into the X-Ray diffractometer (Bruker D8 Advance, UCLouvain) for analysis during 3 hours. In this study a Bruker D8 Advance Diffractometer equipped with a Peltier-cooled energy dispersive scintillation detector (Sol-X) was used. The analysis was programmed using the DifracPlus software program, with the incident monochromatic X-ray beam at an angle (θ) between 2° and 80°. Steps were in increments of 0.015° and counts were collected for 2 seconds per step.

3.6.1 Crystalline phases

Crystalline phase identification was generated from the interpretation of the X-Ray diffractograms using the data base provided by DIFFRAC.EVA software. In an X-Ray diffractogram, each crystalline phase has a pattern characterized by reflections (peaks in intensity) at certain positions. Representative rock-forming minerals in volcanic ash were identified using this diffraction patterns. The final mineralogical composition was validated taking account the formation of volcanic rocks (Hyndman, 1985) and compilations of representative minerals founded in volcanic ash-rocks (Nakagawa and Ohba, 2002).

Once the main mineral phases presented in the ash-rock samples were identified, a semi-quantative analysis was done using the software SIROQUANT. This software package is used for the quantification of crystalline compounds, using the Rietveld method. The Rietveld method uses a least squares approach to refine a theoretical line profile until it matches the measured profile (Rietveld, 1968). The refinement was done taking account some criteria e.g. peak shape, peak width and preferred orientation. As it has been suggested in the SIROQUANT, User Manual (2013), the refinement process consists of successive stages. In each stage, one of the following parameters was adjusted: peak high (scale and instrument zero); unit cell dimensions (W, a, b and c); preferred orientation, peak shape and asymmetry.

The results of the refinement process were evaluated through the fit of a calculated pattern to the observed data by the χ^2 value (chi squared/goodness of fit). χ^2 approaches 1 for a perfect fit, but in general, a good refinement process was considered when a chi squared lower than 3 was reached (SIROQUANT Version 4, User Manual 2013).

The final composition was reported in weight percentage of each mineral phase. Phases with a relative abundance below the detection limit were excluded. As it has been pointed by Pecharsky and Zavalij (2005), the accuracy of the quantitative phase analysis is difficult to estimate rigorously. It varies considerably and is often claimed to be between 1 and 5%. In our study, phases with an abundance higher than 1% are reported.

3.6.2. Amorphous content

SIROQUANT software enabled us to quantify the amorphous content in the volcanic ash-rocks samples by the addition of a spiked phase (metallic silicon) in the original sample prior X-ray powder diffraction analysis (Winburn et al., 2000; Ward and French, 2006; Paque et al., 2016). This spiked, used as internal standard, was added in a known weight percentage (~10% w/w). To obtain a well-mixed powder, the sample (>40μm) and metallic silicon were mechanically homogenized in a shaker for at least 12 hours (SIROQUANT Version 4, User Manual 2013, Ward and French, 2006).

Once a homogenized power was obtained, the X-Ray analysis was normally conducted as it had been described in the previous section. The X-Ray diffractograms were analysed using EVA, only to verify the presence of the phases already determined before. Then the diffractograms were processed by refinement of the Rietvel parameters of each mineral phase, normalized to 100%. If the original sample has a significant proportion of amorphous, the spiked fraction reported is higher than the spiked fraction in the powder mixture. The system can then make a correlation based on the known proportion of metallic silicon within the analysed sample and thereby calculate the proportion of amorphous material in the original (unspiked) sample (Ward and French, 2006). The accuracy in the weight percent determinations of the rock's glass and major crystalline components is in the range 5–10% (Paque et al., 2016).

3.7. MINERAL CHARACTERIZATION OF COMPLEX ROCK ASSEMBLAGES BY EPMA (ELECTRON PROBE MICRO ANALYZER) MAPPING

Typically, mineral assemblages comprise phases of heterogeneous composition. The heterogeneity can be either interphase, representing compositional variation between chemically different mineral phases or, alternatively, intraphase, indicating variation within a mineral phase as a result of primary chemical zoning, solid solution or variation introduced through weathering processes (Pownceby et al., 2006).

Composition and phase distribution analyses in complex rock assemblages was determined using EPMA-based microanalysis. The method used an electron microprobe to collect combined X-ray, backscattered electron and cathodoluminescnence (CL) maps. By scanning over a specified target area, CL wavelength and X-ray element distribution maps of grains are acquired in parallel enabling direct comparison between elemental concentration and textural features. (Pownceby et al., 2006).

In our study, the major and minor element compositions of crystalline phases and glassy groundmasses in the volcanic rocks were determined by EPMA, in the case of the dacitic rock (PUY) (chapter 6) using the JEOL Superprobe at the Institut für Geowissenschaaften, University of Mainz. We employed operating conditions similar to those described in Castro and Dingwell (2009) and Castro el al. (2013). For all of the major elements except Na, we used a focused beam, 15 kv, and 8nA current. Na-analyses were made with a defocused beam (~10 μm) and reduced current (6 nA) and were placed first in the sequence in order to minimize Na-migration. Standardization was based on known compositions of glass and mineral standards. The error on the EPMA measurements for the element composition was estimated to about 0.5-5% (major components >10 wt. %) and 5-15% (minor components <10 wt. %).

3.8. DESIGN OF AN EXPERIMENTAL FLUIDIZED BED SYSTEM TO STUDY DISSOLUTION KINETICS OF POWDERED VOLCANIC MATERIAL

3.8.1. Introduction

Interpretation and modelling of natural geochemical processes on the Earth's surface depend on our understanding of the factors that control the rate of dissolution of minerals. In order to quantify chemical weathering rates for individual minerals, laboratory experiments have been conducted under controlled conditions of temperature, pH, and solution composition (Brantley and Chen, 1995). Laboratory dissolution studies on isolated pure minerals or synthesized phases are the primary basis for the current understanding of weathering kinetics (Stephens and Hearing, 2004).

During the last decades, a large dataset of experimental dissolution rates for various minerals and glass compositions has been produced. These were obtained using a so-called dissolution reactor, but of which the design may vary significantly from one study to another. The main dissolution reactor types are the batch, continuously-stirred, plug flow, and fluidized bed design (e.g., Chou and Wollast, 1984; Rimstidt and Dove, 1986; Brantley and Chen, 1995; Pokrovsky and Schott, 2000, Palandri, 2004; Kaszuba et al. 2013; Ostertat-Henning et al., 2014).

A sound understanding of the advantages and disadvantages of a given type of dissolution reactor is required in order to be able to assess the experimental kinetics data critically. Indeed, some factors of experimental design (and also solid phase preparation) may affect the kinetics of dissolution. For example, low stirring velocities in a dissolution reactor may result in concentration gradients near mineral/glass surfaces, which may slow dissolution reactions (Metzr and Ganor, 2001). In other cases, particle abrasion may lead to faster apparent rates (Petrovich, 1981; Wieland and Stumm, 1992; Lasaga, 1998; Palandri, 2004). This section presents a brief outline of the main types and characteristics of dissolution reactors.

3.8.2. Types of dissolution reactors

3.8.2.1. Batch solid-liquid reactors

Batch reactors consist of agitated or stirred tanks which are set up closed or open to the atmosphere with mineral sample and solution (see Figure 3.5). In a batch reactor all the reactants are added and mixed together. There is no additional amount of reactants, and products are allowed to accumulate. The

only material removed is usually a small aliquot of sample so that the solution/soil ratio is only slightly altered. A batch system allows an easy control of reaction conditions, as pH, ionic strength. On the contrary, desorbed species are not removed and are allowed to accumulate, resulting sometimes in secondary precipitation or in a limited mass transfer of solute (Armacher, 1991; Brantley and Chen, 1995; Brantley, 2005).

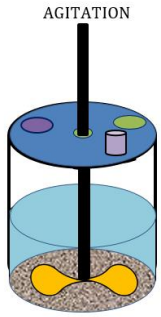

Figure 3.5. Schematic of a simple batch reactor.
Adapted from Amacher (1991).

The reaction rate R (mol cm^{-2} s^{-1}) can then be expressed (Eq. [3.6]) as either the release rate of a given component, or the rate of dissolution of moles of the phase ΔM (mol) per unit time (t). Typically, these rates are then normalized per unit surface area A_s (cm^2 g^{-1}) and per gram of mineral m (g). However, in a batch reactor the measured rate may change as a function of time as the solution chemistry changes, or as minerals precipitate (Brantley and Chen, 1995).

$$R = \frac{\Delta M}{A_s\, m\, t} \qquad [3.6]$$

As recent examples of the use of this kind of reactor, we could mention the work made by: Stephens and Hering (2003) conducting dissolution experiments with volcanic ash soils; Jones et al. (2011) studying the interaction of basaltic riverine particulate material and seawater; or Maters et al. (2016) focusing on the Fe solubility through glass leaching/dissolution experiments.

3.8.2.2. Continuous flow reactors

Flow reactors are open systems in which solute is added to the system and reaction products are removed. In flow reactors the solid phase reacts with a greater mass of solute (*concentration x flow velocity x time*) than in a batch reactor (*concentration x volume*). Advantages of continuous flow systems include the continuous removal of dissolved species, the reduction of diffusion processes, and the possibility of changing the input solution parameters and solution/solid ratios during the experiment (Armacher, 1991; Brantlley, 2005; Cama, 2014).

Interpretation of reaction rates using flow-through reactors is more straightforward than for batch reactors because solution chemistry remains constant during dissolution. The rate of the reaction, R *(mol* cm^{-2} s^{-1}*)* is assessed (Eq. [3.7]) by comparing the input concentration (c_i) to the output concentration (c_o) of a component derived from dissolution of the mineral (Brantley and Chen, 1995; Brantley, 2005):

$$R = \frac{Q\,(c_o - c_i)}{A_s\,m} \qquad [3.7]$$

where Q is the flow rate (L s^{-1}), A_s is the specific surface area of the mineral (cm^2 g^{-1}) and m is its initial mass (g).

The design of continuous flow reactors may vary and one distinguishes the thin-disk, the stirred-flow and the fluidized-bed reactor (Fig. 3.6).

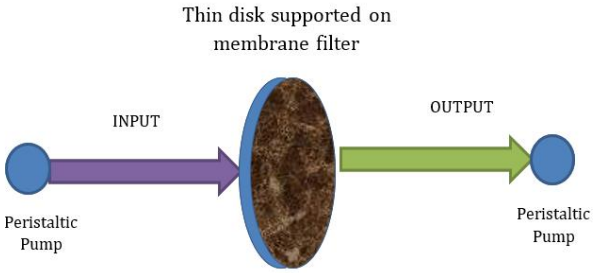

(a) THIN-DISK REACTOR

Figure 3.6. Types of reactors used to obtain kinetic data for dissolution reactions of solids. (a) Thin-Disk reactor, (b) Stirred flow reactor and (c) Fluidized-bed reactor.
Adapted from Amacher (1991).

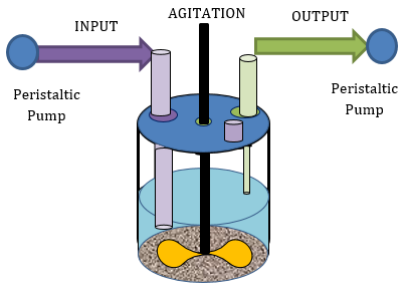

(b) STIRRED FLOW REACTOR

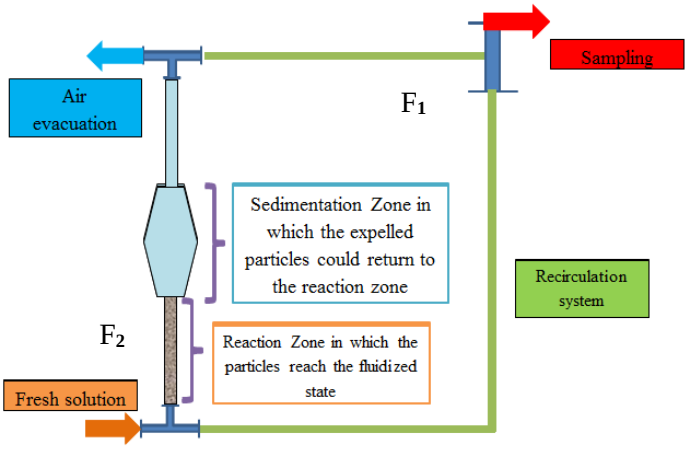

(c) FLUIDIZED-BED REACTOR

Figure 3.6 (continued). Types of reactors used to obtain kinetic data for dissolution reactions of solids. (a) Thin-Disk reactor, (b) Stirred flow reactor and (c) Fluidized-bed reactor.
Adapted from Amacher (1991).

Thin-Disk reactor

In this method a thin disk of dispersed solid phase is deposited on a porous membrane and placed in a holder. A disadvantage of using the thin-disk method is that control over reaction conditions within the thin disk is not usually possible. Although pH and other solution composition variables can be controlled in the input solution, once the solution contacts the thin disk, direct control with feed-back is no longer possible (Armacher, 1991). As an example of the use of the thin-disk method we could mention the study of the kinetics of phosphate and silicate retention by goethite conducted by Miller et al. (1989).

Stirred-Flow reactor

In a stirred-flow through method the reactor is maintained at a constant velocity by a pump, and a fraction collector is used to collect reactor effluent. Mixing is accomplished by a magnetic stirrer (Carski and Sparks, 1985) or even by a propeller connected to a high-torque motor (Miller et al., 1988). Stirred-flow reactors retain all the advantages of the flow methods in general and eliminate all the problems associated with the thin-disk method. Compared to batch reactors, stirred-flow reactors have the advantage that the film or particle diffusion is reduced or eliminated by mixing within the reactor although stirred flow reactors normally have smaller volumes that conventional batch reactors (Armacher, 1991; Brantley and Chen, 1995).

Regarding the application of this kind of reactors in the dissolution study of minerals and glasses we could mention, for instance, the work made by Wolff-Boenisch et al. (2004, 2006) on the effect of crystallinity on dissolution kinetics as a function of chemical composition for natural glasses and silicate minerals using titanium or PE^{TM} mixed flow reactors. In terms of glass dissolution just to mention the work done on basaltic and borosilicate glasses using flow through systems (e.g., Guy and Schott, 1989; Oelkers and Gislason, 2001; Gislason and Oelkers, 2003; Galeczka et al., 2013; Neeway et al., 2018) and rhyolitic volcanic glasses (Yokoyama and Banfield, 2002, Declercq et al., 2013).

Fluidized bed reactor

Fluidization technology has known as the most efficient method for contacting fluid and particles for decades with many applications in the chemical industry (Andrews, 1988; Sabino et al., 2013; Secchi et al., 2013). The fluidized bed reactor, which has its origins in chemical engineering, was used by Chou and

Wollast (1984, 1985) to study albite weathering, by Holmqvist (2001) to study epidote dissolution, among others like, Postma, D. (1990) with the kinetics of nitrate reduction; Griffioen et al. (1999) studying the oxygen consumption in aquifer sediments and Van Hees et al. (2001) with the dissolution of microline, labradorite and a natural soil (C-horizon). The fluidized bed reactor utilizes a slow single-pass flow and a second faster recirculation flow that stirs the mineral powder by suspending the particles in the reactor. A homogeneous, rapidly mixed suspension can be achieved with this type of reactor (Armacher, 1991; Brantley, 2005). Thus, in contrast to the stirred-flow reactor, no additional part is required to maintain the particles in suspension and to homogenise the mixture.

One of the advantages of the fluidized bed reactor is that vigorous mixing in the fluidized bed eliminates strong concentration gradients. Additionally, solute concentrations can be maintained well below saturation levels for various precipitates and thus, secondary precipitation reactions that complicate data analysis and interpretation can be avoided. The effect of reaction conditions (e.g., pH changes) can be studied by changing the input solution composition without manipulating the solid phase (Andrews et al. 1988; Armacher, 1991).

For our dissolution study of powdered volcanic materials, i.e. rock, glass and ash, we selected a fluidized bed system, due to the advantages over a batch system in terms of accumulation and precipitation of secondary phases. Comparing with other variations of continuous flow systems, in a fluidized bed system the circulating fluid keeps the sample in suspension but also homogenizes it, avoiding the introduction of additional parts, like external agitation devices in the stirred-flow method or membranes and holders in the thin-disk method.

3.8.3. Design of the fluidized bed reactor

3.8.3.1. Fluidization of a volcanic rock powder

The Geldart classification (Geldart, 1973; Geldart and Abrahamson, 1978) was used in order to be able to predict the behaviour of a powdered volcanic rock when fluidized. The classification relies on the difference between the density of the solid to be fluidized ρ_s (g cm^{-3}) and that of the fluidizing phase ρ_f (g cm^{-3}) (gas or liquid) and on the mean particle size $\overline{dp}$ (µm). Four groups are usually distinguished: powders in a material belonging to *group A* exhibits dense phase expansion after minimum fluidization velocity; a material belonging to *group B* bubbles at the minimum fluidization velocity; a material

belonging *group C* is difficult to fluidize and a material belonging to *group D* can form stable spouted beds (Fig. 3.7; Levenspiel, 1999).

We assume a range of representative density values of the volcanic powdered material between 2.3 to 3.2 g cm^{-3} (Hyndman, 1985) and a mean particle size of 80 µm (expected size distribution comprised between: 63-100 µm). In Figure 3.7, the Geldart classification is used as an approximation to predict the fluidization behaviour of a volcanic powdered sample (Levenspiel, 1999). Accordingly, volcanic rock particles may be classified as a solid type A, which designates those particles that fluidize easily without the formation of bubbles. Therefore, we expect that the fluidized technology can be applied to investigate volcanic rock powdered dissolution.

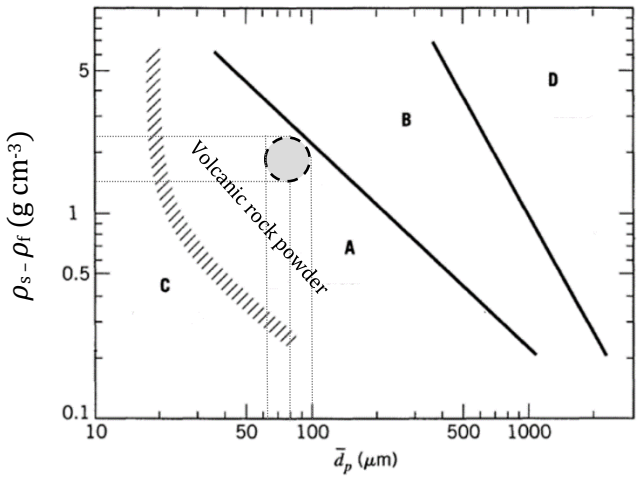

Figure 3.7. Volcanic ash powder in the Geldart classification of solids. *Adapted from Levenspiel (1999).*

3.8.3.2. The phenomenon of fluidization

Fluidization is the operation by which fine solids are transformed into a fluid like state through contact with gas or liquid. In general, if a small quantity of fluid is passed upward through a bed of fine particles, the fluid percolates through the spaces between stationary particles. This is a *fixed bed*. With an increase in flow rate, particles move apart and a few vibrate and move in restricted regions. This is the *expanded bed* (Kunii and Levenspiel, 1969).

At a still higher velocity, a point is reached where all the particles are just suspended by the upward-flowing gas or liquid. At this point the frictional

force between particle and fluid just counterbalances the weight of the particles, the vertical component of the compressive force between adjacent particles disappears, and the pressure drop trough any section of the bed about equals the weight of fluid and particles in that section. The bed is considered to be *fluidized* (Kunii and Levenspiel, 1969).

In liquid-solid systems, an increase in flow rate above minimum fluidization usually results in a smooth, progressive expansion of the bed. At a sufficiently high fluid flow the solids are carried out of the bed with the fluid stream. This state is defined as lean-phase fluidized bed with *pneumatic transport* of solids (Kunii and Levenspiel, 1969).

The different regimes that can develop in a fluidized bed reactor are shown in Figure 3.8. The bed is composed of a layer of material with an initial height L_m. When the fluid starts to circulate at low velocity the particles in the bed keep static, this state is known as a fixed bed. If the flow is increased the fluidization starts and the minimum height of fluidization is reached at L_{mf}. If the flow continues increasing the smooth fluidization is reached at L_f. Finally, if there is a strong increase in the flow rate the particles will be transported with the fluid (pneumatic transport).

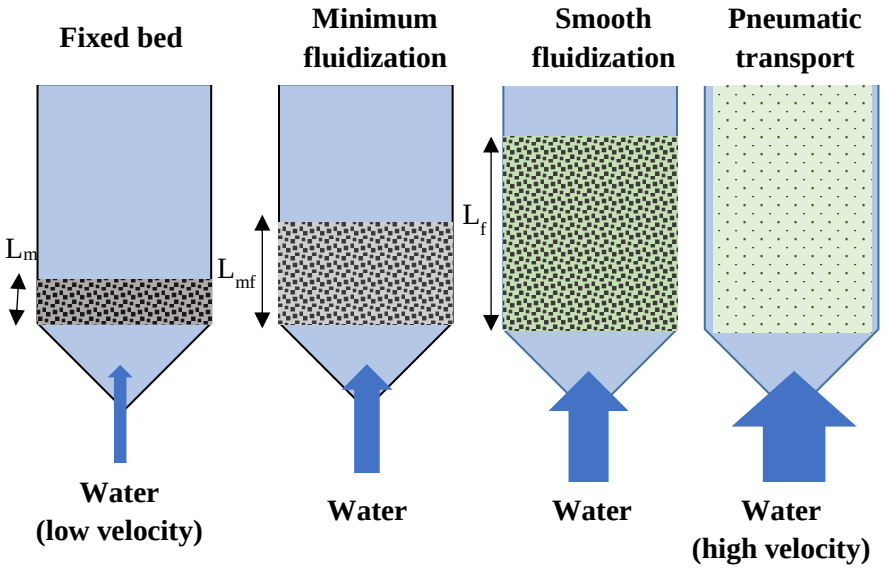

Figure 3.8. Different regimes in a fluidized bed reactor.
Adapted from Kunii and Levenspiel (1969).

The state of fluidization can be described by an equation giving the pressure drop of the fluid trough a packed bed, the Ergun (1952) equation Eq. [3.8]:

$$\frac{\Delta P}{L} g_c = 150 \frac{(1-\varepsilon_m)^2}{\varepsilon_m{}^3} \frac{\mu\ u_m}{(\phi_s\ d_p)^2} + 1.75 \frac{(1-\varepsilon_m)}{\varepsilon_m{}^3} \frac{\rho_p\ u_m{}^2}{\phi_s\ d_p} \qquad [3.8]$$

Where ε_m is the porosity, μ is the fluid viscosity (Poise), u_m is the superficial fluid velocity through a bed of solids (cm s^{-1}), d_p is the size particle (cm), g_c is the conversion factor equals to 980 (gm cm gm-wt^{-1} s^{-2}) and ϕ_s is the sphericity. Porosity has been defined by Eq. [3.9]:

$$\varepsilon_{mf} = 1 - 0.356\ (\log d_P - 1) \qquad [3.9]$$

Where d_p is the particle size [μm]

Sphericity ϕ_s has been defined by Eq. [3.10]:

$$\phi_s = \left(\frac{S_s}{S_p}\right)_{both\ of\ same\ volume} \qquad [3.10]$$

Where S_p is the surface area of each particle (m^2) and S_s corresponds to the surface area calculated for a sphere of the same size as the particle (m^2). With this definition ϕ_s=1 for spheres, and 0< ϕ_s< 1 for all other shapes.

The pressure drop in Eq. [3.8] represents two factors, the viscous and the kinetic energy loses. At low Reynolds (<20) numbers the viscous losses predominate and Eq. [3.8] simplifies to:

$$\frac{\Delta P}{L} g_c = 150 \frac{(1-\varepsilon_m)^2}{\varepsilon_m{}^3} \frac{\mu\ u_m}{(\phi_s\ d_p)^2} \qquad Re_{p,mf} = \frac{d_p\ v_{mf}\ \rho_f}{\mu} < 20 \qquad [3.11]$$

At high Reynolds numbers (>1000) only the kinetic energy losses need to be considered:

$$\frac{\Delta P}{L} g_c = 1.75 \frac{(1-\varepsilon_m)}{\varepsilon_m{}^3} \frac{\rho_p\ u_m{}^2}{\phi_s\ d_p} \qquad Re_{p,mf} > 1000 \qquad [3.12]$$

The solids will be suspended when the pressure drop exceeds the weight of solids. Then onset of fluidization occurs when drag force by upward moving fluid is equal to the weight of particles. This relation is expressed as follows by Eq. [3.13].

$$\Delta p\, A_t = W = \left(A_t\, L_{mf}\right)\left(1 - \varepsilon_{mf}\right)\left[\left(\rho_p - \rho_f\right)\frac{g}{g_c}\right] \quad [3.13]$$

For the drag force on the left side of Eq. [3.13], Δp is the pressure drop across the bed and A_t is the cross-sectional area of tube. In the right side of Eq. [3.13], the weight of particles is composed of three terms, the first is the product $A_t\, L_{mf}$ which is the volume of the bed. The fraction of solids is obtained from the porosity$\left(1 - \varepsilon_{mf}\right)$. The last term $\left[\left(\rho_p - \rho_f\right)\frac{g}{g_c}\right]$ corresponds to the specific weight of solids, where ρ_p is the particle density, ρ_f is the fluid density and g is the acceleration of gravity.

Combining Eq. [3.8] and Eq. [3.13], the velocity of minimum fluidization, u_{mf}, is:

$$\frac{1.75}{\phi_s\, {\varepsilon_m}^3}\left(\frac{d_p\, u_{mf}\, \rho_f}{\mu}\right)^2 + \frac{150\,(1-\varepsilon_m)^2}{{\phi_s}^2 {\varepsilon_m}^3}\left(\frac{d_p\, u_{mf}\, \rho_f}{\mu}\right) = \frac{{d_p}^3 \rho_f\,(\rho_p - \rho_f)\, g}{\mu^2} \quad [3.14]$$

For small particles of small specific weight Eq. [3.8] simplifies to Eq. [3.11] and Eq. [3.14] gives

$$u_{mf} = \frac{{d_p}^2\,(\rho_p - \rho_f)\, g\;\; {\varepsilon_{mf}}^3\, {\phi_s}^2}{150\mu\,(1-\varepsilon_{mf})} \quad Re < 20 \quad [3.15]$$

For large particles Eq. [3.8] simplifies to Eq. [3.12] and Eq. [3.14] becomes

$${u_{mf}}^2 = \frac{d_p\;{\varepsilon_{mf}}^3\,\phi_s\;(\rho_p - \rho_f)\, g}{1.75\;\rho_f} \quad Re > 1000 \quad [3.16]$$

For designing proposes we consider the volcanic powdered material as an homogeneous powder comprised between 63 and 100 µm (d_p = 0.008 cm - 80 µm), with density values ranging from 2.3 to 3.2 g cm^{-3} (Hyndman, 1985), an average specific surface area of 1 m^2 g^{-1} (Delmelle et al., 2004) and an average sphericity of 0.7 (Riley et al., 2003). Then, the minimum fluidized velocity required to maintain a volcanic rock powder in suspension in a fluidized bed reactor is estimated using Eq. [3.15] (ρ_f = 1 g cm^{-3}, g = 980 cm s^{-1} and µ = 0.001 Poise). We found a minimum fluidized rate comprised between 0.2 and 0.4 cm s^{-1}. This corresponds to a low Reynolds number value of 2-3.5, which

agrees with the choice of Eq. [3.15] for Re < 20. Based on this result, it is possible to establish the minimum pumping rate in the fluidized bed reactor, taking in account the internal diameter of the reaction chamber (0.8 cm). The minimum flow to maintain the volcanic rock powder in suspension is 8-14 mL min^{-1}. In practice, we will work at a flow rate of 14 mL min^{-1} (see Figure 3.6c).

The flow within the reactor necessary to maintain the powdered volcanic rock in suspension is provided by the pumping rate (F_1), whereas (F_2) is the rate of addition of new solution into the reactor (see Figure 3.6c). The renewal rate, associated to the feeding flow rate, controls the residence time of the solution in the reactor. The renewal rate (F_2) must be small in comparison to the mixing rate (F_1) to maintain a small difference in concentration between input at the bottom of the fluidized bed and output at the top of the bed. Chou and Wollast (1984) maintained F_2 between 3 and 6% of F_1. Taking into account this criterion, the feeding flow in our system is fixed at 0.4 mL min^{-1} (i.e. 3% of the main circulating flow), which corresponds to a residence time of 3 hours (flow rate 0.4 mL min^{-1} and volume ~ 65 mL).

3.8.4. Description of the fluidized bed reactor

The dissolution experiments are performed in a fluidized bed flow-through system coupled to a continuous extraction system and a temperature control. The reactor consists of a 50 mL polypropylene pipette (BRAND 50±0.1 mL) equipped with one circulation pump (Watson Marlon 90 RPM) to keep the material in suspension (14 mL min^{-1}) and peripheral feeding/extraction system (~0.4 mL min^{-1}). The peripheral system consists of Tygon® tubing (3x5 mm) and feeding/extracting peristaltic pumps (Miniplus 2 GILSON). Figures 3.9 and 3.10 depict the different variations of the system used. For the short-term release of elements coming from volcanic ash (Chapter 4), an automatic sampling regulator system was incorporated to the main system which is presented in Figure 3.9. The dissolution rate of volcanic rocks in the acidic pH range (Chapters 5 and 6) was obtained using the variation of the system presented in Figure 3.10, in which the automatic sampling control has been removed, a check valve was added in the tubing feeding the input solution and a nylon mesh (64 µm) was placed in the top of the pipette to avoid the transport of particles outside the pipette. Figures 3.11, 3.12 and 3.13 show photographs of the fluidized bed system used in this study (version II and I). Figure 3.14 presents the fluidized state reached by the powdered sample during the dissolution experiment.

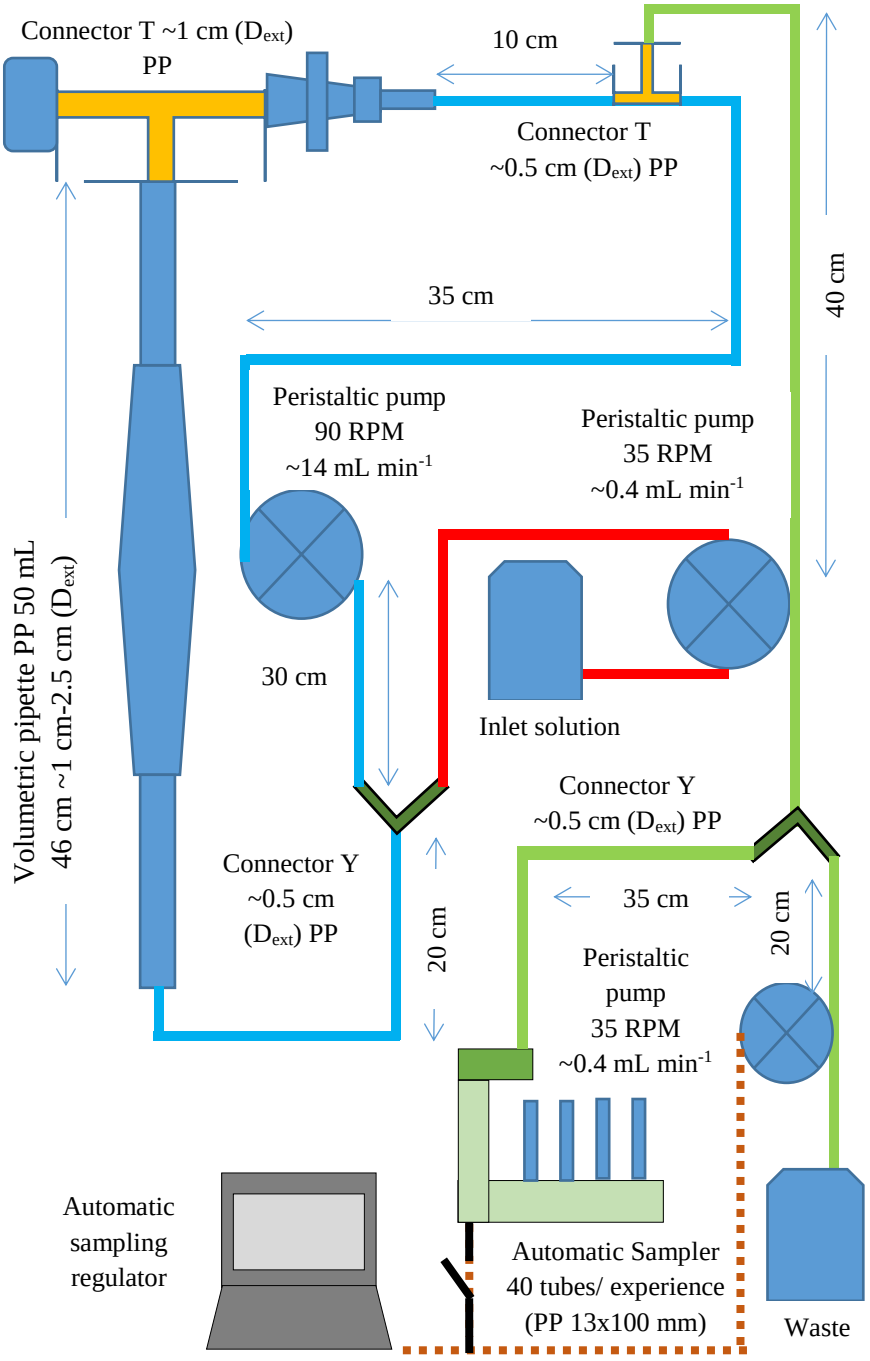

Figure 3.9. Fluidized bed reactor proposed for volcanic ash dissolution (VERSION I Chapter 4).

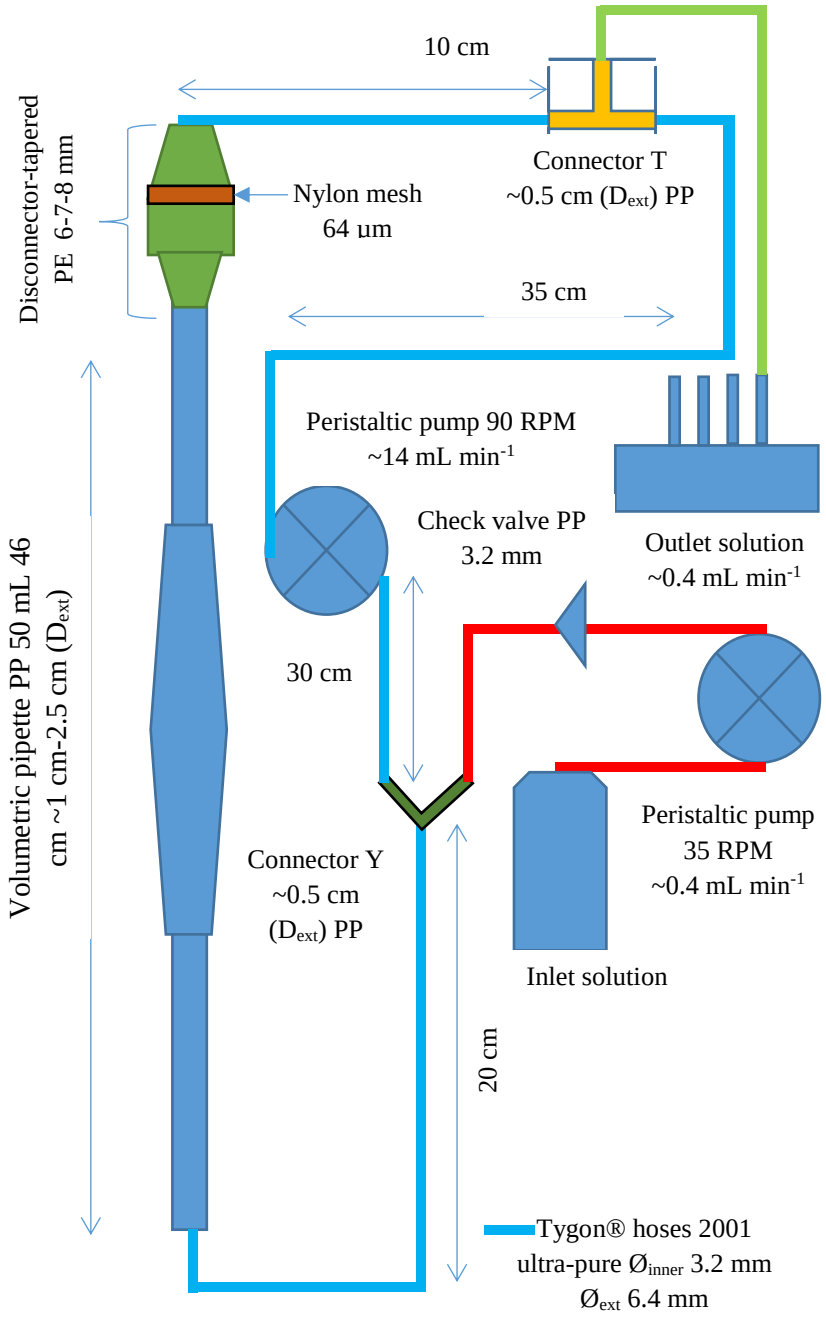

Figure 3.10. Fluidized bed reactor proposed for volcanic rock/ash/glass dissolution (VERSION II Chapters 5 and 6).

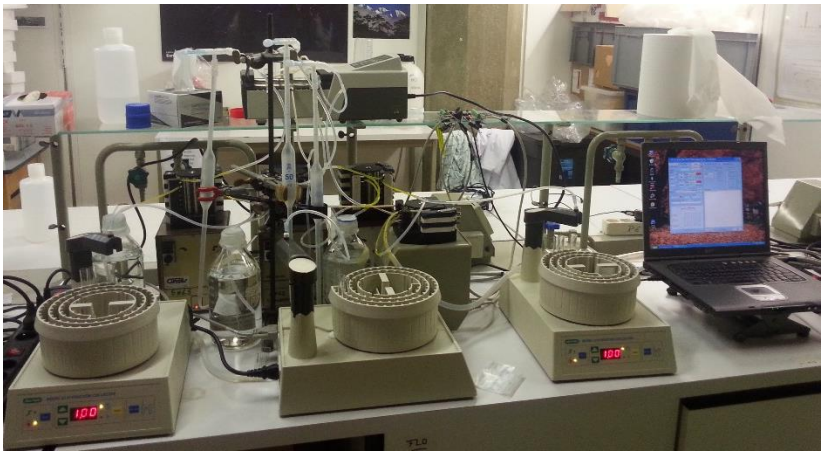

Figure 3.11. Photograph of the fluidized bed system used for volcanic ash dissolution (VERSION I Chapter 4).

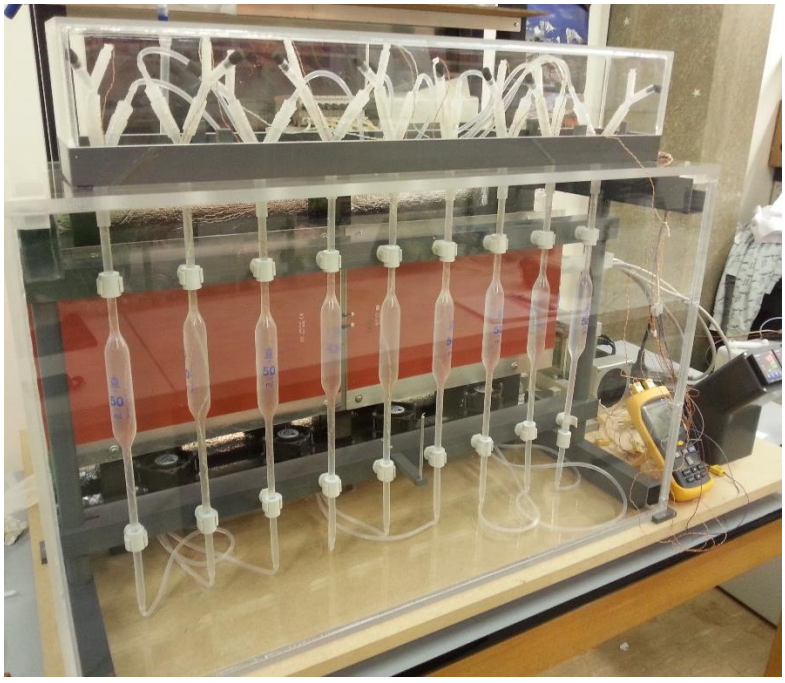

Figure 3.12. Photograph of the fluidized bed system (viewed from the front) used for volcanic rock/ash/glass dissolution (VERSION II Chapters 5 and 6).

Figure 3.13. Photograph of the fluidized bed system (viewed from the back) used for volcanic rock/ash/glass dissolution (VERSION II Chapters 5 and 6)

Figure 3.14. Photograph showing the fluidized state reached by the powdered rock sample during the dissolution experiments.

3.9. DESCRIPTION OF THE MODEL WITCH

3.9.1. Introduction

The WITCH geochemical model is a box model that has been used to simulate water-minerals interactions as a function of time in various environments. In our study, this model is applied to simulate the alteration of a volcanic ash deposit (rhyolitic glass 80%, quartz 7.34%, K-feldspar 6.26% and albite 5.54%), similar to those deposed by a super-eruption in Yellowstone (USA) but incorporating actual data of temperature and runoff. The model provides the evolution of mineralogy due to the chemical weathering, as well the formation of secondary mineral phases (allophane/imogolite and halloysite/kaolinite), the fluxes of released elements (Si, Ca, Na, K, Mg), and carbon dioxide (CO_2) consumption for different time scales (0.1 yr, 1 yr, 10 yrs, 100 yrs, 1000 yrs and 10 000 yrs). In this section, a general description of the WITCH model, as well, the specific version of this model used in our case study for simulating the weathering of a volcanic ash deposit are presented.

3.9.1.1. WITCH development and previous applications

A main challenge for the accurate description of continental weathering is to identify the main factors controlling chemical weathering and to quantify their effect in given environments and at various geometric and time scales. Therefore, a critical step is the building of a numerical model describing the large-scale (watershed-scale) weathering of silicate rocks, based on a description of the weathering processes as mechanistic as possible (including dissolution of primary and secondary minerals and precipitation of secondary minerals and coupled to hydrological processes) (Goddéris et al., 2006).

The WITCH model mainly relies on laboratory kinetics laws to describe chemical weathering in the natural environment. WITCH was applied to estimate the chemical weathering in soil horizons and underlying bedrock of different lithologies (basalt, granite, sandstone, loess), ranging from polar (Mackenzie basin) to tropical settings (Orinoco watershed) (Goddéris et al., 2006, 2009, 2010, 2013; Beaulieu et al., 2010, 2011, 2012).

In the late years, the WITCH model has been coupled to different biological and climatic models. Thus, in order to explore the response of the continental weathering to anthropogenic land use and climate changes, WITCH has been coupled to a model of the continental biospheric productivity (ASPECTS model) (Goddéris et al., 2006, 2009). In another application, the rates of mineral weathering in loess deposited 23 kyr ago were explored using the WITCH model and the GENESIS model for climate simulation (Goddéris et

al., 2010). WITCH model, coupled to a biogeochemistry model (LPJ), has been used to quantify the sensitivity of CO_2 consumption by silicate rock weathering through changes in continental vegetation and drainage at various atmospheric CO_2 levels (Beaulieu et al., 2010, 2011, 2012). WITCH has been also included in a cascade of numerical models, along with models for climate (ARPEGE) and vegetation (CARAIB), to explore the effect of an increase in CO_2 into the future (Goddéris and Brantley, 2013; Goddéris et al., 2013).

3.9.2. The general description of the WITCH model

The WITCH geochemical model is a box model that calculates the time evolution of the enriched solution as a function of time (Goddéris et al., 2006, Goddéris et al., 2013). In this study, the model is applied to estimate the enriched solution obtained from the chemical weathering of a continental size deposit of rhyolitic ash extending from the surface down to 20 cm.

The mass balance is calculated for each time step solving the following differential equation (Eq. [3.17]):

$$\frac{d(z\,\theta\,C_j)}{dt} = F_{top} - F_{bot} + \sum_{i=1}^{n_m} F^i_{weath,j} - \sum_{i=1}^{n_m} F^i_{prec,j} \pm F_{exchange} \quad [3.17]$$

Where C_j is the concentration of the species j. WITCH includes a budget equation for Ca^{2+} , Mg^{2+}, K^+, Na^+, total alkalinity, total aluminium and total silica. z is the thickness of the layer under consideration and θ is the water volumetric content. F_{top} is the input of species from the layer above the given layer in moles per unit time through drainage and F_{bot} is the output of species from the layer at the base of the box in moles per unit time through drainage. n_m is the total number of minerals considered in the simulation. $F_{exchange}$ is the exchange term between the soil solution and the clay-humid complex $F^i_{weath,j}$ is the release of species *j* to solution of the mineral *i* in the box and $F^i_{prec,j}$ is the removal of *j* through precipitation when the solution becomes supersaturated with the respect to mineral *i* (Godderis et al., 2006; Godderis et al., 2013). The dissolution $F^i_{weath,j}$ and precipitation $F^i_{prec,j}$ terms for silicate minerals are calculated using kinetic laws and parameters derived from transition state theory (Eyring, 1935) and laboratory experiments, respectively.

The overall dissolution rate of a mineral R_s is derived using (Schott et al., 2009; Goddéris et al., 2010):

$$R_s = A \cdot S_w \left[\sum_i k_i \cdot \exp\left(\frac{E_a^i}{RT}\right) \cdot a_i^{n_i} \cdot f_{inh}\right] (1 - \Omega^s) \quad [3.18]$$

where *A* stands for the mineral reactive surface, S_w is the moisture saturation (which depends on the water volumetric content, Sverdrup and Warfinge, 1995) of layer *n*, k_i and E_a^i are the dissolution rate constant and activation energy for the *i* species-promoted dissolution, respectively, a_i and n_i represent the activity and the order of reaction with respect to the dissolving species *i*, respectively. The parameter f_{inh} describes the inhibiting effect of aqueous species on proton and hydroxyl-promoted aluminosilicate dissolution reactions. In general, Al^{3+} is regarded as the main inhibiting species (e.g., Oelkers et al., 1994; Oelkers and Schott, 1995; Devidal et al., 1997). The effect of departure from equilibrium on mineral dissolution rates is accounted for by the factor $(1 - \Omega^s)$, where Ω stands for the solution saturation index with respect to the particular solid and *s* reflects stoichiometry (i.e. the number of metal atoms that need to be removed to form one precursor complex during dissolution). $F_{precipitation}$ is computed from Eq. [3.18] when precipitation of secondary phases is allowed to occur, i.e. when the affinity term in equation term is negative (i.e. $\Omega^s > 1$).

Additionally, the solution saturation state is described with the equation 3.19:

$$\Omega = \frac{Q}{K_g} \quad [3.19]$$

Where Q is the activity quotient and K_g is the equilibrium constant for mineral dissociation reaction.

References

American Society for Testing and Materials (2015) ASTM D3663-03(2015), Standard Test Method for surface Area of Catalyst and Catalyst Carriers. ASTM International, West Conshohocken, United States of America, doi: 10.1520/D3663-03R15.

Andrews, G. (1988) Fluidized-bed reactors. Biotechnology and Genetic Engineering Reviews. Vol 6. 151-178.

Armacher, M.C (1991) Methods of Obtaining and Analyzing Kinetic Data. Soils Science Society of America. Rates of Soil Chemical Processes. SSSA Special Publication no.27.

Beaulieu, E., Goddéris, Y., Donnadieu, Y., Labat, D. and Roelandt, C. (2012) High sensitivity of the continental-weathering carbon dioxide sink to future climate change. Letters Nature climate change. Vol 2. 346-349.

Beaulieu, E., Goddéris, Y., Labat, D., Roelandt C., Calmels, D. and Gaillardet, J. (2011) Modeling of water-rock interaction in the Mackenzie basin: Competition between sulfuric and carbonic acids. Chemical Geology 289. 114-123.

Beaulieu, E., Y. Goddéris, D. Labat, C. Roelandt, P. Oliva, and B. Guerrero (2010), Impact of atmospheric CO2 levels on continental silicate weathering, Geochem. Geophys. Geosyst., 11.

Brantley, S.L. (2005) Reaction Kinetics of Primary Rock-forming Minerals under Ambient Conditions. In Surface and ground water, weathering and soils. Drever, J.I., Holland, H.D. and Turekiean K.K. (eds). Treatise on Geochemistry Vol 5. 74-108.

Brantley, S.L., White, A. F. and Hodson, M. (1999) Surface Area of Primary Silicate Minerals. In Growth and Dissolution in Geosystems, Jamtveit, B. and Meakin, P. (Eds.). Kluwer Academic Publishers, Dordrecht, pp. 291-326.

Brantley S.L. and Chen Y. (1995) Chemical weathering rates of pyroxenes and amphiboles; Chemical Weathering rates of silicate minerals; White A.F & Brantley S.L (editors) REVIEWS in MINERALOGY; Volume 31; chapter 4.

Brunauer, S., Emmett, P. H. and Teller, E. (1938) Adsorption of gases in multimolecular layers. Journal of the American Chemical Society, 60(2), 309-319.

Cama, J. (2014) Mineral dissolution and precipitation kinetics: macroscopic, microscopic and nanoscopic techniques. Macla. N°14. Revista de la sociedad Española de mineralogía. 20-28.

Carski, T.H., and Sparks, D.L. (1985) A modified miscible displacement technique for investigating adsorption-desorpotion kinetics in soils. Soil Sci. Soc. Am. J. 49: 114-116.

Castro JM, Dingwell DB (2009) Rapid ascent of rhyolite magma at Chaitén volcano, Chile. Nature 461: 780-784.

Cepuritis, R., Garboczi, E.J., Ferraris, C.F., Jacobsen, S., Sorensen, B.E. (2017) Measurement of particle size distribution and specific surface area for crushed concrete aggregate fine. Advanced Powder Technology 28. 706-720.

Chao, T. T. and Sanzolone, R.F. (1992) Decomposition techniques. Journal of Geochemical Exploration, 44, 65-106.

Chou, L. and Wollast R. (1985) Study of the weathering of albite at room temperature and pressure with a fluidized bed reactor. Geochimica et Cosmochimica Acta Vol. 48, pp 2205-2217.

Chou L. and Wollast R. (1984) Study of the weathering of albite at room temperature and pressure with a fluidized bed reactor. Geochim. Cosmochim. Acta 48/22205-2217.

Declercq, J., Diedrich. T., Perrot M., Gislason S.R., Oelkers E.H. (2013) Experimental determination of rhyolitic glass dissolution rates at 40–200 °C and 2 < pH < 10.1. Geochimica et Cosmochimica Acta 100 (2013) 251–263.

Delmelle P., Villiéras F. and Pelletier M. (2004) Surface area, porosity and water absorption properties of fine volcanic ash particles. Bull Volcanol (2005) 67:160–169.

Devidal, J.L., Schott, J., Dandurand, J.-L. (1997) An experimental study of kaolinite dissolution and precipitation kinetics as a function of chemical affinity and solution composition at 150°C, 40 bars, and pH 2, 6.8, and 7.8. Geochimica et Cosmochimica Acta 61 (24): 5165-5186.

Ergun, S, Orning, A.A. (1952) Fluid Flow Through Packed Columns. Chemical Engineering Progress. 48 89-94.

Ermeling F. (2014) Precision Measurement of the Specific Surface Area of Solids by Gas Adsorption. Bundesanstalt für Materialforschung und prüfung

(BAM). Chapter 4: Microprobing and microstructure analysis. Reference procedure 402.

Eyring, H. (1935) The activated complex in chemical reactions. J. Chem.Phys., 3, 107-115.

Funk, J.E. and Dinger D. (1993) Predictive Process control of Crowded Particulate Suspensions: Applied to Ceramic Manufacturing. Kluwer Academic Publishers. Chapter 39 True Particle Density and Suspension Specific Gravity. pp 624-627.

Galeczka, I., Wolff-Boenisch, D., Jonsson, T., Sigfusson, B., Stefansson, A., Gislason, S.R. (2013) A novel high pressure column flow reactor for experimental studies of CO_2 mineral storage. Applied Geochemistry 30: 91-104.

Geldart, D. and Abrahamson, A. A. (1978) Homogeneous fluidization of fine powders using various gases and pressures, Powder Technol., 19, 133.

Geldart, D. (1973) Types of gas fluidization. Powder Technol., 7, 285.

Gislason S. and Oelkers E.H. (2003) Mechanism, rates, and consequences of basaltic glass dissolution: II. An experimental study of the dissolution rates of basaltic glass as a function of pH and temperature. Geochimica et Cosmochmica Acta, Vol. 67, No. 20, pp. 3817-3832.

Goddéris, Y. and Brantley, S.L. (2013) Earthcasting the future Critical Zone. Elementa: Science of the Anthropocene • 1: 000019. pp. 1-10

Goddéris Y., Brantley S.L., François L.M., Schott J., Pollard D., Déqué M. and Dury M. (2013) Rates of consumption of atmospheric CO_2 through the weathering of loess during the next 100 yr of climate change. Biogeosciences, 10, 135-148,2013.

Goddéris, Y., Williams, J.Z., Schott, J., Pollard, D., Brantley, S.L. (2010) Time evolution of the mineralogical composition of Mississippi Valley loess over the last 10 kyr: Climate and geochemical modeling. Geochimica et Cosmochimica Acta 74. pp 6357-6374

Goddéris Y., Roelandt, C., Schott, J., Pierret M. and François, L.M. (2009) Towards an Integrated Model of Weathering, Climate, and Biospheric Processes. In Oelkers, E.H and Schott, J. (Eds) Reviews in Mineralogy & Geochemistry. Vol 70 pp. 411-434.

Godderis Y., François L., Probst A., Schott J., Moncoulon D., et al. (2006) Modelling weathering processes at the catchment scale: The WITCH numerical model. Geochimica et Cosmochimica Acta, Elsevier, 70, pp.1128-1147. <10.1016/j.gca.2005.11.018>. <hal-00665423>

Griffioen J. Van der Grift, B., Buijs, A.; Hartog, N. (1999) Oxygen consumption of natural reductants in aquifer sediment related to in situ bioremediation. Int. In Situ On-Site Biorem. Symp., 5th, 463-468.

Guy C. and Schott J. (1989) Multisite surface reactions versus transport control during the hydrolysis of a complex oxide. Chem. Geol. 78, 181-204.

Hall, A. (1996) Igneous Petrology. Second Edition. Longman Group. Chapters 8-10.

Holmqvist, J. (2001) Modelling Chemical Weathering in Different Scales. Doctoral Thesis. Department of Chemical Engineering. Lund University, Sweden. Chapter 6 Experimental kinetics 16-23.

HORIBA Scientific (2012) A Guidebook to particle size analysis. https://www.horiba.com/fileadmin/uploads/Scientific/Documents/PSA/PSA_Guidebook.pdf

Hyndman, D.W. (1985) Petrology of Igneous and Metamorphic Rock. Second Edition. McGraw-Hill Book Company. International series in the Earth & Planetary Sciences. Chapter 3. Classification and characteristics of Igneous Rocks. p.65.

ISO 13320:2009 Particle size analysis -- Laser diffraction methods.

ISO 1183-1:2012 Plastics -- Methods for determining the density of non-cellular plastics -- Part 1: Immersion method, liquid pyknometer method and titration method.

ISO 9277:2010 Determination of the specific surface area of solids by gas adsorption -- BET method

Jacquinot, P. (1957) Optique Ondulatoire: Interférences-Diffraction 3. Certificat de Physique Générale. Editions Claude Hermant. Chapitre 9. Diffraction de Fraunhoffer. pp. 127-167.

Jones, M.T., Pearce, C.R., Oelkers, E.H. (2011) An experimental study of the interaction of basaltic riverine particulate material and seawater. Geochimica et Cosmochimica Acta 77: 108-120.

Kaszuba, J., Yardley, B. and Andreani, M. (2013) Experimental perspective of mineral dissolution and precipitation due to carbon dioxide-water-rock interactions. Reviews in Mineralogy and Geochemistry. 77(1). 153-188.

Kunii, D. and Levenspiel, O. (1969) Fluidization Engineering. USA. John Wiley & Sons, Inc.

Lasaga, A.C. (1998) Kinetic Theory in the Earth Sciences. Princeton University Press. Princenton.

Levenspiel, O. (1999) Chemical Reaction Engineering. Third Edition. Chapter 20. Reactors with Suspended Solid Catalyst, Fluidized Reactors of Various Types. 447-470.

Maters, E.C., Delmelle, P., Bonneville, S. (2016) Atmospheric Processing of Volcanic Glass: Effects on Iron Solubility and Redox Speciation. Environmental Science Technology. 5033-5040.

Metz, V. and Ganor, J. (2001) Stirring effect on kaolinite dissolution rate. Geochim. Cosmochim. Acta 65. 3475-3490.

Miller, D.M., Sumner, M.E. and Miller, W.P. (1989) A comparison of batch and flow generated anion adsorption isotherms. Soil Sci. Soc. Am. J. 53:373-380.

Miller, D.M., Miller, W.P. and Summer, M.E. (1988) A continuously stirred tank reactor for solid/solute adsorption studies. p. 201. In Agronomy abstracts. ASA. Madison. WI.

Neeway, J.J., Rieke, P.C., Parruzot, B.P., Ryan, J.V., Asmussen, R.M. (2018) The dissolution behaviour of borosilicate glasses in far-from equilibrium conditions. Geochimica et Cosmochimica Acta 226: 132-148.

Oelkers, E.H. (2001) General kinetic description of multioxide silicate mineral and glass dissolution. Geochimica et Cosmochimica Acta, 65(21) pp. 3703-3019.

Oelkers, E.H, and Gislason S. (2001) The mechanism, rates and consequences of basaltic glass dissolution: I. An experimental study of the dissolution rates of basaltic glass as a function of aqueous Al, Si and oxalic acid concentration at 25°C and pH=3 and 11. Geochimica et Cosmochimica Acta, Vol. 65, No. 21, pp. 3671–3681, 2001.

Oelkers, E.H. and Schott, J. (1995) Experimental study of anorthite dissolution and the relative mechanism of feldspar hydroloysis. Geochimica et Cosmochimica Acta 59 (24): 5039-5053.

Oelkers, E.H., Schott, J., Devidal, J.L. (1994). The effect of aluminum, pH, and chemical affinity on the rates of aluminosilicate dissolution reactions. Geochim. Cosmochim. Acta, 58 (9), 2011-2024.

Ostertat-Henning, C., Risse, A., Thomas, B., Rosenbauer, R., Rochelle, C., Purser, G. . . . Truche, L. (2014) GaMin'11-an international inter-laboratory comparison for geochemical CO_2- saline fluid- mineral interaction experiments. Energy Procedia 63. 5538-5543.

Palandri J.L. and Kharaka, Y.K. (2004) A Compilation of Rate Parameters of Water-Mineral Interaction Kinetics for Application to Geochemical Modeling. U.S. Geological Survey open file report 2004-1068.

Paque, M., Detienne, M., Maters, E.C., Delmelle, P. (2016) Smectites and zeolites in ash from the 2010 summit eruption of Eyjafjallajökull volcano, Island. Bull Volcanol 78: 61.

Pecharsky, V.K. and Zavalij P.Y. (2005) Fundamentals of powder diffraction and structural characterization of materials. Springer. Chapter 4. Preliminary Data Processing and Phase Analysis. pp 388.

Petrovich, R. (1981) Kinetics of dissolution of mechanically comminuted rock-forming oxides and silicates-I. Deformation and dissolution of quartz under laboratory conditions. Geochim. Cosmochim. Acta 45, 1665-1674.

Pokrovsky, O. S. and Schott, J. (2000) Kinetics and mechanism of forsterite dissolution at 25°C and pH from 1 to 12. Geochimica et Cosmochimica Acta. Vol 64. No 19. 3313-3325.

Postma D. (1990) Kinetics of nitrate reduction by detrital Fe (II)-silicates. Geochimica et Cosmochimica Acta 54(3), 903-908.

Pownceby, M.I., MacRae, C.M., Wilson, N.C. (2006) Mineral characterization by EPMA mapping. Mineral Engineering 20. 444-451.

Rietveld, H.M. (1968) A Profile Refinement Method for Nuclear and Magnetic Structures. Journal of Applied Crystallography. 2. pp.65-71.

Riley, C.M., Rose, W.I. and Bluth G.J.S (2003) Quantitative shape measurements of distal volcanic ash. Journal of Geophysical Research, VOL. 108, NO. B10, 2504.

Rimstidt, J.D., Dove, P.M. (1986) Mineral/solution reaction rates in a mixed flow reactor: wollastonite hydrolysis. Geochim Cosmochim Acta 50. 2509-2516.

Sabino, M.E.L.; Passos, M.L.; Branco, J.R., Vitor, J.F.A. (2013) Integrated fluidized bed reactors for silicon production. In Fluidization Engineering. Pratice. Passos, M.L., Barrozo, M.A.S. and Mujumdar, A.S. (eds.). 209-247.

Schott, J., Pokrovsky, O.S. and Oelkers, E.H. (2009) The link between mineral dissolution/precipitation kinetics and solution chemistry. Reviews in Mineralogy & Geochemistry. Vol 70 pp. 207-258.

Secchi, A.R., Neuman, G.A. and Gambetta, R. (2013) Gas fluidized bed polimerization. In Fluidization Engineering. Pratice. Passos, M.L., Barrozo, M.A.S. and Mujumdar, A.S. (eds.). 61-92.

Stephens, J.C. and Hering, J.G. (2003) Factors affecting the dissolution kinetics of volcanic ash soils: dependencies on pH, CO_2 and oxalate. Applied Geochemistry 19. 1217-1232.

Sverdrup, H. and Warfinge, P. (1995) Estimating field weathering rates using laboratory kinetics. Rev. Mineral. 31, 485-541.

Van Hees P. A. W., Lundstrom U. S., and Morth C.M. (2002) Dissolution of microcline and labradorite in a forest O horizon extract: the effect of naturally occurring organic acids. Chemical Geology 189(3-4), 199-211.

Ward, C.R and French, d. (2006) Determination of glass content and estimation of glass composition in fly ash using quantitative X-ray diffractometry. Fuel, 85, 2268-2277.

Ward CR, French D (2006) Determination of glass content and estimationof glass composition in fly ash using quantitative X-ray diffractometry. Fuel 85:2268–2277.

Wieland, E. and Stumm, W. (1992) Dissolution kinetics of kaolinite in acidic solutions at 25°C. Geochim. Cosmochim. Acta 56. 3339-3355.

Winburn RS, Grier DG, McCarthy GJ, Peterson RB (2000) Rietveld quantitative X-ray diffraction analysis of NIST fly ash standard reference materials. Powder Diffract 15:163–172.

Wolff-Boenisch, D., Gislason S. R., Oelkers, E. and Putnis, C.V. (2004) The dissolution rates of natural glasses as a function of their composition at pH 4

and 10.6 and temperatures from 25 to 74°C. Geochimica et Cosmochimica Acta, Vol.68, No. 23, pp 4843-4858.

Wolff-Boenisch D., Gislason S. and Oelkers E. (2006) The effect of crystallinity on dissolution rates and CO_2 consumption capacity of silicates. Geochimica et Cosmochimica Acta 70(2006); 858-870.

Yokoyama, T. and Banfield, J.F. (2002) Direct determination of the rates of rhyolite dissolution and clay formation over 52,000 years and comparison with laboratory measurements. Geochimica et Cosmochimica Acta, Vol. 66, No. 15, pp. 2665-2681.

PART II
DATA CHAPTERS

CHAPTER 4 Dissolution behaviour of a basaltic ash between pH 2 and pH 11 at 20 °C

4.1. INTRODUCTION

Understanding the chemical weathering of aluminosilicate minerals and glasses is important in diverse contexts, including geochemistry and biogeochemical cycles (Oelkers et al., 2001), nuclear waste management (Techer et al., 2000) or even cultural heritage conservation (Verney-Carron et al., 2017). It has been shown that weathering of basaltic glass strongly impacts the chemistry of surface waters as well as the carbon cycle (Dessert et al., 2003). Among the natural aluminosilicates, basaltic glass plays a major role in the global flux and cycling of numerous metals and nutrients. This is due to its widespread occurrence on the ocean floor and in volcanic terrains, emission during volcanic eruption and relative rapid dissolution rate (Oelkers and Gislason, 2001). Therefore, significant efforts have been made to unravel the dissolution rates and alteration mechanism of basaltic glass.

Glasses in contact with an aqueous solution are subject to continuous dissolution, during which altered layers with different compositions form on the surface (Baucke, 1974). Much evidence has accumulated documenting the development of Si-rich cation-depleted layers of varying thickness on many dissolving silicates, especially at low pH (Brantley, 2003). This altered layer has been named variably as 'hydrated glass', 'leached glass', 'gel layer', 'leached layer' or 'residual layer' (Boksay et al., 1967; Chou and Wollast, 1984; Gin et al., 2015; Verney-Carron et al., 2017). It has also been suggested that such layers may not be homogeneous in composition, structure or thickness (e.g., Gout et al., 1997). In contrast, other authors have suggested that leached layers are uniform over the mineral surface (e.g., Schweda et al., 1997; Brantley, 2003). The presence of residual layer on the solid surface has been hypothesized to slow down the dissolution process (Jégou et al., 2000; Gin, 2001; Valle et al., 2010).

In order to explain the formation of a residual or gel layer on glass surfaces, three hypotheses are usually suggested. The first one considers that the layer at the surface results from a selective leaching of the glass. The gel is formed by inter-diffusion between alkalis and hydrogen species (Rana and Douglas, 1961 a, b; Doremus, 1975; Landford et al., 1979) and consists in a residual skeleton of the pristine glass. The second hypothesis is that the gel layer is formed by precipitation from a saturated solution (Crosvisier et al., 1987; 2003; Zhou and Fyfe, 1989; Jercinovic et al., 1990; Daux et al., 1994; Stroncik and Schmincke, 2001). The third hypothesis considers that the gel is formed by in situ silica recondensation (Bunker, 1994; Tsomaia et al., 2003); it is the

preferred view of the community interested in nuclear glass (Jégou et al., 2000; Gin, 2001; Frugier et al., 2008; Valle et al., 2010).

Alteration layers have been described for feldspars dissolved at subneutral pH (Chou and Wollast, 1984, 1985; Casey et al., 1988, 1989; Nesbitt and Muir, 1988; Muier et al., 1989, 1990; Hellmann et al., 1989, 1990 a,b, 1991; Shotyk et al., 1990; Hochella, 1990; Nesbitt et al., 1991; Helmann, 1994, 1995, 1997; Stillings and Brantley, 1995; Gout et al., 1997), glasses (Guy and Schott, 1989; Doremus, 1994; Hamilton et al., 2000, 2001), inosilicates (Brantley and Chen, 1995), and some phyllosilicates (Nagy, 1995; Kalinowski and Schweda, 1996; Brantley, 2003). The development of alteration layers on minerals dissolved under neutral and alkaline conditions has not been thoroughly investigated (Chou and Wollast, 1984; Hellmann et al., 1989, 1990a, Muir et al., 1990; Nesbitt et al., 1991; Hellmann, 1995; Hamilton et al., 2000). Despite the plethora of studies mentioning the presence of an altered layer on aluminosilicates, little is known about the description of alteration layers in polycrystalline materials, which makes the majority of rocks found in nature.

The purpose of this chapter is to study the formation of an altered layer, formed over a polycrystalline material using a classical experimental approach to study glass alteration. For that, a dissolution experiment conducted over a specimen of basaltic ash was carried out using solutions of different pH at 20 °C in a fluidized bed reactor. We determine the cation releases and calculated the dissolution rate at steady state in an attempt to investigate the formation of a residual layer at the surface of the ash.

4.2. MATERIALS AND METHODS

4.2.1. Sample characterisation and preparation

The volcanic ash sample used in this study corresponds to the 23 November 2013 eruption of Mt. Etna, Sicily (Viccaro et al., 2014). The eruption had a Volcanic Explosivity Index of 2 and the total erupted mass was ~$1.3 \pm 1.1 \times 10^9$ kg (Bonaccorso et al., 2014; Andronico et al., 2015). The sample was collected fresh and given to us by the National Institute of Geophysics and Volcanology, Catania, Sicily. The ash material was sieved to obtain a particle size fraction between 63 and 100 µm. The sieved size-fraction corresponded to 30% of the original sample mass. Its composition is that of a basalt (47.05 wt.% SiO_2). The mineralogy of the sieved Etna ash was quantified by the Rietveld refinement method of X-ray diffraction data (Hill et al., 1993; Gonzalez et al., 2003) (see chapter 3 for a detailed description of the method). The ash crystallinity is ~45.6 wt.% and plagioclases (22.8 wt.%) and pyroxenes (13.9 wt.%) are the dominant minerals. According to Viccaro et al.,

(2014), the plagioclases range in composition between An_{47} and An_{91}. Olivine and oxides also occur but in minor amounts (2.5 wt. % and 4.9 wt.%, respectively). The specific surface area, A_{BET}, of the 63-100 µm fraction was determined by the three-point BET method using Kr gas adsorption (Brunauer et al., 1938). The A_{BET} of the sieved ash ~0.45 m^2 g^{-1}. The chemical composition and mineralogy of the 63-100 µm size fraction of the volcanic ash used is presented in Table 4.1.

Table 4.1. Chemical composition and mineralogy of the 63-100 µm size fraction of the Etna ash sample used in this study (A_{BET}~ 0.45 m^2 g^{-1}).

	SiO_2	Al_2O_3	Fe_2O_3	MgO	CaO	Na_2O	K_2O	TiO_2	MnO
Oxide (wt. %)	47.05	15.84	13.31	6.62	10.11	3.34	1.97	0.20	0.20

	Glass	Plagioclase	Pyroxene	Olivine	Fe-oxides
% wt.	54.4	22.8	13.9	2.5	4.9

4.2.2. Experiment conditions

The dissolution experiment was carried out in triplicate using the fluidized bed reactor described in Chapter 3. A peristaltic pump delivered a constant fluid flow of 0.4 mL min^{-1} to the 65-mL reactor. The temperature was kept at 20 °C. The dissolution experiment was performed using the same ash sample in the pH range 2-11 (acidic zone: pH= 2-5 and alkaline zone: pH=8-11). Six input solutions (pH 2, 3, 5, 7.8, 9.8 and 11, and ionic strength of 0.01 mol L^{-1}) were prepared from reagent grade HCl, NH_4OH and NH_4OH (Table A.4.1). At the beginning of the dissolution experiment, the whole system was cleaned thoroughly by circulating a 0.1 mol L^{-1} hydrochloric acid solution for at least 24 h. Deionised water was then fed continuously to the system for at least 12 h. After this period, the first desired input solution was pumped for 24 h prior to the introduction of ~0.5 g of ash material. Prior to the introduction of the ash material, a sample of the circulating solution from each reactor (blank) was taken for subsequent chemical analysis. After 100 h, the input solution was replaced with the next desired input solution composition and the experiment was carried out for another 100 h. The same operation was repeated for each input solution, totalizing 600 h of dissolution for the six different pH conditions. This experimental protocol is similar to that used by Chou and Wollast (1984). The dissolution experiment started in the acidic zone at pH 5 with a decreasing of pH (3 and 2). We then switched the pH conditions to the alkaline zone, beginning at pH 11 and then pH 10 and 8. The pH variations in the output solution throughout the entire duration of the

dissolution experiment are reported in Table 4.2. The sample solution was collected every 20 minutes in 8 mL PS-clear vials during the three first hours following injection of a new input solution, and then after 5, 7, 15, 21, 24, 48, 72, 96 and 100 h. The samples were acidified at 0.5% with nitric acid Suprapur® 15 molar. The concentrations of Si, Al, Fe, Ca, Mg, Na, K and Mn in the ouptput solution were determined by Inductively Coupled Plasma Atomic Emission Spectroscopy (ICP-AES). The detection limit was 10 µg L^{-1} for Si, Na and K, 4 µg L^{-1} for Mn, 3 µg L^{-1} for Fe, 2 µg L^{-1} for Al, 1.5 µg L^{-1} for Mg and 0.8 µg L^{-1} for Ca. The error on the ICP-AES analytical measurements was estimated about 1.5% (>50 ppb) and 0.5% (50-200 ppb). The concentration of the studied cations in the blank solution (pH 5 without ash sample) was: Si 17±2 µg L^{-1}; Ca 5.7±1 µg L^{-1}; Na 3±2 µg L^{-1}, while the concentration of the other cations (Al, Fe, Mg, Mn, K) were under the detection limit.

4.2.3. Theoretical background

When the conditions of far-from equilibrium and steady-state are met, the dissolution rate of a solid (r, in mol m^{-2} s^{-1}) is given by Declercq et al. (2013) and references therein:

$$r_i = \frac{C_i f}{A m} \times s \qquad [4.1]$$

where C_i (mol L^{-1}) is the aqueous concentration of the ith element in the outlet solution minus the blank concentration at the beginning of the experiment, f (L s^{-1}) the solution flow rate, A (m^2 g^{-1}) the reactive surface area of the dissolving material and m (g) the mass of sample. The term s is a stoichiometric factor, relating the number of moles of the ith element in the rock/glass/ash normalised to one mole of silica, i.e. s = 1 when r is calculated from the output solution Si concentrations. It is rarely possible to determine the actual reactive surface area of a dissolving mineral. Thus, A is approximated based on the BET specific surface area, A_{BET}.

4.3. RESULTS

4.3.1. Cation releases

The evolution of the concentrations of cations in the output solution (µmol L^{-1}) as a function of time are shown in Figure 4.2. The concentration of Si increased with decreasing acidity. However, the concentration increased dramatically up to ~850 µmol L^{-1} within the first hour of dissolution at pH 11,

it then rapidly decreased to lower steadier values of 25 µmol L^{-1}. Silicon release dropped further (3-18 µmol L^{-1}) when the pH of the input solution was switched from pH 11 to pH 10. The concentration of Al was the highest at the onset of the dissolution experiment at pH 5, but it dropped sharply within 7 h to reached values < 0.5 µmol L^{-1} at pH 5. At lower pH values, the concentrations of Al increased to 5-19 µmol L^{-1} (pH 3) and 10-22 µmol L^{-1} (pH 2). Dissolved iron followed more or less the same trend as Al, but its concentration reached the detection limit quickly after the pH 2 input solution was replaced with the pH 11 solution.

The release of Ca at the initial stage of dissolution at pH 5 was high (20 µmol L^{-1}), but it decreased after 1 h to reach values in the range 0.5-1.7 µmol L^{-1}. At lower pH values, the concentrations of Ca increased to 4-12 µmol L^{-1} (pH 3) and 6-15 µmol L^{-1} (pH 2). Ca release dropped further (0.5-3 µmol L^{-1}) when the pH of the input solution was switched to alkaline conditions.

Similar to Ca, the initial high concentration of Mg (10 µmol L^{-1}) dropped to lower values within 3 h of dissolution. The highest release occurred during dissolution at pH 2 (5- 22 µmol L^{-1}) and it somehow mimicked the trend displayed by Fe. Sodium and K behaved more or less similarly. They both exhibited high initial concentrations followed by much lower values in the next few hours. Lower pH values in the acidic zone led to an initial distinct increase in concentration which was followed by a steady decrease. In contrast to Si, the replacement of the acidic input solution by the alkaline one (pH 11) did not affect the Na and K releases significantly. At lower alkaline pH values, the concentrations of the monovalent cations tended to decrease below 10 µmol L^{-1}, although few higher values were recorded for K at pH 10. While the release of Mn corresponded to low values (< 0.5 µmol L^{-1}), the variations in its concentration paralleled those observed for Mg and Fe.

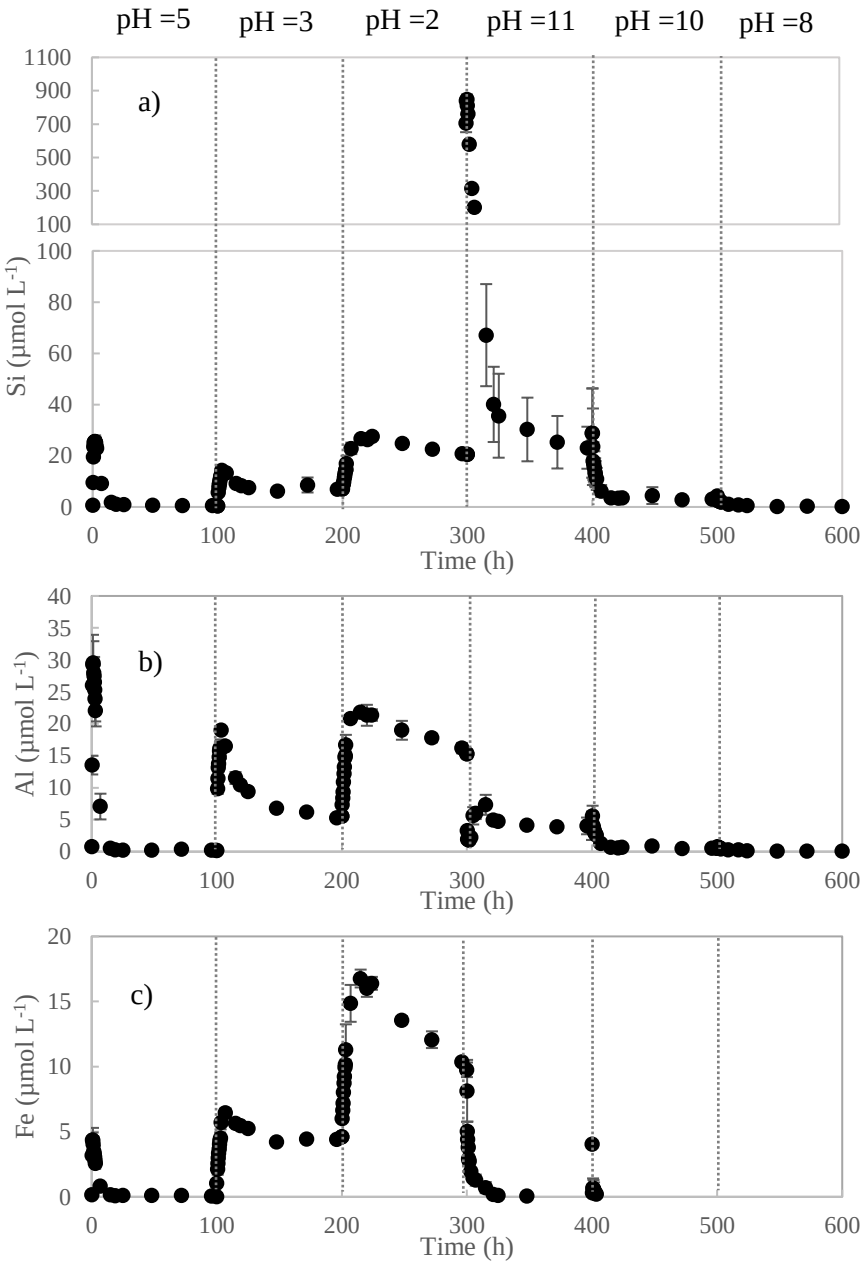

Figure 4.1 (a). Changes in the concentration (µmol L^{-1}) of Si (a), Al (b) and Fe (c) under various pH conditions studied for the dissolution of a basaltic ash.

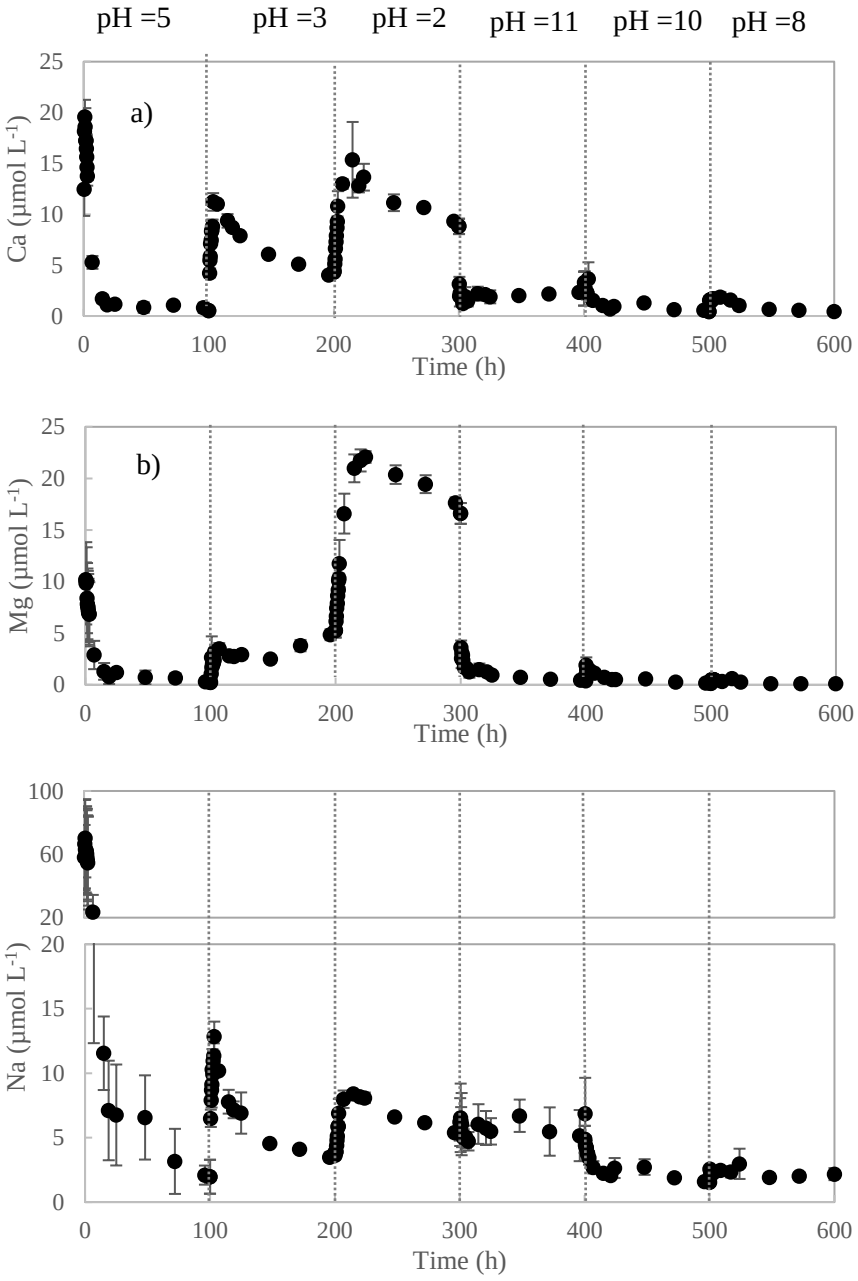

Figure 4.1 (b). Changes in the concentration (µmol L^{-1}) of Ca (a), Mg (b) and Na (c) under various pH conditions studied for the dissolution of a basaltic ash.

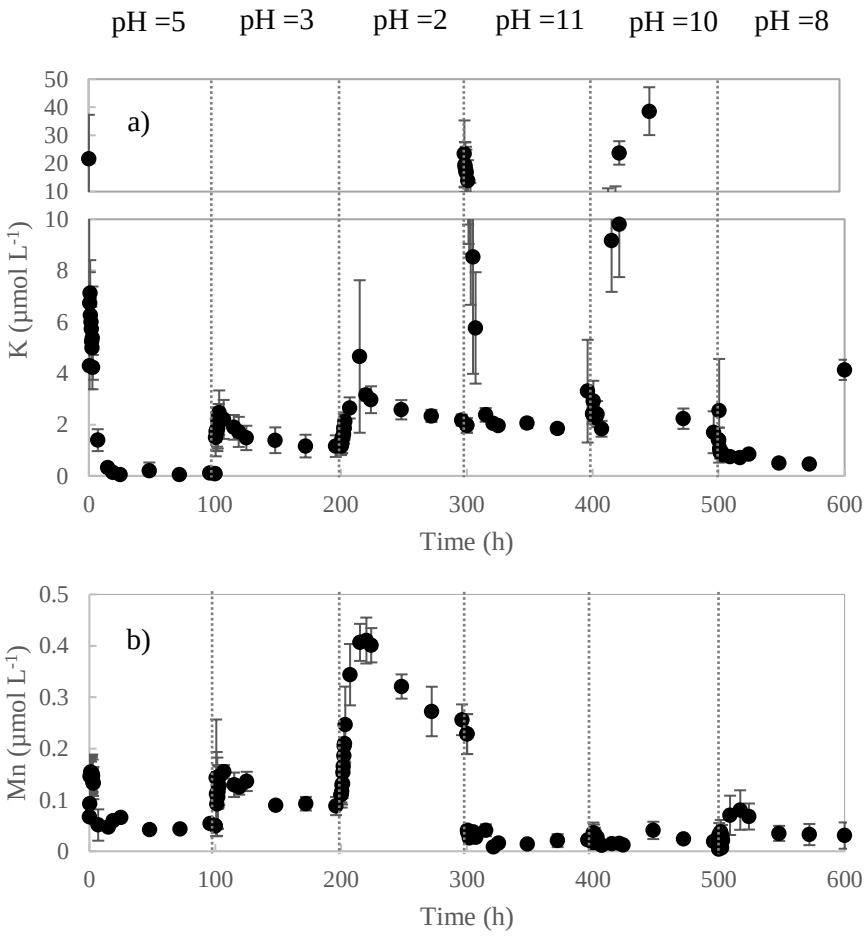

Figure 4.1 (c). Changes in the concentration (µmol L^{-1}) of K (a) and Mn (b) under various pH conditions studied for the dissolution of a basaltic ash.

4.4. DISCUSSION

4.4.1. Dissolution behaviour of cations

Figure 4.1 indicates that dissolution of the ash at the beginning of the experiment is accompanied by a fast but transient release of all cations. This behaviour probably reflects the presence of high-energy sites on the ash surfaces (Holdren and Berner, 1979). For example, partially detached SiO_2 tetrahedra that are bonded to the ash's glass and mineral surfaces, typically corresponding to tips and edges, by only one or two bridging oxygens are prone to dissolve quickly (Oeklers and Gislason, 2001; Gislason and Oelkers, 2003). As dissolution progresses, such high surface energy sites disappear gradually and the rate of Si release decreases towards steadier values. Dissolution of micrometric, high- surface area particles such as glass shards attached to ash grains may also contribute to the high cation releases measured at the beginning of the experiment (Holdren and Berner, 1979).

In parallel, we also note that each replacement of the input solution (corresponding to new pH conditions) almost systematically triggers a high release rate; followed by a decrease in the rate until a new steady state is approached (Fig. 4.1). This cannot be reconciled with preferential dissolution of highly reactive site of an active solid phase. Instead, the observed pattern likely reveals an incongruent dissolution mechanism involving the preferential removal of alkali and alkaline-earth metals from the solid surface due to exchange reactions involving protons in the reactive solution (e.g., Chou and Wollast, 1984; 1985; Wollast and Chou, 1992; Oelkers and Gislason, 2001; Brantley, 2003). These reactions are believed to be responsible for the formation of a residual (or leached) surface layer strongly enriched in Si, Al (and perhaps Fe), the cations that typically act as glass or mineral network formers (Mysen, 1988).

To better illustrate the idea of an incongruent dissolution behavior and the concomitant formation of a residual layer, the ratio *Rx* was defined as the concentration *X* of a given cation *j* (i.e. Al, Fe, Ca and Na) relative to the concentration of Si in the output solutions at steady-state and normalized to the corresponding ratio in the dissolving ash (bulk). If this ratio ($Rx = (Xj/Si)_{solution}/(X_j/Si)_{bulk}$) is greater (smaller) than one, the element is preferentially released from (retained in) the ash relative to Si. These Rx values calculated for ratios for Al, Fe, Ca and Na are displayed as a function of time in Figure 4.2.

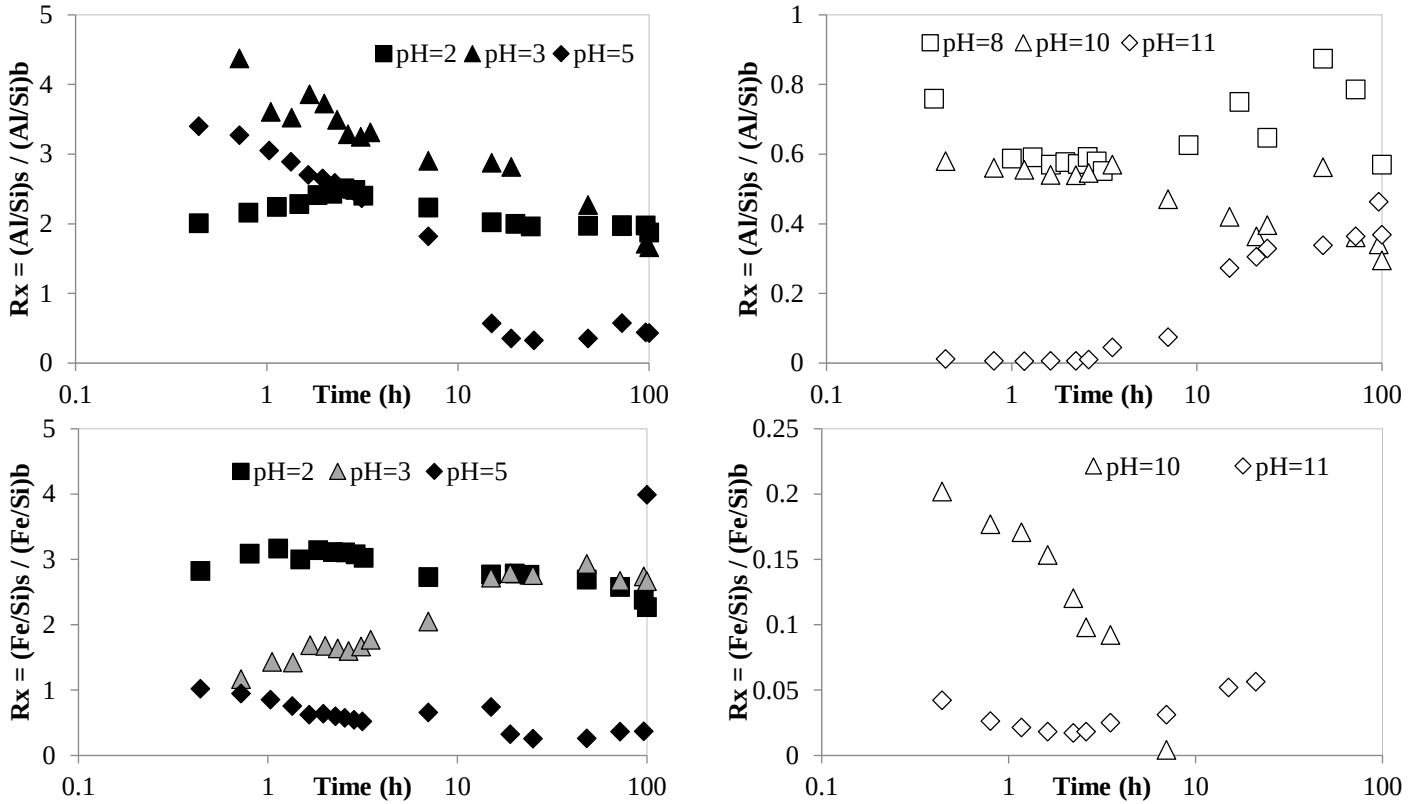

Figure 4.2 (a). Evolution of the ratios (Rx) as calculated for Al and Fe as a function of dissolution time in acid and alkaline conditions

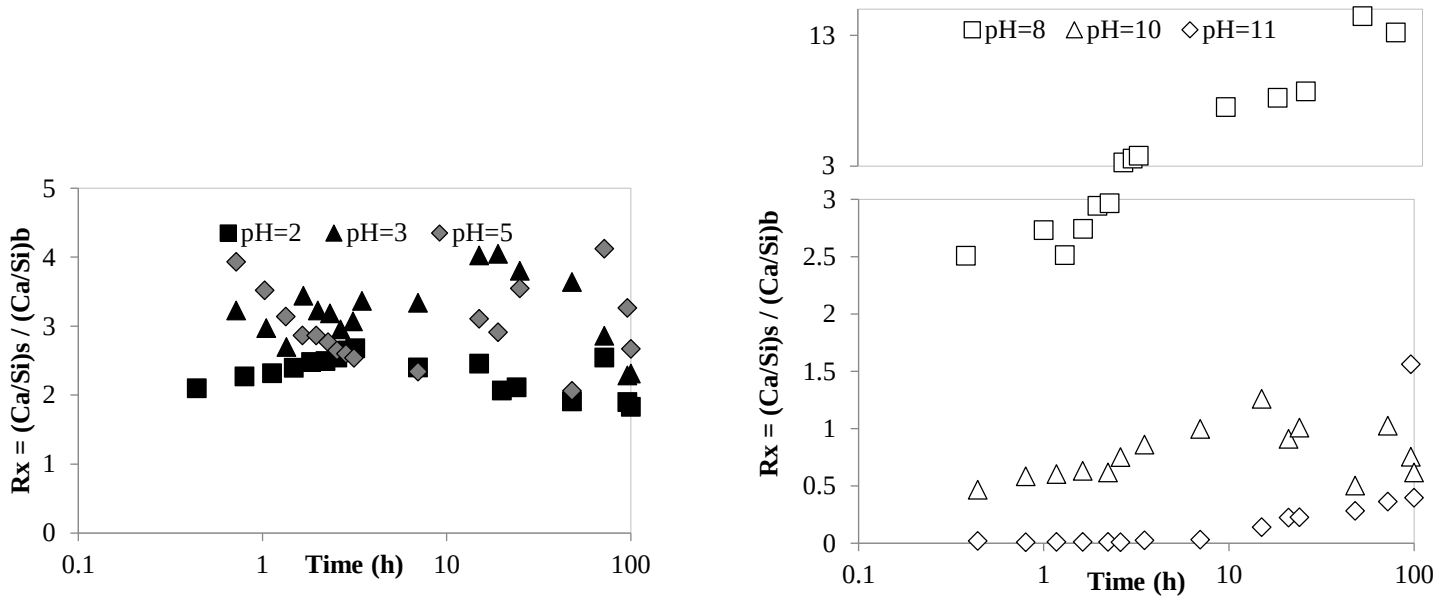

Figure 4.2 (b). Evolution of the ratio (Rx) as calculated for Ca as a function of dissolution time in acid and alkaline conditions.

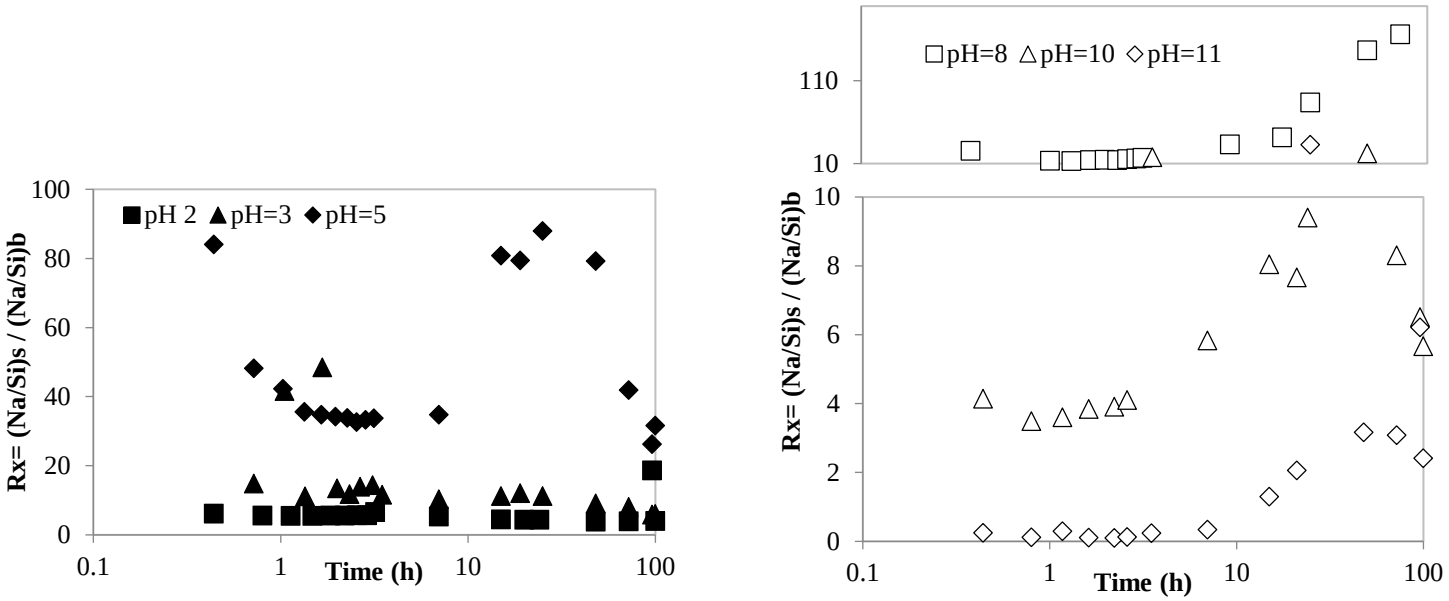

Figure 4.2 (c). Evolution of the ratios (Rx) as calculated for Na as a function of dissolution time in acid and alkaline conditions.

According to Figure 4.2, Al is preferentially released in strong acid conditions (pH 2 and 3), whereas it is retained in the ash material between 10 and 100 h of dissolution after the pH 5 solution was introduced. In alkaline conditions, Al is retained in the ash preferentially over Si. In the same way, in acid conditions Fe is preferentially released in strong acid conditions (pH 2 and 3) bu it is retained at pH 5, departing from the stoichiometric dissolution observed during the first hours (>10 h). In alkaline conditions (pH 10 and 11), Fe tends to be immobile. Calcium is preferentially released in acid conditions (pH 2, 3 and 5) and at pH 8. At pH 10, Ca is released stoichiometrically whereas it is preferentially retained at pH 11. Finally, in the case of Na, this cation is strongly depleted in all the pH conditions either acid or alkaline, with the exception ($Rx<1$) of the release at pH 11 during the first stages of dissolution (>10 h).

These observations corroborate the view that incongruent dissolution takes places on the ash-solution interface and that this mechanism is influenced by the solution pH. Incongruent mechanism of dissolution leads to the formation of a cation (Na, K, Mg, Ca) depleted layer, of which composition evolves according to the pH conditions of the solution in contact with the ash surface, whith a preferential release of cations (Al, Fe, Ca and Na) over Si in acid conditions and the retention of some cations (Al, Fe and Ca) over Si in alkaline conditions. These changes in the chemical composition of the depleted layer are discussed further in section 4.4.4.

4.4.2. Experimental dissolution rates

We applied Eq. [4.1] to calculate a dissolution rate for the basaltic ash at each experimental pH condition, i.e. pH 2, 3, 5, 8, 10 and 11. For each given pH of the input solution, steady-state release of Si and Al was assumed to be reached after 100 h of dissolution. The corresponding pH, Si concentration and calculated dissolution rate values are shown in Table 4.2.

Table 4.2. Si concentrations at steady state (~ 100 h) and logarithm of dissolution rate r_{BET} (mol m^{-2} s^{-1}) at steady state of Etna ash dissolution experiments at 20 °C.

Elapsed time (h)	**pH**	**Si (mol L^{-1}) (x 10^{-6})**	**Log $r_{Si, BET}$ (mol m^{-2} s^{-1})**
100	4.6±0.08	0.50 ± 0.27	-10.83 ± 0.34
200	3.05±0.004	7.12 ± 0.69	-9.68 ± 0.04
300	2.05±0.02	20.56 ± 0.27	-9.21 ± 0.005
400	11.2±0.01	28.85 ± 17.41	-9.07 ± 0.40
500	9.82±0.02	3.45 ± 0.92	-9.99 ± 0.13
600	7.79±0.02	0.18 ± 0.09	-11.27 ± 0.17

The typical dependence of aluminosilicate dissolution on pH can be recognized from Table 4.2. Dissolution decreases with increasing pH in the acid region and increases with increasing pH in the basic region. On this basis, we tested the relationship proposed by Oelkers and Gislason (2001) and which links the dissolution rate to the activities of H^+ and Al^{3+}.

We use the composition of the output solution and the geochemical model PHREEQC (Parkhurst and Appelo, 1999) to calculate a_{Al3+} (see Appendix 4.2.). The results displayed in the plots of Figure 4.3 show that the dissolution of the basalt ash can be represented by two equations that account for the pH effect in the acid (pH 2-5) and alkaline (pH 8-11) zones.

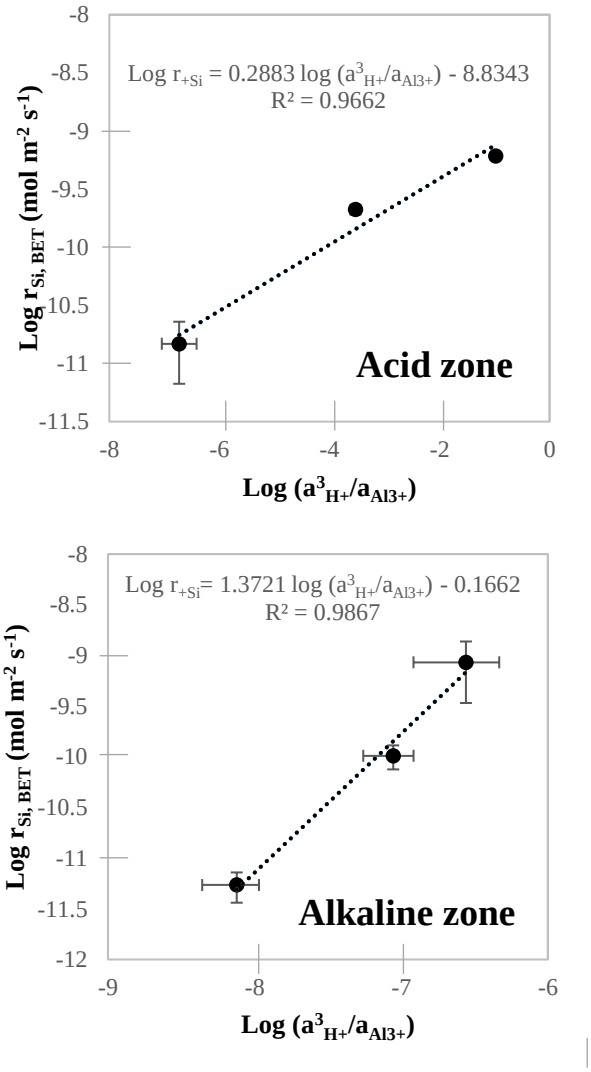

Figure 4.3. Variation of the logarithm of r_{+BET} obtained in the present study at 20 °C with log (a_{H+}^3/a_{Al+3}) in the acidic zone and in the alkaline zone. The solid line represents a least squares fit of the data; the equation and coefficient of determination (R^2) of this line are given in the figure for each zone.

As shown in Figure 4.3 for the acid and alkaline dissolution show a good correlation (R^2= 0.97 for the acid pH 2-3-5 and R^2= 0.99 for the alkaline pH 8-10-11). However, the linear regression relies on three dissolution data points, therefore limiting its robustness. In order to strengthen these two equations, a comparison with other dissolution studies involving aluminosilicates (basaltic glass, plagioclase and pyroxene) is performed.

4.4.3. Comparison of the dissolution rates of the basalt ash with the dissolution rates of its glass and mineral constituents

We noticed that the experimental dissolution rate of the basaltic ash in our study varies with pH in a way similar to what has been shown for the dissolution of basaltic glass (less than 1% of quenched crystals) (Gislason and Oelkers, 2003) and crystalline basalt rock (plagioclase 41 vol. %, pyroxene 34 vol. % and olivine 16 vol. %) (Gudbrandsson et al., 2011). In Figure 4.4, the experimental dissolution rates obtained in this study for basaltic ash at 20 °C are compared with the experimental dissolution rates for basaltic glass at 30 °C (Gislason and Oelkers, 2003) and crystalline basalt at 25 °C (Gudbrandsson et al., 2011).

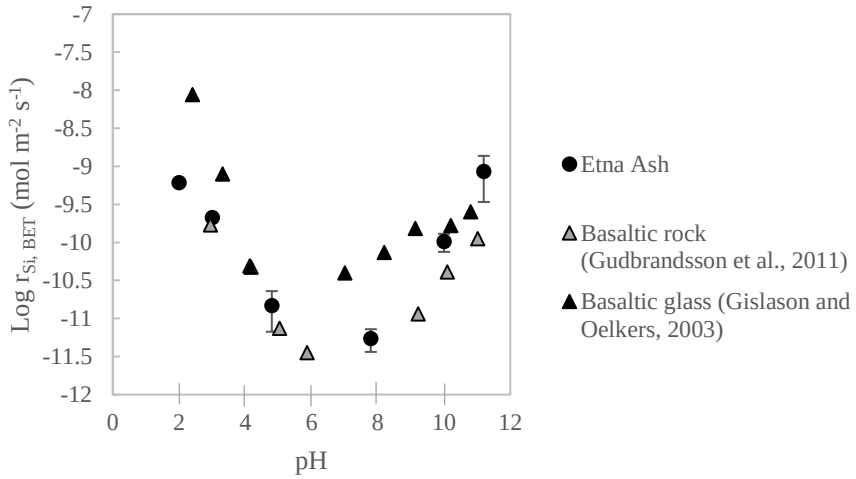

Figure 4.4. Experimental dissolution rates normalized to BET specific surface area in function of pH taken from previous studies for basaltic glass (Gislason and Oelkers, 2003) and for basaltic rock (Gudbrandsson et al., 2011). The experimental dissolution rates obtained in this study for the Etna basaltic ash are also reported.

As observed in Figure 4.4, the experimental dissolution rates obtained in our study for the basaltic ash are comparable to the experimental dissolution values obtained for crystalline and glassy basalt in previous studies. However, we cannot conclude that the ash dissolution could be approached to the dissolution behaviour of the glassy basalt or the crystalline basalt. For instance, the dissolution rate at pH 3 for the ash is closer to that of the crystalline basalt, whereas at pH 10 the dissolution rate of the ash is closer to that of the basaltic glass. For the other pH conditions (2, 5, 8 and 11), a comparison becomes more difficult since dissolution rates for both materials (crystalline vs. glassy) are not directly available from the experimental results at the same pH.

Gudbransson et al. (2011) argued that the measured dissolution rates for a crystalline basalt were equal to those corresponding to the basaltic glass only when the equation of basaltic glass dissolution presented by Gislason and Oelkers (2003) was adapted for the experimental conditions of the crystalline basalt dissolution (aqueous Al concentration of 10^{-5} mol kg^{-1}). Using this same approach, we calculated the dissolution rate values for our studied ash using the dissolution equation reported in the scientific literature for basaltic glass, but incorporating our experimental dissolution conditions (i.e. a_{H+} and a_{Al3+}). However, the volcanic ash contains three major components (basaltic glass, plagioclase and pyroxene), in which the basaltic glass (54.4 wt. %) dominates (Table 4.1). Thus, we also included the dissolution rates for the ash's crystalline components (plagioclase and pyroxene). We estimated the dissolution rates of basaltic glass, plagioclase and pyroxene at different pH values using the relationships of Gislason and Oelkers (2003) (Eq. [4.2]), Gudbransson et al. (2014) (Eq. [4.3] and [4.4]) and Knauss et al. (1993) (Eq. [4.5]), respectively.

The dissolution of basaltic glass is described according to (Gislason and Oelkers, 2003):

$$\log r_{\mathrm{Glass+Si}}\ (\mathrm{mol\ cm^{-2}\ s^{-1}}) = 0.42 \log\left(\frac{a_{H+}^{3}}{a_{Al3+}}\right) - 11.56 \qquad [4.2]$$

Plagioclase dissolution (Gudbransson et al., 2014) depends on pH and the rate laws are:

For pH ≥6

$$\log r_{\mathrm{plagio+Si}}\ (\mathrm{mol\ cm^{-2}\ s^{-1}}) = 0.35 \log\left(\frac{a_{H+}^{3}}{a_{Al3+}}\right) - 11.53 \qquad [4.3]$$

For pH<6

$$\log r_{plagio+Si}\,(\text{mol cm}^{-2}\,\text{s}^{-1}) = (0.004\,\text{An\%} + 0.05)\log\left(\frac{a_{H+}^{3}}{a_{Al3+}}\right) - 0.033\text{An\%} - 14.77 \qquad [4.4]$$

Where An% represents the percentage of anorthite in the plagioclase solid solution

Diopside-pyroxene dissolution (Knauss et al., 1993) is described by:

$$r_{Diopside+Si}\,(\text{mol cm}^{-2}\,\text{s}^{-1}) = -2.88\,x\,10^{-14}\,a_{H+}^{0.18} \qquad [4.5]$$

The calculated rate values are plotted together with the experimental dissolution rates determined at various pH values for the basaltic ash in Figure 4.5.

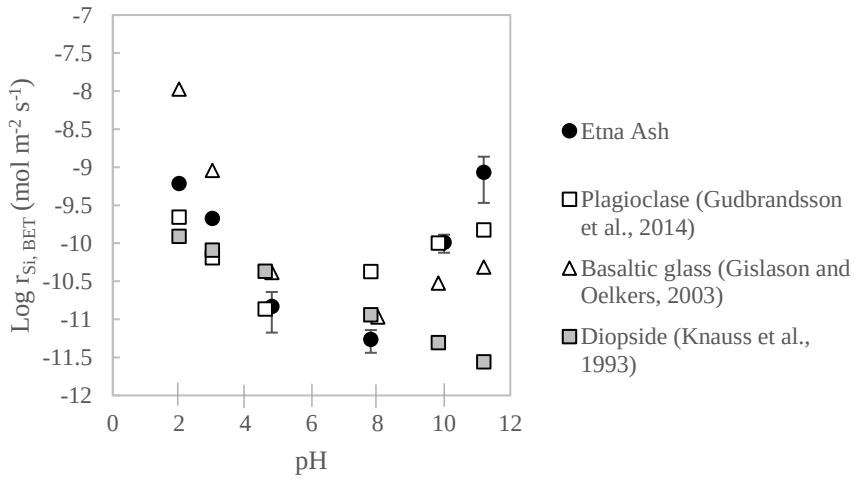

Figure 4.5. Dissolution rates of the main ash components (basaltic glass, plagioclase and pyroxene) as a function of pH. The rates were calculated, by applying the dissolution rates laws reported in previous works (Eq. [4.2]-[4.5]). The experimental dissolution rates obtained for the Etna ash are also shown.

From Figure 4.5, as it was expected, we observe that the dissolution behaviour of the volcanic ash follows the dissolution behaviour of glass and plagioclase; i.e. dissolution rates decreased with increasing pH at acid conditions and they increased with increasing pH at alkaline conditions. However, at lower pH values (2 and 3) the ash dissolution rate is lower than that of basaltic glass but higher than the rates at which plagioclase and diopside dissolve. At pH 5, the dissolution rate is similar to that inferred for plagioclase, which is lower than the dissolution rate of glass and diopside. At pH 8, dissolution of the ash is slower than that of glass and diospside. At pH 10, the dissolution rate of ash approaches that of plagioclase. Finally, at pH 11, the ash dissolves faster than any of its constituents. Therefore, the dissolution behaviour of the ash cannot be explained simply by considering the dissolution rates of its individual constituents, suggesting the occurrence of complex interactions between these.

4.4.4. Thickness of the residual layer

Chou and Wollast (1984) developed a relatively simple calculation to derive the thickness of the residual layer that formed on the surface of dissolving albite due to preferential removal of Na. Here we apply a similar approach to estimate the thickness of a hypothetical cation-depleted layer that would have developed on the ash surface. We assume that (i) the residual layer formed on the ash surface is spatially uniform and (ii) the availability of a cation to be leached from the depleted layer is independent of the other cations. Equation [4.7] was used to perform the calculations.

First, we defined the total amount $M_{i\,t}$ *(µmol)* of the cation *i (Si, Al, Fe, Ca, Mg, Na, K, Mn)* released during the dissolution experiment at certain time t_2 (s):

$$M_{i\,t2} = M_{i\,t1} + \left[C_{i\,t2} + \frac{C_{i\,t1} - C_{i\,t2}}{2}\right] f\,(t_2 - t_1) \qquad [4.6]$$

Where $C_{i\,t}$ stands for the concentration of the cation *i (µmol L^{-1})* at certain time *t (s)* and f (L s^{-1}) the solution flow rate. $M_{i\,t1}$ stands for the total amount of cation *i* release in the previous time interval considered t_1. This calculation would correspond approximately to the area under the concentration curve (Figure 4.1) at t_2 and $C_{i\,t2}$.

Thus, the thickness of the cation *i* dissolved L_i (µm) at certain time *t (s)* could be expressed as:

$$L_{i\,t2} = M_{i\,t2}\,\frac{MW}{\rho} \,/\, (X_i\,A_{BET}\,m) \qquad [4.7]$$

Where *MW* stands for the molecular weight of the ash (647 g mol^{-1}), ρ is the density (3.07 g cm^{-3}), X_i is the abundance of the cation *i* on the depleted layer and it is approximated by the % molar of each cation in the bulk. A_{BET} (m^2 g^{-1}) is the reactive surface area of the dissolving material and m (g) the mass of sample.

In Table 4.3, as a reference, the total amount (µmol) of Si and Al released and the estimated thickness (µm) of these dissolved cations at different time, using Equations [4.6] and [4.7] are presented (see Appendix 4.3 for the rest of studied cations):

Table 4.3. Total amount *M* (µmol) of Si and Al released and the estimated thickness of layer *L* (µm) of these dissolved cations at different time.

Time (h)	**pH**	M_{Si} **(µmol)** X_{Si}=0.17	L_{Si} **(µm)**	M_{Al} **(µmol)** X_{Al}=0.07	L_{Al} **(µm)**
100	5	4.68±0.12	0.024±0.001	4.59±1.88	0.058±0.024
200	3	23.94±1.60	0.121±0.008	29.83±8.18	0.379±0.103
300	2	80.37±3.63	0.405±0.018	74.62±8.83	0.947±0.112
400	11	252.20±31.99	1.27±0.16	85.31±7.72	1.08±0.10
500	10	265.67±40.35	1.34±0.20	88.12±9.21	1.11±0.11
600	8	278.31±49.79	1.40±0.25	90.85±11.59	1.15±0.15

Figure 4.6 displays the evolution of the element specific-thickness of the residual layer throughout the whole duration of the dissolution experiment.

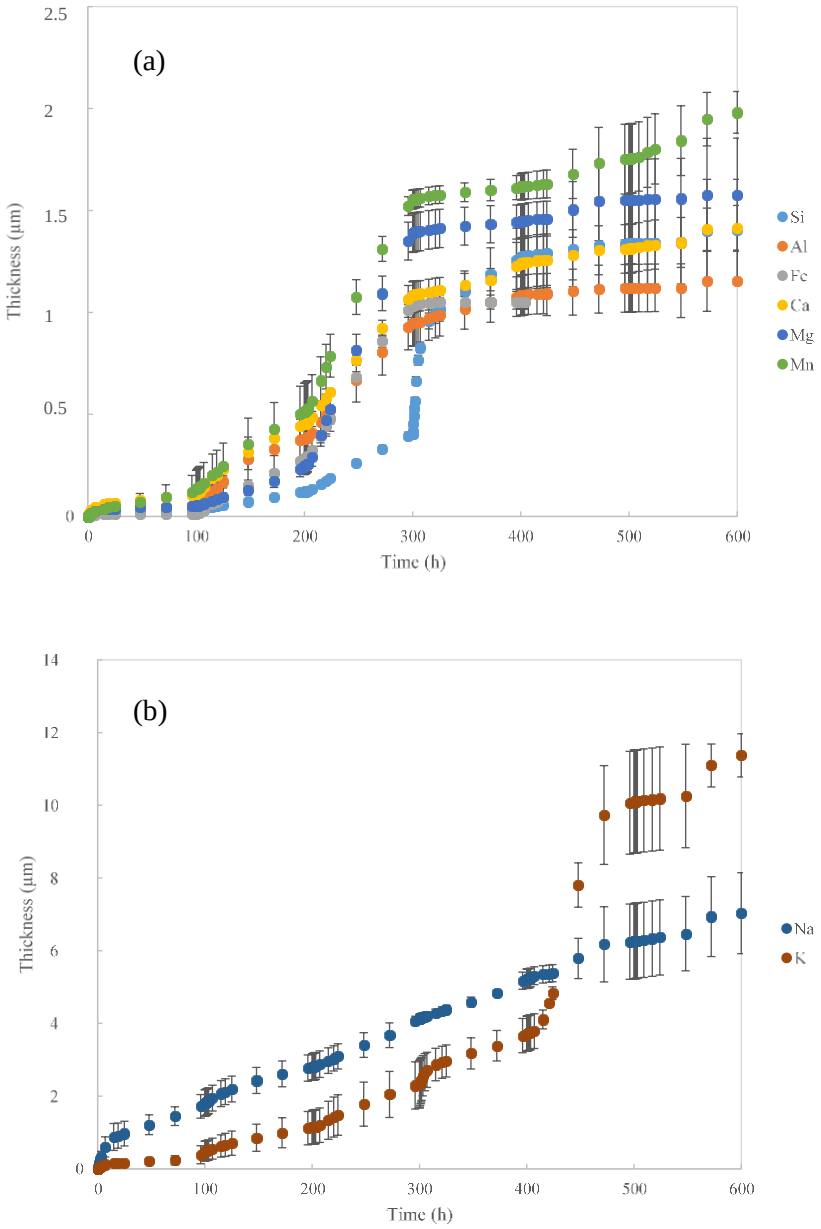

Figure 4.6. Evolution of the calculated thickness of the dissolved layer for the dissolution of Etna ash at 20 °C and pH 2, 3, 5, 8, 10 and 11. For (a) Si, Al, Fe, Ca, Mg and Mn and (b) K and Na.

Sodium and K were the cations most easily removed from the ash surface. At the end of the experiment, the depth of removal is ~7 µm for Na and ~11 µm for K. In comparison, the thickness of the layer depleted with respect to Mg and Mn is comparable (~2 µm). Calcium was removed from a depth of 1.3 µm. Silicon and Al dissolution occurred up to ~1.4 and ~1.1 µm, respectively, in the ash surface. A similar thickness is found for Fe after 400 h of dissolution (Fe concentration was below the detection limit at longer dissolution times).

Clearly, complete removal of all cations occurs only in the top (~1 µm) surface of the ash. For example, at 300 h, if one subtracts the thickness of the dissolved Si layer from the thickness of the dissolved Al layer, one obtains an imaginary thickness where Si has been completely removed but where Al has been retained. The evolution of the composition of the residual layer on the ash surface as a function of pH and at different time points during acid and alkaline dissolution is illustrated in Figure 4.7.

At pH 5, the less soluble cation is Fe followed by Si and Al. Magnesium is less mobile than Ca, whereas Mn, K and particularly Na showed the fastest removal rate. At pH 3, Si exhibited the most sluggish removal, followed by Mg, Fe and Al. The other cations behaved similarly to pH 5. Potassium and Na remain the most reactive cations. At pH 2, the three network formers (assuming that Fe acts as a network former) are difficult to remove from the ash surface, suggesting the existence of a depleted layer of Si on the topmost surface of the ash. Compared with the less acidic conditions (pH 3 and 5), Fe dissolves faster than Si and Al after 100 hours of dissolution at pH 2. At this pH, Mg dissolves faster than Ca. Sodium, and to a lesser extent K and Mn, dissolve even faster.

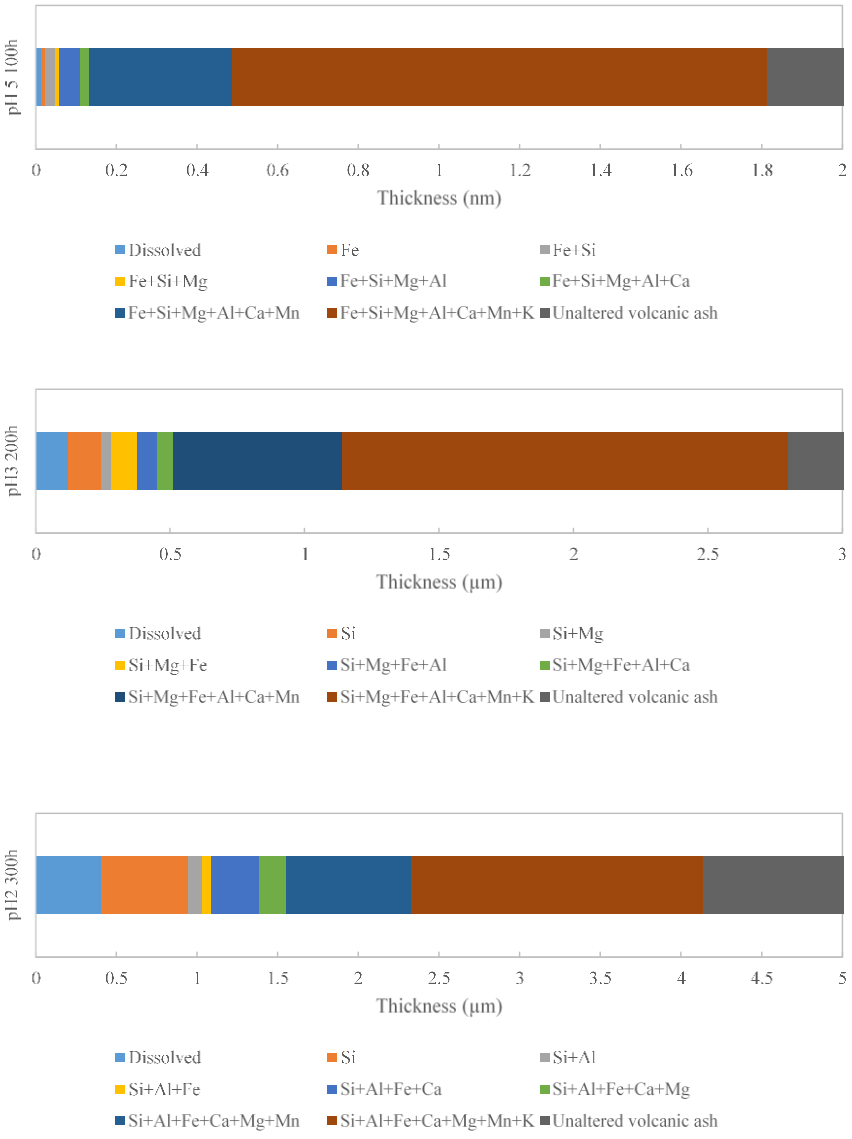

Figure 4.7. Hypothetical representation of the ash surface after 100, 200 and 300 h of dissolution at acidic pH values.

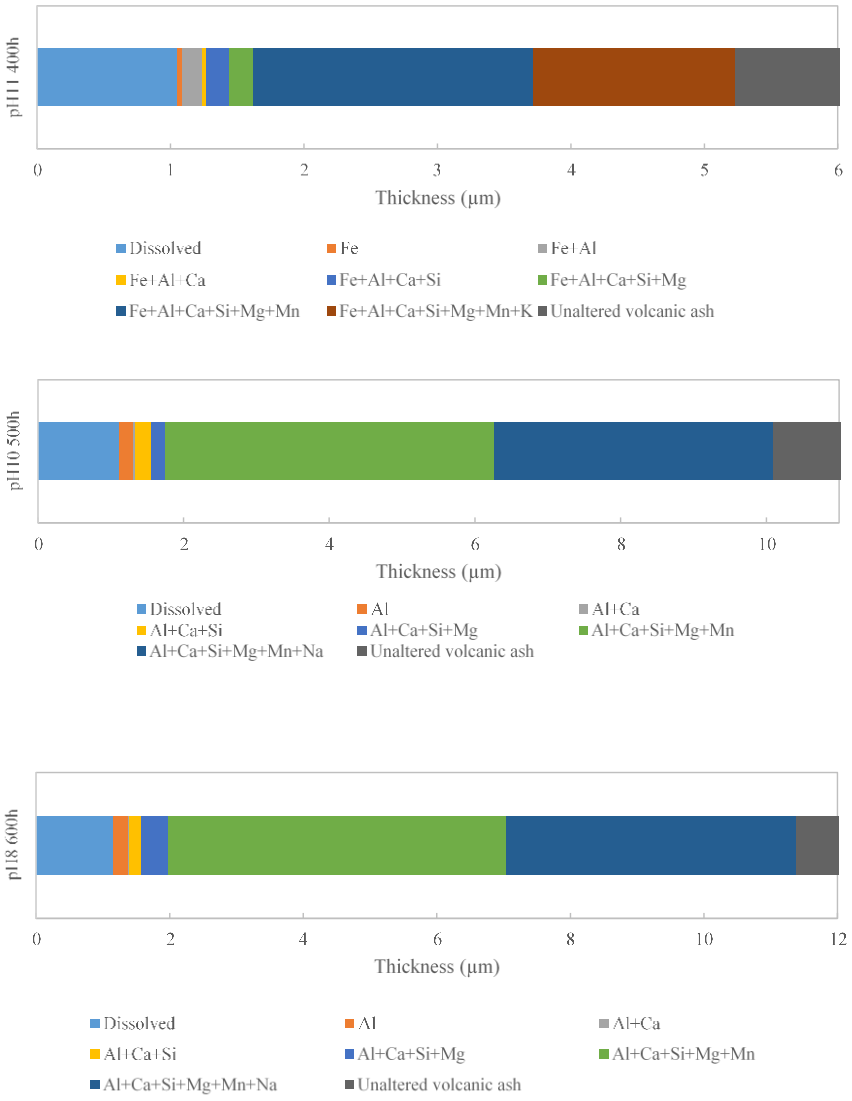

Figure 4.8. Hypothetical representation of the ash surface after 400, 500 and 600 h of dissolution at alkaline pH values.

A different pattern of cation releases from the ash surface is noticed when dissolution takes place in the alkaline zone, as presented in Figure 4.8. The removal of Si is extremely fast at pH 11, whereas Al removal occurs at a lower rate and Fe is barely released. Calcium release tends to be slower than earlier in the acidic dissolution experiment. However, Mg does not follow this tendency. Again, K, Na and Mn are the most mobile cations. Silicon removal decreased sharply at pH 10 and 8, but the behaviour of the other cations parallels that observed at pH 11.

Overall, our results imply that the composition of the residual layer enriched in Si (acid) and Al (alkaline) varies depending on the pH of the reactive solution. It responds rapidly to the changes in pH. As the residual layer builds up, the rate of dissolution decreases until it reaches a quasi-steady state. The dissolution of the superficial part of the residual layer reduces its thickness and releases preferentially the elements enriched in it. The switch to alkaline pH condition after 300 h of dissolution triggers a rapid and high release of Si from the residual layer. In turn, this leads to Al enrichment in the ash surface.

As presented in Figures 4.7 and 4.8, the thickness of the altered layer on the ash surface was estimated to be on the order of a few micrometres. This result is somehow puzzling when compared to the thickness of the altered layer estimated in the study of Chou and Wollast (1984) for albite dissolution. According to Chou and Wollast (1984), after 500 hours of dissolution a layer of 5 Å had dissolved from an albite grain; followed by an altered layer of 15 Å (enriched in Si) and then another altered layer of 13 Å (enriched in Si and Al). In in our experiment the alteration layer on the basaltic ash reached 10 µm after 500 hours (Figure 4.5), i.e. four orders of magnitude greater than the layer thickness inferred by Chou and Wollast (1984) for albite.

The thickness of the alteration layer inferred for the Etna ash agrees better with more recent dissolution experiments involving glass. For example, Valle et al. (2010) found a gel layer of 0.5 µm on the surface of a borosilicate glass (SiO_2 ~47%, Al_2O_3 ~5%, B_2O_3 ~14.5%, CaO ~ 4%, Fe_2O_3 ~ 3%, Na_2O ~ 10.5%) exposed to a pH~8 solution at 90°C during 2 weeks. This increased up to 1.5 µm after 1 month and 13.7 µm after 6 months. In our study, after 100 hours (4.17 days) at pH 8 the "gel-altered layer" devolped a thickness of 1.25 µm (t=501 h: 10.1µm and t=600 h: 11.35 µm), giving a rate of increase of 0.3 µm day^{-1}. This value is only four times higher than that found by Valle et al. (2010) for the borosilicate glass (0.07 µm day^{-1}). The difference could relate to the lower renewal rate of the solution used by these authors, i.e. around 50 times smaller than in our experiment (576 mL day^{-1}). Alternatively, we could invoke a phenomenon of reorganization of the altered layer as it has been described by Girad et al. (2008), which would reduce the thickness of the altered layer due to changes in the internal porosity of the altered layer during dissolution. For the other pH values tested, the development of the

altered layer on the ash surface was on the same order as the previous estimation at pH 8 (pH 5: 0.4 µm day^{-1}; pH 3: 0.2 µm day^{-1}; pH 2: 0.3 µm day^{-1}; pH 11: 0.3 µm day^{-1}; pH 10: 1.17 um day^{-1}).

Nesbitt and Skinner (2001) reacted labradorite with an HCl solution (pH=2, 25 °C). They found a leached layer extending to about 1.5 µm depth after 143 hours of leaching (0.25 µm day^{-1}). This value was used later in a model of glass dissolution proposed by Aradotir et al. (2013). Spadaro et al. (2012) highlighted the presence of an altered layer of 10 µm after exposing a glass sample to volcanic gas emission from Etna during 63 days. Finally, Arab et al. (2008), studying the alteration behavior of borosilicate glasses (pH 8.2, 90 °C), described an alteration layer comprised between 0.8 and 1.4 µm (0.4-0.7 µm day^{-1}) in response to the dissolution of borosilicate glasses at pH 8.2 and 90 °C.

4.4.5. Estimating the diffusivity of cations in the residual layer

Knowing the release of the elements and the thickness of the residual layer formed upon dissolution, it is possible to estimate the diffusion coefficients of the cations (Ca, Mg, Na and K) in the ash at steady state (Chou and Wollast, 1984). The calculation assumes that a constant gradient is established between the solution interface and the fresh ash surface. The concentration of each cation is set at zero at the solution interface, whereas a fixed value corresponding to the molar concentration of each cation in the bulk material is used to represent the fresh ash interface. We used the approach described by Li et al. (2017) to compute the diffusion coefficient, *D(c)* ($cm^2\ s^{-1}$):

$$D(c) = -\frac{1}{2t}\frac{dx}{dc}\int_0^c x\,dc \qquad [4.8]$$

where *c* (mol cm^{-3}) is the concentration of the diffusing cation, *x* (cm) is the distance from the glass surface, and *t(s)* is the time over which diffusion occurs.

The values of *D(c)* at the steady state as calculated for the last four hours of dissolution at each pH condition (i.e. when the steady state was reached) are presented in Table 4.4. The *D(c)* of Ca and Mg are on the order of 10^{-11} and 10^{-12} $cm^2\ s^{-1}$, whereas the *D(c)* of K and Na are ~10^{-10} $cm^2\ s^{-1}$. The diffusivities of Na and K are almost two orders of magnitude larger than those of Ca and Mg. This would confirm that Ca and Mg are more strongly bound in the ash than the alkaline cations. Convincingly, Mehrer et al. (2008) noticed that the diffusivity of Na in soda-lime silicate glass was more than six orders of magnitude faster than the diffusivity of Ca.

Table 4.4. Diffusion coefficients ($cm^2\ s^{-1}$) calculated for the cations (Ca, Mg, Na and K) during the last four hours of dissolution at pH 2, 3, 5, 8, 10 and 11.

Concentration on the surface (mol/cm^3)	**Ca** *0.009*	**Mg** *0.008*	**Na** *0.005*	**K** *0.0027*
pH	**D_{Ca} (cm^2/s) (x 10^{-12})**	**D_{Mg} (cm^2/s) (x 10^{-12})**	**D_{Na} (cm^2/s) (x 10^{-10})**	**D_K (cm^2/s) (x 10^{-10})**
2	-130.3±15.4	-47.1±4	-3.80±0.47	-2.37±0.86
3	-43.3±12.4	-5.52±1.92	-3.01±0.48	-1.44±0.72
5	-4.38±0.93	-	-2.25±0.47	-0.71±0.43
8*	-7.86±5.48	-3.82±0.72	-1.01±0.17	-2.25±0.34
10	-18.9±0.95	-21.3±15.4	-6.31±1.18	-14.77±2.38
11	-19.9±18.6	-34.2±28.9	-4.77±0.62	-3.97±0.78

**Diffusion coefficients calculated between 72 and 100 h, since dissolution values at 96 h were not measured.*

Our calculated *D(Na)* and *D(K)* are much higher than estimates reported previously for Na and K diffusion in feldspars. For example, Chou and Wollast (1984) indicate a *D(Na)* value in albite of 10^{-19} $cm^2\ s^{-1}$, i.e. eight orders of magnitude lower. In contrast, Li et al. (2017) measured *D(Na)* and *D(K)* values in the range of 10^{-10} - 10^{-11} $cm^2\ s^{-1}$ for synthetic aluminosilicate glasses. Verney-Carron et al. (2015) studied the exchange between protons and alkaline cations during the experimental weathering of an ancient stained glass; they found *D* values of ~10^{-14} $cm^2\ s^{-1}$ for an altered thickness of 2 µm. Smets and Loment (1982) investigated the leaching of Na-containing glass at 70 °C and reported *D(Na)* values comprised between 10^{-7} and 10^{-11} $cm^2\ s^{-1}$.

The wide variations in the *D* values found in the scientific literature may arise from different experimental conditions. Our study reveals that the thickness and especially the composition of the residual layer are influenced by pH, which in turn will affect cation diffusion through the residual layer. Nevertheless, the *D(c)* values derived from our dissolution experiments are compatible with the range of values found in other studies.

4.5. CONCLUSIONS

The use of the continuous-flow fluidized bed reactor allowed us to study the kinetics of dissolution of a basaltic ash sample from Etna volcano at pH 2, 3, 5, 8, 10 and 11. We measured the concentration of Si, Al, Fe, Ca, Mg, Mn, Na and K in the output solutions released during dissolution of the ash. It was possible to induce an increase in the dissolution rate of the ash by modifying the pH of the input solution instantaneously. This constitutes a strong evidence for the formation of residual (leached) layer on the ash surface. We estimated this layer to be micrometric in thickness. It develops in response to incongruent dissolution of the ash's constituents. At acidic pH values, the depleted layer is enriched in Si, whereas at alkaline pH values it is probably more enriched in Al.

We calculated the diffusivities of Ca, Mg, Na and K in the leached layers and found values ranging from 4 x 10^{-12} to 130 x 10^{-12} cm^2 s^{-1} (Ca and Mg) and from 0.7 to 15 x 10^{-10} cm^2 s^{-1} (Na and K). This indicates a higher mobility of the alkaline cations compared to the alkaline-earth cations. This finding opens a potential application for the determination of diffusion coefficients during the weathering of aluminosilicates using our fluidized bed system.

Further, computed the experimental dissolution rates of the ash sample at the different pH conditions. The rates vary between 1.5 x 10^{-5} and 61 x 10^{-5} µmol m^{-2} s^{-1}; it decreased with increasing pH at acidic conditions and increased with increasing pH at alkaline conditions. The dissolution behaviour of the ash cannot be explained simply by considering the dissolution rates of its individual constituents, suggesting the occurrence of complex interactions between these.

References

Andronico D., Scollo S. and Cristaldi A. (2015) Unexpected hazards from tephra fallouts at Mt. Etna: The 23 November 2013 lava fountain. J. Volcanol. Getherm. Res., 304. pp: 118-125.

Arab, M., Cailleteau, C, Angeli, F., Devreux, F., Girard, L., Spalla, O. (2008) Aqueous alteration of five-oxide silicate glasses: Experimental approach and Monte Carlo modeling. Journal of Non-Crystalline Solids 354. 155-161.

Aradóttir, E. S. P., Sigfússon, B., Sonnenthal, E. L., Björnsson, G., Jónsson, H. (2013) Dynamics of basaltic glass dissolution-Capturing microscopic effects in continuum scale models. Geochimica et Cosmochimica Acta 121. 311-327.

Baucke F. G. K. (1974) Investigation of surface layers, formed on glass electrode membranes in aqueous solutions, by means of an ion sputtering method. Journal of Non-Crystalline Solids, Volume 14, Issue 1, 1974, pp: 13-31.

Boksay Z., Bouquet G. and Dobos S. (1967) Diffusion processes in surface layers of glass. Phys. Chem. Glass. 8. 140-144.

Bonaccorso A., Calvari S., Linde A., Sacks S. (2014) Eruptive processes leading to the most explosive lava fountain at Etna volcano: The 23 November 2013 episode. Geophys. Res. Lett., 41, 4912-4919.

Brantley S. L. (2003) Reaction Kinetics of Primary Rock-forming Minerals under Ambient Conditions. In: Editors-in-Chief: Heinrich, D.H., Karl, K.T. (Eds.), Treatise on Geochemistry. Pergamon, Oxford, pp: 73-117.

Brantley S. L. and Chen Y. (1995) Chemical weathering rates of pyroxenes and amphiboles. In Chemical Weathering Rates of Silicate Minerals (eds. A. F. White and S. L. Brantley). Mineralogical Society of America, Washington, DC, vol. 31, pp: 119–172.

Brunaue, S., Emmett, P. H. and Teller E. (1938) Adsorption of gases in multimolecular layers. Journal of the American Chemical Society, 60(2), 309-319.

Bunker B.C. (1994) Molecular mechanisms for corrosion of silica and silicate glasses. J. Non-Cryst. Solids 179, 300-308.

Cassey W. H., Westrich R., Arnold G. W., Banfield J. F. (1989) The surface chemistry of dissolving labradorite feldspar. Geochimica et Cosmochimica Acta, Vol. 53, pp: 821-832.

Casey W. H., Westrich, H. R., Arnold, G. W. (1988) The surface chemistry of labradorite feldspar reacted with aqueous solutions at pH = 2, 3, and 12. Geochimica et Cosmochimica. Acta, Vol. 52, pp: 2795-2807.

Chou, L. and Wollast, R. (1985) Steady-state kinetics and dissolution mechanism of albite. American journal of science. Vol. 285. 963-993.
Chou L. and Wollast R. (1984) Study of weathering of albite at room temperature and pressure with a fluidized bed reactor. Geochimica et Cosmochimica Acta Vol 48. 2205-2217.

Crovisier J. L., Advocat T., Dussossoy J. L. (2003) Nature and role of natural alteration gels formed on the surface of ancient volcanic glasses (Natural analogs of waste containment glasses). Journal of Nuclear Materials 321 (2003) 91–109.

Crovisier J. L., Honnorez J., Eberhart J. P. (1987) Dissolution of basaltic glass in seawater: Mechanism and rate. Geochimica et Cosmochimica Acta, Vol. 51 (11), pp: 2977-2990.

Daux V., Crovisier J. L., Hemond C., Petit J. C. (1994) Geochemical evolution of basaltic rocks subjected to weathering: Fate of the major elements, rare earth elements, and thorium. Geochimica et Cosmochimica Acta, Vol. 58 (22), pp: 4941-4954.

Declercq, J., Diedrich. T., Perrot M., Gislason S.R., Oelkers E.H. (2013) Experimental determination of rhyolitic glass dissolution rates at 40–200 °C and 2 < pH < 10.1. Geochimica et Cosmochimica Acta 100 (2013) 251–263.

Dessert C., Dupré B., Gaillardet J., François L.M. and Allègre C.J. (2003) Basalt weathering laws and the impact of basalt weatherin on the global carbon cycle. Chem. Geol. 202; 257-273.

Doremus R. H. (1994) Chemical durability: reaction of water with glass. In Glass Science. Wiley, New York, pp: 215–240.

Doremus R. H. (1975) Interdiffusion of hydrogen and alkali ions in a glass surface. Journal of Non-Crystalline Solids, Vol. 19, pp: 137-144.

Frugier P., Gin S., Minet Y., Chave T., Bonin B., Godon N., Lartigue J-E, Jollivet P., Ayral A., De Windt L., Santarini G. (2008) SON68 nuclear glass

dissolution kinetics: Current state of knowledge and basis of the new GRAAL model. J. Nucl. Mater. 392, 552-567.

Gin S., Jollivet P., Fournier M., Angeli F., Frugier P., Charpentier T. (2015) Origin and consquences of silicate glass passivation by surface layers. Nature Comm. 6:6360.

Gin S., Ribet I. and Coulliard M. (2001) Role and properties of the gel formed during nuclear waste glass alteration: importance of gel formation conditions. J. Nucl. Mater. 298, 1–10.

Girard, L., Arab, M., Spalla, O. (2008) Time resolved alteration process of oxide glasses. Journal of Colloidal and Interface Science 319. 214-225.

Gislason S. and Oelkers E.H. (2003) Mechanism, rates, and consequences of basaltic glass dissolution: II. An experimental study of the dissolution rates of basaltic glass as a function of pH and temperature. Geochimica et Cosmochmica Acta, Vol. 67, No. 20, pp. 3817-3832.

Gonzalez R.M., Edwards T.E., Lorbiecke T.D., Winburn R.S., Webster J.R. (2003) Analysis of geologic material using rietveld quantitative X-Ray diffraction. International Centre for Diffraction Data. Advances in X-ray Analysis. Vol 46. 204-209.

Gout R., Oelkers E. H., Schott J., Wick A. (1997) The surface chemistry and structure of acid-leached albite: New insights on the dissolution mechanism of the alkali feldspars. Geochimica et Cosmochimica Acta, Vol. 61 (14), pp: 3013-3018.

Gudbrandsson S., Wolff-Boenisch D., Gislason S.R. and Oelkers E.H. (2014) Experimental determination of plagioclase dissolution rates as a function of its composition and pH at 22°C. Geochimica et Cosmochimica Acta 139 (2014), 154–172.

Gudbrandsson S, Wolff-Boenisch D., Gislason S.R., Oelkers E.H. (2011) An experimental study of crystalline basalt dissolution from $2 \leq$ pH ≤ 11 and temperatures from 5 to 75°C. Geochimica et Cosmochmica Acta 75 (2011), 5496-5509.

Guy C. and Schott J. (1989) Multisite surface reaction versus transport control during the hydrolysis of a complex oxide. Chem. Geol. 78, London, New York, 181–204.

Hamilton J. P., Brantley S. L., Pantano C. G., Criscenti L. J., and Kubicki J. D. (2001) Dissolution of nepheline, jadeite and albite glasses: toward better

models for aluminosilicate dissolution. Geochimica et. Cosmochimica Acta 65(21), 3683–3702.

Hamilton J. P., Pantano C. G., and Brantley S. L. (2000) Dissolution of albite glass and crystal. Geochimica et Cosmochimica Acta 64, 2603–2615.

Hellmann R., Dran J.-C., and Della Mea G. (1997) The albite water system: Part III. Characterization of leached and hydrogen-enriched layers formed at 300c using MeV ion beam techniques. Geochimica et Cosmochimica Acta Vol. 61, 1575–1594.

Hellmann R. (1995) The albite-water system: Part II. The timeevolution of the stoichiometry of dissolution as a function of pH at 100, 200, and 3008C. Geochimica et Cosmochimica Acta, Vol. 59, 1669–1697.
Hellmann R. (1994) The albite-water system: Part I. The kinetics of dissolution as a function of pH at 100, 200, and 3008C. Geochimica et Cosmochimica Acta, Vol. 58, 595 –611.

Hellmann R., Schott J., Dran J.-C., Petit J.-C., and Della Mea G. (1991) The formation of leached layers on hydrothermally altered albite and albite glass. Terra Abstr. 3(1), 468.

Hellmann R., Eggleston C. M., Hochella M. F., Jr. and Crerar D. A. (1990a) The formation of leached layers on albite surfaces during dissolution under hydrothermal conditions. Geochimica et Cosmochica. Acta, Vol. 54, 1267–1281.

Hellmann R., Schott J., Dran J.-C., Petit J.-C., and Della Mea G. (1990b) A comparison of the dissolution behavior of albite and albite glass under hydrothermal conditions. Geol. Soc. Am.: Ann. Meet. Abstr. A292.

Hellmann R., Eggleston C. M., Hochella M. F., Jr. and Crerar D. A. (1989) Altered layers on dissolving albite: I. Results. Sixth International Symposium on Water–Rock Interaction, WRI-6, 293–296.

Hill R.J., Tsambourakis, G., and Madsen, I.C. (1993). Improved Petrological Modal Analyses from X-ray Powder Diffraction Data by use of the Rietveld Method I. Selected Igneous, Volcanic, and Metamorphic Rocks J. Pet., 34(5), 867-900.

Hochella M. F. J. (1990) Atomic structure, microtopography, composition, and reactivity of mineral surfaces. In Mineral– Water Interface Geochemistry (eds. M. F. Hochella, Jr. and A. F. White). Mineralogical Society of America, Washington, DC, vol. 23, pp: 87–132.

Holdren G.R. Jr and Berner R.A. (1979) Mechanism of feldspar weathering. I. Experimental studies. Geochimica et Cosmochimica. Acta, Vol. 43. 1161-1171.

Jégou C., Gin S. and Larche´ F. (2000) Alteration kinetics of a simplified nuclear glass in an aqueous medium: effects of solution chemistry and of protective gel properties on diminishing the alteration rate. J. Nucl. Mater. 280, 216–229.

Jercinovic M. J., Keil K., Smith M. R., Schmitt R. A. (1990) Alteration of basaltic glasses from north-central British Columbia, Canada. Geochimica et Cosmochimica Acta, Vol. 54 (10), pp: 2679-2696.

Kalinowski B. E. and Schweda P. (1996) Kinetics of muscovite, phiogopite and biotite dissolution and alteration at pH 1–4, room temperature. Geochimica et Cosmochimica Acta, Vol.60, 367–385.

Knauss K., Ngyuen S., Weed C. (1993) Diopside dissolution kinetics as a function of pH, CO_2, temperature and time. Geochimica et Cosmochimica Acta, Vol 57, pp: 285-294.

Lanford W. A., Davis K., Lamarche P., Laursen T (1979) Hydration of soda-lime glass. Journal of Non-Crystalline Solids, Vol. 33 (2), pp: 249-266.

Li X., Jiang, L. Wang, Y., Mohagheghian, I. Dear J.P. Li L., Yan Y. (2017) Correlation between K^+ -Na^+ diffusion coefficient and flexural strength of chemically tempered aluminosilicate glass. Journal of Non-Crystalline Solids 471, 72-81.

Mysen, B.O. (1988) Structure and Properties of Silicate Melts. Elsevier Science & Technology Books, University of California.

Mehrer H., Imre A.W. and Tanguep-Nijokep (2008) Diffusion and ionic conduction in oxide glass. Journal of Physics: Conference Series 106 (2008) 012001.

Muir I. J., Bancroft M., Shotyk W., and Nesbitt H. W. (1990) A SIMS and XPS study of dissolving plagioclase. Geochimica et Cosmochimica Acta, Vol. 54, 2247–2256.

Muir I. J., Bancroft G. M., and Nesbitt H. W. (1989) Characteristics of altered labradorite surface by SIMS and XPS. Geochimica et Cosmochimica Acta, Vol. 53(6), 1235–1241.

Nagy K. L. (1995) Dissolution and precipitation kinetics of sheet silicates. In Chemical Weathering Rates of Silicate Minerals (eds. A. F. White and S. L.

Brantley). Mineralogical Society of America, Washington, DC, vol. 31, pp: 173–225.

Nesbitt, H.W. and Skinner W. M. (2001) Early development of Al, Ca, and Na compositional gradients in laboratory leached in pH 2 HCl solutions. Geochim. Cosmochim. Acta 65. 715-727.

Nesbitt H. W., Macrae N. D., and Shotyk W. (1991) Congruent and incongruent dissolution of labradorite in dilute acidic salt solutions. J. Geol. 99, 429–442.

Nesbitt H. W. and Muir I. J. (1988) SIMS depth profiles of weathered plagioclase and processes affecting dissolved Al and Si in some acidic soil solutions. Nature 334 (6180), 336-338.

Oelkers, E.H. (2001) General kinetic description of multioxide silicate mineral and glass dissolution. Geochim. Cosmochim. Acta 65. 3703-3719.

Oelkers E.H. and Gislason, S.R. (2001) The mechanism rates and consequences of basaltic glass dissolution: I. An experimental study of the dissolution rates of basaltic glass as a function of aqueous Al, Si and oxalic acid concentration at 25°C and pH=3 and 11. Geochimica et Cosmochimica Acta, Vol. 65. 3671-3681.

Oelkers, E. H., Schott, J. and Devidal, J. L. (2001). On the interpretation of closed system mineral dissolution experiments: Comment on "Mechanism of kaolinite dissolution at room temperature and pressure Part II: Kinetic study" by Huertas et al. (1999). Geochimica et Cosmochimica Acta, Vol. 65 (23), 4429-4432.

Parkhurst D. L. and Appelo C. A. J. (1999) User's guide to PHREEQC (version 2) – a computer program for speciation, batch reaction, one-dimensional transport, and inverse geochemical calculations. U.S.G.S. Water Res. Inv. Report. 99-4259.

Rana M. A., Douglas R. W. (1961a) The reaction between glass and water. Part 1. Experimental methods and observations. Phys. Chem. Glasses 2, 179-195.

Rana M. A., Douglas R. W. (1961b) The reaction between glass and water. Part 2. Discussion of the results. Phys. Chem. Glasses 2, 196-204.

Schweda P., Sjöberg L., Södervall U. (1997) Near-surface composition of acid-leached labradorite investigated by SIMS. Geochimica et Cosmochimica Acta, Vol. 61 (10), pp: 1985-1994.

Shotyk W., Nesbitt H. W., and Fyfe W. S. (1990) The behavior of major and trace elements in complete vertical peat profiles from three Sphagnum bogs. Int. J. Coal Geol. 15(3), 163–190.

Smets, B. and Lommen, T. (1982) The leaching of sodium containing glasses: ion exchange or diffusion of molecular water. Journal de Physique Colloques, 43 (C9), pp: C9-649-C9-652.

Spadaro, F., R., Lefèvre, R. A., Ausset, P. (2012) Experimental rapid alteration of basaltic glass: Implications for the origins of atmospheric particulates. Geology 30. 671-674.

Stillings L. L. and Brantley S. L. (1995) Feldspar dissolution at 258C and pH 3: reaction stoichiometry and the effect of cations. Geochimica et Cosmochimica Acta, Vol. 59, 1483–1496.

Stroncik N. A. and Schmincke H. U. (2001) Evolution of palagonite: Crystallization, chemical changes, and element budget. Geochem. Geophys.Geosyst. 2.

Techer, I., Advocat, T., Lancelot, J., Liotard, J. (2000) Basaltic glass: alteration mechanism and analogy with nuclear waste glasses. Journal of Nuclear Materials 282. 40-46.

Tsomaia N., Brantley S. L., Hamilton J. P., Pantano C. G., Mueller K.T. (2003) NMR evidence for formation of octahedral and tetrahedral Al and repolymerization of the Si network during dissolution of aluminosilicate glass and crystal. Am. Mineral. 88, 54-67.

Valle N., Verney-Carron A., Sterpenich J., Libourel G., Deloule E., Jollivet P. (2010) Elemental and isotopic (^{29}Si and ^{18}O) tracing of glass alteration mechanisms. Geochimica et Cosmochimica Acta, Vol. 74 (12), pp. 3412-3431.

Verney-Carron, A., Sessegolo, L., Saheb, M., Valle, N., Ausset, P., Losno, R., Mangin, D., Lombardo, T., Chabas, A., Loisel, C. (2017) Understanding the mechanism of Si-K-Ca glass alteration using silicon isotopes. Geochimica et Cosmochimica Acta, Vol. 203. 404-421.

Verney-Carron, A., Saheb, M., Loisel, C., Duhamel, R. and Remusat, L. (2015) Use of hydrogen isotopes to understand stained glass weathering. Procedia Earth and Planetary Science 13. 64-67.

Viccaro, M., Calcagno, R., Garozzo, I., Giuffrida, M., Nicotra, E. (2014) Continuous magma recharge at Mt. Etna during the 2011-2013 period controls the style of volcanic activity and compositions of erupted lavas. Miner Petrol 109: 67-83.

Wollast R. and Chou L. (1992) Surface reactions during the early stages of weathering of albite. Geochimica et Cosmochimica Acta, Vol. 56, 3113–3121.

Zhou Z. and Fyfe W. S. (1989) Palagonitization of basaltic glass from DSDP Site 335, Leg 37: textures, chemical composition, and mechanism of formation. Am. Min. 74, 1045-1053.

Appendix 4.1. Experimental conditions

Table A.4.1. Composition of inlet solutions used in the experiments performed in the present study.

pH (20°C)	HCl (mol/L)	NH_4Cl (mol/L)	NH_4OH (mol/L)
2	0.01		
3	0.001	0.00900	
5	0.00001	0.00999	
7.79		0.0095	0.0005
9.82		0.004	0.006
11			0.01

Appendix 4.2. The activity of H^+ and Al^{3+} obtained using PHREEQC computer code

Table A.4.2. The activity of H^+ and Al^{3+} obtained using PHREEQC computer code.
(Parkhurst and Appelo, 1999).

Elapsed time (h)	pH	a_{H^+} [1]	a_{Al3+} [1]	Log ($a_{H^+}^3/a_{Al+3}$)
100	4.6±0.08	2.54×10^{-5}	8.84×10^{-8}	-6.73±0.31
200	3.05±0.004	8.98×10^{-4}	2.44×10^{-6}	-3.53±0.03
300	2.05±0.02	8.92×10^{-3}	6.80×10^{-6}	-0.98±0.07
400	11.2±0.01	6.17×10^{-10}	8.50×10^{-28}	-6.56±0.36
500	9.82±0.02	1.50×10^{-10}	3.86×10^{-23}	-7.05±0.20
600	7.79±0.02	1.62×10^{-8}	5.68×10^{-16}	-8.12±0.23

Appendix 4.3. Cation concentration during the dissolution experiment/ ETNA ASH pH 5

Time (h)	Si (µmol L^{-1})	Standard deviation	Al (µmol L^{-1})	Standard deviation	Fe (µmol L^{-1})	Standard deviation	Ca (µmol L^{-1})	Standard deviation
0.2	0.76	0.11	0.78	0.26	0.17	0.02	43.15	10.64
0.44	9.52	1.06	13.54	1.46	3.20	0.16	12.44	2.60
0.72	19.52	1.38	26.01	3.11	4.36	0.57	18.13	1.69
1.03	23.63	2.50	29.25	4.67	4.34	0.95	19.56	1.69
1.34	25.22	1.47	29.51	3.41	4.05	0.58	18.59	1.85
1.65	25.60	2.25	27.98	1.12	3.50	0.28	17.22	0.76
1.96	25.61	2.30	27.47	2.99	3.36	0.60	17.22	1.46
2.27	25.30	1.86	26.49	2.86	3.17	0.56	16.44	1.43
2.54	25.09	2.02	25.32	3.79	3.03	0.88	15.61	2.14
2.84	23.86	2.04	23.91	3.54	2.79	0.62	14.60	1.79
3.14	22.98	0.83	22.04	2.44	2.57	0.20	13.74	0.39
7	9.26	1.45	7.06	2.01	0.83	0.15	5.27	0.63
15	1.83	0.44	0.53	0.175	0.15	0.08	1.68	0.42
19	1.09	0.41	0.27	0.09	0.09	0.07	1.08	0.18
25	0.90	0.54	0.22	0.10	0.11	0.01	1.15	0.17
48	0.67	0.53	0.24	0.13	0.10	0.01	0.84	0.52
72	0.58	0.32	0.34	0.18	0.10	0.07	1.04	0.23
96	0.59	0.11	0.19	0.03	0.06	0.04	0.80	0.50
100	0.50	0.27	0.17	0.03	0.02	0	0.51	0.21

ETNA ASH pH 5

Time (h)	Mg (µmol L^{-1})	Standard deviation)	Na (µmol L^{-1})	Standard deviation	K (µmol L^{-1})	Standard deviation	Mn (µmol L^{-1})	Standard deviation
0.2	120.04	63.76	1347.26	1034.41	21.72	15.61	0.07	0
0.44	10.18	1.68	57.97	20.57	4.28	0.90	0.09	0.04
0.72	9.84	3.99	66.42	27.92	6.73	1.20	0.14	0.03
1.03	10.00	3.33	70.14	24.71	7.11	1.29	0.15	0.03
1.34	8.40	3.40	63.01	27.07	6.26	0.87	0.15	0.02
1.65	7.84	3.43	62.38	27.96	5.99	0.92	0.15	0.04
1.96	7.64	3.40	61.45	26.36	5.73	0.87	0.15	0.03
2.27	7.48	3.27	60.09	28.66	5.23	0.81	0.15	0.04
2.54	7.21	3.07	57.52	27.13	4.99	0.74	0.15	0.03
2.84	6.98	3.09	55.72	28.11	5.38	2.00	0.13	0.03
3.14	6.83	3.11	54.54	29.39	4.23	0.48	0.13	0.03
7	2.89	1.37	23.35	11.02	1.39	0.43	0.05	0.03
15	1.30	0.81	11.54	2.85	0.33	0.11	0.05	0
19	0.80	0.72	7.11	3.86	0.13	0.09	0.06	0
25	1.20	0.34	6.76	3.91	0.05	0	0.06	0
48	0.72	0.67	6.56	3.26	0.20	0.32	0.04	0
72	0.66	0.46	3.16	2.52	0.05	0.04	0.04	0
96	0.31	0.18	2.09	0.74	0.11	0	0.05	0
100	0.24	0.20	1.97	1.32	0.09	0	0.05	0

ETNA ASH pH 3

Time (h)	Si (µmol L^{-1})	Standard deviation	Al (µmol L^{-1})	Standard deviation	Fe (µmol L^{-1})	Standard deviation	Ca (µmol L^{-1})	Standard deviation
100.1	0.50	0.27	0.17	0.03	1.04	1.45	0.51	0.21
100.72	5.75	0.52	9.83	0.80	2.12	0.42	4.21	0.43
101.05	7.52	0.20	11.42	0.34	2.57	0.28	5.451	0.78
101.35	8.67	0.19	13.13	0.65	2.99	0.29	5.831	0.36
101.67	9.27	0.72	13.72	0.60	3.35	0.43	7.09	1.08
102	10.35	0.75	14.80	0.89	3.69	0.54	7.43	0.13
102.33	11.38	0.49	15.72	0.47	4.05	0.47	8.32	1.14
102.66	12.14	0.25	16.12	1.14	4.33	0.61	8.41	0.43
103.1	12.51	0.50	16.04	1.51	4.51	0.67	8.79	0.68
103.48	14.34	0.43	19.02	0.18	5.71	0.27	11.21	0.87
107	13.29	0.44	16.47	0.40	6.45	0.35	10.99	0.35
115	9.18	0.34	11.52	0.93	5.64	0.24	9.35	0.67
119	8.38	0.37	10.42	0.57	5.48	0.09	8.69	0.15
125	7.58	0.78	9.40	0.67	5.26	0.27	7.88	0.12
148	6.20	0.47	6.77	0.50	4.23	0.18	6.06	0.28
172	8.59	2.93	6.18	0.29	4.43	0.24	5.08	0.38
196	6.92	0.60	5.29	0.18	4.42	0.14	4.01	0.33
200	7.12	0.69	5.52	0.37	4.61	0.22	4.28	0.13

ETNA ASH pH 3

Time (h)	Mg (µmol L^{-1})	Standard deviation	Na (µmol L^{-1})	Standard deviation	K (µmol L^{-1})	Standard deviation	Mn (µmol L^{-1})	Standard deviation
100.1	0.24	0.23	1.97	1.31	0.09	0	0.05	0
100.72	1.09	0.19	6.50	0.67	1.49	0.73	0.14	0.11
101.05	2.64	2.05	7.89	0.15	1.75	0.41	0.11	0.08
101.35	1.68	0.10	8.69	1.35	1.67	0.69	0.09	0.06
101.67	2.03	0.43	9.11	0.79	1.76	0.62	0.11	0.07
102	1.98	0.23	10.29	1.57	1.80	0.84	0.10	0.06
102.33	2.10	0.10	9.90	0.75	1.87	0.80	0.12	0.03
102.66	2.27	0.14	10.97	0.80	2.10	0.37	0.13	0.04
103.1	2.44	0.19	11.36	0.95	2.313	0.49	0.13	0.04
103.48	3.20	0.22	12.85	1.15	2.46	0.86	0.15	0.02
107	3.50	0.54	10.20	0.23	2.20	0.76	0.15	0.01
115	2.80	0.29	7.79	0.92	1.89	0.48	0.13	0.02
119	2.74	0.29	7.16	0.65	1.71	0.58	0.12	0.01
125	2.92	0.37	6.91	1.60	1.48	0.47	0.14	0.02
148	2.49	0.31	4.55	0.07	1.39	0.50	0.09	0.004
172	3.80	0.55	4.10	0.19	1.16	0.44	0.09	0.01
196	4.85	0.53	3.49	0.37	1.16	0.42	0.09	0.02
200	5.26	0.67	3.81	0.51	1.20	0.39	0.11	0.02

ETNA ASH pH 2

Time (h)	Si (µmol L^{-1})	Standard deviation	Al (µmol L^{-1})	Standard deviation	Fe (µmol L^{-1})	Standard deviation	Ca (µmol L^{-1})	Standard deviation
200.1	7.12	0.69	5.52	0.36	4.61	0.22	4.28	0.13
200.44	8.68	0.95	7.32	0.19	6.02	0.18	4.44	0.19
200.8	9.25	0.73	8.36	0.27	6.64	0.18	5.10	0.23
201.13	9.98	0.63	9.34	0.20	7.19	0.34	5.60	0.25
201.48	11.49	1.26	10.86	0.49	8.02	0.22	6.62	0.31
201.84	12.24	0.24	12.20	0.46	8.73	0.27	7.28	0.08
202.2	13.21	0.35	13.24	0.43	9.23	0.30	7.88	0.08
202.55	14.29	0.63	14.74	0.65	9.94	0.44	8.68	0.23
202.9	14.70	0.42	15.01	0.75	10.17	0.36	9.27	0.52
203.2	16.97	3.04	16.67	1.60	11.31	1.94	10.78	1.50
207	22.89	2.24	20.80	0.44	14.86	1.42	12.98	0.49
215	26.65	1.21	21.79	0.51	16.76	0.68	15.35	3.72
220	26.39	1.46	21.33	1.64	16.01	0.65	12.80	0.65
224	27.52	1.02	21.37	0.90	16.40	0.50	13.64	1.32
248	24.84	1.30	18.99	1.47	13.57	0.31	11.13	0.82
272	22.60	0.83	17.78	0.68	12.07	0.64	10.66	0.06
296	20.77	0.70	16.20	0.81	10.37	0.31	9.30	0.30
300	20.56	0.27	15.30	0.69	9.76	0.56	8.81	0.75

ETNA ASH pH 2

Time (h)	Mg (µmol L^{-1})	Standard deviation	Na (µmol L^{-1})	Standard deviation	K (µmol L^{-1})	Standard deviation	Mn (µmol L^{-1})	Standard deviation
200.1	5.25	0.68	3.81	0.51	0.09	0	0.11	0.02
200.44	6.16	0.57	3.63	0.23	1.49	0.73	0.12	0.03
200.8	6.65	0.53	3.91	0.38	1.75	0.41	0.13	0.04
201.13	7.41	0.99	3.91	0.10	1.67	0.69	0.13	0.03
201.48	7.88	0.43	4.40	0.20	1.76	0.62	0.15	0.03
201.84	8.64	0.49	4.81	0.26	1.80	0.84	0.16	0.03
202.2	9.19	0.52	5.13	0.30	1.87	0.80	0.19	0.02
202.55	10.09	0.71	5.84	0.08	2.10	0.37	0.20	0.05
202.9	10.32	0.40	5.89	0.34	2.31	0.49	0.21	0.03
203.2	11.76	2.28	6.89	1.11	2.46	0.86	0.25	0.07
207	16.59	1.93	7.98	0.67	2.20	0.76	0.34	0.06
215	20.98	1.35	8.40	0.02	1.89	0.48	0.41	0.04
220	21.74	1.07	8.19	0.12	1.71	0.58	0.41	0.04
224	22.08	0.57	8.09	0.41	1.48	0.47	0.40	0.03
248	20.37	0.90	6.61	0.07	1.39	0.50	0.32	0.02
272	19.44	0.86	6.16	0.09	1.16	0.44	0.27	0.05
296	17.63	0.52	5.41	0.21	1.16	0.42	0.26	0.03
300	16.61	1.01	5.35	0.56	1.20	0.39	0.23	0.04

ETNA ASH pH 11

Time (h)	Si (µmol L^{-1})	Standard deviation	Al (µmol L^{-1})	Standard deviation	Fe (µmol L^{-1})	Standard deviation	Ca (µmol L^{-1})	Standard deviation
300.1	20.56	0.27	15.30	0.69	8.13	2.38	8.81	0.758
300.36	705.15	53.27	3.26	0.46	5.03	0.75	3.13	0.72
300.73	839.43	23.85	1.93	0.28	4.40	0.16	1.93	0.99
301.12	846.99	30.98	1.92	0.23	3.80	0.26	2.24	0.44
301.5	811.55	28.21	1.87	0.24	2.90	0.36	2.20	0.43
301.88	760.14	25.66	1.74	0.34	2.73	0.33	1.81	0.41
303.1	579.32	18.60	2.23	0.17	1.95	0.18	1.22	0.33
305	313.26	7.63	5.61	1.36	1.45	0.21	1.89	0.95
307	201.35	10.05	5.98	0.87	1.28	0.42	1.46	0.51
315	67.10	19.93	7.32	1.56	0.71	0.43	2.19	0.69
321	40.06	14.68	4.91	0.44	0.19	0.11	2.09	0.25
325	35.63	16.39	4.71	0.45	0.12	0.01	1.88	0.64
348	30.27	12.43	4.12	0.41	0.07	0	2.00	0.27
372	25.29	10.255	3.86	0.42	-	-	2.16	0.26
396	23.14	8.21	4.03	1.31	-	-	2.30	0.25
400	28.85	17.41	4.04	2.21	-	-	2.69	1.66

ETNA ASH pH 11

Time (h)	Mg (µmol L^{-1})	Standard deviation	Na (µmol L^{-1})	Standard deviation	K (µmol L^{-1})	Standard deviation	Mn (µmol L^{-1})	Standard deviation
300.1	16.61	1.00	5.35	0.56	1.20	0.39	0.23	0.04
300.36	3.61	0.68	6.21	1.86	1.16	0.30	0.04	0.01
300.73	2.55	0.94	6.54	2.66	1.26	0.37	0.04	0.01
301.12	3.07	0.37	6.30	1.07	1.42	0.53	0.04	0.01
301.5	2.88	0.40	6.05	2.41	1.48	0.34	0.04	0.01
301.88	2.37	0.28	5.30	1.03	1.54	0.36	0.03	0.01
303.1	1.69	0.42	5.01	0.64	1.63	0.40	0.03	0.01
305	1.59	0.34	5.05	0.88	1.84	0.57	0.04	0.005
307	1.27	0.58	4.72	0.72	1.87	0.45	0.03	0.004
315	1.49	0.57	6.05	1.54	2.12	0.35	0.04	0.01
321	1.25	0.25	5.75	1.32	2.65	0.41	0.01	0.005
325	0.94	0.11	5.49	1.02	4.65	2.97	0.02	0.01
348	0.74	0.16	6.70	1.25	3.16	0.22	0.01	0.006
372	0.55	0.09	5.47	1.87	2.97	0.52	0.02	0.01
396	0.46	0.11	5.16	1.98	2.58	0.38	0.02	0.01
400	0.39	0.26	4.87	1.05	2.33	0.24	0.02	0.001

ETNA ASH pH 10

Time (h)	Si (µmol L^{-1})	Standard deviation	Al (µmol L^{-1})	Standard deviation	Fe (µmol L^{-1})	Standard deviation	Ca (µmol L^{-1})	Standard deviation
400.1	28.88	17.46	4.04	2.21	4.04	0	2.68	1.66
400.44	23.52	14.94	5.55	1.63	0.31	0.15	3.29	1.12
400.8	17.95	7.40	4.11	0.72	0.69	0.63	2.51	0.49
401.17	16.79	6.92	3.81	0.68	0.62	0.58	2.46	0.51
401.62	15.28	6.45	3.39	0.55	0.49	0.41	2.33	0.52
402.22	13.59	5.47	3.02	0.41	0.36	0.31	2.25	0.62
402.6	12.81	5.14	2.89	0.42	0.27	0.24	2.23	0.39
403.5	10.95	4.31	2.59	0.48	0.21	0.14	3.65	1.63
407	6.22	2.36	1.25	0.16	-	-	1.52	0.08
415	3.55	0.92	0.68	0.10	-	-	1.01	0.15
421	3.42	0.95	0.57	0.05	-	-	0.68	0.20
424	3.57	1.25	0.64	0.08	-	-	0.91	0.08
448	4.45	3.28	0.85	0.49	-	-	1.28	0.05
472	2.81	0.96	0.48	0.05	-	-	0.60	0.17
496	3.05	1.10	0.53	0.08	-	-	0.56	0.06
500	3.45	0.92	0.50	0.08	-	-	0.41	0.14

ETNA ASH pH 10

Time (h)	Mg (µmol L^{-1})	Standard deviation	Na (µmol L^{-1})	Standard deviation	K (µmol L^{-1})	Standard deviation	Mn (µmol L^{-1})	Standard deviation
400.1	0.92	0.95	4.87	1.04	2.42	0.38	0.02	0.001
400.44	1.90	0.76	6.87	2.77	2.92	0.78	0.04	0.02
400.8	1.50	0.27	4.44	0.70	2.48	0.27	0.04	0.02
401.17	1.49	0.25	4.28	0.73	2.43	0.27	0.02	0.01
401.62	1.50	0.23	4.18	0.58	2.36	0.26	0.03	0.02
402.22	1.42	0.17	3.79	0.53	2.29	0.29	0.02	0.018
402.6	1.40	0.13	3.76	0.42	2.28	0.24	0.02	0.01
403.5	1.38	0.13	3.42	0.53	2.41	0.51	0.03	0.005
407	1.12	0.15	2.70	0.48	1.84	0.31	0.01	0.008
415	0.72	0.17	2.25	0.30	9.16	1.99	0.01	0.007
421	0.52	0.13	2.07	0.28	9.80	2.06	0.01	0.002
424	0.52	0.13	2.64	0.77	23.75	4.18	0.01	0.003
448	0.56	0.03	2.72	0.61	38.62	8.52	0.04	0.02
472	0.26	0.05	1.90	0.02	2.23	0.40	0.02	0.003
496	0.18	0.06	1.59	0.04	1.70	0.82	0.02	0.009
500	0.15	0.06	1.54	0.06	1.40	0.48	0.01	0.009

ETNA ASH pH 8

Time (h)	Si (µmol L^{-1})	Standard deviation	Al (µmol L^{-1})	Standard deviation	Ca (µmol L^{-1})	Standard deviation
500.1	4.36	0.86	0.50	0.08	0.41	0.14
500.38	2.62	0.55	0.79	0.29	1.51	0.45
501	2.53	0.93	0.59	0.06	1.59	0.17
501.3	2.45	0.87	0.58	0.07	1.42	0.19
501.63	2.31	0.86	0.52	0.07	1.46	0.23
501.95	2.31	0.76	0.53	0.06	1.57	0.17
502.27	2.28	0.80	0.52	0.06	1.55	0.25
502.57	2.11	0.71	0.50	0.07	1.60	0.23
502.88	2.05	0.74	0.47	0.07	1.69	0.241
503.1	1.92	0.71	0.42	0.06	1.69	0.29
509	1.07	0.05	0.27	0.07	1.85	0.51
517	0.82	0.26	0.24	0.18	1.55	0.33
524	0.51	0.25	0.13	0.02	1.03	0.46
548	0.19	0.04	0.07	0.02	0.63	0.30
572	0.29	0.06	0.06	0.01	0.54	0.24
600	0.18	0.09	0.04	0.005	0.41	0.30

ETNA ASH pH 8

Time (h)	Mg (µmol L^{-1})	Standard deviation	Na (µmol L^{-1})	Standard deviation	K (µmol L^{-1})	Standard deviation	Mn (µmol L^{-1})	Standard deviation
500.1	0.15	0.06	1.54	0.07	1.40	0.48	0.004	0.003
500.38	0.49	0.22	2.56	0.02	2.54	2.02	0.03	0.02
501	0.48	0.18	2.40	0.40	1.05	0.22	0.03	0.007
501.3	0.47	0.19	2.26	0.31	0.91	0.24	0.02	0.004
501.63	0.47	0.18	2.27	0.29	0.92	0.20	0.04	0.02
501.95	0.48	0.20	2.35	0.42	0.89	0.20	0.02	0.006
502.27	0.50	0.21	2.27	0.32	0.89	0.19	0.01	0.002
502.57	0.48	0.20	2.27	0.30	0.85	0.15	0.03	0.02
502.88	0.48	0.20	2.28	0.35	0.88	0.13	0.02	0.01
503.1	0.46	0.18	2.27	0.30	0.82	0.12	0.02	0.01
509	0.34	0.22	2.46	0.24	0.74	0.03	0.07	0.04
517	0.59	0.25	2.34	0.43	0.71	0.02	0.08	0.04
524	0.27	0.18	2.97	1.17	0.84	0.09	0.07	0.02
548	0.12	0.04	1.92	0.30	0.50	0.01	0.03	0.01
572	0.11	0.03	2.01	0.27	0.46	0.04	0.03	0.02
600	0.11	0.06	2.17	0.46	4.13	0.39	0.03	0.02

Appendix 4.4. Total release of elements during the dissolution experiment

Table A.4.3. Total amount *M* (µmol) of Fe, Ca, Mg, Mn, Na and K released and the estimated thickness of the layer *L* (µm) of these dissolved cations at different time.

Time (h)	pH	M_{Fe} (µmol) X_{Fe}=0.04	L_{Fe} (µm)	M_{Ca} (µmol) X_{Ca}=0.04	L_{Ca} (µm)
100	5	0.59±0.14	0.014±0.003	5.08±0.07	0.111±0.002
200	3	11.90±0.55	0.282±0.013	20.62±0.29	0.451±0.006
300	2	43.71±1.56	1.03±0.04	49.59±2.98	1.08±0.07
400	11	44.39±1.45	1.05±0.03	56.64±5.73	1.24±0.12
500	10	-	-	59.99±5.43	1.31±0.12
600	8	-	-	64.66±4.99	1.42±0.11

Time (h)	pH	M_{Mg} (µmol) X_{Mg}=0.04	L_{Mg} (µm)	M_{Mn} (µmol) X_{Mn}=0.0006	L_{Mn} (µm)
100	5	2.18±0.66	0.05±0.02	0.10±0.07	0.13±0.09
200	3	10.16±1.62	0.24±0.04	0.37±0.10	0.51±0.14
300	2	57.83±3.94	1.39±0.09	1.12±0.03	1.553±0.004
400	11	60.20±3.46	1.44±0.08	1.17±0.04	1.62±0.01
500	10	64.58±8.13	1.55±0.19	1.27±0.12	1.75±0.17
600	8	65.66±11.57	1.58±0.28	1.43±0.07	1.98±0.10

Time (h)	pH	M_{Na} (µmol) X_{Na}=0.01	L_{Na} (µm)	M_K (µmol) X_K=0.005	L_K (µm)
100	5	24.77±4.98	1.81±0.36	2.59±1.43	0.49±0.27
200	3	38.21±4.97	2.80±0.36	6.04±2.46	1.14±0.46
300	2	56.46±1.57	4.13±0.11	12.35±3.45	2.33±0.65
400	11	71.39±3.63	5.22±0.27	19.70±2.56	3.72±0.48
500	10	85.51±14.14	6.26±1.03	53.52±7.52	10.01±1.42
600	8	96.07±15.24	7.03±1.11	60.29±3.15	11.37±0.59

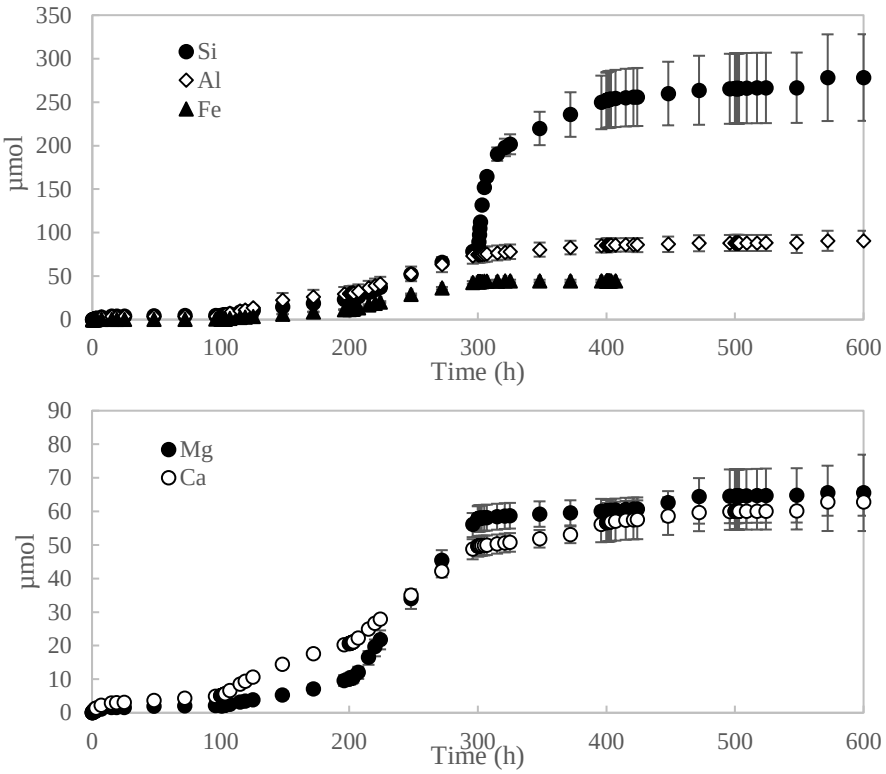

Figure A.4.1. Total amounts of (a) Si, Al and Fe (b) Mg and Ca released during dissolution of Etna ash.

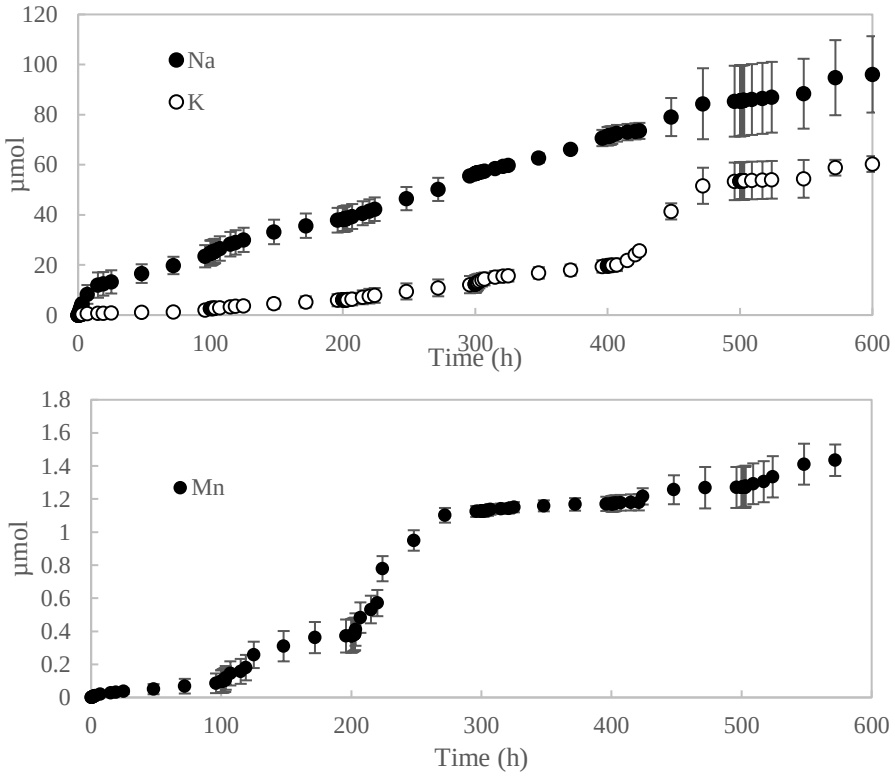

Figure A.4.1. (continued) Total amounts of (a) Na and K and (b) Mn released during dissolution of Etna ash.

CHAPTER 5 Dissolution rates of extrusive magmatic rocks and their artificial glassy counterparts at pH 4 and 25 °C

5.1. INTRODUCTION

Chemical weathering of volcanic rocks influences natural processes by affecting the chemical composition of rivers, lakes and soils where this material has been deposited and/or transported (White et al., 1980, Chadwick and Chorover, 2001, Oelkers et al., 2012, Eiriksdottir et al., 2015). The weathering of both glassy and crystalline Ca, Mg-silicates represents a crucial part in the long-term carbon dioxide cycle and soil formation in volcanic terrains (Gaillardet et al., 1999; Kump et al., 2000; Chadwick and Chorover, 2001; Dessert et al., 2003).

Chemical weathering is characterized in either qualitative terms (e.g., changes in microscopic surface morphologies of mineral grains, etc.) or in quantitative terms focusing on the determination of weathering rates. Weathering rates can be element, or mineral specific. Examples of element-based rates are those reported for annual stream or river discharge, and normalized to the watershed area. Weathering rates based on geographic and volumetric surface areas are referred to as weathering fluxes (White, 2011). Watershed fluxes are commonly defined as the sum of rock-derived base cations solubilized per unit area of geographic surface (Bluth and Kump, 1994; White and Blum, 1995). The quantification of chemical weathering rates from the field is not an easy task and therefore, a great effort is devoted to measuring dissolution kinetics in well-controlled systems and developing theoretical models to express the rate and mechanism of mineral and glass dissolution (White and Brantley, 1995).

Both experimental and field-based approaches have been used to quantify silicate weathering rates. The advantages of the experimental approach is that chemical, physical and biological conditions are tightly constrained and individual parameters, such as mineral compositions, temperature, surface area, and solute composition, are systematically varied to characterize weathering mechanisms (Lasaga, 1998). The principal disadvantage is that such experiments commonly react freshly prepared silicate minerals over relatively short time intervals, thus producing uncertainties when experimental rates are extrapolated to natural, long-term weathering environments (White and Brantley, 2003).

Geochemical modelling codes rely on laboratory kinetics laws to describe chemical weathering in the natural environment (e.g., Goddéris et al., 2006; Schott et al., 2012). Laboratory studies have been performed to determine the dissolution rates of the main components typically reported in volcanic rocks. Thus, there are several studies presenting dissolution rates of aluminosilicate minerals (see Palandri et al., 2004) and glasses (e.g., Gislason and Oelkers, 2003; 2013) as a function of temperature and reactive fluid composition. Some dissolution studies have investigated the effects of chemical composition on natural glass and mineral (plagioclase) dissolution (Wolff-Boenisch et al., 2004; Gudbrandsson et al., 2014). These studies provide relationships describing the dissolution rate of the material as a function of its SiO_2 content.

While there are many investigations of the laboratory dissolution behavior of pure minerals and glasses, only a few studies address the complex dissolution behavior of natural polycrystalline igneous rocks that consist of a mixture of silicate minerals and glass. These rocks are by far the most abundant on Earth. In the laboratory, Gislason and Eugster (1987) measured a 10-time faster dissolution rate for basaltic glass compared to its crystalline equivalent. Hamilton et al. (2000) reported that the dissolution rate of albite was insignificantly different from that of synthetic albite glass, although depletion of Na and Al from the glass was more severe than from the crystalline solid at pH 2. In the field, Stefánsson and Gíslason (2001) found that the chemical denudation rate of mobile elements in river catchments containing glassy basalts in Southwest Iceland was 2-5 times faster than that for catchments comprised of crystalline basalts. Wolff-Boenisch et al. (2006) investigated the effect of crystallinity on dissolution kinetics as a function of chemical composition for natural glasses and silicate minerals. Natural silicate glass dissolution rates were significantly faster than their silicate mineral counterparts only when they were Si-rich. The authors posited that Si-poor glasses and minerals exhibited similar dissolution rates because crystallinity has little effect on Si polymerization in these solids. Wolff-Boenisch et al. (2006)'s study compared the dissolution rates of polycrystalline rocks with those of glasses presenting similar Si contents (similar Si:O ratios). However, they did not measure the dissolution behaviour of a polycrystalline rock with its truly glassy equivalent.

The objective of this chapter study is to compare the far-from equilibrium steady state dissolution rates of natural extrusive igneous rock with those obtained for their strictly glassy analogues. The latter are produced by remelting the natural rocks and quenching them in the laboratory. We used three rocks of basaltic, dacitic and rhyolitic composition. The dissolution experiments were performed in fluidized bed reactor at pH 4 and 25 °C.

5.1.1. Theoretical background

Various processes influence the overall dissolution rate of a mineral in contact with an aqueous solution. These include the ease with which chemical species are transported away from dissolving the mineral surface, the reverse of the dissolution reaction at near to equilibrium conditions, and the far-from-equilibrium dissolution rate (Murphy et al., 1989; Oelkers et al., 1994). In our study, the experimental settings ensured that the measured dissolution rate corresponded to far-from-equilibrium and surface reaction-controlled conditions. Steady state dissolution is reached when the concentration of Si (or Al) released from the mineral being dissolved is constant within analytical uncertainty for more than three residence times. The residence time of the circulating solution in the reactor is defined as the total volume of the reactor divided by the flow rate of the input solution. In our experimental setup, the residence time of our fluidized bed reactor was three hours (flow rate 0.4 mL min^{-1} and volume ~ 65 mL).

When the conditions of far-from equilibrium and steady-state are met, the far-from-equilibrium steady state dissolution rate of a rock/glass (r, in mol m^{-2} s^{-1}) is given by Declercq et al. (2013 and references therein):

$$r_i = \frac{C_i f}{A m} \times s \qquad [5.1]$$

where C_i (mol L^{-1}) is the aqueous concentration of the ith element in the outlet solution minus the blank concentration at the beginning of the experiment, f (L s^{-1}) the solution flow rate, A (m^2 g^{-1}) the reactive surface area of the dissolving rock/glass and m (g) the mass of sample. The term s is a stoichiometric factor, relating the number of moles of the ith element in the rock/glass normalised to one mole of silica, i.e. s = 1 when r is calculated from the outlet solution Si concentrations. It is rarely possible to determine the actual reactive surface area of a dissolving mineral. Thus, A is approximated either based on the BET specific surface area, A_{BET}, or the geometric specific surface area, A_{GEO} (see section 5.4.2).

5.2. MATERIALS AND METHODS

5.2.1. Sample characterization and preparation

Two crystalline igneous extrusive rocks corresponding to low-silica (trachybasalt, ET-R) and high-silica (dacite, UZ-R) compositions were used in the dissolution experiments. An obsidian (rhyolite, LP-R) was also studied. The glassy (crystal-free) materials (ET-G, UZ-G and LP-G) were obtained by

melting subsamples of the powdered crystalline rocks at 1400 °C under standard atmospheric pressure, homogenising and then quenching the melts (Ayris, 2010) at the Department of Earth and Environmental Sciences, Ludwig Maximilians University Munich (LMU), Germany. The bulk chemical compositions of the rock and glass samples as determined by X-ray fluorescence (XRF) are shown in Table A.5.1.

The rock mineralogy was determined by X-ray diffraction (XRD) using a Bruker D8 Advance instrument operated at 40 kV and 20 mA, with a step width of 0.02° and counting time of 2.0 s $step^{-1}$, using Kα radiation sourced from a Cu target anode. All samples were ground to fine powders in an agate mortar prior to analysis. Crystalline minerals were identified using the EVA© software the semi-quantification of crystalline mineral phases based on diffractogram analyses were performed with SIROQUANT software (Hill et al., 1993; Bish, 1993; Gonzalez et al., 2003). The glass content of the crystalline rocks was estimated by spiking the sample with 10 wt.% of an internal standard, i.e metallic Si, followed by re-analysis under the same XRD operating conditions as describe above (Winburn et al., 2000; Ward and French, 2006; Paque et al., 2016). The accuracy in the weight percent determinations of the rock's glass and major crystalline components is in the range 5–10% (Paque et al., 2016) (see section 3.5.2). The mineralogy of the rock samples is summarized in Table A.5.2.

Prior to the dissolution experiments, the rocks and glasses were crushed by wrapping them in several polyethylene plastic bags and careful hammering. The crushed material was then dry sieved in order to retain particles within the 63-100 µm size range. This fraction was ultrasonically cleaned in ethanol several times until no suspended fine material remains after decantation. The cleaned samples were dried overnight at 50 °C.

Particle size analysis of the powdered rock and glass samples was performed by laser diffraction spectroscopy (LS 100Q, Coulter-Beckman particle size analyser) (Jacquinot, 1957; ISO 13320:2009). The particle size distributions of ET-R, UZ-R, LP-R, ET-G, UZ-G and LP-G are presented in Figure A.5.1. These measurements allowed calculation of the specific geometric surface area, A_{geo} ($m^2\ g^{-1}$) of the samples (Brantley et al., 1999):

$$A_{geo} = \frac{6}{\rho * d_{eff}} \quad [5.2]$$

where ρ is the particle density (in kg m^{-3}) and d_{eff} is the effective particle diameter (m). Particle density was measured by triplicates (ISO 1183-1:2012) and by Funk and Dinger (1993) using a 5 mL glass pycnometer (specific gravity bottle 4.9038±0.01 mL: BLAUBRAND NS10/19). In Eq. [5.2], the

value of the numerator posits that the particles have a regular and smooth spherical shape.

Assuming a homogeneous particle size distribution, d_{eff} can be estimated *via* the following expression (Tester et al., 1994; Wolff-Boenisch et al., 2004, 2006):

$$d_{eff} = \frac{d_{max} - d_{min}}{ln\left(\frac{d_{max}}{d_{min}}\right)} \quad [5.3]$$

where d_{max} and d_{min} refer to the maximum and minimum particle size, respectively, of the size fraction used in the dissolution experiment. In our study, $d_{min} = 63\ \mu m$, d_{max}= 100 µm and $d_{eff} = 80\ \mu m$. A more accurate estimation of d_{eff} can be obtained by using the full particle size distribution of the powdered samples. Particle size distribution can be used to calculate the d_{eff} value by dividing the size distribution into a finite amount of bins and assuming equivalent spherical diameters of particles that correspond to the mean size of each bin (Cepuritis et al., 2017):

$$d_{eff} = \sum_{i=dmin}^{dmax} x_i \frac{d_{i+1} - d_i}{ln\left(\frac{d_{i+1}}{d_i}\right)} \quad [5.4]$$

where x_i refers to the volumetric fraction of particles within each size bin d_i and d_{max} and d_{min} refer to the maximum and minimum size bin measured by laser diffraction spectroscopy, corresponding to x_{dmax}=0.99 and x_{dmin}=0.01 respectively.

A_{geo} is merely an estimate that does not consider any surface topography or roughness that might be present in the forms of etch pits, pores and steps. In general, A_{geo} presents a minimum value and tends to underestimate the total surface area. Practically, the total specific surface area, A_{BET}, of a mineral powder is best approached by inert gas adsorption using the Brunauer, Edward and Teller method (or BET method; Brunauer et al., 1938). The A_{BET} of our rock and glass samples was measured by the three-point BET method. Since powdered fresh silicate rocks and glasses generally display low specific surface areas <1 $m^2\ g^{-1}$ (Brantley and Mellott, 2000), Kr was the adsorbate gas (American Society for Testing and Materials, 2015), except for the analysis of LP-G for which N_2 was used. The "surface roughness factor" is defined by the ratio A_{BET}/A_{geo} (Wolff-Boenisch et al., 2004). Table 5.1 shows the A_{geo}, A_{BET} and surface roughness factors for ET-R, UZ-R, LP-R, ET-G, UZ-G and LP-G powders (size fraction 63-100 µm).

Table 5.1. Si:O ratio, density, A_{geo}, A_{BET} and surface roughness factors for the rock and glass powders (size fraction 63-100 µm) used in this study.

Sample	Si:O	Density (kg m^{-3}) x10^3	A_{geo} (m^2 g^{-1}) x 10^{-3}	A_{BET} (m^2 g^{-1}) x 10^{-3}	Surface roughness factor
Rock					
ET-R	0.29	2.71±0.12	33±6	113.7±0.5	3.45 ±0.003
UZ-R	0.33	2.41±0.07	54±3	72±0.8	1.33±0.001
LP-R	0.35	2.42±0.03	48±2	124.3±0.9	2.54±0.001
Glass					
ET-G	0.27	2.54±0.03	44±3	38.2±0.5	0.87±0.001
UZ-G	0.36	2.40±0.08	58±2	57.4±0.4	0.98±0.0003
LP-G	0.39	2.41±0.16	92±6	292±3	3.16±0.002

5.2.2. Dissolution experiments

The dissolution experiments were carried out in a fluidized bed reactor at 25 °C. The dissolution reactor consisted of 50 mL polypropylene pipettes equipped with a circulation pump (Watson Marlon 90 rpm) to keep the material in suspension (~14 mL min^{-1}) (see chapter 3 for details of the dissolution reactor). The solution was pumped through the reactor at a constant rate of 0.4 mL min^{-1} using a peristaltic pump (Miniplus 2 GILSON). All dissolution experiments were performed at a pH value of 4 and an ionic strength, I, of 10 mM. The acid inlet solution was prepared with Millipore™ water and Merck analytical grade NH_4Cl (0.0099 mol L^{-1}) and HCl (0.0001 mol L^{-1}). The concentrations of cations released during the dissolution experiment were ≤5% than the ionic strength of the inlet solution, i.e. I did not change significantly. About 0.5 g of dry rock or glass was precisely weighed and introduced in the reactor.

The dissolution reactor was thoroughly cleaned prior to each dissolution experiment by circulating a 0.1 mol L^{-1} HCl solution during 48 hours. The pH 4 inlet solution was then allowed in the reactor for at least another 24 hours. The presence of pollution (external source of Si, Al, Fe, Ca, Mg, Na and K) in the output solution (blank) was then checked by Inductively Coupled Plasma-Atomic Emission Spectroscopy (ICP-AES). The dissolution experiment could then begin. About 0.5 g (precisely weighed) of dry rock or glass powder was introduced in the reactor and the outlet solution was collected after 24, 48, 72, 96, 120, 150, 175 and 200 h (the steady state dissolution was reached before 200 h in all our dissolution experiments). Then, the output solution was filtered through a 0.2 µm hydrophilic polypropylene membrane filter and analysed for Si, Al, Fe, Ca, Mg, Na and K by Inductively Coupled Plasma-Atomic Emission Spectroscopy (ICP-AES). The detection limit was 10 µg

$L^{-1}$for Si, Na, K and S, 4 µg L^{-1} for Mn, 3 µg L^{-1} for Fe, 2 µg L^{-1} for Al, 1.5 µg L^{-1} for Mg and 0.8 µg L^{-1} for Ca. The error on the ICP-AES analytical measurements was estimated about 1.5% (>50 ppb) and 0.5% (50-200 ppb). The concentration of the studied cations in the blank solution (pH 4 without rock-glass sample) was: Si 17±2 µg L^{-1}; Ca 5.7±1 µg L^{-1}; Na 3±2 µg L^{-1}. Speciation calculations performed with the geochemical model PHREEQC 2.6 (Parkhust and Appelo, 1999) indicated that all output solutions were undersaturated with respect to any mineral phases. Each dissolution experiment was conducted in triplicates.

5.3. RESULTS

5.3.1. Si and Al releases

The evolution with time of the Si and Al concentrations (means of three replicates) released during the dissolution experiment of each rock and glass samples is shown in Figure 5.1. With values ranging from 2.4-3.7 µmol L^{-1}, the Si release from ET-R and ET-G was approximately 8 times larger than that from any of the other rocks and glasses. The release of Si from ET-R fluctuated within a relatively narrow range of concentrations (3.1- 3.6 µmol L^{-1}), whereas for ET-G it increased steadily until it reached steady-state (2.4-3.7 µmol L^{-1}). The dissolution of the UZ and LP glass and rock materials was characterized by a high initial release of Si which then decreased pseudo-exponentially with time. In contrast with Si, the release of Al release from ET-G was more or less steady (2.5-2.8 µmol L^{-1}). Similar to the other glass and rock specimens, the concentration of Al of ET-R decreased pseudo-exponentially as dissolution progressed. The ET materials released at least twice more Al than the other rocks and glasses tested in this study. For both Si and Al releases, steady-state dissolution was achieved after ~150-175 hours in all experiments.

5.3.2. Steady state, far-from-equilibrium dissolution rates

The far-from-equilibrium dissolution rates (in log units) of the rock and glass samples as calculated using Eq. [5.1] and the steady-state concentrations of Si and Al in the outlet solutions are shown in Table 5.2. The rate values are normalized either to the BET (r_{BET}) or specific geometric surface (r_{geo}) area.

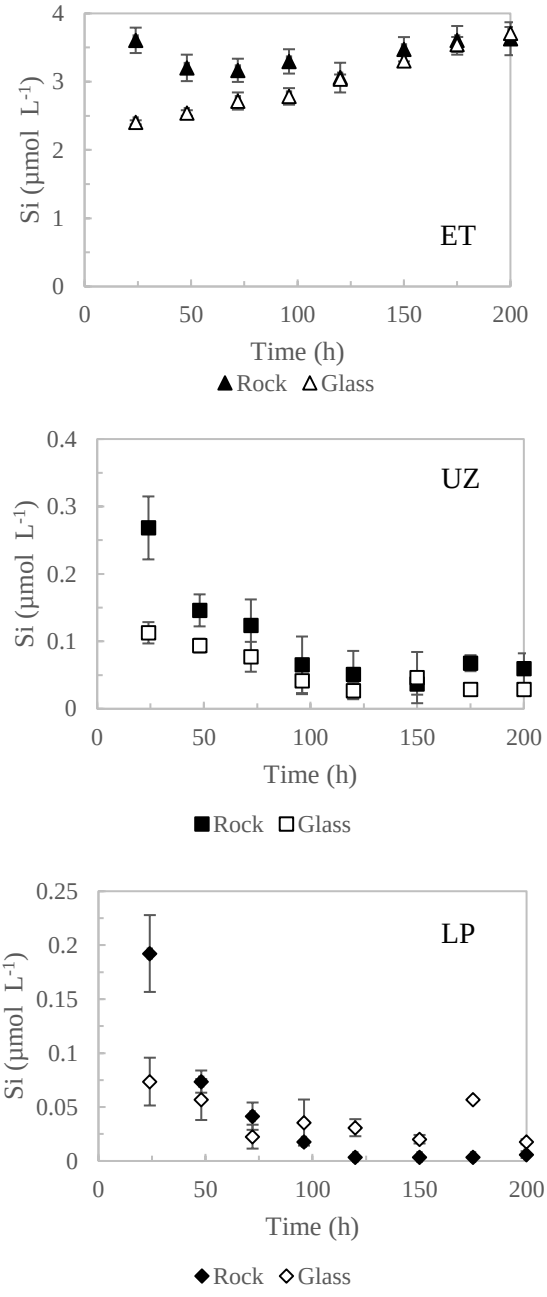

Figure 5.1. Release of Si for rock/glass dissolution at 25 °C and pH 4 as a function of time for (a) basalt-Etna (ET) (b) dacite-Unzen (UZ) (c) rhyolite-Lipari (LP).

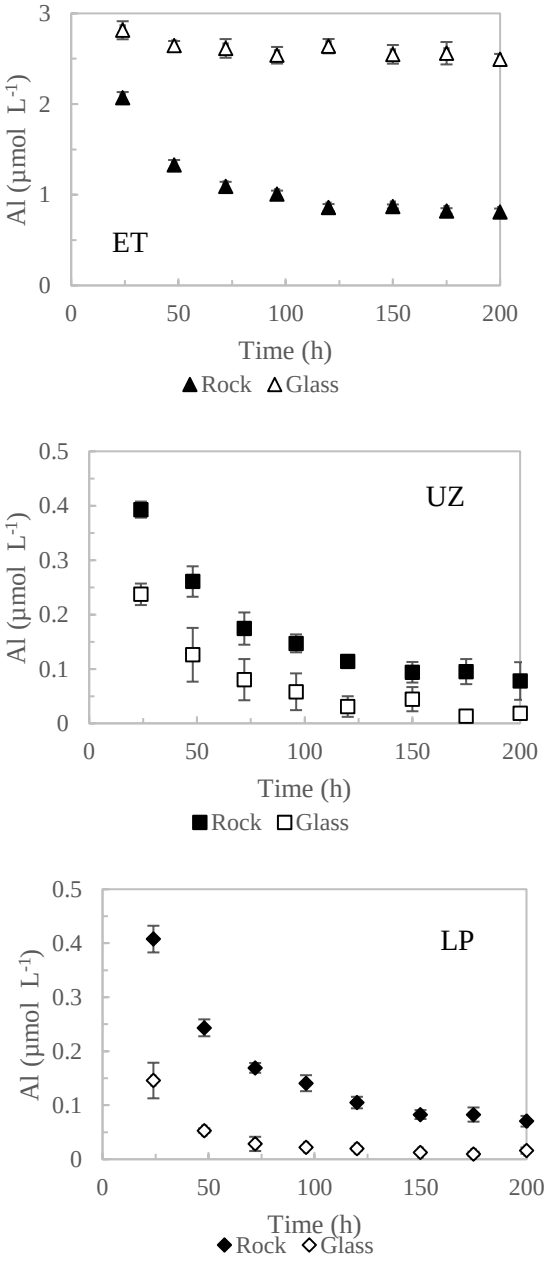

Figure 5.1. (continued). Release of Al for rock/glass dissolution at 25 °C and pH 4 as a function of time for (a) basalt-Etna (ET) (b) dacite-Unzen (UZ) (c) rhyolite-Lipari (LP).

Table 5.2. Si and Al concentrations at steady state (200 h) and logarithm of dissolution at steady state of volcanic rocks/glasses dissolution experiments at 25 °C and 0.4 g min^{-1} at pH 4 normalized to BET and geometrical surface area.

Sample	Si (mol L^{-1}) x 10^{-8}	Al (mol L^{-1}) x 10^{-8}	Log (a^3_{H+}/a_{Al3+})	Log $r_{Si, geo}$ (mol m^{-2} s^{-1})	Log $r_{Si, BET}$ (mol m^{-2} s^{-1})	Log $r_{Al, geo}$ (mol m^{-2} s^{-1})	Log $r_{Al, BET}$ (mol m^{-2} s^{-1})
Rock							
ET-R	362.9±31.9	80.9±5.4	-5.62±0.03	-8.80±0.03	-9.33±0.03	-9.05±0.02	-9.59±0.02
UZ-R	6.88±1.60	7.78±4.55	-4.45±0.28	-10.75±0.10	-10.87±0.10	-10.16±0.21	-10.29±0.21
LP-R	0.59±0.41	7.04±1.34	-4.47±0.04	-11.75±0.39	-12.16±0.39	-10.03±0.06	-10.43±0.06
Glass							
ET-G	370.8±12.9	249.4±10.8	-6.20±0.004	-8.92±0.02	-8.98±0.02	-8.71±0.01	-8.66±0.01
UZ-G	2.85±1.23	1.48±1.28	-3.79±0.33	-11.14±0.22	-11.14±0.22	-10.89±0.35	-10.88±0.35
LP-G	1.78±0.36	1.61±0.58	-3.64±0.44	-11.47±0.09	-11.97±0.09	-10.85±0.35	-11.36±0.16

5.4. DISCUSSION

5.4.1. Stoichiometry of Si and Al releases during dissolution

A plot of r_{Al} vs. r_{Si} for all the rock/glass specimens is used to assess the stoichiometry of the dissolution at steady-state (Fig. 5.2). Except LP-R for which r_{Al} is 53 times higher than r_{Si}, the Si and Al-based rates are comparable, suggesting stoichiometric dissolution of the rock/glass. This result applies for both the A_{BET}- and A_{geo}-normalized dissolutions rates. Recalling that LP-R is a natural rhyolitic glass and LP-G represents its synthetic counterpart, the non-stoichiometric release of Al with respect to Si in LP-R contrasts with the behavior of LP-G. In addition, as noticed above, the r_{Si} values are comparable in both materials. This suggests that the high r_{Al} of LP-R may not be a reliable estimate. Therefore, we will not use the Al-based dissolution rate obtained for LP-R in the rest of the discussion.

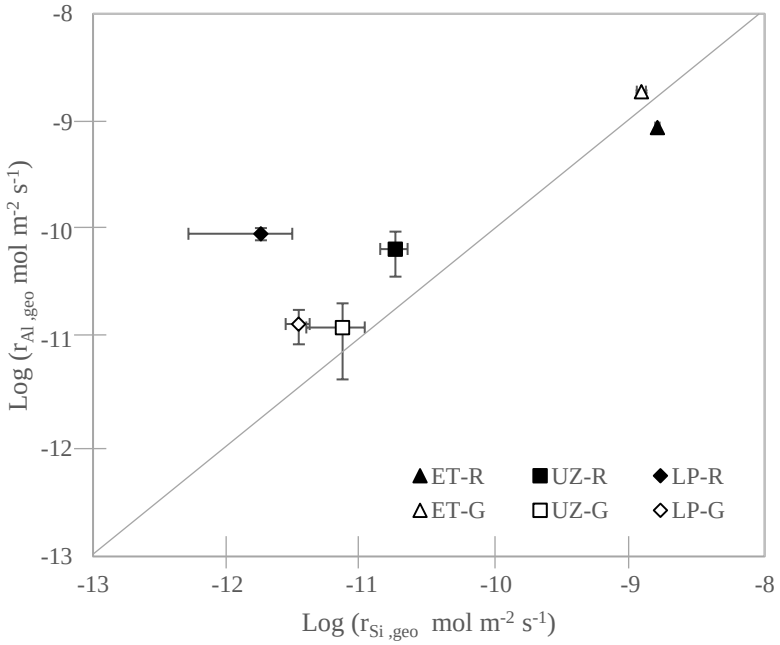

Figure 5.2. Comparison of the dissolution rate values for ET-R, ET-G, UZ-R, UZ-G, LP-R and LP-G as calculated from the Al and Si concentrations in the output solution.

Stoichiometric release of Si and Al during the dissolution of basaltic and rhyolitic glasses was evidenced in previous experiments (Oelkers and Gislason, 2001; Declerq et al., 2013). Although less clear, Gudbrandson et al. (2014) observed a similar behavior in plagioclases. Our data suggest that the rocks showed less stoichiometric behavior compared to their synthetic counterparts. This agree with Gislason and Eugster (1987) who found that basaltic glass dissolved near stoichiometrically at 25 °C, whereas the dissolution of crystalline basalt departed slightly from this behavior.

5.4.2. Dissolution rates of the basalt, dacite and rhyolitic glasses

Previous investigations have highlighted that the dissolution rate of silicate glass increases with decreasing Si content (Petit et al., 1990; Jantzen and Plodicne, 1984; Wolff-Boenisch et al., 2004). Our experimental results agree with this trend (Table 5.2). Based on dissolution rate measurements obtained at pH 4 and 25 °C for natural glasses varying in composition from basalt to rhyolite, Wolff-Boenisch et al. (2004) established a quantitative relationship linking $r_{Si,geo}$ (mol m^{-2} s^{-1}) to the glass silica content:

$$\log r_{Si,geo} = -0.03 \times [SiO_2\ (wt.\%)] - 7.58 \quad [5.5]$$

Eq. [5.5] indicates that $r_{Si,geo}$ varies exponentially with the glass SiO_2 content. Wolff-Boenisch et al. derived a similar expression for $r_{Si,BET}$, but they acknowledged that this reproduce the experimental data less satisfactorily:

$$\log r_{Si,BET} = -0.05 \times [SiO_2\ (wt.\%)] - 7.44 \quad [5.6]$$

The authors attributed the discrepancy to various factors that increase A_{BET} of natural samples but which do not enhance their reactive surface area. For example, the presence on the surface of non-reactive coatings and microstructures as well as the dissolution reactions increase A_{BET} of natural samples but do not enhance their reactive surface area.

The measured dissolution rates of ET-G, UZ-G and LP-G at pH 4 are plotted in Fig. 5.3a. Surprisingly, only the basalt glass sample (low Si:O ratio) falls on the regression line defining the relationship between A_{geo}-normalized dissolution rate and glass silica content (Eq. [5.5]); the silica-rich glasses (UZ-G, LP-G and LP-R) show significantly lower (25-140 times) $r_{Si,geo}$ values than those expected from Eq. [5.5]. One reason for the discrepancy may relate to different particle size distributions. Wolff-Boenisch et al. (2004) worked with a particle size fraction comprised between 45 and 125 µm, whereas we used slightly coarser particles in the size range 63-100 µm. As pointed out by

some authors (Jeschke and Dreybrodt, 2002), finer particles may dissolve faster. However, alone, this effect is unlikely to explain the departure of our samples from Wolff-Boenisch et al.'s prediction. In their calculations of A_{geo}, the authors computed d_{eff} via Eq. [5.3], whereas we used Eq. [5.4]. Although recalculating A_{geo} for our samples using the average particle diameter (Eq. [5.3]) produces lower values (Figure A.5.2) and hence, higher $r_{Si,geo}$, the behavior of UZ-G, LP-G and LP-R still depart largely from the empirical relationship (Fig. 5.3a).

Figure 5.3b compares the experimental $r_{Si,BET}$ values for the ET-G, UZ-G, LP-G and LP-R with the A_{BET}-normalized dissolution rates reported by Wolff-Boenisch et al. (2004). The match between our results and those of Wolff-Boenisch improves but is far from being satisfactory. Wolff-Boenisch et al. (2004) emphasized that the measurement of A_{BET} by different laboratories is subject to uncertainties, and caution should be exerted when comparing $r_{Si,BET}$ across studies. Adopting this view, the authors put more faith in $r_{Si,geo}$ than in $r_{Si,BET}$ estimates. Similar to Wolff-Boenisch's study, we measured the specific surface areas of our samples by the BET method using Kr as the adsorbate gas (except in the case of LP-G for which N_2 was utilized, as this sample had a $A > 1$ m^2 g^{-1}). The measurements showed a good reproducibility (Table 5.1). Therefore, we rule out the possibility that the comparatively low $r_{Si,BET}$ values obtained for the UZ-G, LP-G and LP-R are an artefact of unreliable A_{BET} determinations.

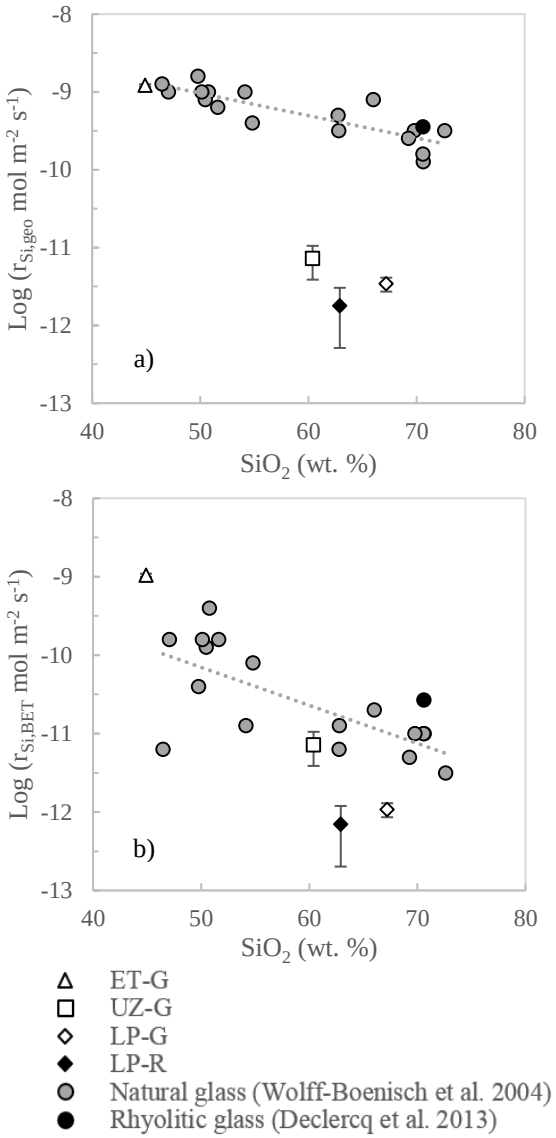

Figure 5.3. The logarithm of dissolution rates for the studied glasses versus the silica content at pH 4 and 25 °C normalized to a) the BET specific surface area and b) the GEO specific surface area. The lines through the data represent a linear least square fit obtained by Wolff-Boenisch et al. (2004) for natural glasses.

Jeschke and Dreybrodt (2002) investigated how the dissolution rate of a mineral relates to its surface morphology. They developed a rigorous mathematical approach to assess which specific surface area should be utilized. According to this study, dissolution of silicates occurs over the entire mineral surface and in such case, dissolution rates are best normalized to the BET specific surface area. Finally, the measured A_{BET} and estimated A_{geo} showed good agreement (surface roughness factor ~1) in the cases of ET-G and UZ-G (Table 5.1). Altogether, we argue that the discrepancies between our $r_{Si,BET}$ values for UZ-G, LP-G and LP-R and those reported by Wolff-Boenisch et al. (2004) for glasses with similar SiO_2 contents are real. We note that the Icelandic rhyolitic samples in Wolff-Boenisch et al.'s study display a higher Fe content (3.7-4.9 wt.% Fe_2O_3) than our LP samples (Table A.5.1). Depending on the redox state of the glass, Fe may act as either a network modifier (Fe^{2+}) or a network former (Fe^{3+}) (Mysen, 1988; Cook et al., 1990, Cooper et al., 1996). Iron in the network forming position may weaken the glass, making it less resistant to dissolution (Ottonello, 2001; Kuryaeva, 2004; Perez et al., 2015; Vercamer, 2016). We tentatively suggest that the greater abundance of Fe in the Icelandic glasses analysed by Wolff-Boenisch et al. is responsible for its comparatively higher dissolution rates.

We recall that the UZ-G and LP-G specimens are synthetic glasses produced by remelting rocks of dacitic and rhyolitic composition, respectively. LP-R is the obsidian rock used to synthesize LP-G, the latter displaying a higher Si:O ratio (0.39 for LP-G vs. 0.35 for LP-R, Table 5.1). The specific surface area of LP-G is ~2 (A_{BET}) and ~2.4 (A_{geo}) times larger than that of LP-R (Table 5.1). According to Table 5.2, the dissolution rates of LP-G and LP-R did not differ significantly. This result diverges from Wolff-Boenisch et al. (2006)'s findings, which predicted that the dissolution rates of natural glasses are higher than those measured for synthetic glasses with similar Si:O ratios. Further, the authors proposed that this effect relates to the cooling history of the glass. Rapidly annealed natural glasses could develop less ordered structures compared to slowly annealed laboratory glasses. As a result, the former would present a more fragmented and disconnected network, which would exhibit many reactive sites prone to dissolution (Hamilton et al., 2001). Based on Ayris (2010), our synthetic glass samples were subjected to a cooling rate of ~0.2 °C s^{-1}. For comparison, Wilding et al. (1996) reported quench rates for natural volcanic glasses from Tenerife ranging from ~10^{-6} to 10 °C s^{-1}. Thus, the cooling rate achieved in the laboratory for producing LP-G could be within the range of values found in the natural environment. This would explain why the dissolution rates of LP-G and LP-R did not differ significantly.

Figure 5.4 displays our dissolution rate determinations (ET-G, UZ-G, LP-G and LP-R) along with the dissolution results obtained for other natural and synthetic glasses in previous studies (Wolff-Boenisch et al., 2006). Although the spread of the data points prevents a firmed conclusion to be reached, our measurements may corroborate Wolff-Boenisch et al.'s view that the difference between the dissolution rates of synthetic and natural glasses with similar Si:O ratios becomes more important in high-silica glasses.

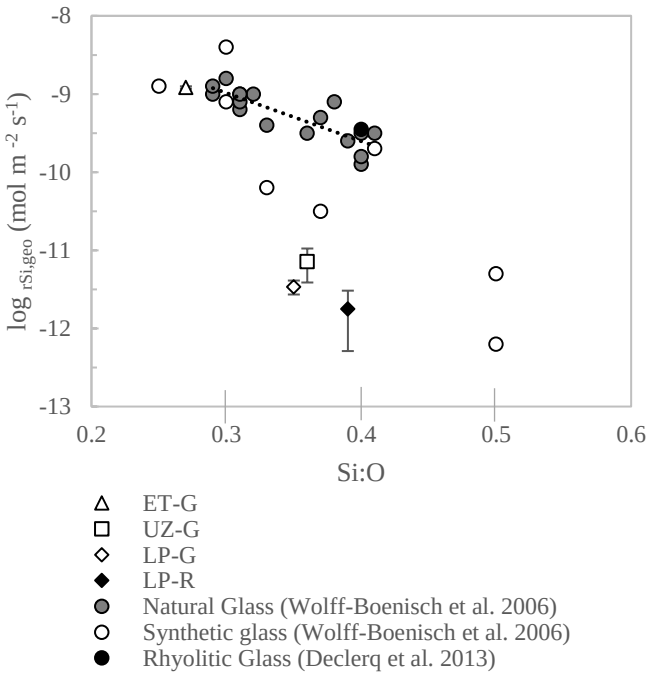

Figure 5.4. The logarithm of dissolution rates for natural and synthetic glasses of different compositions at pH 4 and 25 °C normalized to the GEO specific surface area. The lines through the data represent a linear least square fit presented by Wolff-Boenisch et al. (2006) for natural and synthetic glasses.

5.4.3. Dissolution rates of the crystalline rocks and their glassy counterparts

According to our results (Table 5.2), the dissolution rates of the crystalline rock and the glass differ to various extents, depending on their chemical composition. The faster A_{BET}-normalized dissolution rate measured for the basaltic glass relative to the crystalline basalt agrees with Gislason and Eugster (1987), who indicated that the dissolution rate (at 25 °C and pH 9) varied by a factor of ten between basaltic glass and crystalline basalt. Similarly, Stefánson and Gislason (2001) reported higher releases of Si in Icelandic river catchments containing glassy basalts than in catchments dominated by crystalline basalts. In contrast, Wolff-Boenish et al. (2006) found almost no difference in the dissolution rates of ultramafic glasses and minerals with similar compositions.

The ET-G and ET-R samples exhibit low Si:O ratios <0.30 (Table 5.1). Following Wolff-Boenish et al. (2006), for such compositions, glass and crystalline rocks should display similar dissolution rates. Therefore, the higher $r_{Si,BET}$ of ET-G relative to that of ET-R may simply result from the three-time lower A_{BET} of the former. Similarly, the A_{geo} and $r_{Si,geo}$ of ET-G are slightly (~25%) larger and lower, respectively, than the A_{geo} and $r_{Si,geo}$ of ET-R. Thus, our results seem compatible with Wolff-Boenish et al. (2006).

Wolff-Boenisch et al. also highlighted a compositional effect and concluded that the discrepancy between glass and mineral dissolution rates increases with increasing Si:O ratio of the glass/mineral. Importantly, the inferred trend is more robust when the r_{geo} values were considered. The authors argued that this probably reflects the quasi invariance of A_{geo} during dissolution experiments, whereas A_{BET} tends to increase as the dissolution reaction progresses (Eggelston et al. 1989; Stillings and Brantley 1995; Gautier et al. 2001). In our study, both the $r_{Si,geo}$ and $r_{Si,geo}$ estimates reveal that crystalline dacite dissolved significantly faster than its glassy counterpart, a finding opposite to Wolff-Boenish (2006)'s predictions. However, we note that the relationship established by Wolff-Boenish et al. (2006) which links the discrepancy in glass and mineral dissolution rates to glass/mineral chemistry includes dissolution data for high Si:O ratio compositions corresponding to clay minerals such as smectite, kaolinite and montmorillonite. We question this approach as the layered structure of phyllosilicate minerals, which are the products of rock weathering, likely confer them a different reactivity from that of tectosilicates and inosilicates that typify primary magmatic minerals with similar Si:O ratios. Accordingly, previous studies indicate that mixed layer phyllosilicates (smectites, kaolinite/halloysite, Si:O ratio of 0.39-0.4) are

more stable than albite (Si:O ratio of 0.38) (Jackson et al., 1948; Jackson, 1952; Wieland and Stumm, 1992; Furrer et al.,1993; Nagy, 1995).

The glassy component of UZ-R is rhyolitic in composition (Table A.5.5). As illustrated in Figure 5.5, the dissolution rate normalized to BET specific surface area at acidic pH values of rhyolitic glass is generally lower than that of the plagioclases: anorthite (An_{90-100}), bytownite (An_{70-90}) and labradorite (An_{50-70}). At pH 4, the experimental $r_{Si,BET}$ of UZ-G compares well with the reported dissolution rate of rhyolitic glass, whereas the experimental $r_{Si,BET}$ of UZ-R is closer to the dissolution rate values of the plagioclase minerals such as albite (An_{0-10}) and labradorite (An_{50-70}). It has been reported that the composition of plagioclase phenocrysts on dacites from the 1991 eruption of Mt. Unzen ranged between An_{35} to An_{75} (Nakada and Motomura, 1999). Thus, we posit that the overall rate of dissolution of the dacite rock seems to be significantly influenced by the dissolution of these mineral phases.

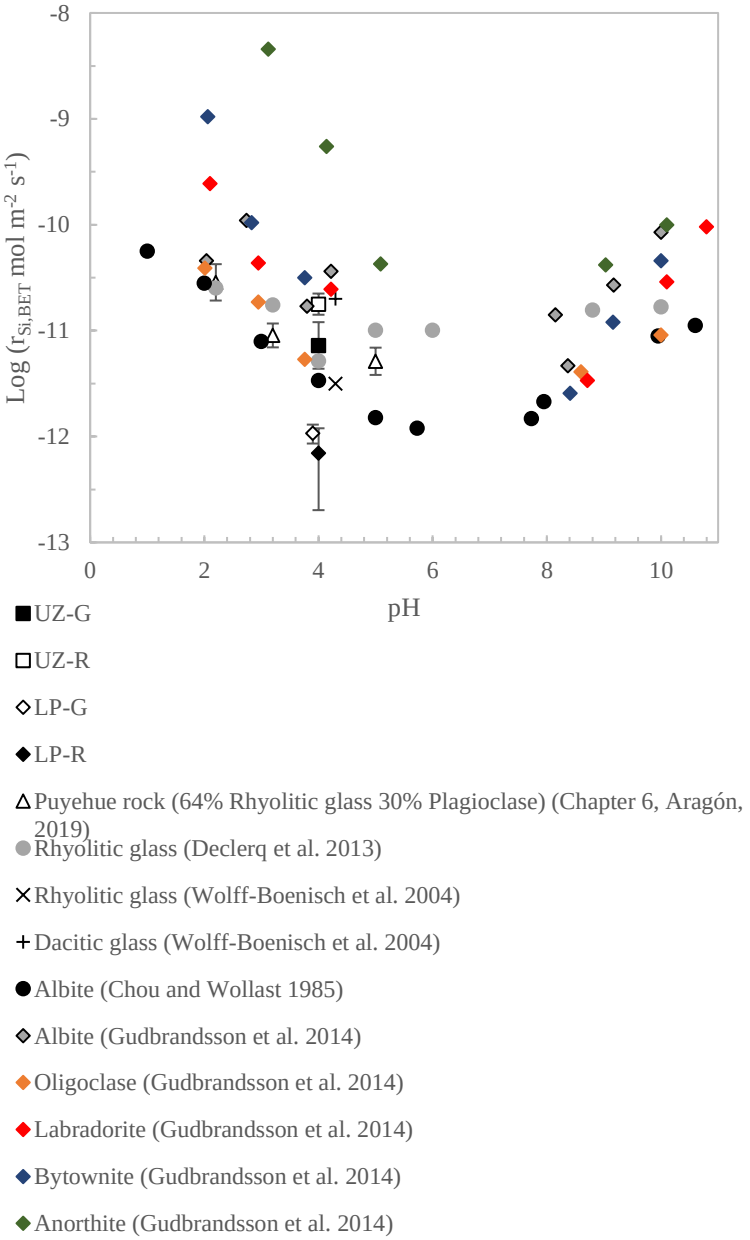

Figure 5.5. Dissolution rates (22-25 °C) of plagioclases, dacitic and rhyolitic glass and rhyolitic rock as a function of the solution pH taken from previous experimental studies (chapter 6 in this study; Wolff-Boenisch et al., 2004; Chou and Wollast, 1985; Gudbrandsson et al., 2014) of mineral and glass dissolution compared to the dissolution rates determined in this study for dacitic rock and glass at pH 4 and 25 °C.

5.4.4. Lifetimes of silicate rocks and glasses subjected to weathering

Knowledge of dissolution rates allows the estimate of the lifetimes of silicate rocks and glasses that are subjected to weathering. Following Lasaga (1998), the time t (s) required to dissolve a spherical grain completely is given by:

$$t = \left(\frac{rad}{V_m \times r_{Si,BET}}\right) \quad [5.7]$$

Where rad (mm) stands for the grain radius and V_m refers to the molar volume ($cm^3\ mol^{-1}$) where a mole of rock/glass is assumed to contain one Si atom. Figure 5.6 shows the lifetimes for glassy and crystalline grains (1 mm in radius) of basaltic, dacitic and rhyolitic compositions as computed from our A_{BET}-normalized dissolution rate measurements at 25 °C and pH 4. As expected from the dissolution rate trend, t increased with increasing silica content. For example, t of a 1-mm radius spherical grain of basaltic glass is almost 1500 times shorter than that of the same grain but with a rhyolitic composition. For comparison, Rowe and Brantley (1993) estimated that acidic waters (pH 1.4 – 2.5) in volcanic environments would dissolve a 1 mm radius grain of the andesitic glass matrix in a dacitic rock (SiO_2 = 64 wt.%) entirely in ~ 90,000 years. This estimate agrees relatively with t of UZ-G at pH 4, i.e. ~114,000 years.

Wolff-Boenisch et al. (2004) derived a relationship to predict t (at 25 °C and pH 4) of a 1-mm spherical glass grain as a function of its SiO_2 content:

$$t_{glass} = 14.47 \times e^{0.079 \times [SiO2\ wt\%]} \quad [5.8]$$

As shown in Figure 5.6, our t estimates strongly depart from the trend inferred by applying Eq. [5.8]. This reflects the lower dissolution rates obtained for the high-silica glasses in our study compared to those reported in Wolff-Boenisch et al. (2004).

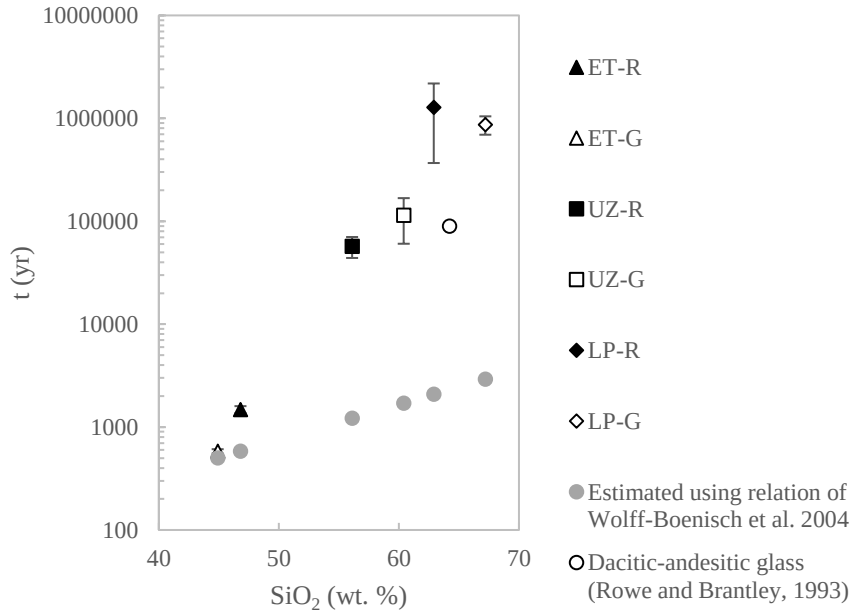

Figure 5.6. Calculated lifetimes of 1 mm radius spheres of two natural volcanic rocks and one natural glass (obsidian) and their synthetic glassy counterparts as a function of their silica content at 25 °C and pH 4. The relation obtained by Wolff-Boenisch et al. (2004) for lifetime of natural glass is also presented.

5.5. CONCLUSIONS

The dissolution rates (r_{BET} and r_{geo}) of the volcanic rocks decrease with increasing SiO_2 content ($r_{basalt} > r_{dacite} > r_{rhyolite}$). Basaltic rock and basaltic glass exhibited significantly higher r_{Si} values than the dacite and rhyolite samples, in accordance with previous studies. The Si and Al-based dissolution rates were comparable, suggesting stoichiometric dissolution of the rock/glass (except LP-R for which r_{Al} was higher than r_{Si},). This result applied for both the A_{BET}- and A_{geo}-normalized dissolutions rates. Our results also suggest that the rocks showed less stoichiometric behavior compared to their glassy counterparts.

We compared our experimental dissolution rates of glasses with the quantitative relationship linking $r_{Si,geo}$ or $r_{Si,BET}$ to the glass SiO_2 content which has been proposed by Wolff-Boenisch et al. (2004). Only the basalt glass sample (low Si:O ratio) conformed to Wolff-Boenisch et al.'s prediction. Using $r_{Si,BET}$ instead of $r_{Si,geo}$ only slightly improved the concordance of our results with those of Wolff-Boenisch et al. (2004).

The r_{Si} for UZ-G, LP-G and LP-R differ from the rates measured previously for glasses with similar SiO_2 contents (Wolff-Boenisch et al. 2004; Declerq et al., 2013). This may relate to different particle size distributions and/or different chemical compositions. For example, the Icelandic basalt glasses analysed by Wolff-Boenisch et al. (2004) contain more Fe than our sample. We rule out the possibility that the comparatively low $r_{Si,BET}$ values obtained for the UZ-G, LP-G and LP-R are an artefact of unreliable A_{BET} determinations.

The r_{Si} of LP-G and LP-R did not differ significantly. This result departs from Wolff-Boenisch et al. (2006)'s findings, who predicted that the dissolution rates of natural glasses (less ordered structure) are higher than those measured for synthetic glasses with similar Si:O ratios due to the different cooling history of the glasses. However, in our case, the cooling rate achieved in the laboratory for producing LP-G is probably within the range of values found in the natural environment, explaining the result observed in our study. Comparing the dissolution rates obtained for ET-G and ET-R, these estimates seemed compatible with the findings of Wolff-Boenish et al. (2006) who found almost no difference in the dissolution rates of ultramafic glasses and minerals with similar compositions.

The $r_{Si,geo}$ and $r_{Si,BET}$ estimates revealed that crystalline dacite dissolved significantly faster than its glassy counterpart, a finding opposite to Wolff-Boenish (2006)'s predictions. Thus, we posit that the overall rate of dissolution of the dacite rock seemed to be significantly influenced by the dissolution of the mineral phase (labradorite). The dacite glass counterpart compared well with the reported dissolution rate of rhyolitic glass.

Knowledge of dissolution rates allowed the estimate of the lifetimes *(t)* of silicate rocks and glasses that are subjected to weathering. As expected from the dissolution rate trend, t increased with increasing silica content. For example, t of a 1-mm radius spherical grain of basaltic glass is almost three orders of magnitude shorter than that of the same grain but with a rhyolitic composition.

In Figure 5.7, a summary of the main findings of this chapter is presented:

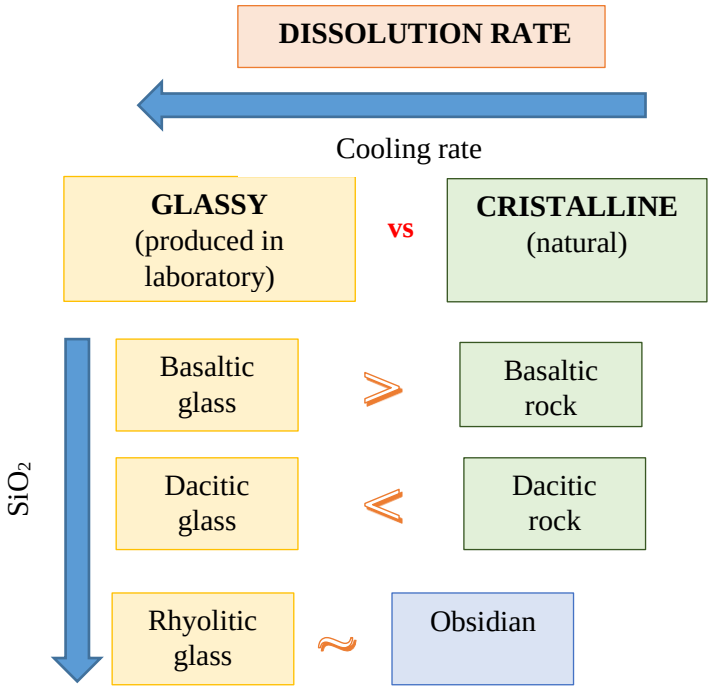

Figure 5.7. Summary of the main findings of chapter 5.

References

American Society for Testing and Materials (2015) ASTM D3663-03(2015) Standard Test Method for Surface Area of Catalysts and Catalyst Carriers. ASTM International, West Conshohocken, United States of America, doi: 10.1520/D3663-03R15.

Ayris, P. (2010) High temperature SO_2 chemisorption on model systems-Implication for in-plume processes. PhD Thesis, Environment Department, University of York, pp.184-188.

Bish, D.L., Post, J.E. (1993) Quantitative mineralogical analysis using the Rietveld full-pattern fitting method. Am Mineral 78: 932-940.

Bluth G.S. and Kump L.R. (1994) Lithologic and climatic controls on river chemistry. Geochim. Cosmochim. Acta 58. Pp. 2341-2359.

Brantley S. L. and Mellott N. P. (2000) Surface area and porosity of primary silicate minerals. Am. Mineral. 85, 1767–1783.

Brantley, S.L., White, A. F. and Hodson, M. (1999) Surface Area of Primary Silicate Minerals. In Growth and Dissolution in Geosystems, Jamtveit, B. and Meakin, P. (Eds.). Kluwer Academic Publishers, Dordrecht, pp. 291-326.

Brunauer, S., Emmett, P. H. and Teller, E. (1938) Adsorption of gases in multimolecular layers. Journal of the American Chemical Society, 60(2), 309-319.

Cepuritis, R., Garboczi, E.J., Ferraris, C.F., Jacobsen, S., Sorensen, B.E. (2017) Measurement of particle size distribution and specific surface area for crushed concrete aggregate fine. Advanced Powder Technology 28. 706-720.

Cook, G.B., Cooper, R.F. and Wu, T. (1990) Chemical diffusion and crystalline nucleation during oxidation of ferrous iron-bearing magnesium aluminosilicte glass. Journal of Non-Crystalline Solids, 120. 207-222.

Cooper, R.F., Fanselow, J.B., Poker, D.B. (1996) The mechanism of oxidation of a basaltic glass: Chemical diffusion of network-modifying cations. Geochimica et Cosmochimica Acta, Vol.60, No 17. Pp. 3253-3265.

Chadwick, O.A. and Chorover, J. (2001) The chemistry of pedogenic threshodks. Geoderma 100, 321-353.

Chou, L. and Wollast, R. (1985) Steady-state kinetics and dissolution mechanism of albite. American Journal of Science, Vol. 285, pp. 963-993.

Declercq, J., Diedrich. T., Perrot M., Gislason S.R., Oelkers E.H. (2013) Experimental determination of rhyolitic glass dissolution rates at 40–200 °C and 2 < pH < 10.1. Geochimica et Cosmochimica Acta 100 (2013) 251–263.

Dessert, C., Dupré, B., Gaillardet, J., François, L.M., Allègre, C.J., (2003) Basalt weathering laws and the impact of basalt weathering on the global carbon cycle. Chem. Geol. 202, 257–273.

Doremus, R.H. (1994) Glass Science. Wiley, New York.

Eiriksdottir, E.S., Gislason, S.R., Oelkers, E.H. (2015) Direct evidence of the feedback between climate and nutrient, major, and trace element transport to the oceans. Geochimica et Cosmochimica Acta 166. 249-266.

Eggleston, C.M., Hochella, Jr. MF., Parks, G.A. (1989) Sample preparation and aging effects on the dissolution rate and surface composition of diopside. Gecohim. Cosmochim Acta 53: 797-804.

Funk, J.E. and Dinger D. (1993) Predictive Process control of Crowded Particulate Suspensions: Applied to Ceramic Manufacturing. Kluwer Academic Publishers. Chapter 39 True Particle Density and Suspension Specific Gravity. pp 624-627.

Furrer, G., Zysset, M., Schindler, P.W. (1993) Weathering kinetics of montomorillonite: Investigations in batch and mixed-flow reactors. In: Manning D.A.C., Hall, P.L., Hughes, C.R. (eds) Geochemistry of Clay-Pore Fluid Interactions. Chapman & Hall, London. p. 243-262.

Gaillardet, J., Dupré, B., Louvat, P., Allègre, C.J. (1999) Global silicate weathering and CO_2 consumption rates deduced from the chemistry of the large rivers. Chem. Geol. 159, 3–30.

Gautier, J., Oelkers, E. and Schott, J. (2001) Are quartz dissolution rates proportional to B.E.T surface areas? Geochim. Cosmochim. Acta, 65, 1059.

Gislason, S.R. and Oelkers, E.H. (2003) The mechanism, rates and consequences of basaltic glass dissolution: II. An experimental study of the dissolution rates of basaltic glass as a function of pH and temperature from 6°C to 150°C. Geochim. Cosmochim. Acta 67, 3817-3832.

Gíslason, S.R., Arnórsson, S., (1990) Saturation state of natural waters in Iceland relative to primary and secondary minerals in basalts. In: Spencer,

R.J., Chou, I.-M. (Eds.), Fluid Mineral Interactions. A Tribute to H.P. Eugster, vol. 2. Geochemical Society, Special Publication, pp. 373-393.

Gislason, S.R., Eugster, H.P. (1987) Meteoric water–basalt interactions. I. A laboratory study. Geochim. Cosmochim. Acta 51, 2827–2840.

Godderis Y., François L., Probst A., Schott J., Moncoulon D., et al. (2006) Modelling weathering processes at the catchment scale: The WITCH numerical model. Geochimica et Cosmochimica Acta, Elsevier, 70, pp.1128-1147.

Gonzalez, R.M., Edwards, T.E., Lorbiecke, T.D., Winburn, R.S., Webster, J.R. (2003) Analysis of geologic material using rietveld quantitative X-Ray diffraction. International Centre for Diffraction Data. Advances in X-ray Analysis. Vol 46. 204-209.

Gudbrandsson S., Wolff-Boenisch D., Gislason S.R. and Oelkers E.H. (2014) Experimental determination of plagioclase dissolution rates as a function of its composition and pH at 22°C. Geochimica et Cosmochimica Acta 139 (2014) 154–172.

Hamilton J. P., Pantano C. G., and Brantley S. L. (2000) Dissolution rates of albite crystal and glass. Geochim. Cosmochim. Acta 64, 2603–2615.

Hamilton, J.P., Brantley, S.L., Pantano, C.G., Criscenti, L.J., Kubicki, J.D., (2001) Dissolution of nepheline, jadeite and albite glasses. Toward better models for aluminosilicate dissolution. Geochim. Cosmochim.Acta 65, 3683–3702.

Harrison, M.T. (2010) Review of Glass Dissolution Rates for use in the Disposal System Safety Case Performance Assessment Models. NNL (10) 10734. Issue 3.

Hill R.J., Tsambourakis, G., and Madsen, I.C. (1993). Improved Petrological Modal Analyses from X-ray Powder Diffraction Data by use of the Rietveld Method I. Selected Igneous, Volcanic, and Metamorphic Rocks J. Pet., 34(5), 867-900.

Holtz, F., Sato, H., Lewis, J., Behrens, H. and Nakada, S. (2005) Experimental Petrology of the 1991-1995 Unzen Dacite, Japan. Part I: Phase Relations, Phase Composition and Pre-eruptive Conditions. Journal of Petrology. Vol 46. No.2. p.319-337.

ISO 13320:2009 Particle size analysis -- Laser diffraction methods.

ISO 1183-1:2012 Plastics -- Methods for determining the density of non-cellular plastics -- Part 1: Immersion method, liquid pyknometer method and titration method.

Jackson, M.L., Tyler, S.A., Willis, A.L., Bourbeau, G.A., Pennington, R.P. (1948) Weathering sequence of clay-size minerals in soils and sediments. I. Fundamental generalizations. J Phys Coll Chem 52: 1237-1260.

Jackson, P.M., Hseung, Y., Corey, R.B., Evans, E.J., Vanden Heuvel, R.C. (1952) Weathering sequence of clay-size minerals in soils and sediments. II. Chemical weathering of layer silicates. Soil Sci Soc Am Proc 16:3-6.

Jacquinot, P. (1957) Optique Ondulatoire: Interférences-Diffraction 3. Certificat de Physique Générale. Editions Claude Hermant. Chapitre 9. Diffraction de Fraunhoffer. pp 127-167.

Jantzen, C.M. and Plodinec, M.J. (1984) Thermodynamic model of natural, medieval and nuclear waste durability. J. Non-Crist. Solids 67. 207-223.

Jeschke A. A. and Dreybrodt W. (2002) Dissolution rates of minerals and their relation to surface morphology. Geochim. Cosmochim. Acta 66, 3055–3062.

Kump, L.R., Brantley, S.L., Arthur, M.A. (2000) Chemical weathering, atmospheric CO_2, and climate. Annual Rev. Earth Planet. Sci. 28, 611–667.

Kuryaeva (2003) Degree of Polymerization of Aluminosilicates Glasses and Melts. Glass Physics and Chemistry. Vol.30. pp. 157-166.

Lasaga, A.C. (1998) Kinetic theory in Earth Sciences. Princeton University Press, New Jersey.

Mysen, B.O. (1988) Structure and properties of silicate melts. Elsevier Science & Technology Books, University of California, pp.354.

Murphy W.M., Oelkers, E.H. and Lichtner, P.C. (1989) Surface reaction versus diffusion control of mineral dissolution and growth rates in geochemical process. Chem. Geol. 78, 357-380.

Nagy, K.L. (1995) Dissolution and precipitation kinetics of sheet silicates. In Chemical weathering rates of silicate minerals (eds. A.F. White and S.L. Brantley) Rev. Mineral. 31, 173-233.

Nakada, S. and Motomura, Y. (1999) Petrology of the 1991-1995 eruption at Unzen: effusion pulsation and groundmass crystallization. Journal of Volcanology and Geothermal Research 89. p. 173-196.

Oelkers, E.H., Jones, M.T., Pearce, C.R., Jeandel, C., Eiriksdottir, E.S., Gislason, S.R. (2012) Riverine particulate material dissolution in seawater and its implications for the global cycles of the elements. C.R. Geoscience 344, 646-651.

Oelkers, E.H. and Gislason, S.R. (2001) the mechanism, rates and consequences of basaltic glass dissolution: I. An experimental study of the dissolution rates of basaltic glass as a function of aqueous Al, Si, and oxalic acid concentration at 25°C and pH=3 and 11. Geochim. Cosmochim. Acta 65, 367-3681.

Oelkers, E.H. Schott, J. and Devidal, J.-L. (1994) The effect of aluminium, pH and chemical affinity on the rates of aluminosilicate dissolution reactions. Geochim. Cosmochim. Acta 58, 2011-2024.

Ottonello, G., Moretti, R., Marini, L., Vetuschi Zuccolini, M. (2001) Oxidation state of iron in silicate glasses and melts: a thermochemical model. Chemical Geology 174. pp. 157-179.

Palandri J.L. and Kharaka Y.K. (2004) A compilation of rate parameters of water-mineral interaction kinetics for application to geochemical modeling. U.S. Geological Survey. Open file report 2004-1068.

Paque, M., Detienne, M., Maters, E.C., Delmelle, P. (2016) Smectites and zeolites in ash from the 2010 summit eruption of Eyjafjallajökull volcano, Island. Bull Volcanol 78: 61.

Papelis, C., Um, W., Russell, C.E. and Chapman, J.B. (2000) Part3. Measuring the specific surface area of natural and man-made glasses. Effects of formation process, morphology, and particle size. In Determination of Reactive Surface Area of Melt Glass. Bourcier, W.L., Roberts, S., Smith, D.K., Hulsey, S., Newton, L., Sawvel, A. (eds.) Lawrence Livermore National Laboratory. Livermore, California. pp: 56-76.

Parkhurst, D.L. and Appelo, C.A.J. (1999) User's guide to PHREEQC (Version 2)- A computer program for speciation, batch-reaction, one-dimensional transport, and inverse geochemical calculation. U.S.G.S. Wat.Res.Inv Report. 99-4259.

Perez, A., Rossano, S., Trcera, N., Verney-Carron, A., Huguenot, D., van Hullebusch, E.D., Catillon, G., Razafitianamaharavo, A., Guyot, F. (2015) Impact of iron chelators on short-term dissolution of basaltic glass. Geochimica et Cosmochimica Acta 162. pp. 83-98.

Petit, J.C., Della Méa, G., Dran, J.-C., Magonthier, M.C., Mando, P.A. and Paccagnella, A. (1990) Hydrated-layer formation during dissolution of complex silicate glasses and minerals; Geochim. Cosmochim. Acta 54, 1941-1955.

Rowe, Jr., G.L. and Brantley, S. (1993) Estimation of the dissolution rates of andesitic glass, plagioclase and pyroxene in a flank aquifer of Poás Volcano, Costa Rica, Chemical Geology. Vol 105. 1-3: 71-87.

Schott, J., Oelkers, E.H., Bénézeth, P., Goddéris, Y., François, L. (2012) Can accurate kinetic laws be created to describe chemical weathering? C.R. Geosciences 344: 568-585.

Shade, J.W. (1981) Comparison of glass and ceramic leaching behavior by natural analogs. Nucl. Chem. Waste Manage. 2: 219-228.

Stefánsson, A., Gíslason, S.R. (2001) Chemical weathering of basalts, Southwest Iceland. Effect of rock crystallinity and secondary minerals on chemical fluxes to the ocean. Am. J. Sci. 301, 513–556.

Stillings, L. and Brantley, S. (1995) Feldspar dissolution at 25°C and pH 3: Reaction stoichiometry and the effect of cations. Geochimica et Cosmochimica Acta 59(8): 1483-1496.

Tester, J.W., Worley, W.G., Robinson, B.A., Grigsby, C.O. and Feerer, J.L. (1994) Correlating dissolution kinetics in pure water from 25 to 625°C. Geochim. Cosmochim. Acta 58: 2407-2420.

Vercamer, V. (2016). Spectroscopic and Structural Properties of Iron in Silicate Glasses. PhD thesis. Material chemistry. Université Pierre et Marie Curie - Paris VI, 2016. English. <NNT: 2016PA066077>.<tel-01458771>.

Ward CR, French D (2006) Determination of glass content and estimationof glass composition in fly ash using quantitative X-ray diffractometry. Fuel 85:2268–2277.

White, A.F. (2011) Natural Weathering Rates of Silicate Minerals. US Geological Survey. In: Geochemistry of Earth Surface Systems form the treatise on Geochemistry. Eds. Holland, H.D. and Turekian, K.K. Academic Press. First edition. pp. 205-235.

White, A.F., Brantley, S.L. (2003) The effect of time on the weathering of silicate minerals: why do weathering rates differ in laboratory and field. Chemical Geology 202. pp.479-506.

White A.F. and Blum, A.E. (1995) Effects of climate on chemical weathering rates in watersheds: Geochimica et Cosmochimca Acta, 59, pp 9776-9782.

White A.F & Brantley S.L. (1995) Chemical weathering rates of silicate minerals: an overview. In Chemical Weathering Rates of Silicate Minerals. Eds. White, A.F & Brantley S.L. Reviews in Mineralogy. Volume 31. pp. 1-22.

White, A.F., Claassen, H.C. and Benson, L.V. (1980) The effect of dissolution of volcanic glass on the water chemistry in a tuffaceous aquifer. Rainier Mesa, Nevada, U.S.G.S. Water Supply Paper. 1535-Q.

Wieland, E., Stumm, W. (1992) Dissolution kinetics of kaolinite in acidic aqueous solutions at 25°C. Geochim Cosmochim Acta 56. 3339-3355.

Wilding, M., Webb, S., Dingwell, D., Ablay, G., Marti, J. (1996) Cooling rate variation in natural volcanic glasses from Tenerife, Canary Islands. Contrib Mineral Petrol 125/ 151-160.

Winburn RS, Grier DG, McCarthy GJ, Peterson RB (2000) Rietveld quantitative X-ray diffraction analysis of NIST fly ash standard reference materials. Powder Diffract 15:163–172.

Wolff-Boenisch, D., Gislason, S.R., Oelkers, E.H. (2006) The effect of crystallinity on dissolution rates and CO_2 consumption capacity of silicates. Geochimica et Cosmochimica Acta 70. 858-870.

Wolff-Boenisch, D., Gislason S. R., Oelkers, E. and Putnis, C.V. (2004) The dissolution rates of natural glasses as a function of their composition at pH 4 and 10.6 and temperatures from 25 to 74°C. Geochimica et Cosmochimica Acta, Vol.68, No. 23, pp 4843-4858.

Yang, W. H. and Kirkpatrick, r. (1989) Hydrothermal reaction of albite and a sodium aluminosilicate glass: A solid-state NMR study. Geochim. Cosmochim. Acta 53: 805-819.

Appendix 5.1. Chemical and mineralogical composition of the samples presented in this study

Table A.5.1. Bulk chemical compositions of the samples used in this study
Calculated from the elemental composition presented by Ayris, (2010).

	Chemical composition (wt. %)					
Sample	**ETNA**		**UNZEN**		**LIPARI**	
Origin	Mt. Etna, Italy		Mt. Unzen, Japan		Lipari, Italy	
Year of eruption	2002		1991		729	
Element	**ET-R**	**ET-G**	**UZ-R**	**UZ-G**	**LP-R**	**LP-G**
SiO_2	46.8	44.9	56.1	60.4	62.9	67.2
Al_2O_3	15.7	16.2	14.1	14.8	11.9	12.5
CaO	10.3	11.0	4.5	4.5	0.8	0.7
Fe_2O_3	11.1	13.2	5.7	4.6	1.8	1.8
K_2O	2.1	2.3	2.1	2.3	4.0	5.5
MgO	6.3	6.5	3.1	2.3	0.0	0.0
Na_2O	3.6	3.5	3.3	3.5	3.9	3.7
P_2O	0.6	0.6	0.3	0.0	0.0	0.0
TiO_2	1.8	1.8	0.7	0.7	0.0	0.0

Table A.5.2. Mineralogy of the rock samples.

	WEIGHT %					
	Amorphous	**Crystalline**				
Sample	**Glass**	**Pl**	**Px**	**Ol**	**Ox**	**Am**
ET-R	18	42	26	5	7	-
UZ-R	28	51	8	-	--	11
LP-R	>95	-	-	-	-	-

Pl: plagioclase, Px: pyroxene, Ol: olivine, Ox: Fe-Ti oxides, Am: amphibole.

Table A.5.3. Chemical formula of the rocks and glasses presented in this study.

Sample	**Chemical Formula**
ET-R	$Al_{0.40}Ca_{0.24}Fe_{0.18}K_{0.06}Mg_{0.20}Na_{0.15}SiO_{3.49}$
ET-G	$Al_{0.43}Ca_{0.26}Fe_{0.22}K_{0.07}Mg_{0.21}Na_{0.15}SiO_{3.60}$
UN-R	$Al_{0.30}Ca_{0.09}Fe_{0.08}K_{0.05}Mg_{0.08}Na_{0.11}SiO_{3.07}$
UN-G	$Al_{0.29}Ca_{0.08}Fe_{0.06}K_{0.05}Mg_{0.06}Na_{0.11}SiO_{2.79}$
LP-R	$Al_{0.22}Ca_{0.01}Fe_{0.02}K_{0.08}Na_{0.12}SiO_{2.82}$
LP-G	$Al_{0.22}Ca_{0.01}Fe_{0.02}K_{0.10}Na_{0.11}SiO_{2.54}$

Appendix 5.2. Particle size distribution of the samples used in this study

Table A.5.4. D10, D50 and D90 of the samples obtained from the particle size distribution.

Sample	D_{10} [m] x 10^{-6}	D_{50} [m] x 10^{-6}	D_{90} [m] x 10^{-6}
ET-R	70	97	133
ET-G	63	95	140

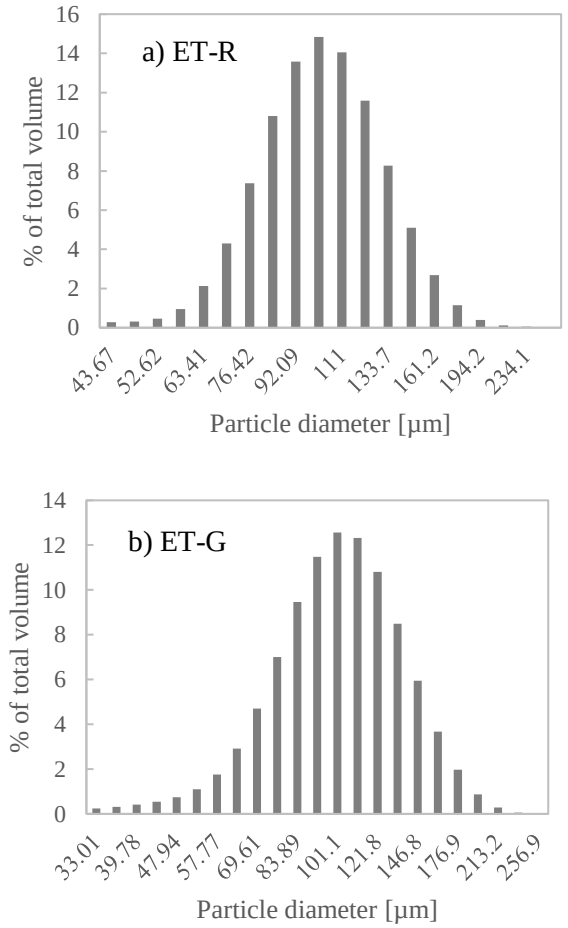

Figure A.5.1. Particle size distribution of the samples used in this study: (a) ET-R (basalt/rock), (b) ET-G (basalt/glass), (c) UZ-R (dacite/rock), (d) UZ-G (dacite/glass), (e) LP-R (rhyolite/obsidian) and (f) LP-G (rhyolite/glass).

Table A.5.4 (continued). D10, D50 and D90 of the samples obtained from the particle size distribution.

Sample	D_{10} [m] x 10^{-6}	D_{50} [m] x 10^{-6}	D_{90} [m] x 10^{-6}
UN-R	65	98	134
UN-G	64	95	130

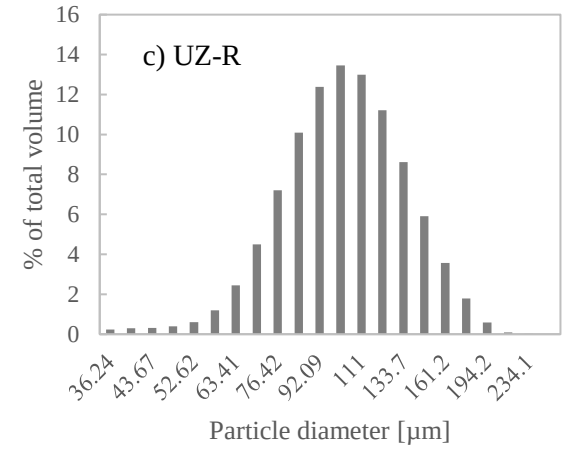

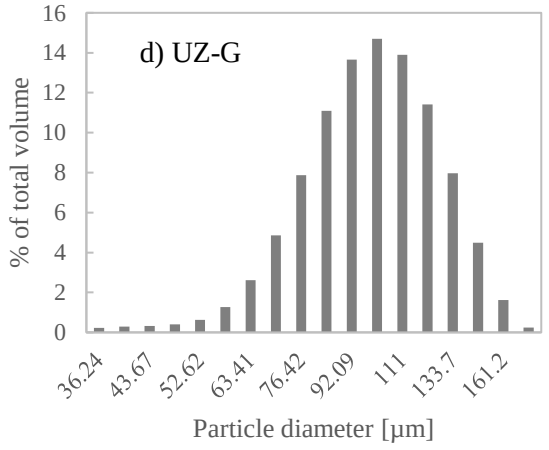

Figure A.5.1 (continued). Particle size distribution of the samples used in this study: (a) ET-R (basalt/rock), (b) ET-G (basalt/glass), (c) UZ-R (dacite/rock), (d) UZ-G (dacite/glass), (e) LP-R (rhyolite/obsidian) and (f) LP-G (rhyolite/glass).

Table A.5.4 (continued). D10, D50 and D90 of the samples obtained from the particle size distribution.

Sample	D_{10} [m] x 10^{-6}	D_{50} [m] x 10^{-6}	D_{90} [m] x 10^{-6}
LP-R	70	101	145
LP-G	23	78	125

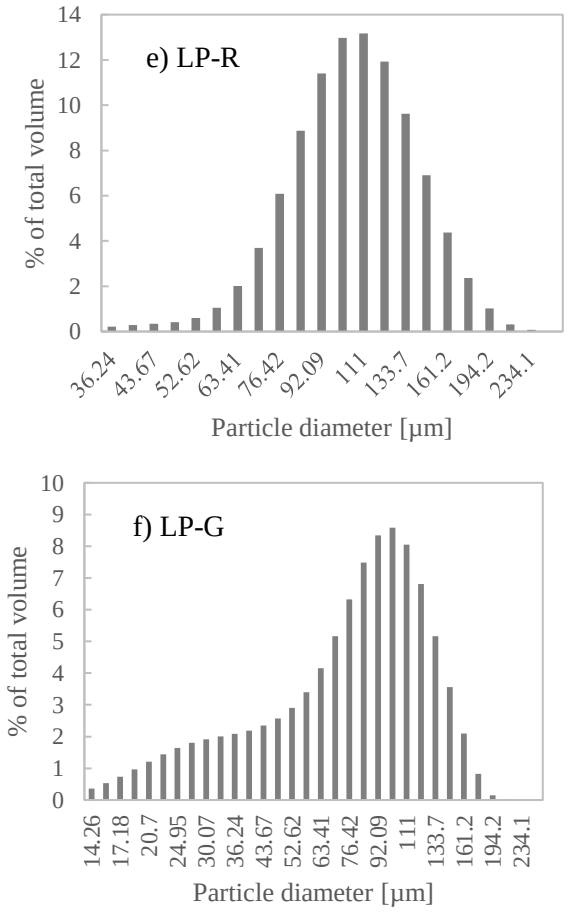

Figure A.5.1 (continued). Particle size distribution of the samples used in this study: (a) ET-R (basalt/rock), (b) ET-G (basalt/glass), (c) UZ-R (dacite/rock), (d) UZ-G (dacite/glass), (e) LP-R (rhyolite/obsidian) and (f) LP-G (rhyolite/glass).

Appendix 5.3. Study of the variation of the geometric specific surface area

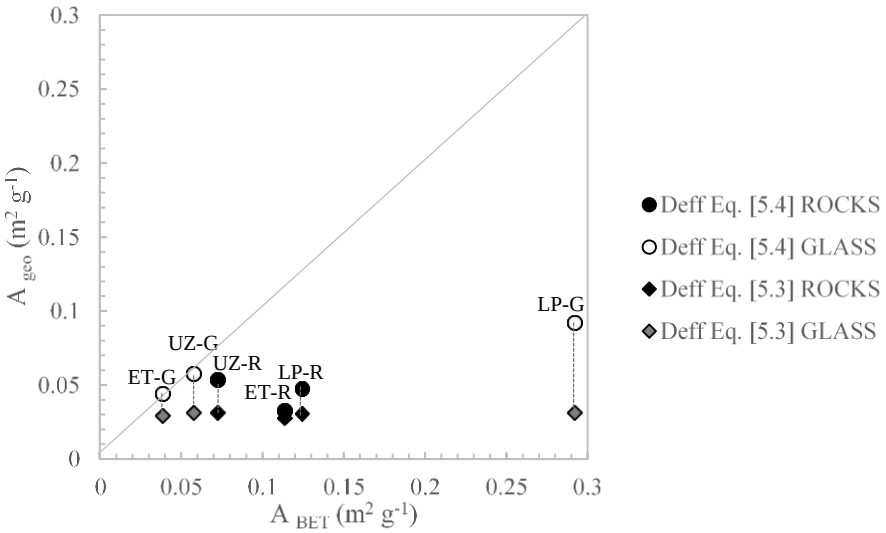

Figure A.5.2. Comparison between the A_{geo} (m^2 g^{-1}) versus the A_{BET} (m^2 g^{-1}) for the samples used in this study. Additionally, a second estimate is also presented for the values of A_{geo} (m^2 g^{-1}) using Eq. [5.3] instead of the initial Eq. [5.4] in order to present the difference between the methods to obtain D_{eff}.

Appendix 5.4. Average compositions of groundmass glass, plagioclase, pyroxene and amphibole in a dacite from Mt. Unzen eruption (1991)

Table A.5.5. Chemical compositions of the main components (groundmass glass, plagioclase, pyroxene, and amphibole) found in a dacite from Mt. Unzen eruption (1991).

Taken from Nakada and Motomura (1999) and Holtz et al. (2005).

	Chemical composition (wt. %)			
Element	**Groundmass glass**	**Plagioclase**	**Pyroxene**	**Amphibole**
SiO_2	74.4	55.1	52.3	46.4
Al_2O_3	11.2	28.4	1.9	8.0
CaO	1.1	11.8	20.9	11.0
FeO	1.4	0.5	5.9	13.9
K_2O	4.0	0.4	0.0	0.5
MgO	0.3	0.1	16.5	13.5
Na_2O	2.8	3.8	0.2	1.3
TiO_2	0.4	0.06	0.3	1.2

CHAPTER 6 Experimental dissolution study of polycrystalline volcanic rocks (basalt-andesite-dacite-rhyolite) from 2≤pH≤5 at 20 °C

6.1. INTRODUCTION

Quantification and understanding of mineral weathering have important implications for many environmental problems, such as the relationship between silicate weathering and global climate over geological timescales (Berner, 1992). The atmospheric CO_2 consumption by chemical weathering of Ca- Mg silicate rocks has a direct link with global climate (Beaulieu et al., 2012) as demonstrated by laboratory experiments (Pronost et al., 2011), field test (Matter et al., 2011) and geochemical modelling (Goddéris et al., 2013). The application of geochemical models opens a new perspective to quantify weathering in future scenarios. Nowadays, the challenge for geoscientists is to determine most accurate parametric laws to describe weathering of aluminosilicates derived either from field observations or from laboratory (Goddéris and Brantley, 2013).

Both experimental and field-based approaches have been used to quantify silicate weathering rates. The advantages of the experimental approach are that chemical, physical and biological conditions are tightly constrained and individual parameters, such as mineral compositions, temperature, surface area, and solute composition, are systematically varied to characterize weathering mechanisms (Lasaga, 1998). The principal disadvantage is that such experiments commonly react freshly prepared silicate minerals over relatively short time intervals, thus producing uncertainties when experimental rates are extrapolated to natural weathering environments. (White and Brantley, 2003).

Weathering rates of aluminosilicates have been extensively quantified in the latest years, either for silicate minerals or for natural and synthetic glasses. The laboratory rate equations reported for dissolution rates of minerals are usually used as input data in geochemical modelling codes to assess the temporal evolution of fluids during water-rock interaction both in natural systems and in industrial processes (Goddéris et al., 2009). Regarding the dissolution of pure minerals, Palandri et al. (2004) have compiled kinetics parameters for over 70 minerals, including for all the major classes of silicates. Those rate parameters are for surface controlled reactions at conditions that are far from equilibrium, mainly pure minerals. In the case of more complex mineral arrangements, like plagioclase solid solutions/exsolutions, the study of Gudbrandsson et al. (2014) is presented an attempt to determine

experimentally the dissolution rates of plagioclase as a function of their composition using mixed-flow reactor techniques.

In terms of glass dissolution just to mention the work done on basaltic and borosilicate glasses (e.g., Guy and Schott, 1989; Oelkers and Gislason, 2001; Gislason and Oelkers, 2003) and rhyolitic volcanic glasses (Yokoyama and Banfield, 2002, Declerq et al., 2013) using flow through systems. There are also studies of glass leaching behavior in order to understand the role of glass in natural process (Cailleteau et al.,2008) and the potential utility as nuclear waste host (Rajmohan et al., 2010).

As it has been presented, there is a plethora of dissolution studies performed on individual minerals and glasses, however the studies focused on polycrystalline and poly-mineral rocks are less frequent among dissolution studies. In fact, most extrusive igneous rocks are polycrystalline rocks, and much less is known. Accounting for multi-mineral rock dissolution studies, we could mention the work done on a metabasalt (actinolite and chlorite) by Critelli et al. (2014), on serpentinite (antigorite and magnetite) by Critelli et al. (2015), on a multi-mineral sediment (quartz, smectite, plagioclase and K-feldspar) by Beckingham et al. (2016, 2017), on carbonate rich shale (calcite, illite, quartz) by Deng et al. (2017), on carbonate rock (calcite and dolomite) by Levenson et al. (2017), on organic rich shale (calcite, quartz, kaolinite) by Kreisserman and Emmanuel (2018).

In this study we focused on the chemical weathering of igneous volcanic rocks, as a proxy to better understand the dissolution of a polycrystalline rock, incorporating the current data available in literature for laboratory dissolution rates of aluminosilicates. In case of volcanic igneous rocks, according to the degree of crystallization, it is possible to identify mineral crystals embedded in a glassy matrix, whose proportion is governed by the rate of cooling, composition and viscosity of the parent magma (Hyndman, 1985). Thus, taking into account the presence of these two main components of the rock (amorphous and crystalline); we assessed how well the reported rates of individual minerals can describe the whole rock dissolution, and then we analyzed if the dissolution rates of igneous extrusive polycrystalline rocks can be inferred from their individual components. Towards this goal in this study, whole rock dissolution experiments of four different specimens of volcanic rocks were performed in a fluidized bed reactor.

6.2. MATERIALS AND METHODS

6.2.1. Characterisation of the crystalline rock samples

We measured the dissolution rates of four crystalline igneous rocks corresponding to a basalt, an andesite, a dacite and a rhyolite. The chemical composition of each rock is detailed in Appendix 6.1. The mineralogy of each rock was determined by X-ray powder diffraction using a Bruker D8 Advance instrument operated at 40 kV and 20 mA, with a step width of 0.02° and counting time of 2.0 s $step^{-1}$, using Kα radiation sourced from a Cu target anode. All samples were ground to fine powders in an agate mortar prior to analysis. Crystalline minerals were identified using the EVA© software the semi-quantification of crystalline mineral phases based on diffractogram analyses were performed with SIROQUANT software (Hill et al., 1993; Bish, 1993; Gonzalez et al., 2003). The glass content of the crystalline rocks was estimated by spiking the sample with 10 wt. % of an internal standard, i.e metallic Si, followed by re-analysis under the same XRD operating conditions (Winburn et al., 2000; Ward and French, 2006; Paque et al., 2016). The accuracy in the weight percent determinations of the rock's glass and major crystalline components is in the range 5–10% (Paque et al., 2016). The mineralogy of the four rocks is reported in Table 6.1 and a more detailed geochemical description of each rock is provided in Appendix 6.1, the X-ray diffractograms of the samples are presented in Appendix 6.7.

Table 6.1. Mineralogy and specific surface area (A_{BET}) of the basalt, andesite, dacite and rhyolite rocks.

Rock	Origin	Glass	Plagioclase	Pyroxene	Olivine	Amphibole	Fe-Ti oxides	Apatite	A_{BET}
		wt.%							$m^2 g^{-1}$
Basalt	Katla volcano, Iceland	24.0	36.4	28.3	4.1		6.8		0.216
Andesite	Tungurahua volcano, Ecuador	36.8	48.4	11.8	2.7				0.094
Dacite	Guagua Pichincha volcano, Ecuador	31.7	52.4	5.7		9.1		1.1	0.126
Rhyolite	Puyehue volcano, Chile	64.4	30.3	3.7			1.6		0.096

Prior to the dissolution experiments, the rocks and glasses were crushed by wrapping them in several polyethylene plastic bags and careful hammering. The crushed material was then dry sieved in order to retain particles within the 63-100 µm size range. This fraction was ultrasonically cleaned in ethanol several times until no suspended fine material remains after decantation. The cleaned samples were dried overnight at 50 °C. The specific surface area of the rock powders was measured by gas adsorption using the three point Brunauer, Edward and Teller method (A_{BET}; Brunauer et al., 1938). Since powdered fresh silicate rocks and glasses generally display low specific surface areas <1 $m^2\ g^{-1}$ (Brantley and Mellott, 2000), Kr was the adsorbate gas (American Society for Testing and Materials, 2015). The A_{BET} values are given in Table 6.1.

6.2.2. Dissolution experiments

The dissolution experiments were carried out in a fluidized bed reactor at 20 °C. The dissolution reactor consisted of 50 mL polypropylene pipettes equipped with a circulation pump (Watson Marlon 90 rpm) to keep the material in suspension (~14 mL min^{-1}) (see Chapter 3 for details of the dissolution reactor). The solution was pumped through the reactor at a constant rate of 0.4 mL min^{-1} using a peristaltic pump (Miniplus 2 GILSON). All dissolution experiments were performed at pH values of 2, 3 and 5 and an ionic strength, I, of 10 mM. The acid inlet solutions were prepared with Millipore™ water and Merck analytical grade NH_4Cl and HCl. Composition of all inlet solution are listed in Table A.6.9. The concentrations of cations released during the dissolution experiment were ≤5% than the ionic strength of the inlet solution, i.e. I did not change significantly. About 0.5 g of dry rock or glass was precisely weighed and introduced in the reactor.

The dissolution reactor was thoroughly cleaned prior to each dissolution experiment by circulating a 0.1 mol L^{-1} HCl solution during 48 hours. The desired pH inlet solution was then allowed in the reactor for at least another 24 hours. The presence of pollution (external source of Si, Al, Fe, Ca, Mg, Na and K) in the output solution was then checked by Inductively Coupled Plasma-Atomic Emission Spectroscopy (ICP-AES). The dissolution experiment could then begin. About 0.5 g (precisely weighed) of dry rock or glass powder was introduced in the reactor and the outlet solution was collected after 24, 48, 72, 96, 120, 150, 175 and 200 h (the steady state dissolution was reached before 200 h in all our dissolution experiments). Then, the output solution was filtered through a 0.2 µm hydrophilic polypropylene membrane filter and analysed for Si, Al, Fe, Ca, Mg, Na and K by Inductively Coupled Plasma-Atomic Emission Spectroscopy (ICP-AES).

The detection limit was 10 µg $L^{-1}$for Si, Na, K and S, 4 µg L^{-1} for Mn, 3 µg L^{-1} for Fe, 2 µg L^{-1} for Al, 1.5 µg L^{-1} for Mg and 0.8 µg L^{-1} for Ca. The error on the ICP-AES analytical measurements was estimated about 1.5% (<50 ppb) and 0.5% (50-200 ppb). The concentration of the studied cations in the blank solution (pH 4 without rock-glass sample) was: Si 17±2 µg L^{-1}; Ca 5.7±1 µg L^{-1}; Na 3±2 µg L^{-1}. Speciation calculations performed with the geochemical model PHREEQC 2.6 (Parkhust and Appelo, 1999) indicated that all output solutions were undersaturated with respect to any mineral phases. Each dissolution experiment was conducted in triplicates.

6.2.3. Calculations

Experimental dissolution rates

The concentration of Si in the output solutions were used to calculate the far-from-equilibrium steady state dissolution rates (r in mol m^{-2} s^{-1}):

$$r = \frac{C_{Si} \cdot f}{A \cdot m} \quad [6.1]$$

where C_{Si} (mol L^{-1}) designates the aqueous Si concentration in the output solution at certain time minus the blank concentration at the beginning of the experiment, f (L s^{-1}) represents the fluid flow rate, A (m^2 g^{-1}) and m (g) refer to the specific surface area and mass of the solid placed in the reactor, respectively. The surface area used throughout this study was obtained from BET analysis (A_{BET}).

Theoretical dissolution rates

We surmise that the steady state, far-from-equilibrium dissolution rates measured for the basalt, andesite, dacite and rhyolitic rocks at pH 2, 3 and 5 can be estimated by combining the dissolution rates of their constitutive glass and mineral components. The expression of the theoretical dissolution rate, noted r^*, takes the following form (Gudbrandsson et al., 2011):

$$r^* = \sum_{i=0}^{N} x_i \, r_i^* \quad [6.2]$$

where r_i^* (mol m^{-2} s^{-1}) is the dissolution rate of the rock's ith component (glass, plagioclase, pyroxene, etc.) and x_i is the relative surface area of the rock's ith component, i.e. the ratio of its specific surface area to the total BET surface area A of the cleaned powdered rock. As a first estimate, x_i is approximated by distributing A among its glass and mineral components as a

function of their volume fraction. This approach parallels that adopted in previous studies (Gudbrandsson et al., 2011; Critelli et al., 2014). The mineral volumetric fractions of the basalt, andesite, dacite and rhyolite rocks are reported in Table A.6.10. The mineralogy of our rock samples varies but the assemblage glass + plagioclases ± pyroxenes typically represents ≥89% of the total rock mass (Table 6.1). Therefore, we posited that the dissolution of these components drives the rate at which the rock dissolves, i.e. the contribution to Si release from dissolution of the minor mineral phases present in the rock is neglected in Eq. [6.2].

The individual dissolution rates of the glass, plagioclase and pyroxene (if any) constituents present in the crystalline rocks can be computed from existing rate laws established for temperature, pH and ionic strength conditions comparable to our experimental measurements (Table A.6.11, Gislason and Oelkers, 2003; Declerq et al., 2013; Gudbrandsson et al., 2014; Palandri et al., 2014). Thus, Eq. [6.2] can be rewritten as:

$$r^* = \left[x_{glass} \cdot 10^{-5.6}\, e^{-\left(\frac{25.5}{R \cdot T}\right)} \left(\frac{a_{H^+}^3}{a_{Al^{3+}}} \right)_{glass}^{\frac{1}{3}} \right] + \left[x_{plagio} \cdot 10^{-(0.033\ An\% + 14.77)} \left(\frac{a_{H^+}^3}{a_{Al^{3+}}} \right)_{plagio}^{(0.004\ An\% + 0.05)} \right] + \left[x_{pyrox} \cdot 10^{-\left(9.02 + \frac{80.0\ x\ 10^3}{2.3025\ RT} + 0.60\ pH\right)} \right] \quad [6.3]$$

where R (J mol^{-1} K^{-1}) is the gas constant, T (K) the temperature and a_{H^+} and $a_{Al^{3+}}$ the aqueous activity of $H^+$and Al^{3+}, respectively. Since the dissolution experiments were conducted at fixed pH conditions, a_{H^+} is known. We use the geochemical code PHREEQC (Parkhust and Appelo, 1999) to compute $a_{Al^{3+}}$ in the outlet solution at steady state.

As indicated in Appendix 6.1, the composition of the glassy component is basaltic, andesitic and rhyolitic in the basalt, andesite and dacite and rhyolite rocks, respectively. Since the dissolution kinetics of andesitic glass is not known, dissolution of the andesite's glass component was approximated based on the rate law of rhyolitic glass as given by Declerq et al. (2013). Plagioclase is a continuous solid solution series with endmembers represented by albite ($NaAlSi_3O_8$) and anorthite ($CaAl_2Si_2O_8$). Using previous petrological descriptions of the studied rocks (see Appendix 6.1), we represent the plagioclase constituent as a simple mixture of albite and anorthite in known proportions. For pyroxenes, as presented in Appendix 6.1., we represented them as a simple mixture of enstatite and wollastonite in know proportions.

6.3. RESULTS

6.3.1. Composition of the output solutions

The concentrations of Si, Al, Ca, Mg, Na and K measured at the different time points in the output solutions are shown in Figure 6.1 (a-g). The data are also presented in Appendix 6.5. Irrespective of the pH of the input solution, the dissolution of the basalt and andesite rocks produced much larger (one to two orders of magnitude) concentrations of Si in the output solutions compared to the dissolution of the dacite and rhyolite. The basalt rock released also more Si than the andesite. At pH 2, there was a rapid initial release of Si transitioning to a slower and steadier release over time.

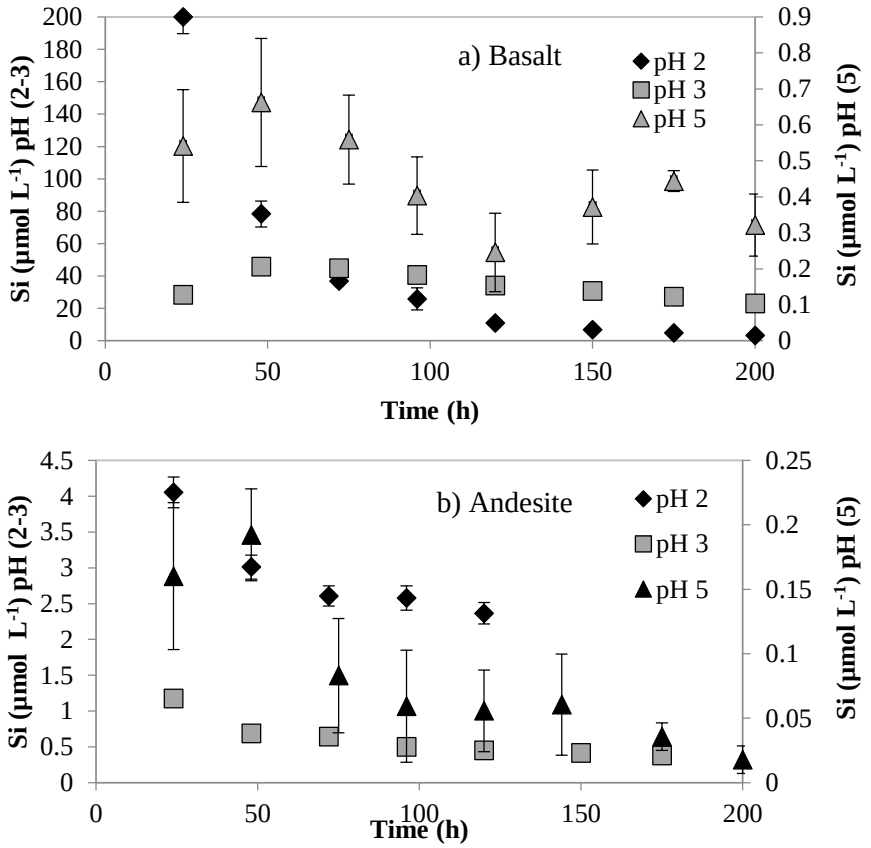

Figure 6.1 (a). Release of Si (µmol L^{-1}) for rock dissolution at 20 °C and pH 2, 3 and 5 as a function of time for the (a) basalt (b) andesite (c) dacite and (d) rhyolite rocks.

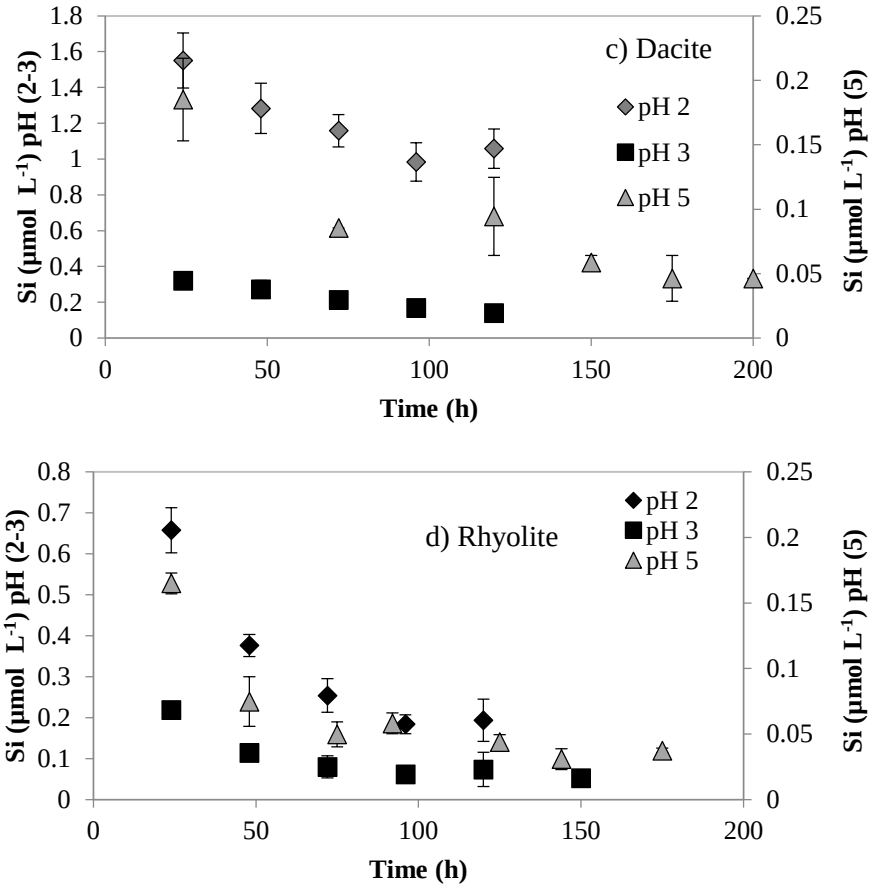

Figure 6.1 (a) (continued). Release of Si (µmol L^{-1}) for rock dissolution at 20 °C and pH 2, 3 and 5 as a function of time for the (a) basalt (b) andesite (c) dacite and (d) rhyolite rocks.

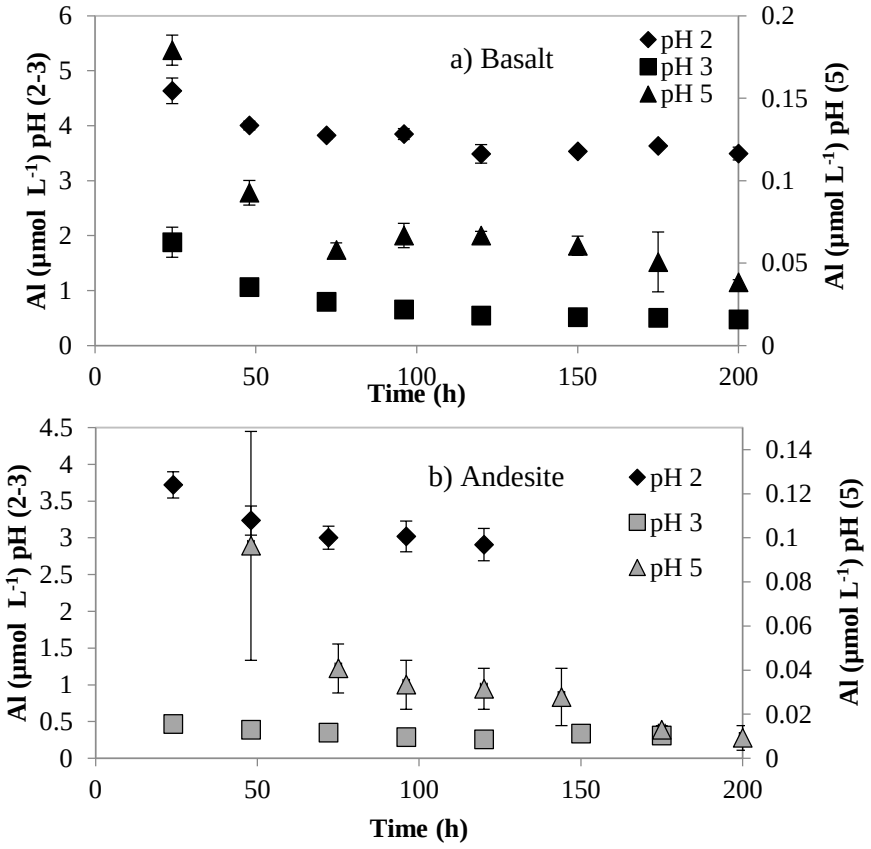

Figure 6.1 (b). Release of Al (µmol L^{-1}) for rock dissolution at 20 °C and pH 2, 3 and 5 as a function of time for the (a) basalt (b) andesite (c) dacite and (d) rhyolite rocks.

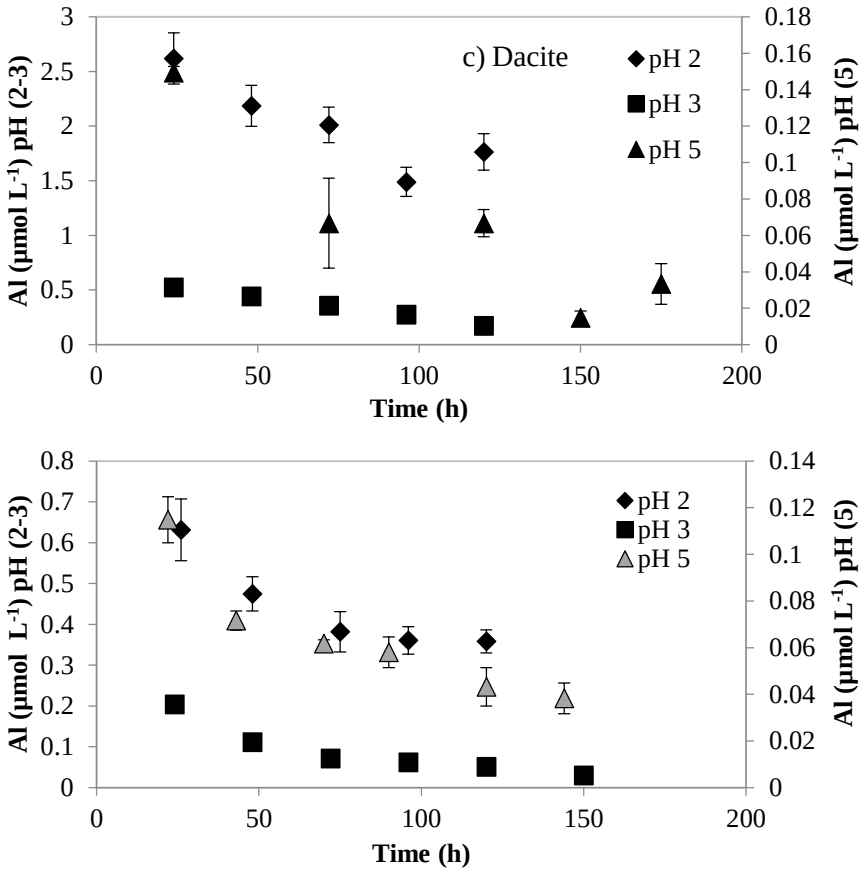

Figure 6.1 (b) (continued). Release of Al (µmol L^{-1}) for rock dissolution at 20 °C and pH 2, 3 and 5 as a function of time for the (a) basalt (b) andesite (c) dacite and (d) rhyolite rocks.

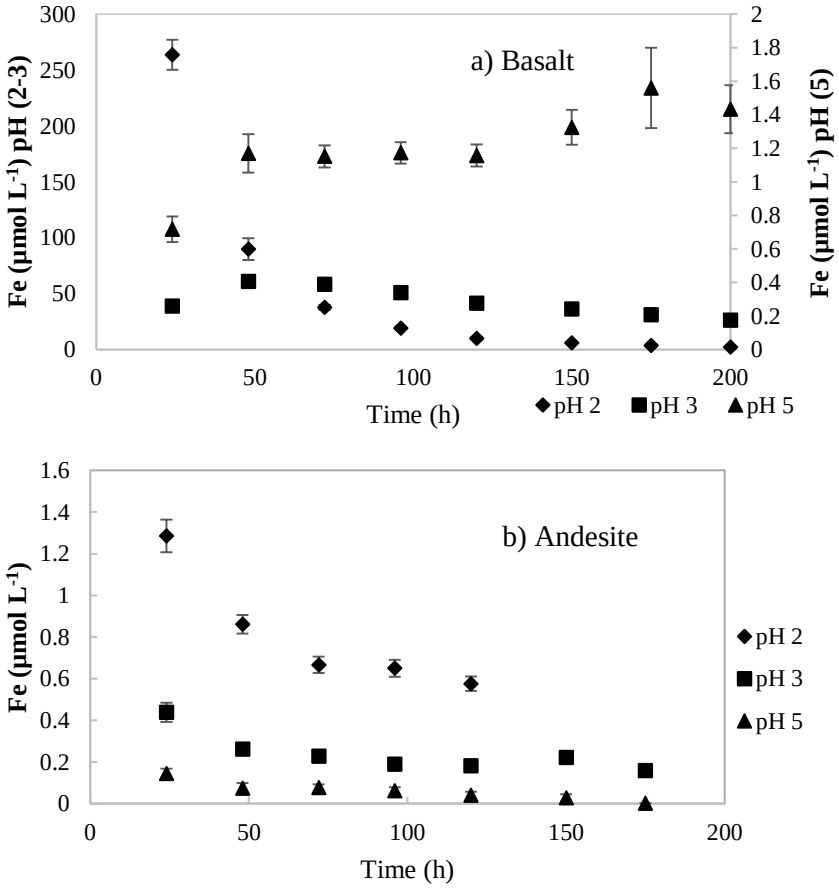

Figure 6.1 (c). Release of Fe (µmol L^{-1}) for rock dissolution at 20 °C and pH 2, 3 and 5 as a function of time for the (a) basalt (b) andesite (c) dacite and (d) rhyolite rocks.

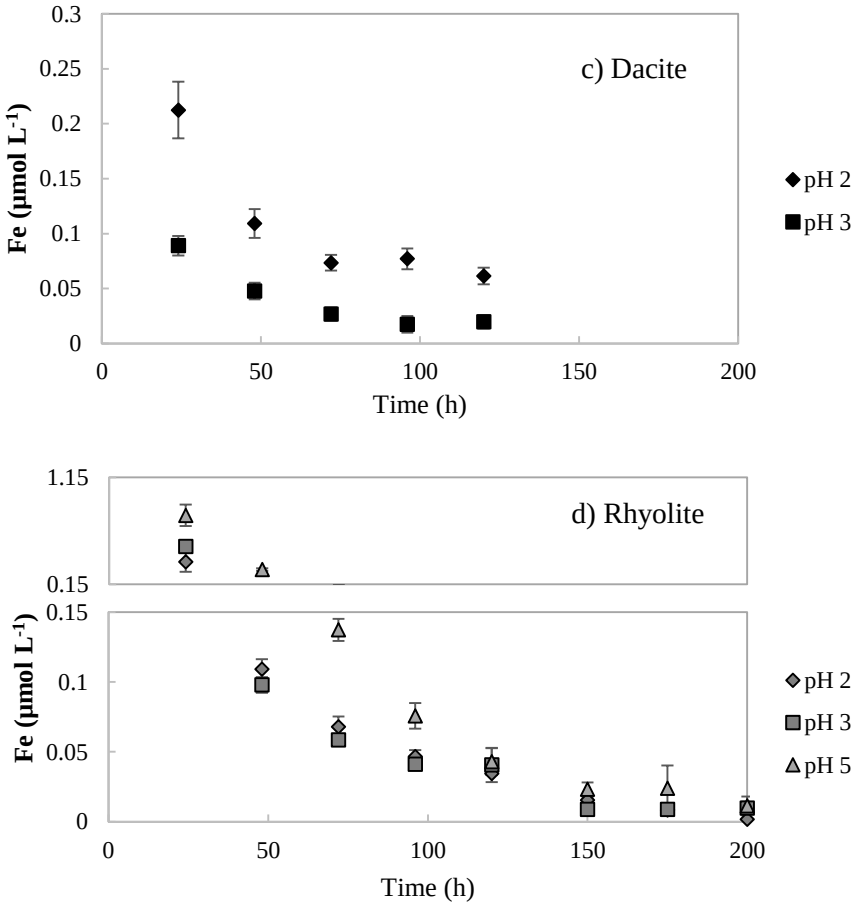

Figure 6.1 (c) (continued). Release of Fe (µmol L^{-1}) for rock dissolution at 20 °C and pH 2, 3 and 5 as a function of time for the (a) basalt (b) andesite (c) dacite and (d) rhyolite rocks.

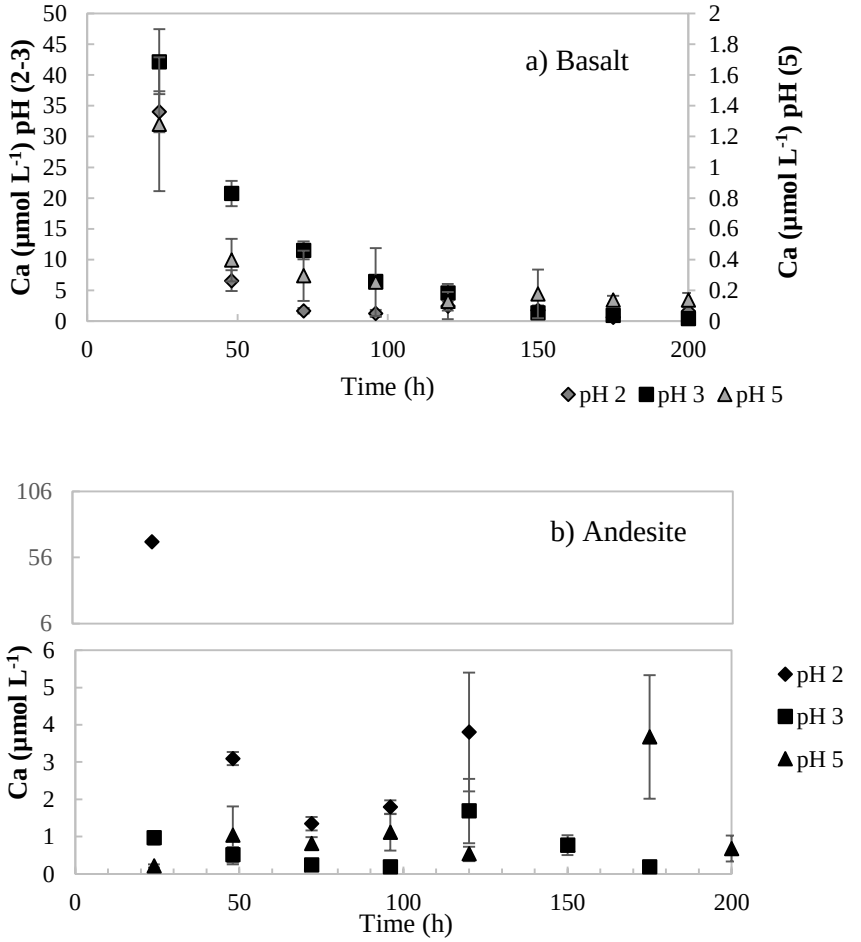

Figure 6.1 (d). Release of Ca (µmol L^{-1}) for rock dissolution at 20 °C and pH 2, 3 and 5 as a function of time for the (a) basalt (b) andesite (c) dacite and (d) rhyolite rocks.

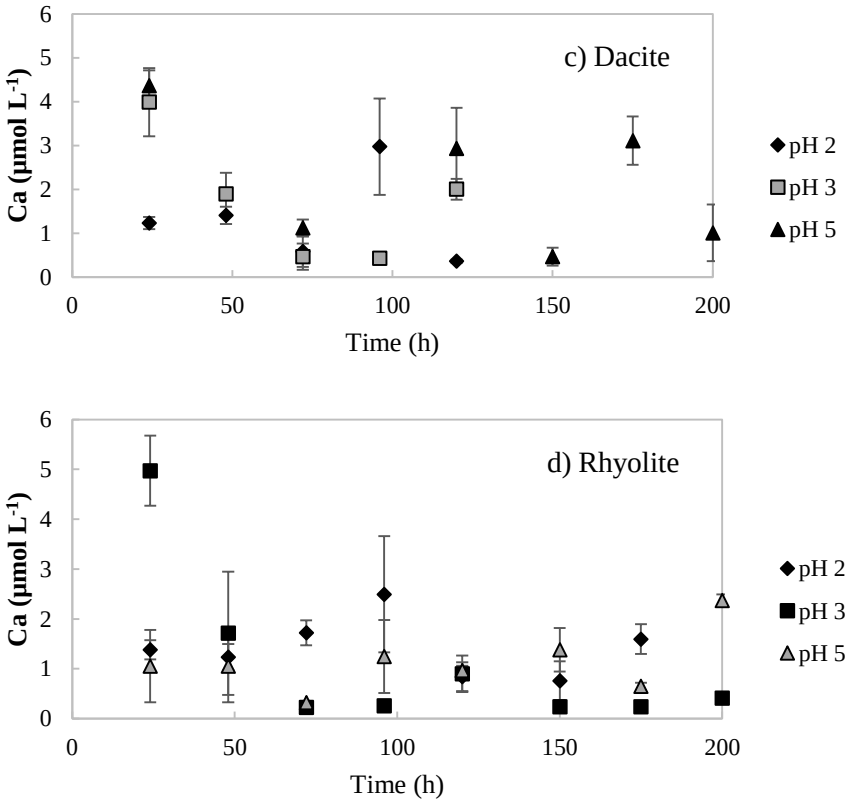

Figure 6.1 (d) (continued). Release of Ca (µmol L^{-1}) for rock dissolution at 20 °C and pH 2, 3 and 5 as a function of time for the (a) basalt (b) andesite (c) dacite and (d) rhyolite rocks.

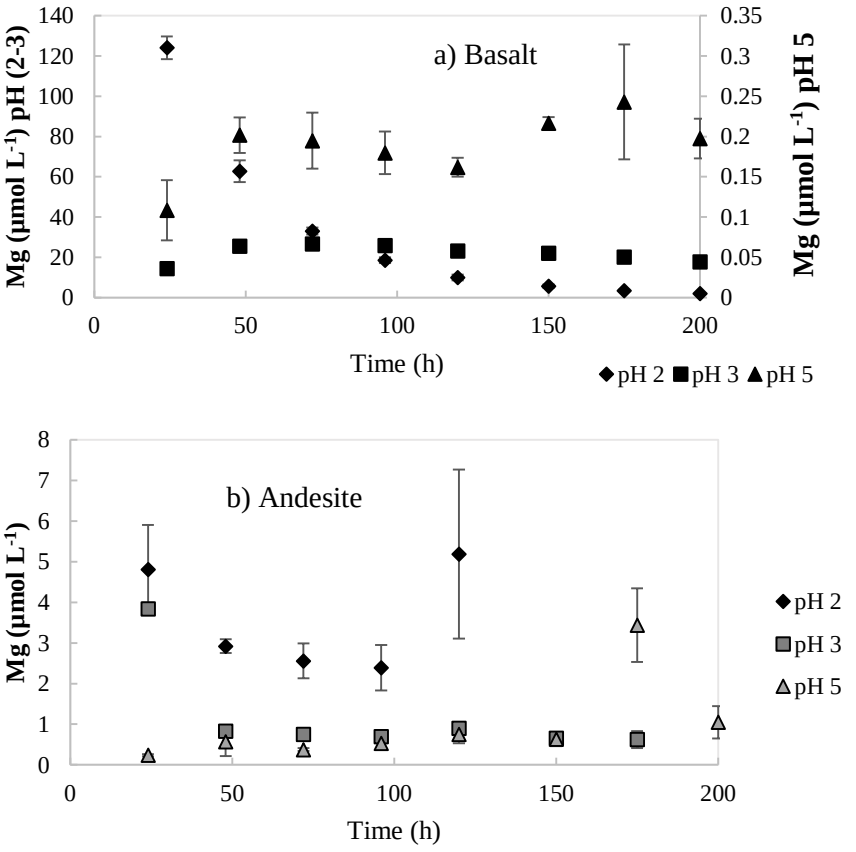

Figure 6.1 (e). Release of Mg (µmol L^{-1}) for rock dissolution at 20 °C and pH 2, 3 and 5 as a function of time for the (a) basalt (b) andesite (c) dacite and (d) rhyolite rocks.

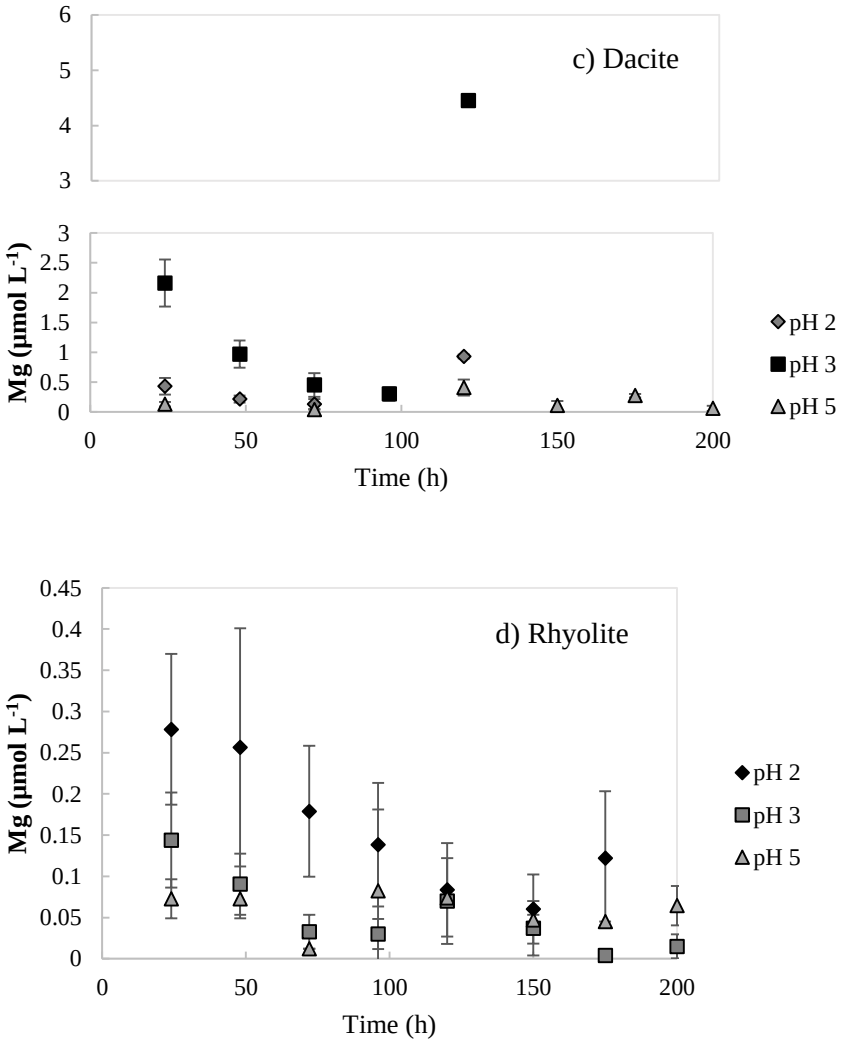

Figure 6.1 (e) (continued). Release of Mg (µmol L^{-1}) for rock dissolution at 20 °C and pH 2, 3 and 5 as a function of time for the (a) basalt (b) andesite (c) dacite and (d) rhyolite rocks.

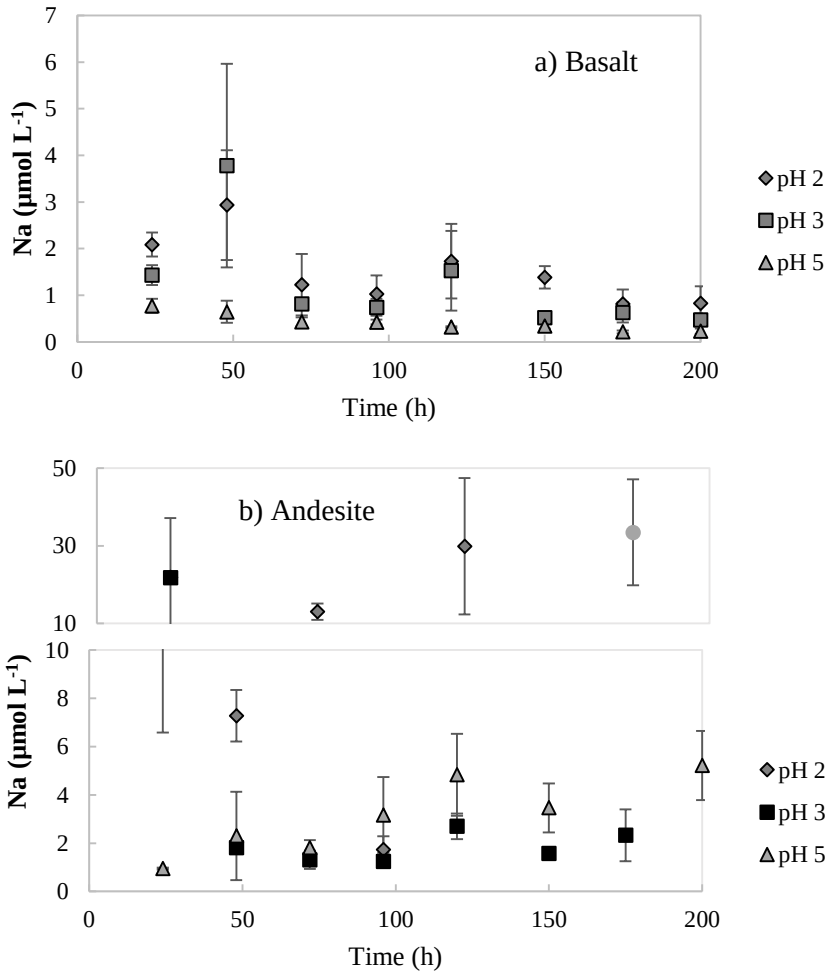

Figure 6.1 (f). Release of Na (µmol L^{-1}) for rock dissolution at 20 °C and pH 2, 3 and 5 as a function of time for the (a) basalt (b) andesite (c) dacite and (d) rhyolite rocks.

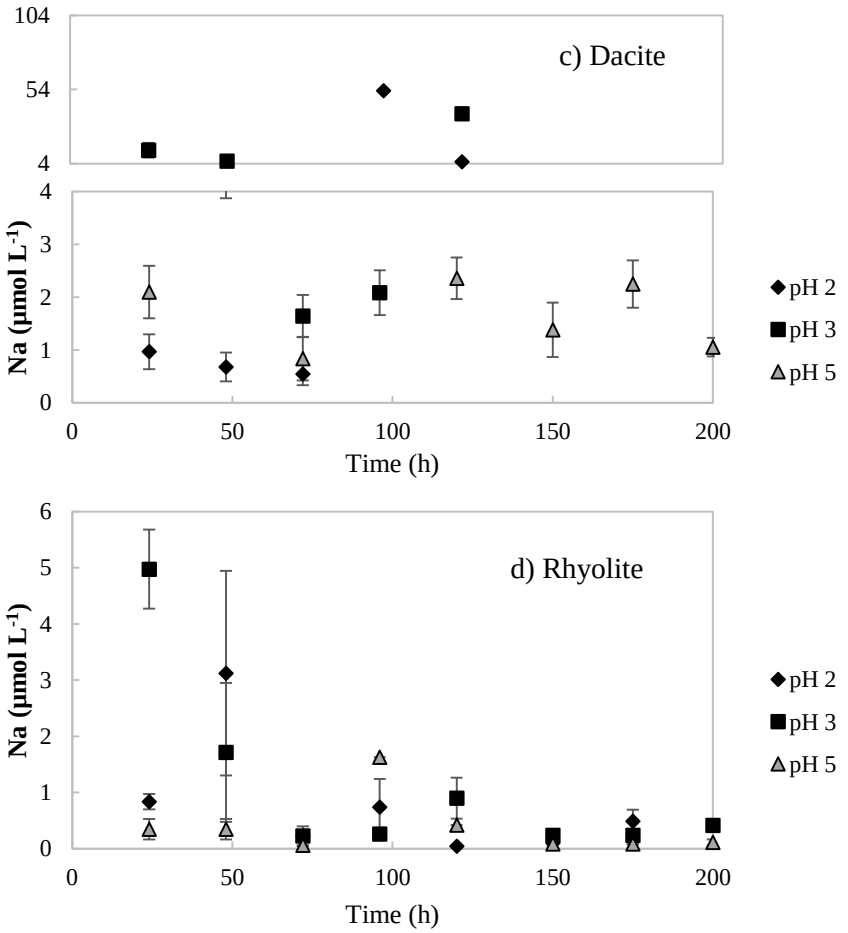

Figure 6.1 (f) (continued). Release of Na (µmol L^{-1}) for rock dissolution at 20 °C and pH 2, 3 and 5 as a function of time for the (a) basalt (b) andesite (c) dacite and (d) rhyolite rocks.

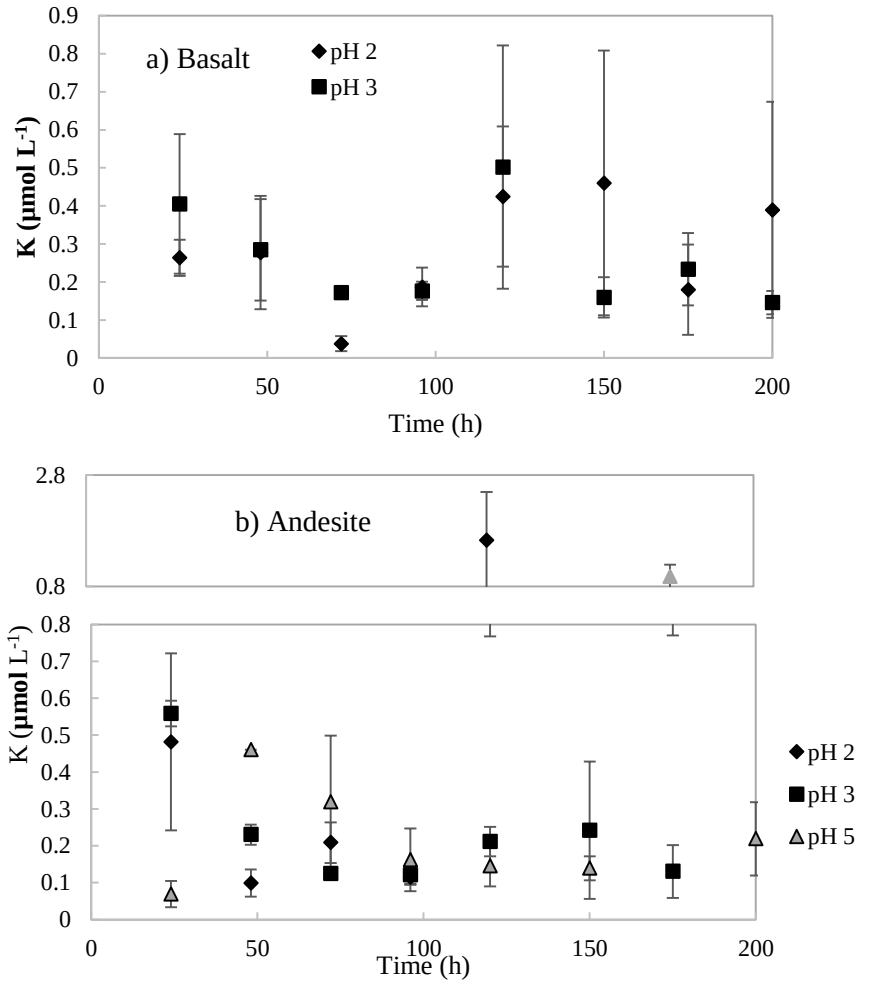

Figure 6.1 (g). Release of K (µmol L^{-1}) for rock dissolution at 20 °C and pH 2, 3 and 5 as a function of time for the (a) basalt (b) andesite and (c) dacite rocks.

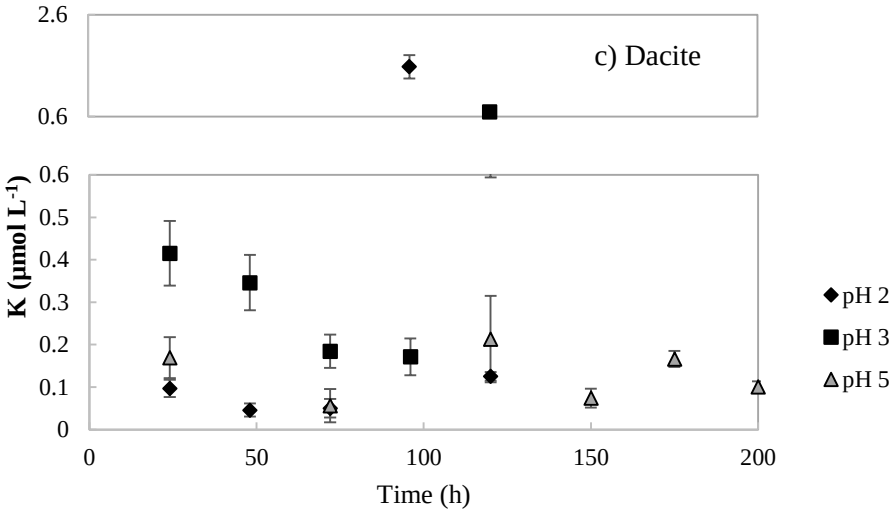

Figure 6.1 (g) (continued). Release of K (µmol L^{-1}) for rock dissolution at 20 °C and pH 2, 3 and 5 as a function of time for the (a) basalt (b) andesite and (c) dacite rocks.

Steady-state Si and Al release rates were achieved between 100 and 200 h of dissolution, depending on pH (Fig. 6.1.a and 6.1.b). At steady-state, the concentration of Si in the output solutions from the andesite and dacite subjected to dissolution at pH 2 remained higher than those obtained at pH 3 and 5. This was not the case for the basalt and rhyolite rocks. The release of Al during rock dissolution was always highest at pH 2. The evolution of the concentrations of Ca, Mg, Na and K in the output solutions over time was more erratic and no simple pattern could be inferred. This may reflect cation-proton exchange reactions occurring on the surfaces of the rock's mineral and glass constituents (Oelkers et al., 2009). The saturation state of the output solution with respect to mineral phases was computed at steady-state using PHREEQC. The results of these calculations indicate that all output solutions were undersaturated with respect to any mineral phases.

6.3.2 Experimental and theoretical dissolution rates

The steady-state, far-from-equilibrium Si release rates (r) at pH 2, 3 and 5 for the basalt, andesite, dacite and rhyolite were calculated using Eq. [6.1]. Rates measured in this study are shown in Table 6.2; they range from ~$10^{-11.4}$ to $10^{-8.8}$ mol m^{-2} s^{-1}. They are compared to the theoretical rates (r^*) computed by applying Eq. [6.3]. The results indicate that the theoretical values are systematically higher than the experimental ones by a factor varying within a large range, i.e. from ~1.7 up to 155. Although the theoretical rate calculations entail significant uncertainties related to variable mineral compositions and the effect of reactive solution composition other than pH on rates, the large discrepancies between the r^* and r values already suggest that other variables control the overall dissolution rate of the crystalline rocks tested.

Table 6.2. Dissolution rates measured in this study (r) compared to the theoretical rates (r^*) for the basalt, andesite, dacite and rhyolite.

pH	r (mol m^{-2} s^{-1})	r^* (mol m^{-2} s^{-1})	Log r (mol m^{-2} s^{-1})	Log r^* (mol m^{-2} s^{-1})	r^*/r
Basalt	**r x 10^{11}**	**r^* x 10^{11}**			
2	29.28±2.97	1888.9	-9.53±0.04	-7.72	64.51
3	160.72±11.37	913.67	-8.79±0.03	-8.03	5.68
5	2.86±0.54	383.3	-10.54±0.08	-8.42	134.12
Andesite	**r x 10^{11}**	**r^* x 10^{11}**			
2	35.34±2.41	311.29	-9.45±0.03	-8.51	8.80
3	5.81±1.07	201.80	-10.24±0.08	-8.70	34.75
5	0.57±0.21	88.30	-11.24±0.07	-9.05	154.83
Dacite	**r x 10^{11}**	**r^* x 10^{11}**			
2	12.60±0.50	45.51	-9.90±0.02	-9.34	3.61
3	1.54±0.65	2.76	-10.81±0.20	-10.56	1.79
5	0.42±0.13	1.03	-11.37±0.14	-10.99	2.45
Rhyolite	**r x 10^{12}**	**r^* x 10^{12}**			
2	28.6±10.7	419.85	-10.54±0.17	-9.38	14.69
3	9.01±2.29	131.11	-11.04±0.11	-9.88	14.56
5	5.13±1.48	8.90	-11.29±0.13	-11.05	1.73

6.4. DISCUSSION

6.4.1. Element releases

The ratios of the concentration of each element j ($j = Al, Ca, Mg, Na$) relative to Si in the output solutions (pH 2, 3 and 5) at steady-state normalized to the corresponding ratio in the dissolving rocks (X_j) are displayed in Table 6.3. A ratio equals to one indicates that the release rate of the element of interest is stoichiometric relative to Si. If X_j is greater (smaller) than one, the element is preferentially released (retained in the rock) relative to Si. According to these results, Ca, Mg and Na are preferentially released from the rocks at the three pH conditions tested in the study, i.e. the release of these cations is non-stoichiometric at steady-state. The only exception is Ca, which may behave stoichiometrically during steady-state dissolution of the basalt at pH 5 and the dacite at pH 2. In addition, a X_{Ca}value < 1 is obtained for the dissolution of the basalt at pH 3 (but not at pH 2). This result contrasts with the reaction of a synthetic crystalline basalt at pH 2.7 in a batch-reactor which led to a X_{Ca}value > 1 after 300 h of dissolution (Tosca et al., 2004). However, Gudbrandsson et al. (2011) also reported sluggish Ca release during steady-state dissolution of a basalt rock at low pH values (2 and 3) in a mixed flow reactor, although they did not provide an explanation for their observation.

The release of Ca and Mg into solution during silicate rock dissolution is an important rate-limiting step for atmospheric CO_2 consumption through the formation of Ca-Mg carbonates (e.g., Oelkers et al., 2008; Gislason et al. 2009; Schaef et al., 2010; Gudbrandsson et al., 2011). Therefore, we will focus on the behaviour of these two cations during dissolution of the basalt, andesite, dacite and rhyolite rocks. In crystalline volcanic rocks, plagioclases and glass are the main constituents susceptible to release Ca during dissolution. Magnesium occurs in more mafic minerals, such as forsterite, olivine, pyroxene and amphibole as well as in glass. The mineralogy of the studied rocks is given in Appendix 6.1.

Table 6.3. $X_{Al}, X_{Ca}, X_{Mg}, X_{Na}$ values corresponding to the dissolution of the basalt, andesite, dacite and rhyolite rocks at pH 2,3 and 5.

pH	X_{Al}	X_{Ca}	X_{Mg}	X_{Na}
Basalt				
2	3.40±0.30	1.58±0.87	3.72±0.60	2.18±0.97
3	0.06±0.01	0.06±0.03	4.60±0.38	0.17±0.05
5	0.37±0.10	1.33±0.57	3.66±1.08	6.04±2.26
Andesite				
2	3.59±0.36	9.03±3.82	19.68±7.99	95±56
3	25.62±4.70	2.69±1.42	14.71±5.41	46±22
5	16.27±13.80	214±168	528±375	2216±1461
Dacite				
2	5.40±0.76	1.12±0.17	9.88±1.09	40.5±4.4
3	4.04±1.46	46.8±15.4	361±111	2198±678
5	2.33±0.78	71.0±45.0	14.24±10.18	185±31
Rhyolite				
2	25.00±3.42	761±156	244±164	80±35
3	1.69±1.23	277±195	60.5±55.7	95±67
5	2.05±0.10	1291±92	147±55	21.3±9.9

At steady state (with respect to Si release), X_i values above 1 may point to preferential dissolution of one or several of the rock's constituents (mineral and glass) that would be enriched in cation i relative to the bulk rock material. The release of Mg from the crystalline basalt at any pH values may reflect such behaviour because the Mg/Si ratio in solution matches the ratio reported for the rock's pyroxene. This conforms with the generally higher reactivity of pyroxene and olivine compared to basaltic glass and plagioclases (Lasaga 1984; Schott et al., 1985; Murphy and Helgeson, 1987, 1989; Oelkers et al., 2001; Pokrovsky and Schott, 2000; Gislason and Oelkers, 2003; Gudbrandsson et al., 2014). Similarly, Mg release during the experiment dissolution of the andesite and dacite rocks may be driven by the reactivity of amphibole and pyroxene, respectively, although in both cases Mg occurs in excess of what would be expected from stoichiometric dissolution of the minerals. This may reveal the effect of Mg-proton exchange reactions, which are faster than the breaking of Si–O–Si bridging bonds. For the rhyolite rock, Mg originates only from the glass but the X_{Mg} value > 1 cannot be attributed to stoichiometric dissolution of this constituent since its Mg/Si ratio is much smaller than that measured in the output solution (Appendix 6.6). Again, one can evoke the rapid release of Mg from the glass through proton exchange reactions.

Similar to Mg, the release rate of Ca in the dissolution experiments at pH 2, 3 and 5 does not scale with the Si release rate. Calcium is a typical constituent of glass and plagioclases. Appendix 6.6.3 and Appendix 6.6.4 show that the Ca/Si ratio is much higher (100-1000 times) in the output solution than in the glass and plagioclase constituents of the dacite and rhyolite rocks. The difference is less marked for the andesite experiments and almost nil in the case of the basalt (except at pH 3 where the dissolved Ca/Si ratio is lower than the solid Ca/Si ratios). Thus, the basalt's glass and plagioclase may approach stoichiometric dissolution at pH 2 and 5. This is clearly not the case of the other rock compositions for which the Ca release rates probably relate to fast exchange reactions involving protons. The releases of Na and K upon dissolution of the four crystalline rock are more erratic but are also likely controlled by the variable reactivity of the glass and mineral constituents.

6.4.2. Far-from equilibrium steady-state dissolution rates

Previous experimental determinations of dissolution rates of crystalline silicate rocks are sparse. Moreover, these were conducted at various conditions (different in duration, temperature, solution composition) and simple comparison with our results is not straightforward. At pH 3 and 5 (and correspondent temperature), our basalt rock dissolves 10 and 4 times, respectively, faster than the Stapafell crystalline basalt studied by

Gudbrandsson et al. (2011). These authors indicate that their basalt rock did not contain glass; its mineralogy being dominated by plagioclase, pyroxene and olivine. Using the equation reported by Gislason and Oelkers (2003), the dissolution rate of basaltic glass at pH 3 and 25 °C is ~$10^{-8.8}$ mol m^{-2} s^{-1}. This rate is significantly faster than the values found for plagioclases (Gudbrandsson et al., 2014) and pyroxenes (Schott et al., 1985; Murphy and Helgeson, 1987, 1989; and Rimstidt and Dove, 1986; Palandri et al., 2004) under the same acidity conditions. Thus, the presence of glass (24 wt. %) in our basalt rock may account for the comparatively higher dissolution rates at pH 3 and 5. However, at pH 2, the dissolution rate reported by Gudbrandsson et al. (2011) for the Stapafell crystalline basalt (r = ~$10^{-9.5}$ mol m^{-2} s^{-1}) is close to our measurement (r ~$10^{-9.5}$ mol m^{-2} s^{-1}), apparently contradicting our previous hypothesis. This point is discussed further below.

The dissolution rates of five andesitic tephra varying slightly in composition were determined in batch reactors at pH 4 and room temperature (but not reported) by Welch et al. (2015). The authors emphasised that the rate values were more representative of mineral reactivity at pH ~5 owing to the consumption of protons by the dissolution reaction in the batch reactor. The experimentally-derived rates varied between $10^{-12.1}$ and $10^{-11.3}$ mol m^{-2} s^{-1}. These values are compatible with that inferred in our study for the andesitic rock at pH 5 (r ~$10^{-11.2}$ mol m^{-2} s^{-1}, Table 6.2). Yokohama and Banfield (2002) investigated the dissolution of a powdered glass-dominated rhyolite rock at pH 6 and 20 °C using a flow-through reactor. The far-from equilibrium steady-state dissolution rate was $10^{-12.3}$ mol m^2 s^{-1}, i.e. a value approximately tenfold lower than that derived for our rhyolite rock at pH 5.

At the three pH values tested, r tends to decrease with increasing rock Si content (Fig. 6.2). Based on a compilation of published dissolution rates for natural aluminosilicate glasses and minerals with various compositions, Wolff-Boenisch et al. (2006) highlighted an inverse relationship between r and Si:O ratio. The dependency of dissolution rate on composition has been explained by considering that the breaking of Si–O–Si bridging bonds is the rate limiting step of the dissolution reaction (Brantley and Chen, 1995; Brantley, 2003). Our dissolution rate estimates suggest that the same reasoning applies to crystalline volcanic rocks, i.e. the bulk Si:O ratio dictates the ease with which the rock dissolves, despite the fact that it comprises glass and mineral constituents with different Si:O ratio values and in various proportions. In addition, dissolution rates increase with decreasing pH (Fig. 6.2). This is consistent with the dissolution behaviour of silicates where rates increase with decreasing pH at acidic conditions and increase with increasing pH at basic conditions (e.g., Blum and Lasaga, 1991; Welch and Ullman, 1993).

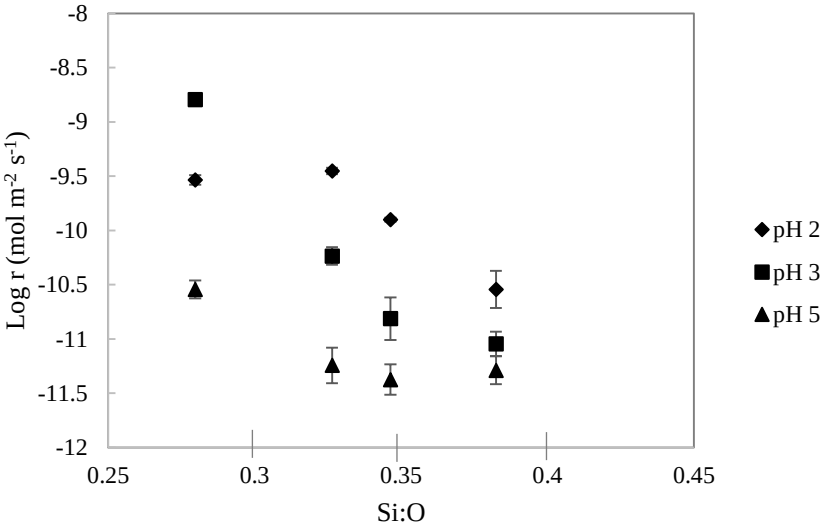

Figure 6.2. Dissolution rates in function of the Si:O ratio for the basalt (Si:O=0.28), andesite (Si:O=0.33), dacite (Si:O=0.35) and rhyolite (Si:O=0.38) rocks.

Two dissolution experiments seem to depart from the general behaviour described above: the basalt rock at pH 2 which produced a r value comparable to that derived for the andesite at the same pH, and the rhyolite rock at pH 5 which dissolved at a rate on par with that of the dacite at the same pH. The dissolution of the crystalline basalt at pH 2 is also more than five times slower than at pH 3 (Table 6.2), a result that does not conform with the known pH-dependency of reaction rate. Therefore, we suspect a systematic error in the measurement of dissolved Si concentration in the output solution from the pH 2 dissolution experiment. The similar dissolution behaviour of the dacite and rhyolite rocks at pH 5 could relate to a diminution of the effect of increasing Si:O ratio on the dissolution rate of S-rich rocks as the pH of the reactive solution increases.

6.4.3. Theoretical dissolution rates versus experimental dissolution rates

According to the results reported in Table 6.2, Eq [6.2] overestimates, in some cases largely, the actual rock dissolution rates, although no simple pattern could be inferred. This may indicate that the theoretical contribution of one or several reactive components to Si release is larger than that measured at the end of the dissolution experiment at steady state. Some authors emphasize that the chemical dissolution rate of a crystalline rock is influenced by the

abundances of its lower-reactivity mineral constituents (White and Brantley, 2003; Wigley et al., 2013). In other words, the presence of a small amount of a low-reactivity phase in a rock may produce a large reduction in its overall dissolution rate (Israeli and Emmanuel, 2018). Conversely, major mineral constituents may limit exposure of the minor phases to the reactive solution (Critelli et al., 2014). In addition, the proportions of the glass and mineral surface areas that can react with the solution change with time as dissolution does not progress at the same pace for the rock constituents. These considerations call for a reassessment of our initial assumption that the reactive surface areas of the glass and minerals initially present in the basaltic, andesite, dacite and rhyolite rocks are directly proportional to the volume fractions that these components occupy.

Critelli et al. (2014) found that the dissolution rates of major minerals present in a metabasalt are not influenced by the presence of other and less abundant minerals. The authors suggested that the same conclusion applies to multi-mineral rocks. In our study, the andesite and dacite rocks contain minor pyroxenes and amphibole, respectively (Table 6.1). Thus, we repeated the dissolution rate calculations but the value of x_i associated with the pyroxenes (andesite) and amphibole (dacite) terms in Eq [6.2] was reduced iteratively until obtaining a good match between the estimated and measured dissolution rate (i.e. $r^*/r \sim 1 \pm 0.5$). As shown in Table 6.4, this approach reconciled the calculated and experimental values satisfactorily, possibly implying that the dissolution rates measured for pure glass and plagioclase minerals are approximately equal to corresponding rates during dissolution of the andesite and dacite rocks.

In the cases of the basalt and rhyolite samples, neither a mineral phase nor the glass can a priori be neglected in the theoretical calculation of the whole rock dissolution rate since these constituents are major ones (Table 6.1). Nevertheless, we note that the experimentally-derived rates of dissolution of the rhyolite at pH 2, 3 and 5 are close to the dissolution values reported for rhyolitic glass in the same pH window, but are significantly slower than those predicted for plagioclase dissolution at the same acidity conditions (Fig. 6.3). This may reflect a minor contribution from plagioclases to Si release during dissolution of the rhyolite rock. Accordingly, we obtain a good agreement between the measured and calculated dissolution rates by neglecting or decreasing the relative surface area of plagioclases in Eq. [6.2] (Table 6.4).

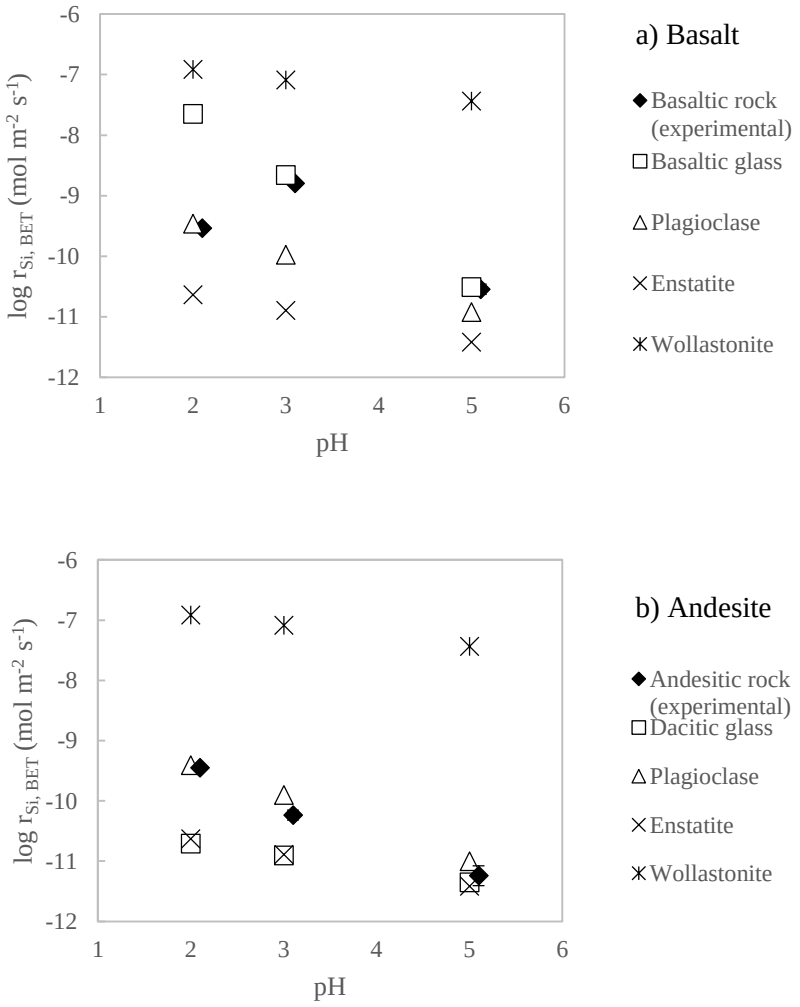

Figure 6.3. Graphs showing the dissolution rates of glass, plagioclase and pyroxene at pH 2, 3 and 5 as derived from their characteristic rate laws (Table A.6.11). The dissolution rate values measured experimentally for the (a) basalt, (b) andesite, (c) dacite and (d) rhyolite rocks are also plotted.

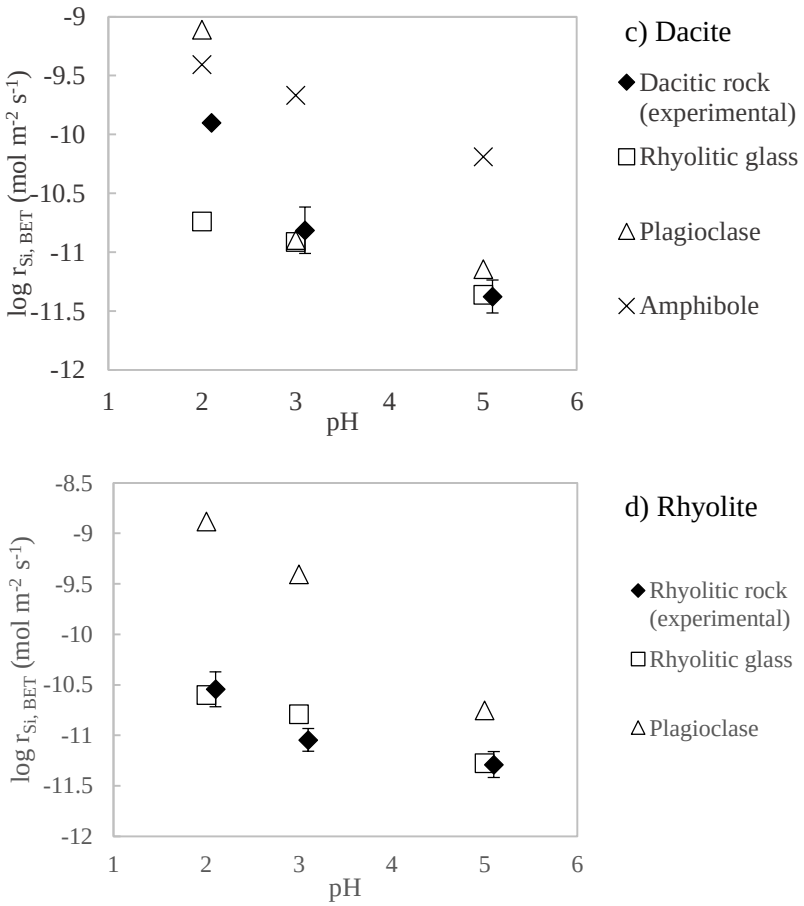

Figure 6.3 (continued). Graphs showing the dissolution rates of glass, plagioclase and pyroxene at pH 2, 3 and 5 as derived from their characteristic rate laws (Table A.6.11). The dissolution rate values measured experimentally for the (a) basalt, (b) andesite, (c) dacite and (d) rhyolite rocks are also plotted.

The dissolution rates determined at pH 2, 3 and 5 for the basalt rock, which is comprised of three major components (i.e. glass, plagioclases and pyroxenes), depart significantly from the theoretical estimates (Table 6.2). At pH 2, the measured rate value is compatible with that at which dissolution of individual plagioclases occurs, although this observation must be weighed against the possibility that Si release was underestimated (see above). At pH 3 and 5, it is close to the dissolution rate of basaltic glass (Fig. 6.3). The dissolution of wollastonite and enstatite is much faster and slower, respectively, than those determined for the basalt rock hosting them. Based on these observations, there is no solid rationale for adjusting the relative surface areas of the three main rock constituents. Rather, we surmise that they all drive dissolution of the basalt rock, but no simple behaviour can be deciphered.

Table 6.4. Theoretical dissolution rate values for the andesite, dacite and rhyolite rocks after the iterative adjustment of the relative surface areas, x_i, of their main rock's constituents. The experimental dissolution rates are also shown for comparison.

pH				r (mol m^{-2} s^{-1})	r* (mol m^{-2} s^{-1})	Log r (mol m^{-2} s^{-1})	Log r* (mol m^{-2} s^{-1})	r^*/r
Andesite	x_{glass}	$x_{plagioclase}$	$x_{pyroxene}$					
Initial	**0.38**	**0.5**	**0.10**	**r x 10^{11}**	**r^* x 10^{11}**			
2	0.38	0.5	0.003	35.34±2.41	35.39	-9.45±0.03	-9.45	1.00
3	0.38	0.5	0.00	5.81±1.07	6.75	-10.24±0.08	-10.17	1.16
5	0.38	0.5	0.00	0.57±0.21	0.67	-11.24±0.07	-11.17	1.17
Dacite	x_{glass}	$x_{plagioclase}$	$x_{amphibole}$					
Initial	**0.33**	**0.54**	**0.08**	**r x 10^{11}**	**r^* x 10^{11}**			
2	0.33	0.20	0.00	12.60±0.50	16.11	-9.90±0.02	-9.79	1.28
3	0.33	0.54	0.01	1.54±0.65	1.31	-10.81±0.20	-10.88	0.85
5	0.33	0.54	0.01	0.42±0.13	0.60	-11.37±0.14	-11.22	1.41
Rhyolite	x_{glass}	$x_{plagioclase}$						
Initial	**0.66**	**0.31**		**r x 10^{12}**	**r^* x 10^{12}**			
2	0.77	0.00	-	28.6±10.7	19.36	-10.54±0.17	-10.71	0.68
3	0.66	0.00	-	9.01±2.29	10.74	-11.04±0.11	-10.97	1.17
5	0.66	0.10	-	5.13±1.48	5.29	-11.29±0.13	-11.27	1.02

6.5. CONCLUSIONS

Regarding the composition of the output solutions in the dissolution experiments, irrespective of the pH of the input solution, the dissolution of the basalt and andesite rocks produced much larger (one to two orders of magnitude) concentrations of Si compared to the dissolution of the dacite and rhyolite. The basalt rock released also more Si than the andesite. The release of Al during rock dissolution was always highest at pH 2. The evolution of the concentrations of Ca, Mg, Na and K over time was more erratic and no simple pattern could be inferred. Calcium, Mg and Na are preferentially released from the rocks at the three pH conditions tested in the study, i.e. the release of these cations is non-stoichiometric at steady-state.

At the three pH values tested (2, 3 and 5), experimental dissolution rates tended to decrease with increasing rock Si content. The bulk Si:O ratio dictated the ease with which the rock dissolves, despite the fact that it comprises glass and mineral constituents with different Si:O ratio values and in various proportions. In addition, dissolution rates increased with decreasing pH.

Theoretical dissolution rates for the rocks studied were calculated assuming that the reactive surface areas of the glass and minerals initially present in them are directly proportional to the volume fractions that these components occupy. The theoretical values were systematically higher than the experimental ones by a factor varying within a large range, i.e. from ~1.7 up to 155, suggesting that other variables control the overall dissolution rate of the crystalline rocks tested.

A second approach was proposed to calculate the dissolution rate values of the rocks, in which the adjustment of the relative surface areas of the main rock constituents was considered. This second approach reconciled the calculated and experimental values satisfactorily for andesite, dacite and rhyolite rocks. Thus, dissolution rates measured for pure glass and plagioclase minerals were approximately equal to corresponding rates during dissolution of the andesite and dacite rocks, with no influence of the minor rock components, pyroxenes and amphibole, respectively. In the case of the rhyolitic rock, this approach reflected a minor contribution from plagioclases to Si release during dissolution. However, in the case of basalt, there was no solid rationale for adjusting the relative surface areas of the three main rock constituents (i.e. glass, plagioclases and pyroxenes), suggesting a more complex behaviour.

References

American Society for Testing and Materials (2015) ASTM D3663-03(2015), Standard Test Method for surface Area of Catalyst and Catalyst Carriers. ASTM International, West Conshohocken, United States of America, doi: 10.1520/D3663-03R15.

Beaulieu, E., Goddéris, Y., Donnadieu, Y., Labat, D. and Roelandt, C. (2012) High sensitivity of the continental-weathering carbon dioxide sink to future climate change. Nature climate change. Vol 2. pp 346-349.

Beckingham, L.E., Steefel, C.I., Swift, A.M., Voltolini, M., Yang, L., Sheets, J.M., Cole, D.R., Kneafsey, T.J., Mitnick, E.H., Zhang, S., Gautier, L., Ajo-Franklin, J.B., DePaolo, D.J., Mito, S. and Xue, Z. (2017) Evaluation of accessible mineral surface areas for improved prediction of mineral reaction rates in porous media. Geochimica et Cosmochimica Acta 205: 31-49.

Beckingham, L.E., Mitnick, E.H., Steefel, C.I., Zhang, S., Voltolini, M., Swift, A.M., Yang, L., Cole, D.R., Sheets, J.M., Ajo-Franklin, J.B., DePaolo, D.J., Mito, S., Xue, Z. (2016) Evaluation of mineral reactive surface area estimates for prediction of reactivity of a multi-mineral sediment. Geochimica et Cosmochimia Acta 188: 310-329.

Berner, R.A. (1992) Weathering, plants and the long term carbon cycle. Geochimica et Cosmochimica Acta 70, 1402-1420.

Bish, D.L., Post, J.E. (1993) Quantitative mineralogical analysis using the Rietveld full-pattern fitting method. Am Mineral 78: 932-940.

Blum, A.E., Lasaga, A.C. (1991). The Role of Surface Speciation in the Dissolution of Albite. Geochimica et Cosmochimica Acta, 55(8): 2193-2201.

Brantley, S.L. (2003) Reaction Kinetics of Primary Rock-forming Minerals under Ambient Conditions. In: Editors-in-Chief: Heinrich, D.H., Karl, K.T. (Eds.), Treatise on Geochemistry. Pergamon, Oxford, pp. 73-117.

Brantley S. L. and Mellott N. P. (2000) Surface area and porosity of primary silicate minerals. Am. Mineral. 85, 1767–1783.

Brantley, S.L. and Chen, Y. (1995) Chemical weathering rates of pyroxenes and amphiboles. In Chemical Weathering Rates of Silicate Minerals (eds. A.F. White and S.L. Brantley). Mineralogical Society of America, Washington, D.C. 119-172.

Brunauer, S., Emmett, P. H. and Teller, E. (1938) Adsorption of gases in multimolecular layers. Journal of the American Chemical Society, 60(2), 309-319.

Cailleteau, C., Angeil, F., Deveux F., Gin S., Jestin J., Jollivet P. and Spalla O. (2008) Insight into silicate-glass corrosion mechanisms. Nat. Mater. 7, 978–983.

Critelli, T., Marini L., Schott J., Mavromatis V., Apollaro, C., Rinder, T., De Rosa, R., Oelkers, E.H. (2015) Dissolution rate of antigorite from a whole-rock experimental study of serpentinite dissolution from 2 < pH < 9 at 25°C: Implications for carbon mitigation via enhanced serpentinite weathering. Applied Geochemistry 61 (2015) 259–271.

Critelli, T., Marini, L., Schott, J., Mavromatis, V., Apollaro, C., Rinder, T., De Rosa, R., Oelkers, E.H. (2014). Dissolution rates of actinolite and chlorite from a whole-rock experimental study of metabasalt dissolution from 2 ≤ pH ≤ 12 at 25°C. Chem. Geol. 390, 100–108.

Declercq, J., Diedrich. T., Perrot M., Gislason S.R., Oelkers E.H. (2013) Experimental determination of rhyolitic glass dissolution rates at 40–200 °C and 2 < pH < 10.1. Geochimica et Cosmochimica Acta 100 (2013) 251–263.

Deng, H., Voltolini, M., Molins, S., Steefel, C., DePaolo, D., Ajo-Franklin, J., Yang, L. (2017) Alteration and Erosion of Rock Matrix Bordering a Carbonate-Rich Shale Fracture. Environ. Sci. Technol. 51: 8861-8868.

Gislason S., Oelkers E.H., Eiriksdottir E. S., Kardjilov M. I., Gisladottir G., Sigfusson B., Snorrason A., Elefsen S., Hardardottir J., Torssander P., Oskarsson N. (2009) Direct evidence of the feedback between climate and weathering. Earth and Planetary Science Letters 277 (2009) 213–222.

Gislason S. and Oelkers E.H. (2003) Mechanism, rates, and consequences of basaltic glass dissolution: II. An experimental study of the dissolution rates of basaltic glass as a function of pH and temperature. Geochimica et Cosmochmica Acta, Vol. 67, No. 20, pp. 3817-3832.

Goddéris, Y., Brantley, S.L., François, L.M., Schott, J., Pollard, D., Déqué, M. and Dury M. (2013) Rates of consumption of atmospheric CO_2 through the weathering of loess during the next 100yr of climate change. Biogeosciences, 10, 135-148.

Goddéris Y. and Brantley, S.L (2013) Earthcasting the future Critical Zone. Elementa: Science of the Anthropocene • 1: 000019.

Goddéris, Y., Roelandt, C., Schott, J., Pierret, M.C., François, L.M. (2009) Towards an Integrated Model of Weathering, Climate, and Biospheric Processes. Reviews in Mineralogy & Geochemistry. Vol.70 pp. 411-434.

Gonzalez, R.M., Edwards, T.E., Lorbiecke, T.D., Winburn, R.S., Webster, J.R. (2003) Analysis of geologic material using rietveld quantitative X-Ray diffraction. International Centre for Diffraction Data. Advances in X-ray Analysis. Vol 46. 204-209.

Gudbrandsson S., Wolff-Boenisch D., Gislason S.R. and Oelkers E.H. (2014) Experimental determination of plagioclase dissolution rates as a function of its composition and pH at 22°C. Geochimica et Cosmochimica Acta 139 (2014) 154–172.

Gudbrandsson S., Wolff-Boenisch D., Gislason S., Oelkers E. H. (2011) An experimental study of crystalline basalt dissolution from 2 6 pH 6 11 and temperatures from 5 to 75 C. Geochimica et Cosmochimica Acta 75 (2011) 5496–5509.

Guy C. and Schott J. (1989) Multisite surface reactions versus transport control during the hydrolysis of a complex oxide. Chem. Geol. 78, 181-204.

Hill R.J., Tsambourakis, G., and Madsen, I.C. (1993). Improved Petrological Modal Analyses from X-ray Powder Diffraction Data by use of the Rietveld Method I. Selected Igneous, Volcanic, and Metamorphic Rocks J. Pet., 34(5), 867-900.

Hyndman, D.W. (1985) Petrology of Igneous and Metamorphic Rock. Second Edition. McGraw-Hill Book Company. International series in the Earth & Planetary Sciences. Chapter 3. Classification and characteristics of Igneous Rocks. chapter 3.

Israeli, Y. and Emmanuel, S. (2018) Impact of grain size and rock composition on simulated rock weathering. Earth Surf. Dynam., 6, 319–327.

Kreisserman Y. and Emmanuel, S. (2018) Release of Particulate Iron Sulfide during Shale-Fluid Interaction. Environ. Sci. Technol. 52, 638-643.

Lasaga, A.C. (1998) Kinetic Theory in the Earth Sciences. Princeton University Press. Princenton.

Lasaga, A.C. (1984) Transition state theory. In Lasaga, A.C., Kirkpatrick, R.J. (eds.) Kinetics of Geochemical Processes. Rev Mineral 8:1-68.

Levenson, Y., Ryb, U., Emmanuel, S. (2017) Comparison on field and laboratory weathering rates in carbonate rocks from an Eastern Mediterranean drainage basin. Earth Planet. Sc. Lett., 465, 176-183.

Murphy W.M., Oelkers, E.H. and Lichtner, P.C. (1989) Surface reaction versus diffusion control of mineral dissolution and growth rates in geochemical process. Chem. Geol. 78, 357-380.

Murphy W.M. and Helgeson, H.C. (1987) Thermodynamic and kinetic constraints on reaction rates among minerals and aqueous solutions. III. Activated complexes and the pH-dependence of the rates of feldspar, pyroxene, wollastonite, and olivine hydrolysis. Geochimica et Cosmochimica Acta 52 (12), 3137-3153.

Matter, J.M., Broecker, W.S., Gislason, S.R., Gunnlaugsson, E., Oelkers, E.H., Stute, M., Sigurdardóttir, H., Stefansson, A., Alfreðsson, H.A., Aradóttir, E.S., Axelsson, G., Sigfússon, B., Wolff-Boenisch, D., (2011) The CarbFix Pilot Project – storing carbon dioxide in basalt. Energy Procedia 4, 5579–5585.

Oelkers E.H., Golubev S.V., Chairat C., Pokrovsky O.S. and Schott J. (2009) The surface chemistry of multi-oxide silicates. Geochimica et Cosmochimica Acta 73, 4617-4634.

Oelkers, E. H., Golubev, S. V., Chaierat, C., Pokrovsky, O. S. and Schott, J. (2008) The surface chemistry of multi-oxide silicates. Geochimica et Cosmochica. Acta 72 (12), A698.

Oelkers, E. H., Schott, J. and Devidal, J. L. (2001). On the interpretation of closed system mineral dissolution experiments: Comment on "Mechanism of kaolinite dissolution at room temperature and pressure Part II: Kinetic study" by Huertas et al. (1999). Geochimica et Cosmochimica Acta 65 (23), 4429-4432.

Oelkers, E.H. (2001) General kinetic description of multioxide silicate mineral and glass dissolution. Geochimica et Cosmochimica Acta, 65(21), 3703-3019.

Oelkers, E.H, and Gislason S. (2001) The mechanism, rates and consequences of basaltic glass dissolution: I. An experimental study of the dissolution rates of basaltic glass as a function of aqueous Al, Si and oxalic acid concentration at 25°C and pH=3 and 11. Geochimica et Cosmochimica Acta, Vol. 65, No. 21, 3671–3681, 2001.

Palandri J.L. and Kharaka Y.K. (2004) A compilation of rate parameters of water-mineral interaction kinetics for application to geochemical modeling. U.S. Geological Survey. Open file report 2004-1068.

Paque, M., Detienne, M., Maters, E.C., Delmelle, P. (2016) Smectites and zeolites in ash from the 2010 summit eruption of Eyjafjallajökull volcano, Island. Bull Volcanol 78: 61.

Parkhurst D.L. and Appelo C.A.J. (1999) User's guide to PHREEQC (Version 2) – a computer program for speciation, bacth reaction, one-dimensional transport, and inverse geochemical calculations. In USGS, Restin, VA, USA, pp. 99-4259.

Pokrovsky, O. S. and Schott, J. (2000) Kinetics and mechanism of forsterite dissolution at 25°C and pH from 1 to 12. Geochimica et Cosmochimica Acta. Vol 64. No 19. 3313-3325.

Pronost, J., Beaudoin, G., Tremblay, J., Larachi, F., Duchesne, J., Hébert, R., Constantin, M., (2011) Carbon sequestration kinetic and storage capacity of ultramafic mining waste. Environ. Sci. Technol. 45, 9413–9420.

Rajmohan, N., Fruger, P. and Gin, S. (2010) Composition effects on synthetic glass alteration mechanism: Part 1. Experiments. Chem. Geol. 279, 106–119.

Rimstidt, J.D., Dove, P.M. (1986) Mineral/solution reaction rates in a mixed flow reactor: wollastonite hydrolysis. Geochim Cosmochim Acta 50. 2509-2516 Schaef et al. 2010.

Schott, J. and Berner, R. (1985) Dissolution mechanism of pyroxenes and olivines during weathering. In the Chemistry of Weathering (ed. J.I. Drever). Kluwer Academic Publishers. Hingham. MA.

Tosca N. J., McLennan S. M., Lindsley D. H., Schoonen M. A. A. (2004) Acid-sulfate weathering of synthetic Martian basalt: The acid fog model revisited. Journal of Geophysical Research, Vol. 109, E05003, doi: 10.1029/2003JE002218, 2004.

Ward CR, French D (2006) Determination of glass content and estimationof glass composition in fly ash using quantitative X-ray diffractometry. Fuel 85:2268–2277.

Welch S. A., Goldsmith S. T., Carey A. E. (2015) Impact of trace mineral phases on the total solute flux from andesitic volcanics. Applied Geochemistry 63 (2015) 527-539.

Welch S. A. and Ullman W. J. (1993) The effect of organic acids on feldspar dissolution rates and stoichiometry. Geochimica et Cosmochimica Acta 57, 2725-2736.

White F. and Brantley S. L. (2003) The effect of time on the weathering of silicate minerals: why do weathering rates differ in the laboratory and field? Chemical Geology 202 (2003) 479–506.

Wigley, M., Dubacq, B., Kampman, N., Bickle, M. (2013) Controls of sluggish, CO_2-promoted, hematite and K-feldpsar dissolution kinetics in sandstones. Earth and Planetary Science Letters 362: 76-87.

Winburn RS, Grier DG, McCarthy GJ, Peterson RB (2000) Rietveld quantitative X-ray diffraction analysis of NIST fly ash standard reference materials. Powder Diffract 15:163–172.

Wolff-Boenisch, D., Gislason, S.R., Oelkers, E.H. (2006) The effect of crystallinity on dissolution rates and CO2 consumption capacity of silicates. Geochimica et Cosmochimica Acta 70. 858-870.

Yokoyama, T. and Banfield, J.F. (2002) Direct determination of the rates of rhyolite dissolution and clay formation over 52,000 years and comparison with laboratory measurements. Geochimica et Cosmochimica Acta, Vol. 66, No. 15, pp. 2665-2681.

Appendix 6.1. Mineralogical analysis of the studied samples

A.6.1.1. Basaltic rock: Katla (E-934)

The only historical eruption in the Katla system outside of the central volcano was the 934-940 AD Eldjá Fires, which is the largest known flood-lava eruption on Earth during the historical period. Eldjá lava is characterised as a transitional alkali basalt (Oladóttir, 2005, 2007). The 934 AD Eldgjá products are sparsely porphyritic (≤2 vol. %) transitional alkali basalts, containing ≤ 2 mm subhedral to euhedral phenocryst of plagioclase (An_{65-92}), clinopyroxene ($En_{40}Fs_{17}Wo_{43}$-$En_{46}Fs_{8}Wo_{46}$), olivine (Fo_{70-89}), and magnetite. The bulk of the erupted tephra has groundmass glass compositions identical to and slightly more evolved than the whole-rock compositions (Thordarson et al. 2001). The chemical composition of Katla rock and its components is presented in Table A.6.1.

Table A.6.1. Chemical composition of Katla rock and its components (wt. %).

Component (wt. %)	**Whole Rock [1]**	**Glass [1]**	**Plagioclase [2]**	**Pyroxene[2]**
SiO_2	46.97	47.01	57.65	54.04
TiO_2	4.46	4.67		
Al_2O_3	12.74	12.57	26.60	
Fe_2O_3	15.34	15.77		
MnO	0.21	0.23		
MgO	5.28	5.07		24.71
CaO	10.06	10.01	8.49	21.24
Na_2O	2.89	2.87	5.88	
K_2O	0.69	0.75	1.37	
P_2O_5	0.52	0.52		
An (%)			41	
Ab (%)			50	
Or (%)			8	
En (%)				43
Fs (%)				13
Wo (%)				44

[1]Thordarson et al. (2001) [2] Calculated from data of Jakobsson (1979)

The chemical formula for the main constituents of the basaltic rock is presented in Table A.6.2:

Table A.6.2. Chemical formula of the main components of Katla rock.

Rock	Chemical Formula
Whole rock	$Al_{0.32}Ca_{0.32}Fe_{0.24}K_{0.02}Mg_{0.17}Na_{0.12}SiO_{3.57}$
Glass	$Al_{0.31}Ca_{0.32}Fe_{0.25}K_{0.02}Mg_{0.16}Na_{0.12}SiO_{3.57}$
Plagioclase	$Al_{1.36}Ca_{0.56}K_{0.08}Na_{0.51}Si_{2.55}O_8$
Pyroxene	$Ca_{1.08}Mg_{1.25}Si_{1.83}O_6$

References

Jakobsson, S.P. (1979) Petrology of Recent basalt of the Eastern Volcanic Zone, Iceland. Acta Naturalia Islandica 26. pp. 37-38.

Oladóttir, B. A., Sigmarsson, O., Larsen G., Thordarson, T. (2007) Katla volcano, Iceland: magma composition, dynamics and eruption frequency as recorded by Holocene tephra layers. Bull Volcanol 70:475-493

Oladóttir, B. A., Larsen, G., Þórðarson, Þ., Sigmarsson, O. (2005) The Katla volcano S-Iceland: Holocene tephra stratigraphy and eruption frequency. JÖKULL No. 55. 53-74.

Thordarson, T., Miller, D.J., Larsen, G., Self, S., Sigurdsson, H. (2001) New estimates of sulfur degassing and atmospheric mass-loading by the 934 AD Eldgjá eruption, Iceland. Journal of Volcanology and Geothermal Research 108. 33-54.

A.6.1.2. Andesitic rock: Tungurahua (TUNG-PS-25B Glassy block 14 July 2006)

The Tungurahua rock is a juvenile glassy block. Juveniles blocks from the pyroclastic flow deposits are dark, vesicular, porphyritic (~10-20 vol. % phenocrysts) andesites. The mineral assemblage consists of plagioclase, clinopyroxene, orthopyroxene and magnetite, with scarce olivine cyrstals. Plagioclase is the most abundant phenocryst phase (5-15 vol. %). Clinopyroxene phenocrysts (2-4 vol. %) show diopsidic or augitic compositions. Orthopyroxene appears in andesitic samples as euhedral phenocryst or microphenocryst (2-4 vol. %). Olivine is an accessory phase in andesitic samples (<1 vol. %). Fe-Ti oxides appear as microphenocrysts and microlites in the matrix (<1-2 vol. %), as well as inclusions in clinopyroxene, orthopyroxene, and plagioclase phenocrysts. They correspond to titanomagnetite crystals (8-14 wt. % TiO_2). The July 14th samples show dacitic glass (64.7±1.6 wt. % SiO_2) (Samaniego, 2011). The chemical composition of Tungurahua rock and its components is presented in Table A.6.3.

Table A.6.3. Chemical composition of Tungurahua rock and its components (wt. %).

Component (wt. %)	**Whole Rock** [1]	**Glass**[1] [2]	**Pl** [1]	**Pyroxene**[1]		**Olivine** [1]
				Cl-Px	**O-Px**	
SiO_2	57.9	62.84	57.73	50.28	51.94	37.32
TiO_2	0.87	0.87	0.01	0.72	0.38	0.04
Al_2O_3	16.8	6.25	29.19	3.42	1.17	0.03
Fe_2O_3	7.32	13.27	0.79[3]	9.56[3]	19.91[3]	26.60[3]
MnO	0.11	0.18	0.00	0.28	0.45	0.40
MgO	4.33	5.65	0.03	14.47	23.37	35.19
CaO	6.88	2.94	8.99	19.68	1.77	0.14
Na_2O	3.95	2.51	6.18	0.43	0.06	0.03
K_2O	1.69	3.59	0.66		0.02	
P_2O_5	0.25	0.66				
An (%)			42.91			
Ab (%)			53.37			
Or (%)			3.72			
En (%)				42.40	64.75	
Fs (%)				16.19	31.70	
Wo (%)				41.40	3.55	

[1] Samaniego et al. (2011) [2] Calculated from data of Samaniego et al. (2011) [3] Total iron as FeO.

Pl: plagioclase; Cl-Px: clinopyroxene; O-Px: orthopyroxene

The chemical formula for the main constituents of the andesitic rock is presented in Table A.6.4:

Table A.6.4. Chemical formula of the main components of Tungurahua rock.

Rock	Chemical Formula
Whole rock	$Al_{0.34}Ca_{0.18}Fe_{0.1}K_{0.04}Mg_{0.11}Na_{0.13}SiO_{3.06}$
Glass	$Al_{0.11}Ca_{0.07}Fe_{0.17}K_{0.07}Mg_{0.13}Na_{0.08}SiO_{2.78}$
Plagioclase	$Al_{1.46}Ca_{0.57}Fe_{0.02}K_{0.03}\ Mg_{0.002}Na_{0.51}Si_{2.46}O_8$

References

Samaniego, P., Le Pennec, J., Robin, C. and Hidalgo, S. (2011) Petrological analysis of the pre-eruptive magmatic process prior to the 2006 explosive eruptions at Tungurahua volcano (Ecuador) Journal of Volcanology and Geothermal Research 199 (2011) 69-84

A.6.1.3. Dacitic rock: Guagua Pichincha (PICH 158 B)

The dacitic rock sample is from the 1999 Guagua Pichincha eruption (PICH 158 B). According to García-Aristizabal et al. (2007) and Samaniego et al. (2010) the dacite is porphyritic (~30-35 vol. %) with phenocrysts of plagioclase (10-20 vol. %), amphibole (<10 vol. %), orthopyroxene (<5 vol. %) and Fe-Ti oxides (<1-2 vol. %). The groundmass in mostly glass with a rhyolitic composition (73.1-79.6 wt. % SiO_2). Plagioclase is the most abundant phenocryst, with a euhedral form and a wide compositional range (An_{30-80}). Amphibole is the most important mafic mineral. Guagua Pichincha amphibole divides into two compositional groups: (1) low-Al amphiboles (mostly magnesium-hornblendes, with 5.3-10.5 wt. % Al_2O_3); and (2) high-Al amphiboles (scarce tschermakite and magnesium-hastingsite, with 10.9-14.7 wt. % Al_2O_3). In Table A.6.5., the chemical composition of Guagua Pichincha rock and its components is presented.

Table A.6.5. Chemical composition of Guagua Pichincha rock and its components (wt. %).

Component (wt. %)	**Whole Rock [1]**	**Glass [2]**	**Plagioclase [1]**	**Amphibole [1]**
SiO_2	62.42	75.87	54.6	43.89
TiO_2	0.48	0.97	0.02	1.44
Al_2O_3	16.33	1.81	28.05	11.02
Fe_2O_3	5.98	13.05	0.23	13.05
MnO	0.09	0.18	0.02	0.20
MgO	3.72	0.55	0.001	13.61
CaO	5.49	-	10.78	10.72
Na_2O	3.97	3.12	5.16	1.99
K_2O	1.58	4.07	0.22	0.54
P_2O_5	0.14	0.39	0.00	0.04
An (%)			36.60	
Ab (%)			62.37	
Or (%)			1.03	

[1] Samaniego et al. (2010) [2] Calculated from data of Samaniego et *al. (2010)* [3] *Total iron as FeO.*

The chemical formula for the main constituents of the dacitic rock is presented in Table A.6.6:

Table A.6.6. Chemical formula of the main components of Guagua Pichincha rock.

Rock	Chemical Formula
Whole rock	$Al_{0.31}Ca_{0.13}Fe_{0.07}K_{0.03}Mg_{0.09}Na_{0.12}SiO_{2.89}$
Glass	$Al_{0.02}Fe_{0.13}K_{0.07}Mg_{0.01}Na_{0.08}SiO_{2.36}$
Plagioclase	$Al_{1.46}Ca_{0.72}Fe_{0.08}K_{0.012}Na_{0.44}Si_{2.42}O_8$

References

Garcia-Aristizabal, A., Kumagai H., Samaniego, P., Mothes, P., Yepes H., Monzier, M. (2007) Seismic, petrologic, and geodetic analyses of the 1999 dome-forming eruption of Guagua Pichincha volcano, Ecuador. Journal of Volcanology and Geothermal Research 161 (2007) 333–351.

Samaniego, P., Robin, C., Chazot, G., Bourdon E. and Cotten Joseph (2010) Evolving metasomatic agent in the Northern Andean subduction zone, deduced from magma composition of the long-lived Pichincha volcanic complex (Ecuador) Contrib Mineral Petrol (2010) 160:239–260.

A.6.1.4. Rhyolitic rock: Puyehue (PUY_2013_003)

The Puyehue-Cordón Caulle volcanic complex is located in the Southern Volcanic Zone of the Chilean Andes. The erupted products of the 2013 activity are mainly rhyolitic, containing approximately 69.5 wt. % SiO_2. The phenocryst assemblage comprises the following euhedral phases, in order of decreasing abundance: plagioclase, orthopyroxene, clinopyroxene, magnetite and ilmenite. Accessory phases include apatite and pyrhotite. The crystals often form intergrowth clusters but may also be found separate and enclosed in highly vesicular microlite-free glass. The plagioclase phenocrysts contain about 37 mol % anorthite. Plageoclase phenocrysta assemblage may include som rare Ca-rich plagioclase. Pyroxene occurs as both ortho- and clinopyroxene (Castro et al., 2013, Schipper et al., 2015). In Table A.6.7., the chemical composition of Puyehue rock and its components is presented.

Table A.6.7. Chemical composition of Puyehue rock and its components (wt. %).

Component (wt. %)	**Whole Rock [1]**	**Glass [2]**	**Plagioclase [2]**	**Pyroxene [2]**	**Fe-Ti oxides[2]**
SiO_2	69.95	75.58	65.03	50.60	11.95
TiO_2	0.70	0.52	0.12	0.65	16.47
Al_2O_3	14.35	11.31	20.55	0.94	2.24
Fe_2O_3	4.66	2.56	0.74	28.47	61.97
MnO	0.12	0.09	0.01	1.42	0.96
MgO	0.55	0.09	0.03	11.95	1.98
CaO	2.29	0.45	4.39	5.74	0.90
Na_2O	5.13	2.54	7.27	0.21	0.80
K_2O	2.75	4.70	1.09	0.14	0.33
P_2O_5	0.12	-	-	-	-
An (%)			30.94		
Ab (%)			62.83		
Or (%)			6.23		

[1] Castro et al., (2013) [2] Major and minor element compositions of all crystalline phases and glassy groundmasses were determined by EPMA using the JEOL Superprobe at the Institut für Geowissenschaaften, University of Mainz.

The chemical formula for the main constituents of the rhyolitic rock is presented in Table A.6.8:

Table A.6.8. Chemical formula of the main components of Puyehue rock.

Rock	Chemical Formula
Whole rock	$Al_{0.24}Ca_{0.05}Fe_{0.05}K_{0.05}Mg_{0.012}Na_{0.14}SiO_{2.46}$
Glass	$Al_{0.17}Ca_{0.009}Fe_{0.002}K_{0.08}Mg_{0.002}Na_{0.06}SiO_{2.36}$
Plagioclase	$Al_{1.06}Ca_{0.29}Fe_{0.02}K_{0.06}\ Mg_{0.002}Na_{0.62}Si_{2.86}O_8$

References

Castro, J.M., Schipper, C.I., Mueller, S.P., Militzer, A.S., Amigo, A., et al. (2013) Storage and eruption of near-liquidus rhyolite magma at Cordón Caulle, Chile. Bulletin of Volcanology, Springer Verlag, 75 (702), pp.1-17.

Castro, J.M. & Dingwell, D., B., (2009) Rapid ascent of rhyolitic magma at Chaitén volcano Chile. Nature. Vol461. 780-783.

Schipper, C.I, Castro, J.M., Tuffen, H., Wadsworth, F.B., Chappell, D., Pantoja, A.E., Simpson, M.P., Le Ru, E.C. (2015) Cristobalite in the 2011-2012 Cordón Caulle eruption. Bull Volcanol 77:34.

Appendix 6.2. Experimental conditions

Table A.6.9. Composition of the input solutions used in the dissolution experiments.

pH (20°C)	HCl (mol/L)	NH_4Cl (mol/L)
2	0.01	
3	0.001	0.00900
5	0.00001	0.00999

Appendix 6.3. Mineral volumetric fractions of the basalt, andesite, dacite and rhyolite rocks

Table A.6.10. Mineral volumetric fractions of the basalt, andesite, dacite and rhyolite rocks.

Rock	Glass	Plagioclase	Pyroxene	Olivine	Amphibole	Fe-Ti oxides	Apatite
				vol.%			
Basalt	26.8	40.5	24.9	3.7		3.9	
Andesite	37.9	49.7	9.8	2.3			
Dacite	32.6	53.8	4.9		7.7		0.9
Rhyolite	65.6	30.6	3.0			0.8	

Appendix 6.4. Estimated dissolution rates based on kinetics laws of glasses (basaltic and rhyolitic) and plagioclase from literature

Table A.6.11. Dissolution kinetic laws for pure silicate minerals and volcanic glasses.

	Kinetic law
AMORPHOUS	$r_+ = A\, e^{-\left(\frac{Ea}{RT}\right)} \left(\frac{a_{H^+}^3}{a_{Al^{3+}}}\right)^{1/n}$
Basaltic glass[a] (48 wt.% SiO_2)	$\mathrm{r_{Glass+Si}}\ (\mathrm{mol\ cm^{-2}\ s^{-1}}) = 10^{-5.6}\, e^{-\left(\frac{25.5\ kJ/mol}{RT}\right)} \left(\frac{a_{H^+}^3}{a_{Al^{3+}}}\right)^{1/3}$
Rhyolitic glass[b] (70 wt.% SiO_2)	$\mathrm{r_{Glass+Si}}\ (\mathrm{mol\ cm^{-2}\ s^{-1}}) = 1.4\ x10^{-5}\, e^{-\left(\frac{55.15\ kJ/mol}{RT}\right)} \left(\frac{a_{H^+}^3}{a_{Al^{3+}}}\right)^{1/11.1}$
CRYSTALLINE	
Feldspar (Plagioclase)[c]	For pH<6 $\log \mathrm{r_{plagio+Si}} = (0.004\,\mathrm{An\%} + 0.05) \log\left(\frac{a_{H+}^3}{a_{Al3+}}\right) - 0.033\mathrm{An\%} - 14.77$ $*\ \log \mathrm{r_{plagio+Si}}\ [\mathrm{mol\ cm^{-2}\ s^{-1}}]$ ** *An% represents the percent anorthite in the plagioclase solid solution*
Pyroxene (Enstatite)[d]	$\log \mathrm{r_{Enstatite+Si}}\ (\mathrm{mol\ m^{-2}\ s^{-1}}) = -9.02 - \frac{80.0\ x\ 10^3}{2.3025\ RT} - 0.60\ pH$
(Wollastonite)[e]	$\log \mathrm{r_{Wollastonite+Si}}\ (\mathrm{mol\ m^{-2}\ s^{-1}}) = -5.37 - \frac{54.7\ x\ 10^3}{2.3025\ RT} - 0.40\ pH$
Amphibole Hornblende[f]	$\log \mathrm{r_{Hornblende+Si}}\ (\mathrm{mol\ m^{-2}\ s^{-1}}) = -7.00 - \frac{75.5\ x\ 10^3}{2.3025\ RT} - 0.6\ pH$

Taken from (a) Gislason et al. (2003) (b) Declerq et al. (2012) (c) Gudbransson et al. (2014) (d) Palandri et al. (2004). Based on Schott et al. (1985) (e) Palandri et al. (2004). Based on Murphy and Helgeson (1987; 1989) and Rimstidt and Dove (1986) (f) Palandri et al. (2004). Based on Sverdrup (1990).

Appendix 6.5. Average concentrations (µmol L^{-1}, three replicates) of Si, Al, Fe, Ca, Mg, Na and K in the output solutions as measured during the dissolution of the basalt, andesite, dacite and rhyolite rocks

BASALT
pH 2

Time (h)	Average Si(µmol L^{-1})	Standard deviation	Average Al(µmol L^{-1})	Standard deviation
24	199.98	10.33	4.64	0.23
48	78.30	8.07	4.00	0.08
72	36.77	2.20	3.82	0.06
96	25.79	6.83	3.85	0.10
120	10.95	1.38	3.49	0.17
150	6.85	0.76	3.54	0.04
175	4.73	0.42	3.63	0.05
200	3.22	0.27	3.49	0.11

Time (h)	Average Fe(µmol L^{-1})	Standard deviation	Average Ca(µmol L^{-1})	Standard deviation
24	263.63	13.41	34.01	3.34
48	89.79	9.73	6.59	1.70
72	37.70	2.27	1.71	0.46
96	19.19	1.65	1.29	0.57
120	9.95	1.53	2.46	2.12
150	5.82	0.97	1.79	0.76
175	3.63	0.42	0.66	0.15
200	2.31	0.27	1.64	0.89

Time (h)	Average Mg(µmol L^{-1})	Standard deviation	Average Na(µmol L^{-1})	Standard deviation
24	124.06	5.60	2.09	0.26
48	62.70	5.42	2.93	1.18
72	32.99	1.71	1.23	0.66
96	18.58	1.38	1.03	0.40
120	10.03	1.42	1.73	0.80
150	5.74	0.80	1.39	0.24
175	3.49	0.47	0.81	0.31
200	2.01	0.27	0.83	0.36

BASALT
pH 2

Time (h)	Average K(µmol L^{-1})	Standard deviation
24	0.26	0.05
48	0.28	0.15
72	0.04	0.02
96	0.19	0.05
120	0.42	0.18
150	0.46	0.35
175	0.18	0.12
200	0.39	0.28

BASALT
pH 3

Time (h)	Average Si(µmol L^{-1})	Standard deviation	Average Al(µmol L^{-1})	Standard deviation
24	28.32	1.24	1.88	0.27
48	45.83	2.79	1.07	0.09
72	44.82	3.63	0.80	0.09
96	40.57	2.53	0.66	0.07
120	34.04	2.37	0.54	0.07
150	30.72	1.62	0.52	0.05
175	27.10	1.89	0.51	0.07
200	23.03	1.36	0.47	0.06

Time (h)	Average Fe(µmol L^{-1})	Standard deviation	Average Ca(µmol L^{-1})	Standard deviation
24	38.80	1.21	42.16	5.29
48	60.94	3.60	20.75	2.04
72	58.24	4.71	11.51	1.46
96	50.91	3.11	6.47	0.93
120	41.57	2.81	4.62	1.45
150	36.29	1.83	1.36	0.42
175	31.24	2.07	0.97	0.73
200	26.16	1.35	0.45	0.22

BASALT
pH 3

Time (h)	Average Mg(µmol L^{-1})	Standard deviation	Average Na(µmol L^{-1})	Standard deviation
24	14.38	0.68	1.43	0.21
48	25.56	1.47	3.78	2.18
72	26.67	1.80	0.81	0.12
96	25.94	1.71	0.74	0.18
120	23.21	1.60	1.52	0.86
150	22.08	1.18	0.52	0.11
175	20.09	1.35	0.63	0.22
200	17.74	1.05	0.47	0.14

Time (h)	Average K(µmol L^{-1})	Standard deviation
24	0.40	0.18
48	0.29	0.13
72	0.17	0.01
96	0.18	0.02
120	0.50	0.32
150	0.16	0.05
175	0.23	0.09
200	0.15	0.03

BASALT
pH 5

Time (h)	Average Si(µmol L^{-1})	Standard deviation	Average Al(µmol L^{-1})	Standard deviation
24	0.54	0.16	0.18	0.01
48	0.66	0.18	0.09	0.01
72	0.56	0.12	0.06	0.00
96	0.40	0.11	0.07	0.01
120	0.25	0.11	0.07	0.00
150	0.37	0.10	0.06	0.01
175	0.44	0.03	0.05	0.02
200	0.32	0.09	0.04	0.00

BASALT
pH 5

Time (h)	Average Fe(µmol L^{-1})	Standard deviation	Average Ca(µmol L^{-1})	Standard deviation
24	0.72	0.08	1.28	0.43
48	1.17	0.12	0.40	0.14
72	1.15	0.07	0.30	0.16
96	1.17	0.06	0.25	0.22
120	1.16	0.07	0.13	0.06
150	1.33	0.10	0.18	0.16
175	1.56	0.24	0.14	0.03
200	1.43	0.14	0.14	0.05

Time (h)	Average Mg(µmol L^{-1})	Standard deviation	Average Na(µmol L^{-1})	Standard deviation
24	0.11	0.04	0.78	0.15
48	0.20	0.02	0.65	0.24
72	0.19	0.03	0.43	0.10
96	0.18	0.03	0.43	0.05
120	0.16	0.01	0.32	0.02
150	0.22	0.01	0.34	0.06
175	0.24	0.07	0.21	0.03
200	0.20	0.02	0.23	0.06

ANDESITE
pH 2

Time (h)	Average Si(µmol L^{-1})	Standard deviation	Average Al(µmol L^{-1})	Standard deviation
24	4.05	0.21	3.72	0.18
48	3.01	0.17	3.24	0.20
72	2.61	0.14	3.00	0.16
96	2.58	0.17	3.02	0.21
120	2.36	0.15	2.91	0.22

ANDESITE
pH 2

Time (h)	Average Fe(µmol L^{-1})	Standard deviation	Average Ca(µmol L^{-1})	Standard deviation
24	1.29	0.08	68.05	0.46
48	0.86	0.04	3.09	0.17
72	0.67	0.04	1.35	0.18
96	0.65	0.04	1.79	0.19
120	0.58	0.03	3.81	1.59

Time (h)	Average Mg(µmol L^{-1})	Standard deviation	Average Na(µmol L^{-1})	Standard deviation
24	4.81	1.10	21.85	15.27
48	2.92	0.17	7.28	1.07
72	2.56	0.43	13.02	2.13
96	2.39	0.56	1.73	0.55
120	5.19	2.08	29.88	17.57

Time (h)	Average K(µmol L^{-1})	Standard deviation
24	0.48	0.24
48	0.10	0.04
72	0.21	0.05
96	0.11	0.02
120	1.63	0.86

ANDESITE
pH 3

Time (h)	Average Si(µmol L^{-1})	Standard deviation	Average Al(µmol L^{-1})	Standard deviation
24	1.18	-	0.47	0.01
48	0.69	0.02	0.39	0.02
72	0.64	0.02	0.35	0.03
96	0.50	-	0.29	0.02
120	0.45	0.04	0.26	0.01
150	0.42	0.03	0.34	0.01
175	0.38	0.06	0.31	0.03

ANDESITE
pH 3

Time (h)	Average Fe(µmol L^{-1})	Standard deviation	Average Ca(µmol L^{-1})	Standard deviation
24	0.44	0.05	0.96	0.18
48	0.26	0.02	0.51	0.21
72	0.23	0.02	0.24	0.04
96	0.19	0.02	0.18	0.14
120	0.18	0.02	1.69	0.86
150	0.22	0.02	0.77	0.07
175	0.16	0.03	0.18	0.09

Time (h)	Average Mg(µmol L^{-1})	Standard deviation	Average Na(µmol L^{-1})	Standard deviation
24	3.84	0.15	21.76	0.15
48	0.83	0.08	1.81	0.26
72	0.75	0.09	1.31	0.38
96	0.70	0.03	1.24	0.12
120	0.90	0.10	2.70	0.53
150	0.65	0.05	1.57	0.05
175	0.62	0.21	2.32	1.07

Time (h)	Average K(µmol L^{-1})	Standard deviation
24	0.56	0.03
48	0.23	0.03
72	0.12	0.01
96	0.12	0.03
120	0.21	0.04
150	0.24	0.19
175	0.13	0.07

ANDESITE
pH 5

Time (h)	Average Si(µmol L^{-1})	Standard deviation	Average Al(µmol L^{-1})	Standard deviation
24	0.16	0.06	0.33	0.15
48	0.19	0.04	0.10	0.05
72	0.08	0.04	0.04	0.01
96	0.06	0.04	0.03	0.01
120	0.06	0.03	0.03	0.01
150	0.06	0.04	0.03	0.01
175	0.04	0.01	0.01	0.002
200	0.02	0.01	0.01	0.005

Time (h)	Average Fe(µmol L^{-1})	Standard deviation	Average Ca(µmol L^{-1})	Standard deviation
24	0.15	0.02	0.21	0.04
48	0.07	0.02	1.03	0.78
72	0.08	0.02	0.81	0.17
96	0.06	0.02	1.12	0.50
120	0.04	0.02	0.54	0.19
150	0.03	0.02	0.77	0.27
175	0.002	0	3.67	1.66
200	-	-	0.68	0.35

Time (h)	Average Mg(µmol L^{-1})	Standard deviation	Average Na(µmol L^{-1})	Standard deviation
24	0.24	0.03	0.95	0.04
48	0.57	0.35	2.30	1.83
72	0.38	0.04	1.81	0.32
96	0.53	0.13	3.17	1.57
120	0.75	0.22	4.83	1.70
150	0.63	0.17	3.46	1.02
175	3.44	0.90	33.46	13.65
200	1.05	0.40	5.22	1.43

ANDESITE
pH 5

Time (h)	Average K(µmol L^{-1})	Standard deviation
24	0.07	0.03
48	0.46	0
72	0.32	0.18
96	0.16	0.08
120	0.15	0.06
150	0.14	0.03
175	0.98	0.21
200	0.22	0.10

DACITE
pH 2

Time (h)	Average Si(µmol L^{-1})	Standard deviation	Average Al(µmol L^{-1})	Standard deviation
24	1.55	0.15	2.62	0.23
48	1.28	0.14	2.19	0.19
72	1.16	0.09	2.01	0.16
96	0.98	0.11	1.49	0.13
120	1.06	0.11	1.76	0.17

Time (h)	Average Fe(µmol L^{-1})	Standard deviation	Average Ca(µmol L^{-1})	Standard deviation
24	0.21	0.02	1.23	0.14
48	0.11	0.01	1.41	0.20
72	0.07	0.01	0.58	0.34
96	0.08	0.01	2.98	1.10
120	0.06	0.01	0.37	0.04

DACITE
pH 2

Time (h)	Average Mg(µmol L^{-1})	Standard deviation	Average Na(µmol L^{-1})	Standard deviation
24	0.43	0.14	0.97	0.33
48	0.21	0.06	0.68	0.27
72	0.13	0.08	0.54	0.21
96	7.78	0.16	53.25	0.70
120	0.93	0.03	5.29	0.17

Time (h)	Average K(µmol L^{-1})	Standard deviation
24	0.10	0.02
48	0.05	0.01
72	0.05	0.02
96	1.58	0.20
120	0.12	0.01

DACITE
pH 3

Time (h)	Average Si(µmol L^{-1})	Standard deviation	Average Al(µmol L^{-1})	Standard deviation
24	0.32	0.04	0.52	0.04
48	0.27	0.05	0.44	0.04
72	0.21	0.04	0.36	0.04
96	0.17	0.04	0.27	0.03
120	0.14	0.04	0.17	0.03

Time (h)	Average Fe(µmol L^{-1})	Standard deviation	Average Ca(µmol L^{-1})	Standard deviation
24	0.09	0.01	3.99	0.78
48	0.05	0.01	1.90	0.48
72	0.03	0.006	0.47	0.30
96	0.02	0.008	0.43	0.09
120	0.02	0.006	2.01	0.24

DACITE
pH 3

Time (h)	Average Mg(µmol L^{-1})	Standard deviation	Average Na(µmol L^{-1})	Standard deviation
24	2.16	0.39	12.98	4.94
48	0.97	0.23	5.64	1.77
72	0.45	0.20	1.64	0.40
96	0.30	0.11	2.08	0.43
120	4.46	0.12	37.64	0.78

Time (h)	Average K(µmol L^{-1})	Standard deviation
24	0.42	0.08
48	0.35	0.07
72	0.18	0.04
96	0.17	0.04
120	0.70	0.10

DACITE
pH 5

Time (h)	Average Si(µmol L^{-1})	Standard deviation	Average Al(µmol L^{-1})	Standard deviation
24	0.19	0.03	0.15	0.003
72	0.09	0	0.07	0.02
120	0.09	0.03	0.07	0.01
150	0.06	0.005	0.01	0.004
175	0.05	0.02	0.03	0.01
200	0.05	0	-	-

Time (h)	Average Ca(µmol L^{-1})	Standard deviation	Average Mg(µmol L^{-1})	Standard deviation
24	4.36	0.36	0.13	0.04
72	1.13	0.19	0.04	0
120	2.93	0.93	0.41	0.14
150	0.47	0.20	0.11	0.08
175	3.11	0.55	0.27	0.03
200	1.01	0.64	0.06	0.04

DACITE
pH 5

Time (h)	Average Na(µmol L^{-1})	Standard deviation	Average K(µmol L^{-1})	Standard deviation
24	2.10	0.50	0.17	0.05
72	0.84	0.41	0.06	0.04
120	2.35	0.39	0.21	0.10
150	1.38	0.52	0.07	0.02
175	2.25	0.45	0.17	0.02
200	1.05	0.18	0.10	0.01

RHYOLITE
pH 2

Time (h)	Average Si(µmol L^{-1})	Standard deviation	Average Al(µmol L^{-1})	Standard deviation
24	0.66	0.05	0.63	0.08
48	0.38	0.03	0.47	0.04
72	0.25	0.04	0.38	0.05
96	0.18	0.02	0.36	0.03
120	0.19	0.05	0.36	0.03
150	0.07	0.02	0.30	0.04
175	0.04	0.004	0.30	0.05

Time (h)	Average Fe(µmol L^{-1})	Standard deviation	Average Ca(µmol L^{-1})	Standard deviation
24	0.36	0.09	1.38	0.19
48	0.11	0.01	1.23	0.26
72	0.07	0.01	1.72	0.25
96	0.05	0.004	2.49	1.16
120	0.03	0.001	0.84	0.29
150	0.01	0.001	0.76	0.39
175	0.01	0.001	1.60	0.30

RHYOLITE
pH 2

Time (h)	Average Mg(µmol L^{-1})	Standard deviation	Average Na(µmol L^{-1})	Standard deviation
24	0.28	0.09	0.84	0.14
48	0.26	0.14	3.12	1.82
72	0.18	0.08	0.22	0.18
96	0.14	0.08	0.74	0.50
120	0.08	0.06	0.04	0
150	0.06	0.04	0.10	0.08
175	0.12	0.08	0.49	0.21

RHYOLITE
pH 3

Time (h)	Average Si(µmol L^{-1})	Standard deviation	Average Al(µmol L^{-1})	Standard deviation
24	0.22	0.01	0.20	0.01
48	0.11	0.02	0.11	0.02
72	0.08	0.03	0.07	0.01
96	0.06	0.02	0.06	0.01
120	0.07	0.04	0.05	0.01
150	0.05	0.01	0.03	0.005
175	0.02	0	0.01	0.005
200	0.03	0.02	0.01	0.004

Time (h)	Average Fe(µmol L^{-1})	Standard deviation	Average Ca(µmol L^{-1})	Standard deviation
24	0.50	0.03	4.97	0.70
48	0.10	0.006	1.71	1.24
72	0.06	0.003	0.22	0.07
96	0.04	0.002	0.26	0.01
120	0.04	0.01	0.90	0.37
150	0.01	0	0.24	0.06
175	0.01	0	0.24	0.06
200	0.01	0.004	0.41	0.11

RHYOLITE
pH 3

Time (h)	Average Mg(µmol L^{-1})	Standard deviation	Average Na(µmol L^{-1})	Standard deviation
24	0.14	0.06	4.97	0.70
48	0.09	0.04	1.71	1.24
72	0.03	0.02	0.22	0.07
96	0.03	0.02	0.26	0.01
120	0.07	0.05	0.90	0.37
150	0.04	0.03	0.24	0.06
175	0.004	0	0.24	0.06
200	0.02	0.01	0.41	0.11

RHYOLITE
pH 5

Time (h)	Average Si(µmol L^{-1})	Standard deviation	Average Al(µmol L^{-1})	Standard deviation
24	0.16	0.01	0.11	0.01
48	0.07	0.02	0.07	0.004
72	0.05	0.01	0.06	0.002
96	0.06	0.01	0.06	0.01
120	0.04	0.005	0.04	0.01
150	0.03	0.01	0.04	0.01
175	0.04	0.002	0.03	0.002
200	0.04	0.002	0.02	0

Time (h)	Average Fe(µmol L^{-1})	Standard deviation	Average Ca(µmol L^{-1})	Standard deviation
24	0.79	0.10	1.06	0.73
48	0.29	0.01	1.06	0.73
72	0.13	0.01	0.32	0.03
96	0.07	0.01	1.25	0.73
120	0.04	0.01	0.96	0.09
150	0.02	0.005	1.38	0.44
175	0.02	0.01	0.65	0.07
200	0.01	0.006	2.37	0.12

RHYOLITE
pH 5

Time (h)	Average Mg(µmol L^{-1})	Standard deviation	Average Na(µmol L^{-1})	Standard deviation
24	0.07	0.02	0.35	0.18
48	0.07	0.02	0.35	0.18
72	0.01	0	0.06	0
96	0.08	0.10	1.63	0
120	0.07	0	0.42	0
150	0.05	0.006	0.08	0.01
175	0.04	0	0.08	0.01
200	0.06	0.02	0.11	0.05

Appendix 6.6. Evolution of Ca/Si, Mg/Si and Na/Si rations in the output solution as function of time

6.6.1.BASALT

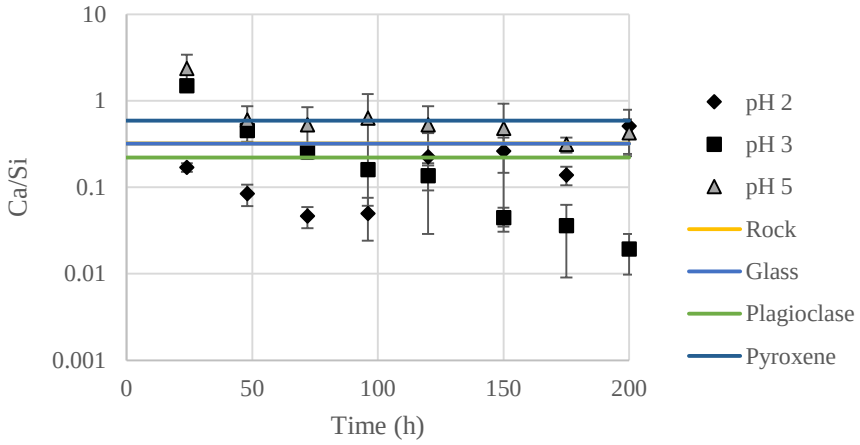

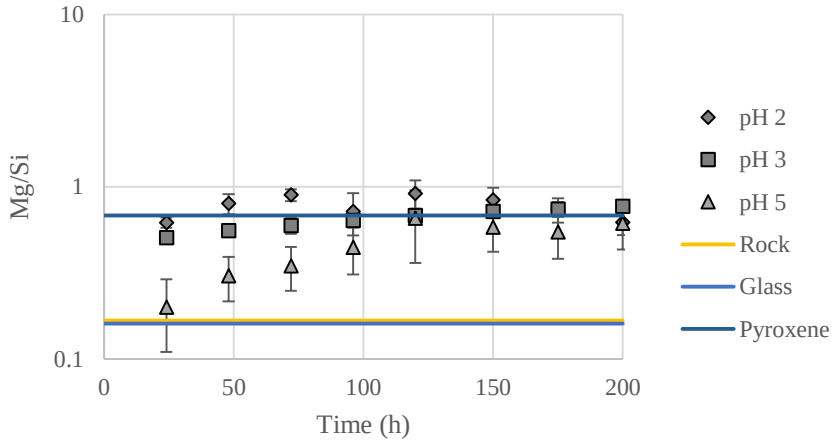

6.6.1.BASALT

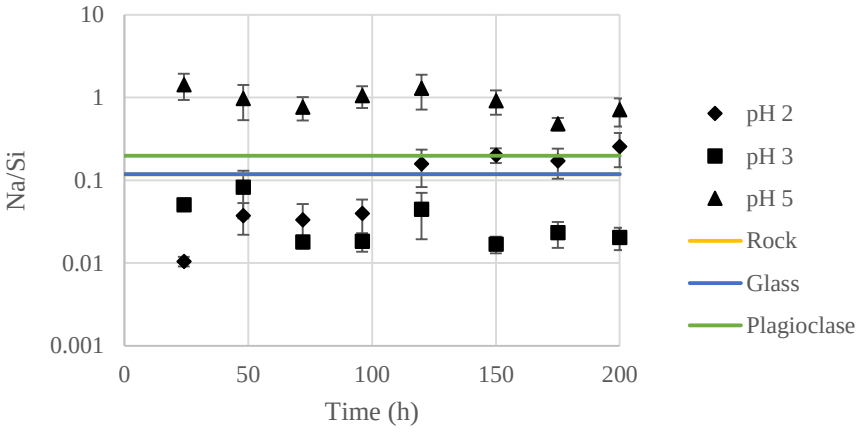

6.6.2. ANDESITE

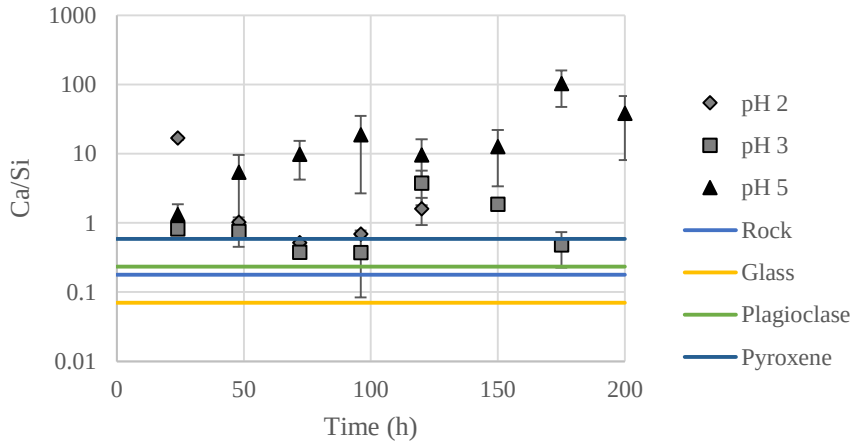

6.6.2. ANDESITE

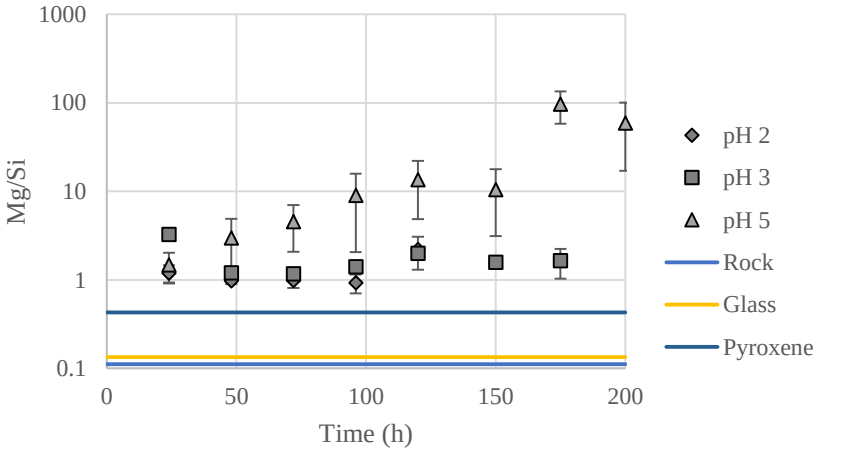

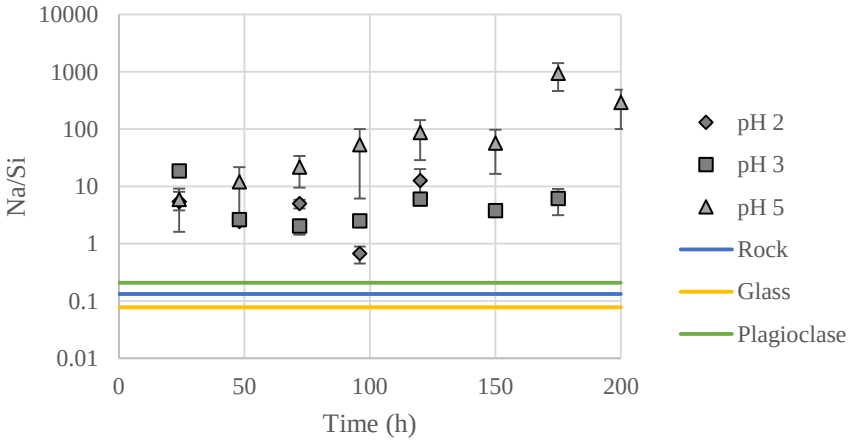

6.6.3. DACITE

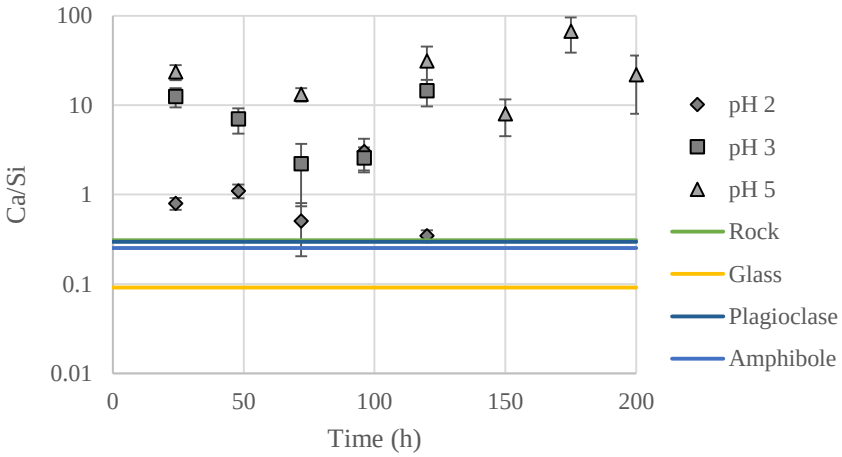
100
10
1
0.1
0.01
Ca/Si
0
50
100
150
200
Time (h)
pH 2
pH 3
pH 5
Rock
Glass
Plagioclase
Amphibole

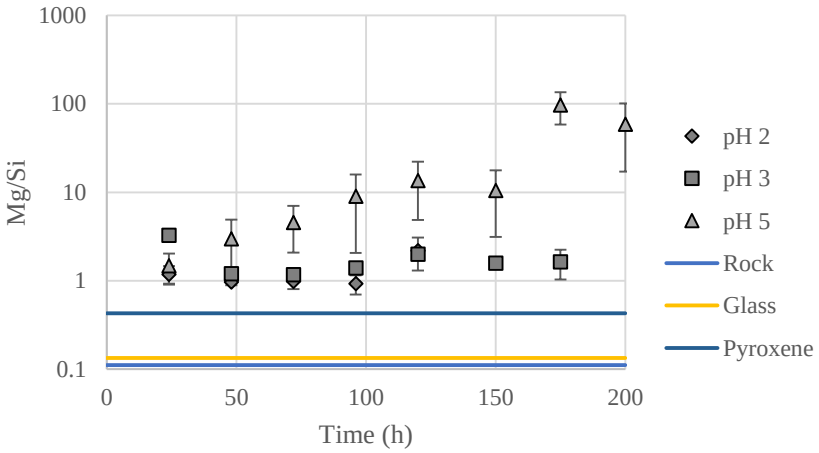
1000
100
10
1
0.1
Mg/Si
0
50
100
150
200
Time (h)
pH 2
pH 3
pH 5
Rock
Glass
Pyroxene

6.6.3. DACITE

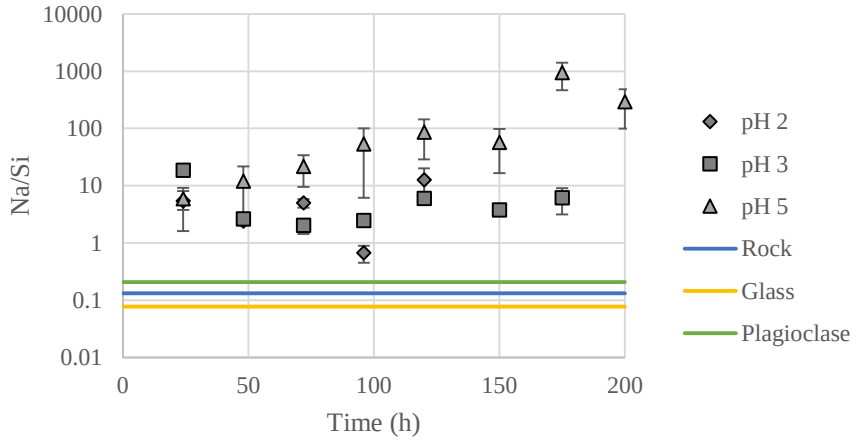

6.6.4. RHYOLITE

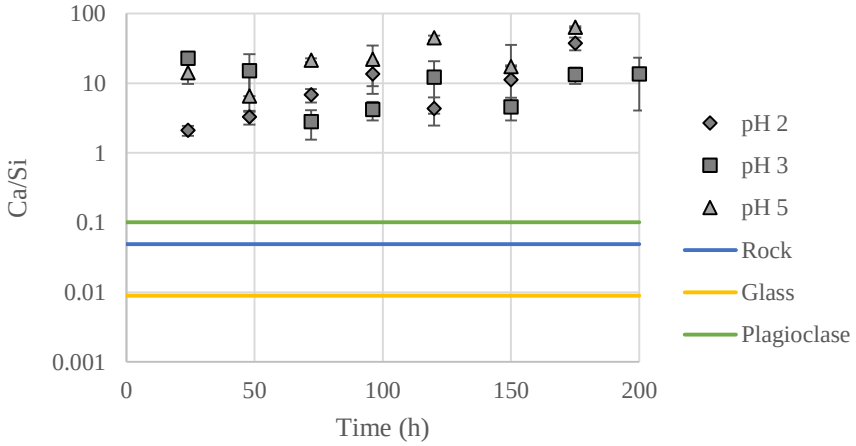

6.6.4. RHYOLITE

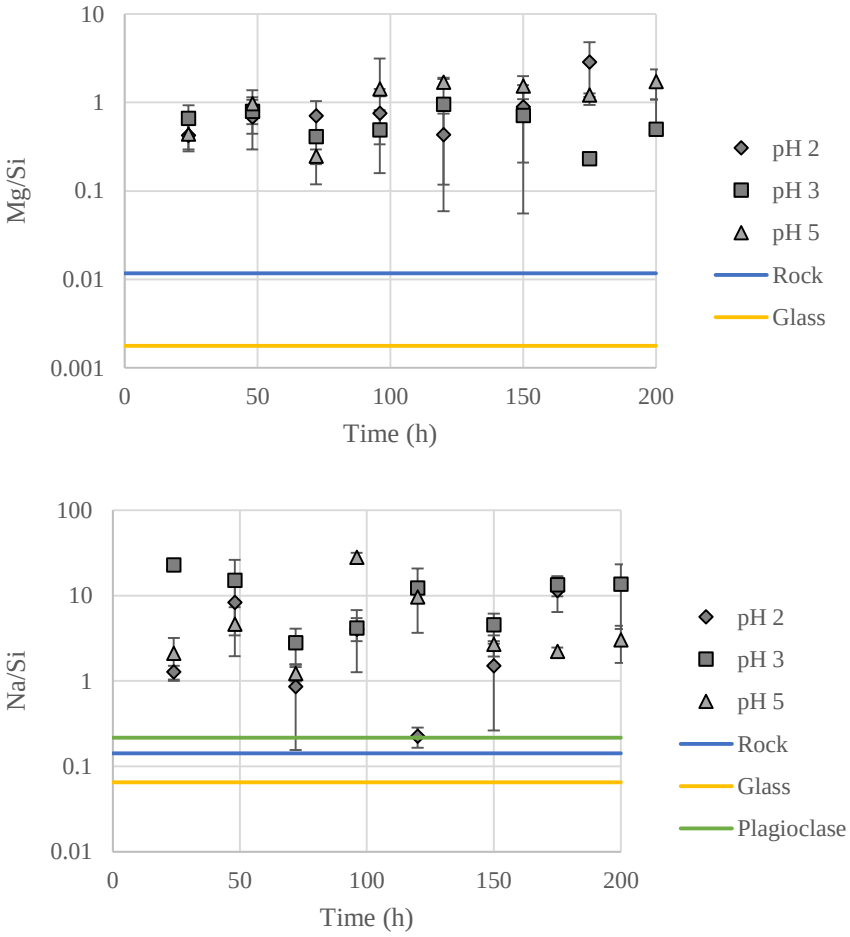

Appendix 6.7. X-ray (XRD) diffractograms of the rock samples, spiked with metallic Si, used in this study

6.7.1. Basalt

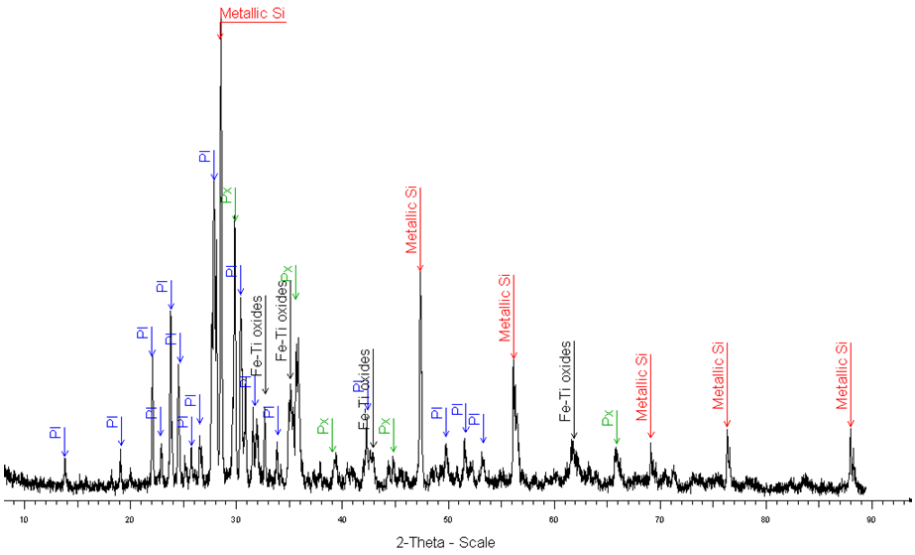

Figure A.6.7.1. Analysis of the XRD diffractogram of the basaltic rock sample (Katla) spiked with metallic Si in the EVA software. The peaks corresponding to metallic Si (red); plagioclase (Pl: blue); pyroxene (Px: green) and Fe-Ti oxides (black).

6.7.2. Andesite

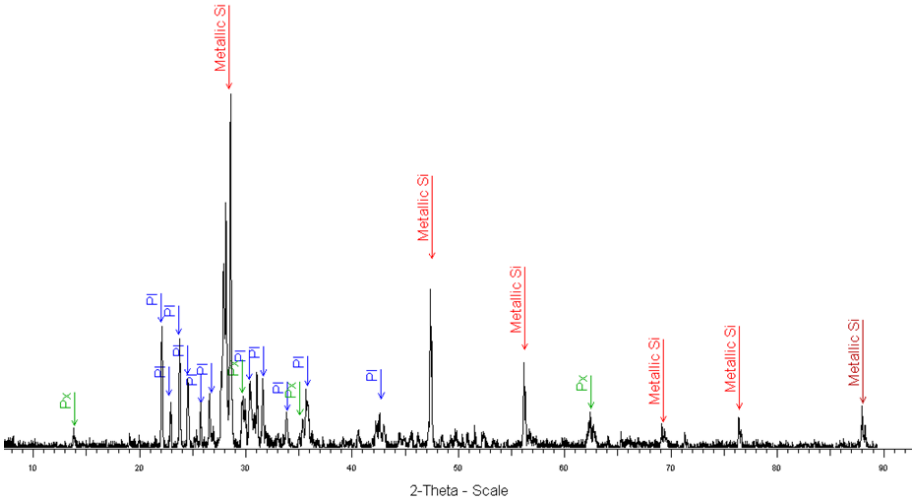

Figure A.6.7.2. Analysis of the XRD diffractogram of the andesitic rock sample (Tungurahua) spiked with metallic Si in the EVA software. The peaks corresponding to metallic Si (red); plagioclase (Pl: blue) and pyroxene (Px: green).

6.7.3. Dacite

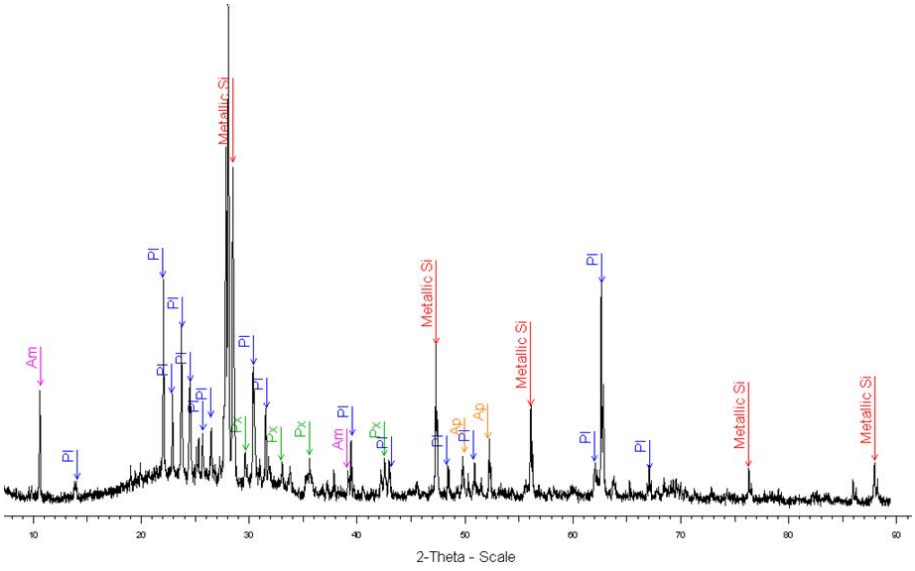

Figure A.6.7.3. Analysis of the XRD diffractogram of the dacitic rock sample (Guagua Pichincha) spiked with metallic Si in the EVA software. The peaks corresponding to metallic Si (red); plagioclase (Pl: blue); pyroxene (Px: green); amphibole (Am: magenta) and apatite (Ap: orange).

6.7.4. Rhyolite

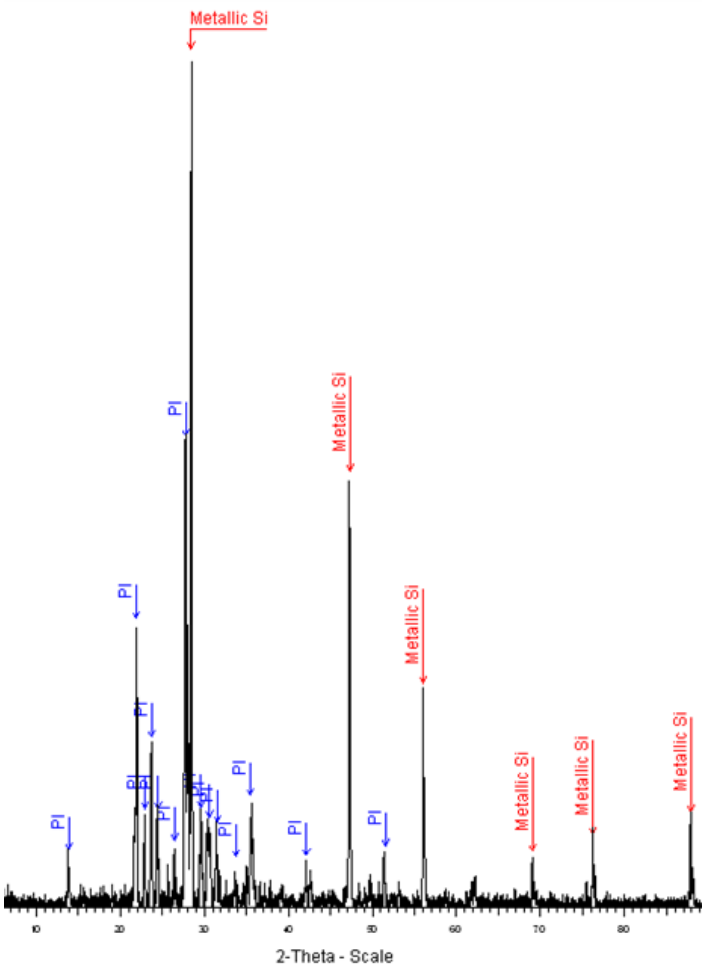

Figure A.6.7.4. Analysis of the XRD diffractogram of the rhyolitic rock sample (Puyehue) spiked with metallic Si in the EVA software. The peaks corresponding to metallic Si (red) and plagioclase (Pl: blue).

CHAPTER 7 Impact of a continent-size tephra deposit on chemical weathering fluxes and atmospheric CO_2 consumption

7.1. INTRODUCTION

Enormous volcanic eruptions occur sporadically at the Earth's surface (Self, 2006; Rougier et al., 2018). These include the flood basalt eruptions that built large igneous provinces over periods of several hundreds of thousands of years. Examples include the Columbia River flood basalts (~2 Ma) in USA, the Deccan Traps (~65 Ma ago) in India and the Siberian Traps (~251-252 Ma ago) in Russia. There is evidence that these eruptions disgorged vast amounts of CO_2 gas into the atmosphere, possibly impacting the global carbon cycle significantly (Self et al., 2006; Delmelle et al., 2015). Conversely, emplacement of fresh basaltic rocks across large area is thought to amplify chemical weathering over geological time scales, resulting in net drawdown of atmospheric CO_2 (Dessert et al., 2001; Dessert et al., 2003). Thus, the formation and weathering of large basaltic provinces exerted an important control on the geochemical and climatic changes on Earth.

Short-lived supereruptions powered by the explosive release of huge volumes (> 1000 km^3) of silicic magmas are another type of episodic volcanic event that has the potential to disrupt geochemical processes at the Earth's surface. Toba (~74 ka ago) in Indonesia, Yellowstone Caldera (~640 ka ago) in USA and La Pacana (~2-4 Ma ago) in Chile belong to this class of eruptions. Compared to flood basalts, and although sizeable, CO_2 emissions from supereruptions probably had a minor effect on the atmospheric C reservoir (Frölicher et al., 2011). Importantly, the tephra expelled by these explosive volcanic events form extensive deposits, known as ignimbrites, blanketing areas of up to several millions of km^2, i.e. a surface area much larger than that covered by lavas from flood basalt eruptions. However, the contribution of such continent-size tephra deposits to the global weathering flux into the ocean and long-term drawdown of atmospheric CO_2 has never been assessed. While silicic igneous rocks should weather less rapidly than mafic ones (Oliva et al., 2003), the predominance of fine-grained tephra in ignimbrites (Sparks et al., 1997) confer them a high surface area, potentially compensating for the subdued chemical reactivity. The tephra material is also typically glassy and thus, more reactive than its crystalline chemical equivalent. Furthermore, tephra deposits are porous, allowing efficient removal of the weathering products and thus, maintenance of far-from equilibrium conditions. A recent study concluded that the return period for supereruptions may be as low as 17 ka (Rougier et al., 2018) has been been estimated to 17 ka. As such, it is

important to characterise the potential effect of such events on the biogeochemical cycles of important elements such as carbon and silicon.

Mechanistic models that incorporate physical descriptions of the below ground hydrology and weathering reactions have been used successfully to predict weathering of continental rocks where time and climate are the variables (Maher et al., 2009; Goddéris et al., 2010; Moore et al., 2012; Goddéris et al., 2013). Here we use the WITCH model (Goddéris et al., 2006; Goddéris et al., 2010) to simulate the weathering of a continent-size tephra deposit. WITCH calculates the changes in the mineral assemblage that occurs as water drains vertically through the weathering profile. It provides the chemical composition of pore water as a function of depth which assists the computation of the dissolved element fluxes leaving the deposit. The calculations can be performed for weathering occurring over annual to multimillennial timescales. In this study, we address the following question: given modern climate conditions, what will be the effect of weathering of a continent-size tephra deposit on the geochemical fluxes of Si and base cations, and on the consumption of atmospheric CO_2. We investigate this question by using the spatial distribution of a deposit formed by a supereruption at Yellowstone Caldera as modelled by Mastin et al. (2014).

7.2. MODEL SET-UP

7.2.1. Continent-size tephra deposit

We simulated the weathering of a continent-size tephra deposit from an eruption of the Yellowstone Caldera in Wyoming, USA. Tephra from the last large Yellowstone eruptions (2.1 Ma, 1.3 Ma, and 640 ka) spread over tens of thousands of km^2 across North America (Christiansen, 2001). Mastin et al. (2014) estimated the distribution of tephra fall that would result from a modern-day Plinian supereruption at Yellowstone volcano under different eruptive scenarios. We used Mastin et al.'s results for a one-week long supereruption that produced 330 km^3 of tephra, dense-rock equivalent. The total terrestrial surface area covered by the tephra deposit is ~5.4 x 10^6 km^2. We considered a maximum deposit thickness of 20 cm. While thicker tephra accumulations are likely to occur in the immediate vicinity of the volcanic source, they typically represent a small contribution to the total surface area affected by tephra (Mastin et al., 2014).

The Yellowstone tephra fall deposit was divided into five isopachs with thickness values of 0.3, 0.7, 2, 7 and 20 cm (Fig. 7.1). The surface areas of the isopachs are ~13 x 10^6, 9.6 x 10^6, 7.4 x 10^6, 4.6 x 10^6 and 2.5 x 10^6 km^2, respectively. For each isopach, the tephra deposit was subdivided into *n* vertical layers of roughly equivalent thickness, i.e. *n* = 1, 2, 3, 5 and 8 for the 0.3, 0.7, 2, 7 and 20 cm isopach, respectively (Fig. S7.1). This allowed similar water residence times at each depth of the tephra deposit.

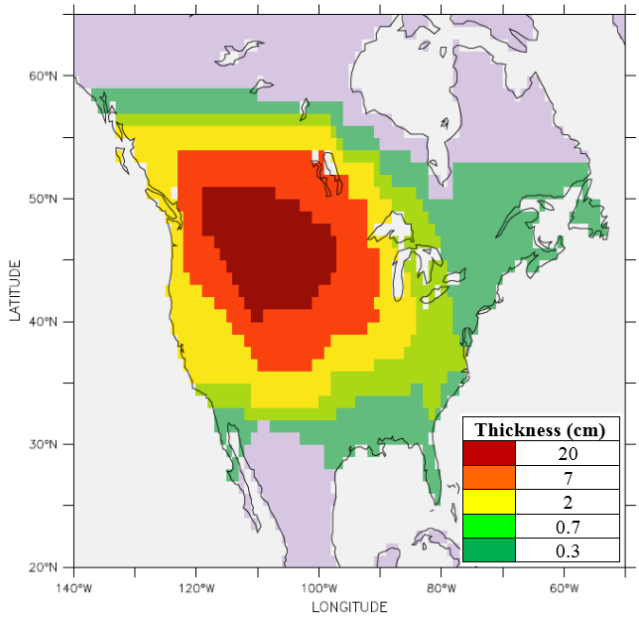

Figure 7.1. Distribution of tephra from a one-week long Yellowstone eruption as modelled by Mastin et al. (2014). The tephra deposit is divided into five isopachs corresponding to deposit thicknesses of 0.3, 0.7, 2, 7 and 20 cm.

7.2.2. The WITCH model

Weathering of a continent-size tephra deposit that would result from a Yellowstone eruption was simulated using the geochemical code WITCH (Goddéris et al., 2006; Goddéris et al., 2009). WITCH is a numerical box model initially developed to predict weathering processes in soil profiles and in river catchments above silicate bedrock. The model has been coupled to biospheric and climate models to investigate rock weathering and atmospheric CO_2 consumption under various conditions (e.g., Le Hir et al., 2009; Beaulieu et al., 2010; Goddéris et al., 2010; Roeland et al., 2010; Beaulieu et al., 2012; Goddéris et al., 2013).

Briefly, WITCH computes the amount of dissolved and precipitated mineral phases resulting from vertical drainage of water through *n* layers of a

weathering profile as a function of time. A mass balance is computed for each layer at each time step using:

$$\frac{d\,(z\cdot\theta\cdot C)}{dt} = F_{top} - F_{bottom} + F_{weathering} - F_{precipitation} \pm F_{exchange} \quad [7.1]$$

where C is the concentration of a given species in layer *n* of thickness z and water volumetric content θ, F_{top} and F_{bottom} are the input flux from the *n-1* layer above and output flux from the *n+1* layer below, respectively, $F_{weathering}$ represents additions from dissolution of primary and secondary minerals, $F_{precipitation}$ accounts for losses through precipitation of secondary minerals and $F_{exchange}$ describes fluxes associated with cation exchange reactions involving clay minerals and organic matter. The last term is not considered in our model set-up. Since WITCH does not include a nucleation model, mineral precipitation rates are assumed to be proportional to the reactive surface areas of the minerals.

The dissolution $F_{weathering}$ and precipitation $F_{precipitation}$ terms for silicate minerals in Equation [7.1] are calculated using kinetic laws derived from the transition state theory (Eyring, 1935; Lasaga, 1981). The overall dissolution rate of a mineral in layer *n* is the sum of three parallel elementary reactions involving protons, hydroxyls and water. We did not consider reactions with organic ligands as organic matter was posited to be absent from the deposit. The limitations of this assumption are discussed in section 7.4.5. The overall dissolution rate of a mineral R_s is derived using (Schott et al., 2009; Goddéris et al., 2010):

$$R_s = A \cdot S_w \left[\sum_i k_i \cdot \exp\left(\frac{E_a^i}{RT}\right) \cdot a_i^{n_i} \cdot f_{inh}\right] (1 - \Omega^s) \quad [7.2]$$

where *A* stands for the mineral reactive surface, S_w is the moisture saturation (which depends on the water volumetric content (Sverdrup and Warfinge, 1995) of layer *n*, k_i and E_a^i are the dissolution rate constant and activation energy for the *i* species-promoted dissolution, respectively, a_i and n_i represent the activity and the order of reaction with respect to the dissolving species *i*, respectively. The parameter f_{inh} describes the inhibiting effect of aqueous species on proton and hydroxyl-promoted aluminosilicate dissolution reactions. In general, Al^{3+} is regarded as the main inhibiting species (e.g., Oelkers et al., 1994; Oelkers and Schott, 1995; Devidal et al., 1997). The effect of departure from equilibrium on mineral dissolution rates is accounted for by the factor $(1 - \Omega^s)$, where Ω stands for the solution saturation index with respect to the particular solid and *s* reflects stoichiometry (i.e. the number of metal atoms that need to be removed to form one precursor complex during

dissolution). $F_{precipitation}$ is computed from Eq. [7.2] when precipitation of secondary phases is allowed to occur, i.e. when the affinity term in equation term is negative (i.e. $\Omega^s > 1$).

The WITCH database contains kinetic laws and thermodynamic parameters for 31 minerals (Goddéris et al., 2006). Kinetic data for the minerals included in our study are summarized in Table 7.1.

Table 7.1. Kinetic dissolution constants at 25 °C (mol m^{-2} s^{-1}) and activation energy (kJ mol^{-1}) of the dissolution reactions promoted by protons (H), hydroxyl (OH) and water (w), as used in the WITCH model. The symbol n is the reaction order with respect to H- or OH-promoted dissolution. n.e.: no effect. Further details can be found in Goddéris et al. (2006; 2010).

	pk_H E_a^H n_H	pk_{OH} E_a^{OH} n_{OH}	pk_w E_a^w
Albite (An_6)[(a)]	9.50 60 0.5	9.95 50 0.3	12.60 67
K-feldspar[(b)]	9.65 60 0.5	10.70 50 0.3	12.85 67
Quartz[(c)]	n.e. n.e. n.e.	11.00 85 0.25	13.40 85

(a) Fitting using with the framework of Eq. [7.2]; data reported by Blum and Stillings (1995) for albite. We assumed that the anorthite content (An_6) did not modify the rate of albite dissolution. (b) Fitting of data for orthoclase as reported by Blum and Stillings (1995). (c) Dove (1994).

In order to compute the dissolution of the tephra's glass constituent, we used the rate equation for rhyolitic glass obtained experimentally by Declerq et al. (2013):

$$r_+ = A\, e^{-\left(\frac{Ea}{RT}\right)} \left(\frac{a_{H^+}^3}{a_{Al^{3+}}}\right)^{1/n} \quad [7.3]$$

where r_+ is the dissolution rate (mol cm $^{-2}$ s^{-1}), A a pre-exponential factor, Ea the activation energy, n the stoichiometric factor, R the gas constant, T the absolute temperature and a_{H^+} and $a_{Al^{3+}}$ the activity of H^+ and Al^{3+}, respectively.

Weathering reactions involving glass-rich tephra often lead to precipitation of short-range order clay-size minerals known as allophanes and to a minor extent, imogolite (Harsh, 2012). Depending on drainage condition, halloysite may also form. Since the kinetics of allophane and imogolite precipitation is not known, we approximated their rate of formation to that described for amorphous silica (Rimstidt and Bathes, 1980). For halloysite, precipitation was quantified based on kaolinite precipitation rate (Drever, 1997). The solubility products of primary and secondary minerals along with the enthalpy of their dissolution reactions are listed in Table 7.2.

Table 7.2. Equilibrium constants at 25 °C and enthalpies of reaction for dissolution of minerals considered in the WITCH model.

	Dissolution reaction	pK_{eq}	ΔH_R^0 (kJ mol^{-1})
Albite	$NaAlSi_3O_8+4H_2O+H^+ \rightarrow Na^+ + Al^{3+} + 3H_4SiO_4$	-2.29	-73.82
Orthoclase	$KAlSi_3O_8+4H_2O+H^+ \rightarrow K^+ + Al^{3+} + 3H_4SiO_4$	0.022	-49.93
Quartz	$SiO_2+2H_2O \rightarrow H_4SiO_4$	3.98	25.06
Rhyolitic Glass[a]	$Al_{0.19}Ca_{0.005}Fe_{0.02}K_{0.09}Mg_{0.001}Na_{0.08}SiO_{2.40} +1.6H_2O+0.8H^+ \rightarrow 0.19Al^{3+}+0.005Ca^{2+}+0.002Fe^{3+}+ +0.09K^+ + 0.0013Mg^{2+}+0.08Na^+ + H_4SiO_4$	2.71	14.00
Allophane[b](imogolite)	$0.5Al_2SiO_3(OH)_4+3\ H^+ \rightarrow Al^{3+}+1.5\ H_2O+0.5\ H_4SiO_4$	-6.0	-96.80
Halloysite[a] (kaolinite)	$Al_2Si_2O_5(OH)_4+6H^+ \rightarrow 2Al^{3+} +2\ H_2O+2\ H_4SiO_4$	-12.5	166.66

Data for mineral and aqueous species are from SUPCRT(SPEQ03.DAT) (see Goddéris et al., 2006) except for Al^{3+} (Caster et al., 1993; Wesolowski and Palmer, 1994) and H_4SiO_4 (Walther and Hegelson, 1977). (a) assumed to be controlled by equilibrium with amorphous silica; Drever (1997) (b) Rimstidt and Barnes (1980).

7.2.3. Model inputs

The mineralogy, reactive surface area A, water volumetric content θ and CO_2 partial pressure of the tephra deposit are important controls of weathering intensity (e.g., Brantley et al., 2008). Values for these variables must be fed in WITCH. We used the mineralogy of the rhyolitic tephra from the Lava Creek Tuff eruption (0.64 Ma ago) as determined by Christiansen (2001) (Table 7.3). We hypothesised the mineralogy of the tephra to be homogeneous across the entire deposit. A value of 1 m^2 g^{-1} was taken as representative of the reactive surface area of tephra (Delmelle et al., 2015). We set a fixed value of 0.2 for θ of the tephra deposit and we did not account for the potential influence of dissolution and precipitation of mineral phases in the tephra deposit on θ. As biomass was absent in the tephra deposit, a biogenic source of CO_2 is excluded from our model. The partial pressure of CO_2 in the tephra deposit's pore spaces was set arbitrarily to eight times that in the atmosphere, i.e. 3.12 x 10^{-3} atm.

Table 7.3. Mineralogy of the rhyolitic tephra from the Lava Creek Tuff eruption (0.64 Ma ago) as reported by Christiansen (2001).

	wt.%
rhyolitic glass $Al_{0.19}Ca_{0.005}Fe_{0.02}K_{0.09}Mg_{0.001}Na_{0.08}SiO_{2.40}$	80.0
quartz	7.34
k-feldspar (Or_{50}-Or_{60})	6.26
albite (An_{10}-An_{20})	5.54

The CRU TS dataset (v.2.1; http://www.cru.uea.ac.uk/) provided spatial climate data covering North America at a grid resolution of 0.5 x 0.5 degree (Mitchell and Jones, 2005). The rainwater reacting with the tephra deposit did not contain any dissolved species. Terrestrial runoff estimates over the tested area were obtained from the UNH-GRDC Composite Runoff Fields V1.0 dataset (http://www.compositerunoff.sr.unh.edu; Fekete et al., 2000). The runoff is assumed to be equal to the vertical drainage of the weathering profile for each grid element. Figure S7.2 in the supplementary material shows the spatial distributions of the average temperature and runoff of the area covered by the tephra deposit.

Weathering of the continent-size deposit was simulated with WITCH over different periods, namely 0.1, 1, 10, 100, 1000 and 10,000 yr. In order to reduce computational time, an acceleration factor was introduced for simulations spanning 100, 1000 and 10,000 yr. A more detailed description of the model adapted to our case study is presented in Appendix 7.1.

7.3. RESULTS

7.3.1. Spatial variations in the Si and cation weathering fluxes

Si weathering fluxes

Figure 7.2 shows the spatial distribution of the flux of Si (kmol km^{-2} yr^{-1}) after 0.1, 1, 10, 100, 1,000 and 10,000 yr of weathering of the continent-size rhyolitic tephra deposit as simulated by WITCH. The highest flux values always occur in the northern Rocky Mountains (500-800 kmol Si km^{-2} yr^{-1}). The Superior Upland, Central Lowland, Interior Low Plateaus, Interior Highlands, southern part of the Appalachian Highlands, north of the Cascade-Sierra Mountains and north of the Pacific Border and Southern and Central Rocky Mountains are characterized by intermediate Si fluxes (100-500 kmol Si km^{-2} yr^{-1}). The rest of the United States typically displays low weathering flux values < 100 kmol Si km^{-2} yr^{-1}.

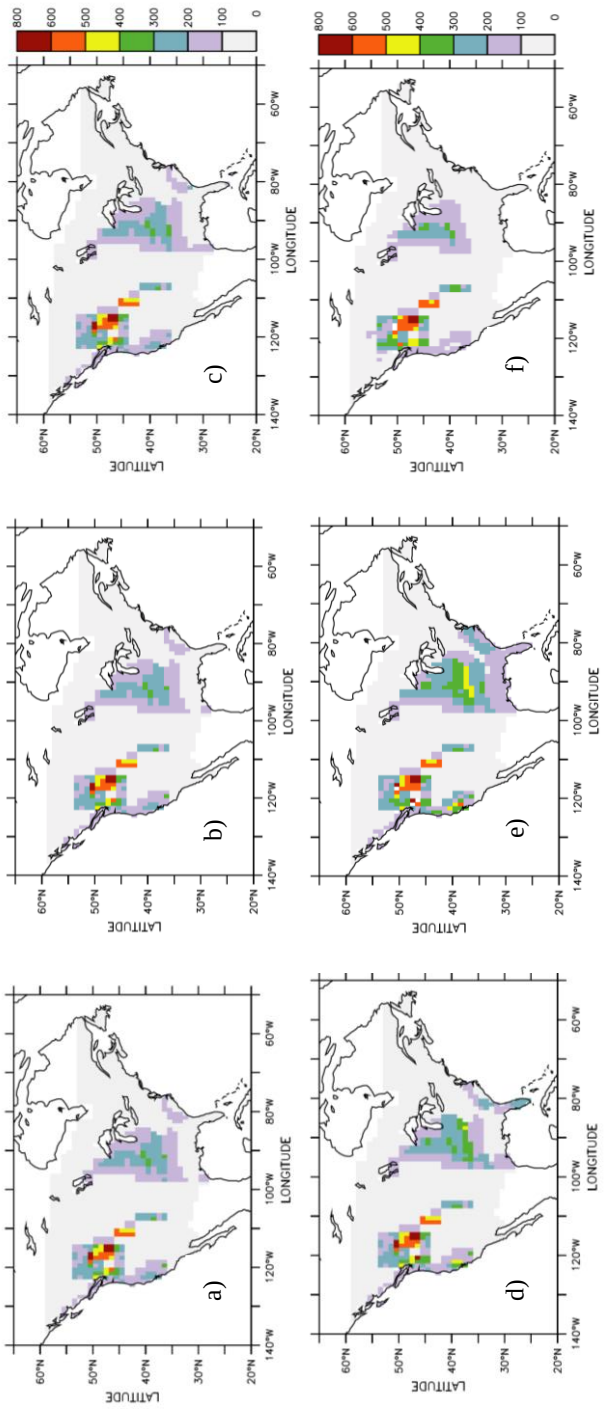

Figure 7.2. Distribution maps of the flux (kmol km^{-2} yr^{-1}) of Si after 0.1 (a), 1 (b), 10 (c), 100 (d), 1000 (e) and 10,000 (f) yr of weathering of the continent-size rhyolitic tephra deposit.

Although the spatial distribution of Si weathering fluxes evolves with time, the general pattern is conserved. Silicon flux increases after 10 yr of weathering in some regions of the West Gulf Coastal Plain (100-200 kmol Si km^{-2} yr^{-1}). Similarly, the Florida peninsula and interior of the Coastal Plains display higher flux values after 100 and 1,000 yr, respectively. Depending on location, the Interior Highlands and Interior Low Plateaus produce higher or lower Si weathering after 1,000 yr. The flux decreases in the Coastal Plain and southern part of the Appalachian Highlands. Irrespective of the physiographic region, there is a general reduction in Si fluxes after 10,000 yr of tephra weathering.

Ca and Mg weathering fluxes

The spatial distribution of Ca weathering fluxes resembles that described for Si (Fig. 7.3). The northern Rocky Mountains exhibit the highest values, i.e. 18-30 kmol Ca km^{-2} yr^{-1}, whereas lower fluxes (3-18 kmol Ca km^{-2} yr^{-1}) are found in the Superior Upland, Central Lowland, Interior Low Plateaus, Interior Highlands, north of the Cascade-Sierra Mountains, north of the Pacific Border and Rocky Mountains System. Elsewhere, the Ca weathering flux is less than 3 kmol Ca km^{-2} yr^{-1}.

After 1 yr of simulation, Ca weathering flux (3-6 kmol Ca km^{-2} yr^{-1}) increases in the Great Plains, specifically the eastern part of the High Plains and the Plains Border. In contrast, the fluxes decline to values < 3 kmol Ca km^{-2} yr^{-1} in the south of the Central Lowland, Interior Highlands and Interior Low Plateaus after 10 yr of weathering. Calcium weathering is also reduced (12-15 kmol Ca km^{-2} yr^{-1}) in the northern Rocky Mountains. For longer time scales (100, 1,000 and 10,000 yr), the Rocky Mountains is the only region where a significant flux of Ca is sustained (3-6 kmol Ca km^{-2} yr^{-1}).

The behaviour of Mg release in response to weathering of the tephra deposit follows closely that of Ca, although the fluxes are typically lower (Fig. 7.4). Magnesium weathering increases in the northern part of the Great Plains in the first 10 yr, but the fluxes decrease across all regions after 100 yr to reach values < 1 kmol Mg km^{-2} yr^{-1} after 1,000 yr.

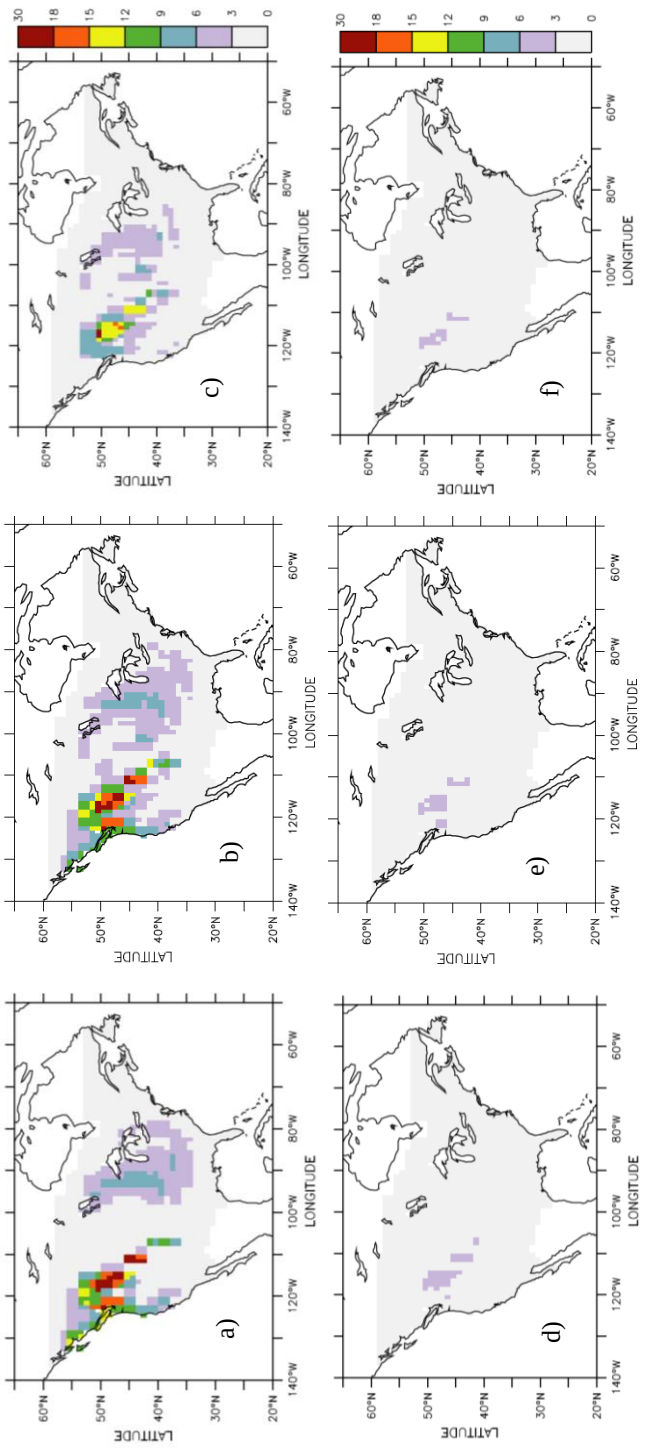

Figure 7.3. Distribution maps of the flux (kmol km^{-2} yr^{-1}) of Ca after 0.1 (a), 1 (b), 10 (c), 100 (d), 1000 (e) and 10,000 (f) yr of weathering of the continent-size rhyolitic tephra deposit.

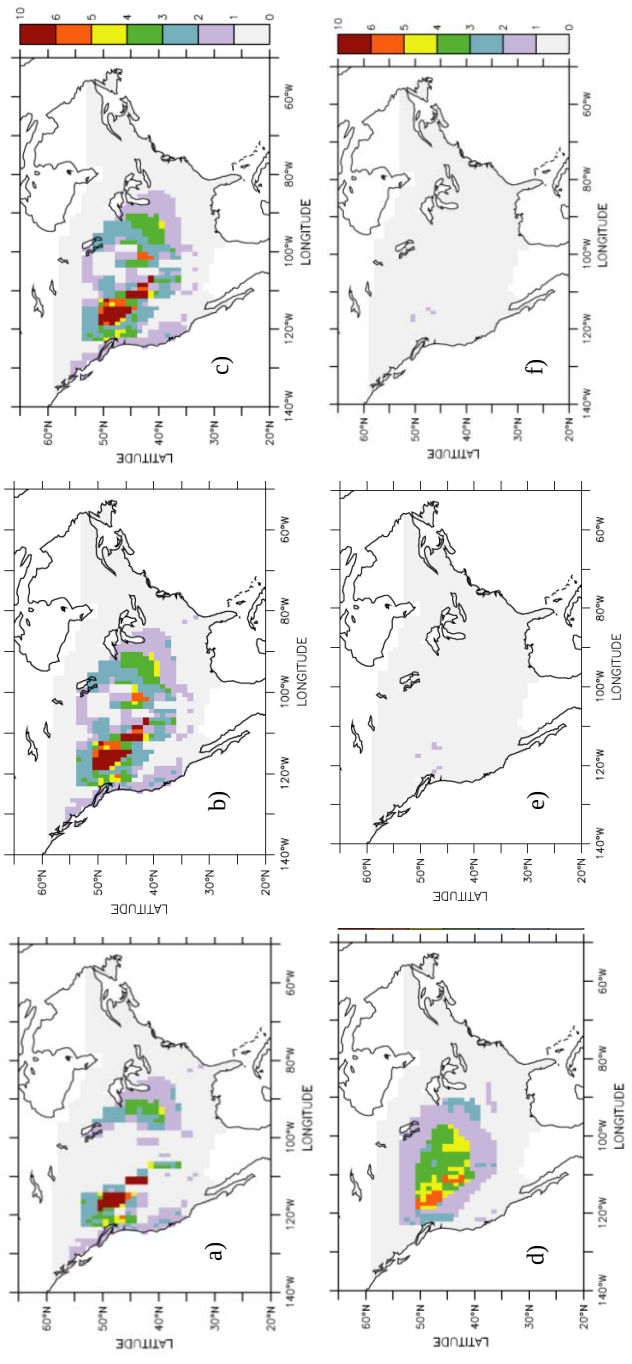

Figure 7.4. Distribution maps of the flux (kmol km^{-2} yr^{-1}) of Mg after 0.1 (a), 1 (b), 10 (c), 100 (d), 1000 (e) and 10,000 (f) yr of weathering of the continent-size rhyolitic tephra deposit.

Na and K weathering fluxes

The fluxes of Na generated through weathering of the continent-size tephra deposit generally exceed those of Ca and Mg (Fig. 7.5). Again, the highest values (42-80 kmol Na km^{-2} yr^{-1}) coincide with the northern Rocky Mountains. Lower weathering fluxes (7-42 kmol Na km^{-2} yr^{-1}) occur in areas corresponding to the Superior Upland, Central Lowland, Interior Low Plateaus, Interior Highlands, southern part of the Appalachian Highlands, north of the Cascade-Sierra Mountains, north of the Pacific Border, Rocky Mountains System and south of the Coastal Plain, including the Florida Peninsula. Other regions have weathering flux values < 7 kmol Na km^{-2} yr^{-1}.

Contrary to Ca and Mg, significant Na weathering persisted after 100 yr. After 10 yr, the Na flux increases (7-14 kmol Na km^{-2} yr^{-1}) in some parts of the West Gulf Coastal Plain. The interior of the Atlantic Coastal Plains and some areas in the Interior Low Plateaus and the Pacific Border also display comparatively higher flux values (14-21 and 42-80 kmol Na km^{-2} yr^{-1}, respectively) after 1,000 yr. A significant reduction in Na release occurs in the Interior Highlands, Interior Low Plateaus, Coastal Plain, southern part of the Appalachian Highlands and south of the Pacific Border after 10,000 yr of weathering. The weathering of K closely mimics that of Na, although the fluxes are slightly lower (Fig. 7.6).

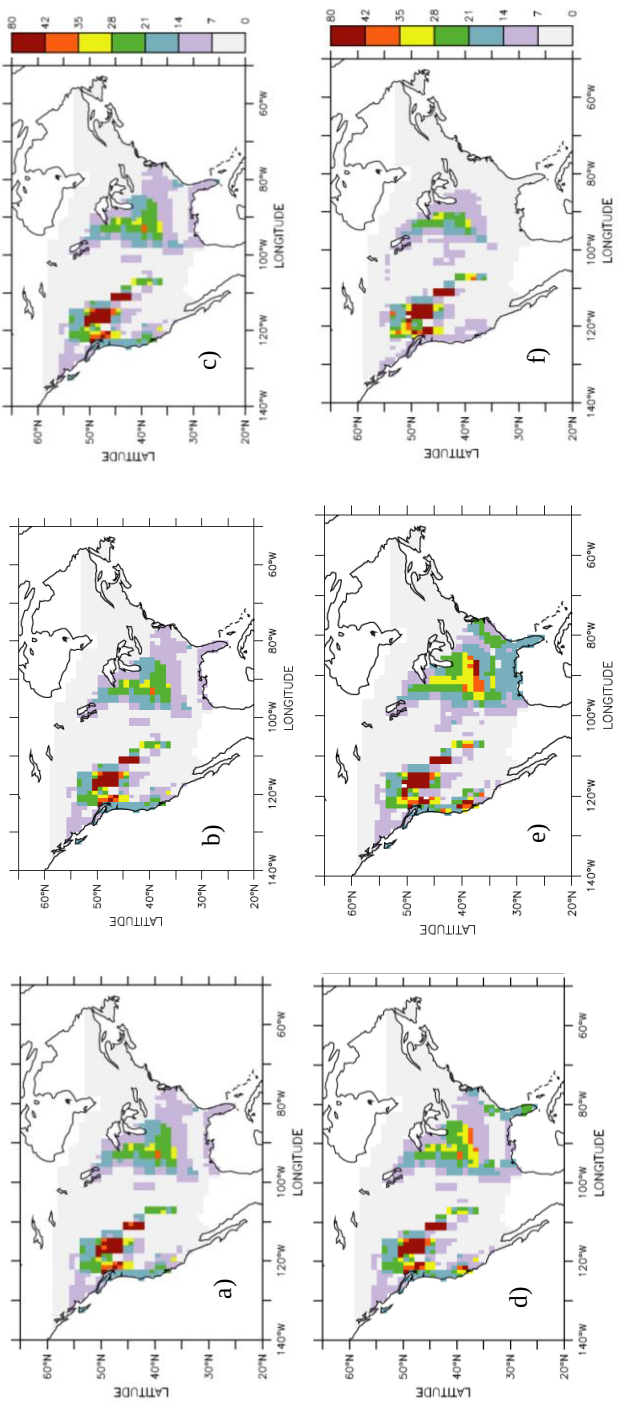

Figure 7.5. Distribution maps of the flux (kmol km^{-2} yr^{-1}) of Na after 0.1 (a), 1 (b), 10 (c), 100 (d), 1000 (e) and 10,000 (f) yr of weathering of the continent-size rhyolitic tephra deposit.

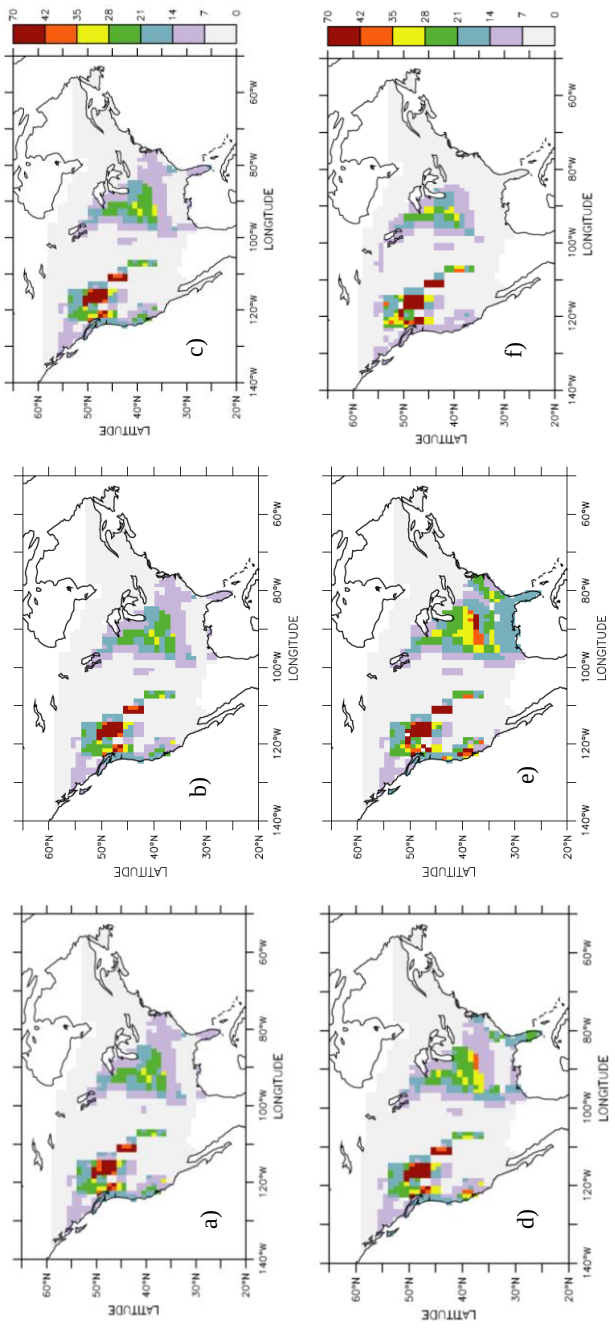

Figure 7.6. Distribution maps of the flux (kmol km^{-2} yr^{-1}) of K after 0.1 (a), 1 (b), 10 (c), 100 (d), 1000 (e) and 10,000 (f) yr of weathering of the continent-size rhyolitic tephra deposit.

7.3.2. Temporal variations in the Si and cation weathering fluxes

The temporal evolution of the total fluxes of Si, Ca, Mg, Na and K generated by weathering of the continent-size tephra deposit is shown in Fig. 7.7. The total weathering flux of Si varies between ~833 and 1,308 Gmol yr^{-1}. It increases by ~24% between 0.1 and 1,000 yr, but it then decreases sharply (~36%) after 10,000 yr of weathering. Much lower flux values are found for the other cations, i.e. Ca: 5-40; Mg: 1.2- 19, Na: 80-131 and K: 81-123 Gmol yr^{-1}. The total fluxes of Na and K follow the same trend as Si. In contrast, a pulse of Ca occurs during the first year and after that, the flux gradually becomes smaller. At the end of the simulation, the total Ca flux is only ~13% of the initial release. Magnesium exhibits a similar behaviour, except that the total flux begun to decrease later, i.e. after 100 yr of weathering.

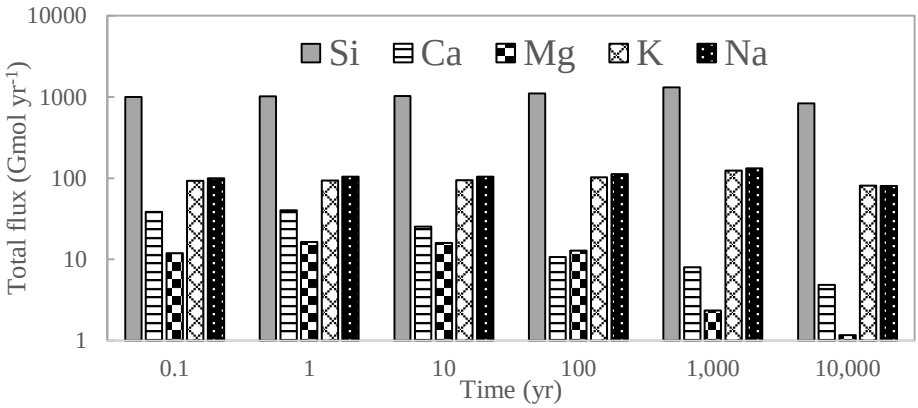

Figure 7.7. Total fluxes of Si, Ca, Mg, K and Na after 0.1, 1, 10, 100, 1000 and 10,000 yr of weathering of the continent-size rhyolite tephra deposit.

7.3.3. CO_2 consumption

In WITCH, the instantaneous atmospheric CO_2 consumption by weathering is calculated as the flux of bicarbonate (HCO_3^-) required to balance the cation release by the dissolution of the tephra's silicate components (i.e. glass and minerals) integrated over the whole weathering profile (Goddéris et al., 2010).According to the simulation results, weathering of the continent-size tephra deposit consumes ~0-10 kmol CO_2 km^{-2} y^{-1} in the arid Midwest and up to 100-200 kmol CO_2 km^{-2} y^{-1} in the northern Rocky Mountains and areas in the North-eastern part of the continent (Fig. 7.8). Carbon dioxide consumption decreases with time, notably in south of the Coastal Plain, including the Florida Peninsula.

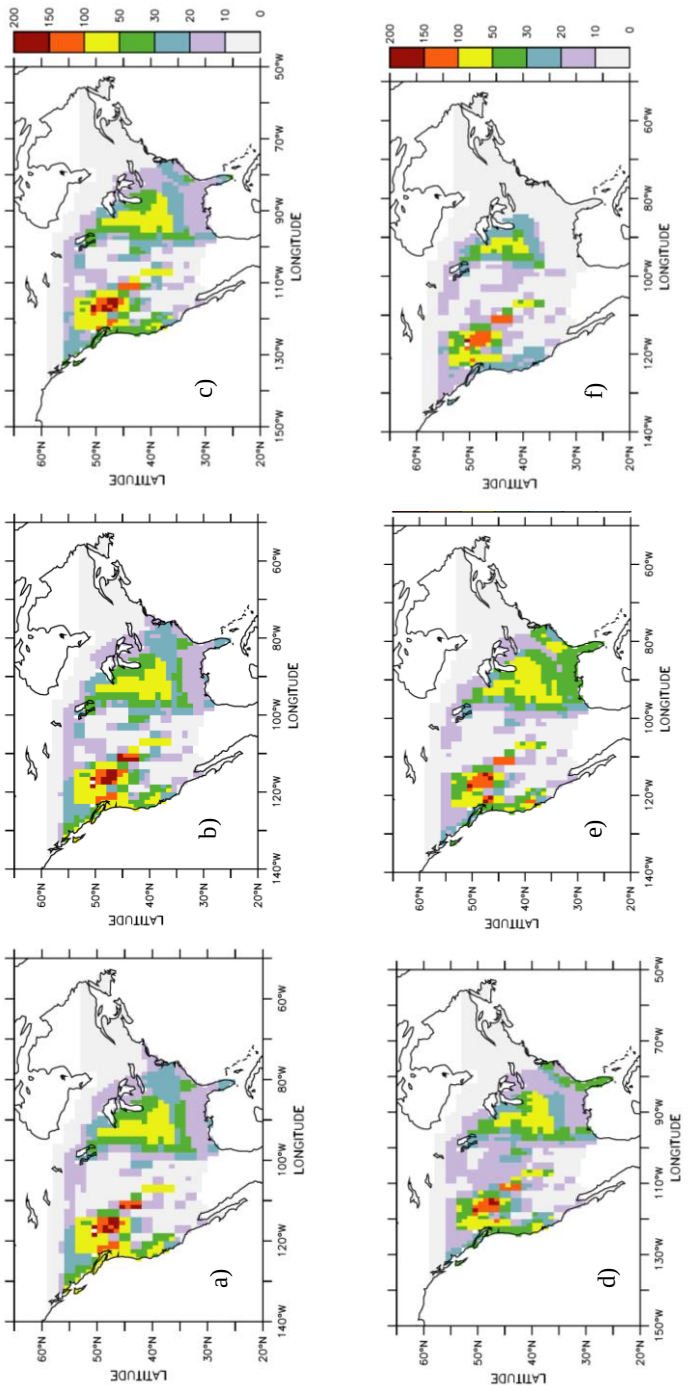

Figure 7.8. Distribution maps of CO_2 consumption (kmol km^{-2} yr^{-1}) after 0.1 (a), 1 (b), 10 (c), 100 (d), 1000 (e) and 10,000 (f) yr of weathering of the continent-size rhyolitic tephra deposit.

Figure 7.9 shows the total consumption of CO_2 (Gmol yr^{-1}) by chemical weathering of the continent-size tephra deposit as computed after 0.1, 1, 10, 100, 1,000 and 10,000 yr. The first thousand years of weathering produces a total CO_2 drawdown of ~261-310 Gmol yr^{-1}. However, total CO_2 consumption decreases by ~45% after 10,000 yr of weathering.

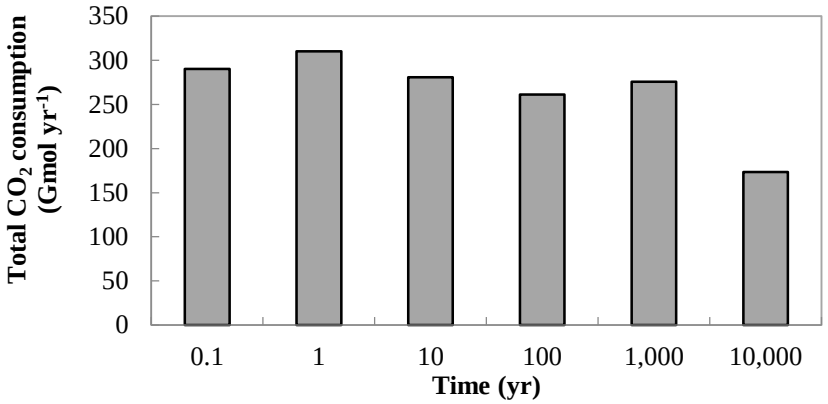

Figure 7.9. Total CO_2 consumption (Gmol yr^{-1}) by chemical weathering of the continent-size rhyolitic tephra deposit.

7.4. DISCUSSION

7.4.1. Influence of tephra deposit thickness and runoff on weathering fluxes

The spatial variations in the Si and base cation fluxes generated by chemical weathering of the continent-size tephra deposit (Figs. 7.1 to 7.5) are the result of the complex interplay between deposit thickness, runoff and temperature. High weathering fluxes, irrespective of the element considered, generally coincide with regions of thick tephra accumulations and elevated runoff values (i.e. short solution residence time). Chemical weathering rates of silicate rocks, and thus fluxes, often increase in tandem with runoff as the removal of weathering products by aqueous transport can drive departure from thermodynamic equilibrium (i.e. transport-controlled weathering) (White and Blum, 1995; Oliva et al., 2003; Dessert et al., 2003; Beaulieu et al., 2010; Maher, 2010; Goddéris et al., 2012). The Great Plains region displays relatively low runoff values and is also characterised by smaller weathering fluxes when compared to other regions covered by a similar or thinner tephra deposit but where higher runoffs prevail, such as the Rocky Mountains, the Interior Highlands and the Appalachian Highlands. A dependence of weathering on temperature does not manifest clearly in our simulations as

parallel variations in runoff and deposit thickness exert a larger influence on weathering fluxes. In a weathering system controlled by solution transport, the effect of temperature on weathering rates occurs largely in response to changes in mineral solubility and not mineral kinetics (White, 2008; Maher, 2010). Thus, the tephra deposit thickness and drainage conditions are the dominant factors controlling the spatial distribution of the Si and base cation fluxes.

7.4.2. Control of the tephra deposit mineralogy on weathering fluxes

The fluxes of Si, Na and K originate from weathering of glass, albite and K-feldspar present in the tephra. In contrast, Ca and Mg releases originate from glass dissolution only. As shown in Figure 7.10, the glassy component always largely dominates the release of Si during weathering of the tephra deposit, irrespective of the deposit thickness and despite the fact that rhyolitic glass should dissolve at a much slower rate (i.e. at least one order of magnitude) than albite and K-feldspar (Declerq et al., 2013; Gudbrandsson et al., 2014). This result implies that weathering of the tephra deposit is transport-limited and essentially controlled by mineral solubilities, the rhyolitic glass being more soluble than the feldspars (Table 7.2).

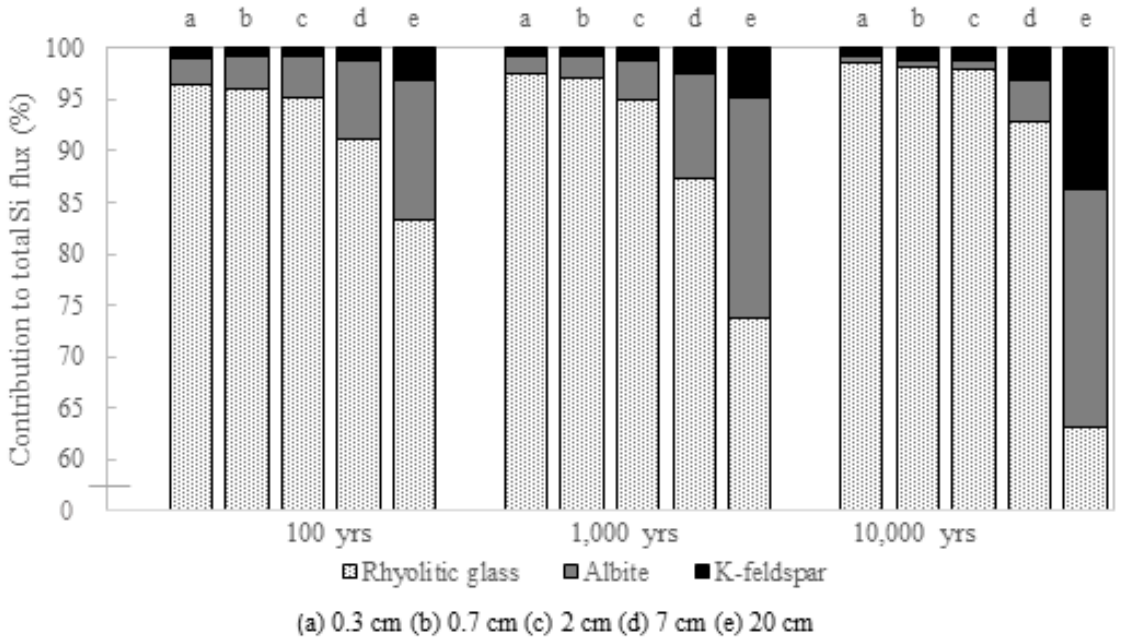

Figure 7.10. Relative contributions of the glass, albite and K-feldspar constituents of the rhyolitic tephra deposit to the total Si flux generated after 100, 1000 and 10,000 yr of weathering.

Inspection of Figure 7.11 reveals that the pore water saturates with respect to glass as it percolates deeper in the tephra deposit. Consequently, strong suppression of glass dissolution occurs below 7 cm and the tephra's glass content hardly decreases (Fig. S7.3). The saturation state of pore waters with respect to albite and K-feldspar also evolves with depth in the deposit (Fig. 7.11). However, the feldspars are comparatively more strongly undersaturated in high runoff regions (e.g., Rocky Mountains) and more strongly oversaturated in low-runoff regions (e.g., Great Plains), a tendency that is particularly manifest for K-feldspar. This indicates that, in contrast to glass, dissolution of the primary minerals in the deeper layers of the tephra deposit remains effective under high drainage conditions. At lower runoff values, weathering is transport-limited and the reactivity of K-feldspar is lower than that of albite due to greater thermodynamic saturation of the former mineral (White, 2008; Goddéris et al., 2010; Goddéris et al., 2013). This explains why the initial content of albite in the bottom layers (> 7 cm) of the tephra deposit is reduced by ~70%, whereas that of K-feldspar decreases only by ~30% (Fig. S7.3).

Ten thousand years of chemical weathering leads to significant removal (up to ~60%) of glass in the upper layers (< 2 cm) of the continent-size tephra deposit (Fig. S7.3). The contents of albite and K-feldspar are also strongly reduced. This is accompanied by a significant reduction in the total weathering fluxes of Si and base cations (Fig. 7.7). The advance of the weathering front deeper in the tephra deposit cannot balance the mass losses in the surface layers because the increase in the saturation state of the percolating pore water with respect to glass, albite and K-feldspar limits weathering rates at depth (see above). Thus, weathering fluxes are a non-linear function of tephra deposit thickness. In contrast to the other cations, the fluxes of Ca and Mg start to decrease after only 10 years of weathering (Fig. 7.7). Again, this reflects the rapid inhibition of glass dissolution (i.e. the only source of Ca and Mg) in response to a thermodynamic control on weathering.

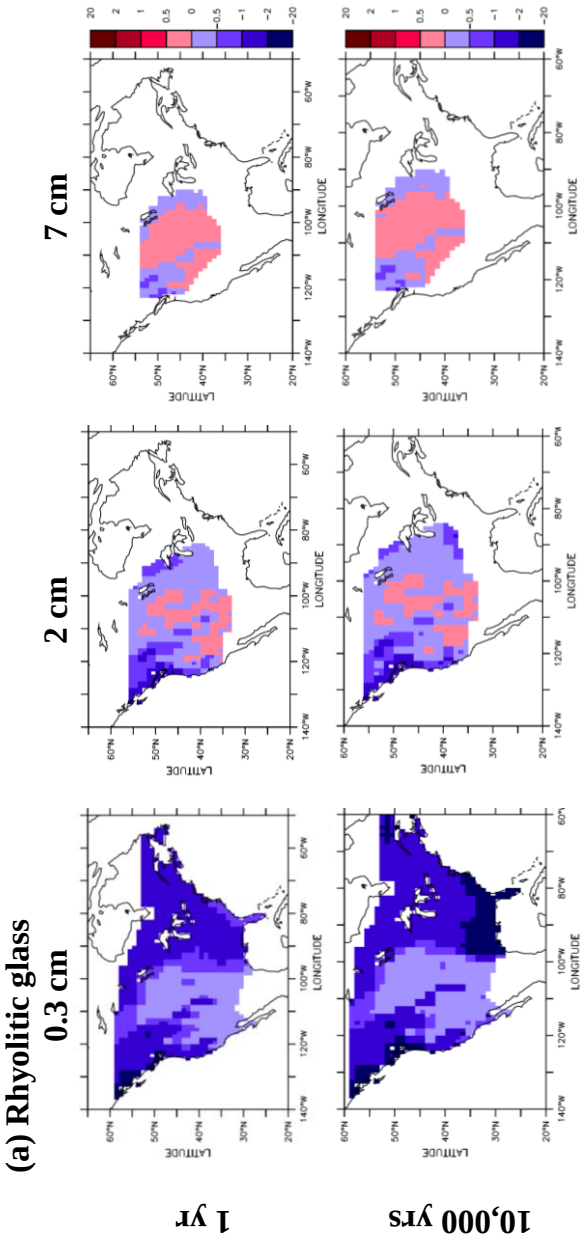

Figure 7.11. Distribution maps of the saturation indices of (a) glass, (b) albite and (c) K-feldspar for pore water at tephra deposit depths of 0.3, 2 and 7 cm as calculated after 1 and 10,000 yr of weathering.

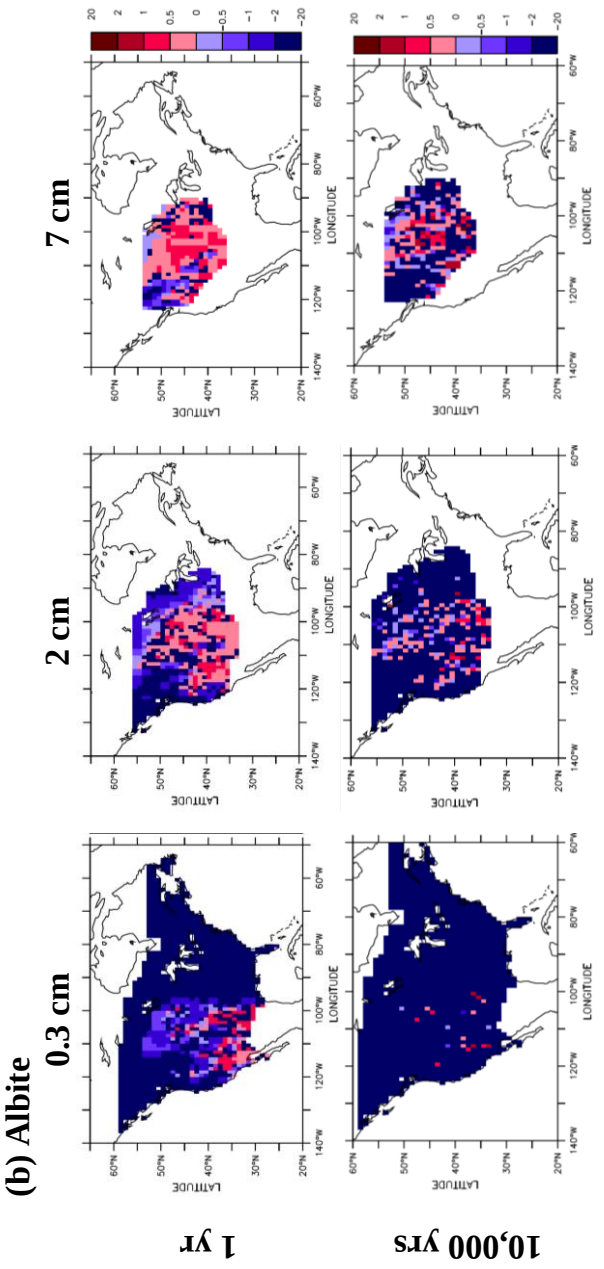

Figure 7.11. (continued). Distribution maps of the saturation indices of (a) glass, (b) albite and (c) K-feldspar for pore water at tephra deposit depths of 0.3, 2 and 7 cm as calculated after 1 and 10,000 yr of weathering.

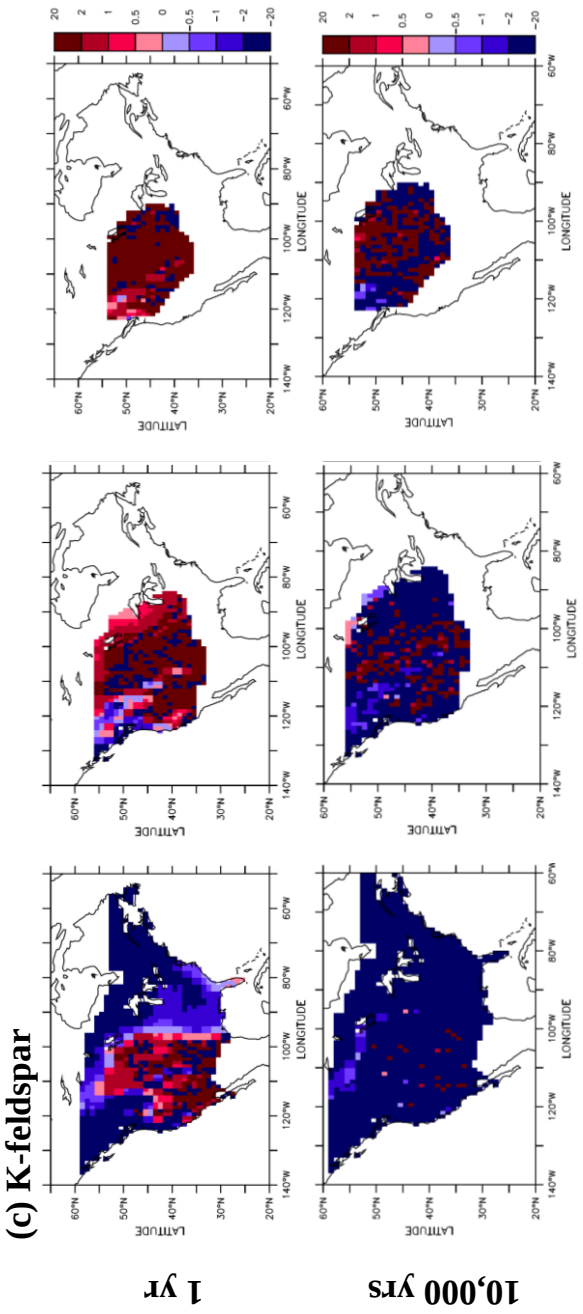

Figure 7.11. (continued). Distribution maps of the saturation indices of (a) glass, (b) albite and (c) K-feldspar for pore water at tephra deposit depths of 0.3, 2 and 7 cm as calculated after 1 and 10,000 yr of weathering.

Ten thousand years of chemical weathering leads to significant removal (up to ~60%) of glass in the upper layers (< 2 cm) of the continent-size tephra deposit (Fig. S7.3). The contents of albite and K-feldspar are also strongly reduced. This is accompanied by a significant reduction in the total weathering fluxes of Si and base cations (Fig. 7.7). The advance of the weathering front deeper in the tephra deposit cannot balance the mass losses in the surface layers because the increase in the saturation state of the percolating pore water with respect to glass, albite and K-feldspar limits weathering rates at depth (see above). Thus, weathering fluxes are a non-linear function of tephra deposit thickness. In contrast to the other cations, the fluxes of Ca and Mg start to decrease after only 10 years of weathering (Fig. 7.7). Again, this reflects the rapid inhibition of glass dissolution (i.e. the only source of Ca and Mg) in response to a thermodynamic control on weathering.

7.4.3. Weathering flux response

The Si flux generated by weathering of the continent-size rhyolitic tephra deposit varies between <100 and 800 kmol km^{-2} yr^{-1}, depending on location but irrespective of the period during which weathering was simulated (Fig. 7.2). These estimates are in the lower value range reported for granitic catchments under a large variety of climates (Oliva et al., 2003), but are considerably lower than the Si fluxes associated with the weathering of basaltic lithologies (~4.5 x 10^5-12.2 x 10^6 kmol Si km^{-2} yr^{-1}; Dessert et al. 2003). As discussed above, the spatial fluctuations in the Si flux originating from tephra weathering reflect primarily the combined effects of runoff and deposit thickness variability.

The total Si weathering flux from the continent-size tephra deposit ranges between 833 (10,000 yr) and 1308 (1000 yr) Gmol Si yr^{-1}. These values are upper bound estimates that do not account for retention of dissolved Si within the fluvial system. The natural retention of Si within lakes and wetlands may decrease its export from the continent to the ocean by at least ~15% (Dürr et al., 2011; Lauerwald et al., 2013). Factoring this effect in our model predictions produces a total flux of dissolved Si in the range ~708-1112 Gmol yr^{-1}. This compares to the annual export of dissolved Si from North America of 786 Gmol yr^{-1}, which is also roughly equivalent to that (~752 Gmol yr^{-1}) carried by the Amazon river (which drains silicate-dominated lithologies) into the Atlantic Ocean (Dürr et al., 2011). Thus, the model results suggest that weathering of a continent-size tephra deposit by a modern supereruption at Yellowstone will have a large impact on the transfer of dissolved Si from the North America continent to the ocean, potentially altering the Si budget of coastal waters for several thousands of years.

The base cation (Na + K + Ca + Mg) flux produced by weathering of the Yellowstone tephra deposit varies between ~18 and 190 kmol km^{-2} yr^{-1} and ~18 and 158 kmol km^{-2} yr^{-1} after 1 and 10,000 yr of weathering, respectively. For comparison, cationic weathering fluxes of ~3.8 x 10^3 kmol km^2 yr^{-1} and 3.1-31.7 x 10^3 kmol km^{-2} yr^{-1} have been reported for volcanic rocks in Luzon, Philippines (Schopka et al., 2011) and andesitic lithologies in Panama (Harmon et al., 2013), respectively. A major difference is that the cationic flux in these regions is dominated by Ca and Mg, whereas it is Na and K that drive it in our simulations. This relates to the absence of Ca and Mg silicates in the mineralogy of the rhyolitic tephra from Yellowstone. The total base cation flux from the continent-size tephra deposit ranges from 167.6 (10,000 yr of weathering) to 254.0 (1 yr of weathering) Gmol yr^{-1}. These values are about 2.6 to 1.7 times lower than the cationic mass flux inferred for the Amazon river (Gaillardet et al., 1999).

7.4.4. CO_2 consumption response

The spatial variations in the predicted CO_2 consumption by chemical weathering of the continent-size tephra deposit (Fig. 7.8) simply mirror the simultaneous effects of runoff and tephra deposit thickness on the weathering fluxes (see section 7.4.3). The annual consumption of CO_2 (up to 200 kmol km^{-2} yr^{-1}) is within the range of values obtained for present-day weathering of acid volcanic rocks on the North American continent, i.e. ~100 and 500 kmol CO_2 km^{-2} yr^{-1} (Moosdorf et al., 2011). However, much higher values have been reported for volcanic terrains elsewhere. For example, Goldsmith et al. (2008) calculated CO_2 consumption fluxes of 1182-2,390 kmol km^{-2} yr^{-1} for the Taranaki region rivers, which drain soils formed from andesitic pyroclasts on North Island, New Zealand. In Luzon, weathering of volcanic rocks consumes on average 3,580 kmol CO_2 km^{-2} yr^{-1} (Schopka et al., 2011). The rate of CO_2 drawdown by chemical weathering of the ~65 Ma Deccan Traps' basalts is 580-2,540 kmol km^{-2} yr^{-1} (Dessert et al., 2003).

The total amount of atmospheric CO_2 that would be consumed yearly if North America was covered by a tephra deposit from a supereruption of Yellowstone compares to the CO_2 drawdown by silicate rock weathering in the Amazon basin (~0.32 x 10^3 Gmol CO_2 yr^{-1}; Gaillardet et al., 1999). However, it is more than an order below the present-day total CO_2 consumption in North America (i.e. ~4.2 x 10^3 Gmol CO_2 yr^{-1}; Mossdorf et al. 2011), and it represents less than 3% of the global value of ~11.7-11.9 x 10^3 Gmol CO_2 yr (Gaillardet et al., 1999; Moon et al., 2014). While weathering of fresh basaltic rocks emplaced during flood basalt eruptions such as the Deccan Traps and Central Atlantic Magmatic Province may bring atmospheric CO_2 below pre-eruptive concentration levels (e.g. Kump et al., 2000), our modelling results indicate

that the influence of an extensive continental tephra deposit, blanketing areas of up to several millions of km^2, on atmospheric CO_2 is comparatively minor.

7.4.5. Limitations of the model

The hydrology of the tephra deposit, or of any weathering profile, exerts a crucial control on weathering processes. A deposit that drains well favours the removal of dissolved cations liberated by dissolution reactions. Drainage is determined primarily by porosity, which depends on the particle size distribution and compaction of the deposit. In general, tephra particle size decreases with distance from the volcanic vent and therefore, one may expect a concomitant change in the deposit porosity. However, silicic eruptions such as those produced by Yellowstone volcano are typically associated with a large proportion of very fine tephra (< 63 μm) (Sparks et al., 1997), arguing for a relatively invariant deposit porosity across most of the affected area.

Another important control on the hydrology of a weathering profile is evapotranspiration, which in turn is governed by the presence of vegetation. In our study, we assumed complete destruction of flora by the tephra deposit. This is a simplistic hypothesis since plants that are not completely buried by tephra are likely to survive (Ayris and Delmelle, 2012). To our knowledge, there is no studies of the decline in vegetation following a supereruption. Furthermore, depending on location, climate conditions and other ecological factors, vegetation will begin to recolonize the tephra-blanketed land quickly, i.e. within a few decades. In turn, through evapotranspiration, vegetation recovery will impact on drainage of the tephra deposit. The presence of plants will also modulate the below-ground partial pressure of CO_2, which was assumed to be invariant in our simulations.

Allophanes are short-range order hydrous aluminosilicates that commonly form in volcanic soils derived from tephra weathering. Since the thermodynamic properties of allophanes are poorly described, we approximated their solubility product using that of amorphous silica. This is a simplification that also does not account for the well-known dependence of allophane precipitation on pH (Shoji et al., 1993). Further, data on the kinetics of precipitation/dissolution of allophanes are lacking. In addition, allophane formation in weathered tephra is responsible for the development of a substantial cation exchange capacity. While WITCH can accommodate the calculation of ion exchange reactions, our model neglected them.

7.5. CONCLUSIONS

Supereruptions are catastrophic volcanic events that can blanket continent-size areas with fine-grained tephra. Through chemical weathering of such voluminous deposits, these eruptions have the potential to enhance the geochemical fluxes of elements exported to the ocean and to decrease the atmospheric concentration of CO_2. Using the mechanistic model WITCH, we simulated the weathering of a rhyolite tephra material deposited across USA by a modern-day supereruption of Yellowstone Caldera eruption. We simulated 0.1, 10, 100, 1000 and 10,000 yr of weathering. The model results showed that tephra deposit thickness and drainage conditions are the main factors dictating the spatial distribution of the Si and base cation fluxes generated though weathering. We also found that weathering is transport-limited and that mineral solubility exerted a key control on the development of the weathering front in the deposit. Thus, weathering fluxes are a non-linear function of tephra deposit thickness.

Weathering of the continent-size deposit generated on average a yearly Si flux more than three orders of magnitude lower than that reported for basaltic lithologies. Despite the low value, the total flux of tephra-derived dissolved Si is on par with the annual export from North America and that carried by the Amazon river. This finding highlights the multimillenial impact of a continent-size tephra deposit on the transfer of dissolved Si to the ocean. While significant, the calculated cationic weathering fluxes were substantially lower than those reported elsewhere for volcanic terrains with mixed lithologies. The average annual consumption of atmospheric CO_2 resulting from weathering of the rhyolite tephra is also much small compared to the estimates made for these regions. This difference is largely due to the absence of Ca- and Mg-silicate minerals in the modelled rhyolite tephra. Finally, the total amount of atmospheric CO_2 that would be consumed yearly due to weathering of the continent-size tephra deposit is less than 3% of the global weathering-induced CO_2 drawdown. Overall, we conclude that a supereruption will enhance considerably the weathering flux of Si during thousands of years but will have a relatively minor impact on CO_2 drawdown. The mechanistic simulation of tephra weathering would benefit from a better knowledge of the thermodynamics and kinetics of precipitation/dissolution of short-range order allophane minerals that typically form in tephra-derived volcanic soils.

References

Ayris, P.M and Delmelle, P (2012) The immediate environmental effects of tephra emission. Bulletin of Volcanology 74:1905-1936.

Beaulieu, E., Goddéris, Y., Donnadieu, Y., Labat, D., Roelandt, C. (2012) High sensitivity of the continental-weathering carbon dioxide sink to future climate change. Letters Nature Climate Change Vol 2. 1419. 346-349.

Beaulieu, E., Goddéris, Y., Labat, D., Roelandt, C., Oliva, P., Guerrero, B. (2010) Impact of atmospheric CO_2 levels on continental silicate weathering. Geochmistry Geophysics Geosystems. Vol 11. No7. doi:10.1029/2010GC003078.

Blum, A.E. and Stillings, L.L. (1995) Feldspar dissolution kinetics. In Chemical Weathering Rates of Silicate Minerals, vol. 31 (eds. A.F. White and S.L., Brantley); Reviews in Mineralogy, pp 291-351.

Brantley, S.L, Golhaber, M.B., Ragnarsdottir, K.V. (2008) Crossing disciplines and scales to understand the Critical Zone. Elements 3. 307-314.

Caster, S., Dandurand, J.-L., Schott, J., Gout, R. (1993) Boehmite solubility and aqueous aluminium speciation in hydrothermal solutions (90-350 °C): experimental study and modeling. Geochim. Cosmochim Acta 57. 4869-4884.

Christiansen, R.L. (2001) The Quaternary and Pliocene Yellowstone Plateau Volcanic Field of Wyoming, Idaho, and Montana. Geology of Yellowstone National Park. USGS. Professional Paper 729-G.

Delmelle, P., Villiéras, F., Pelletier, M. (2005) Surface area, porosity and water adsorption properties of fine volcanic ash particles. Bulletin of Volcanology 67. 160-169.

Delmelle, P., Maters, E., Oppenheimer, C. (2015) Volcanic Influences on the Carbon, Sulfur, and Halogen Biogeochemical Cycles. Chapter 50 In: Sigurdsson, H., Houghton, B., Rymer, H., Stix, J., McNutt, S. (Eds), The Encyclopedia of Volcanoes. Second Edition, pp.881-893.

Declerq, J., Diedrich, T., Perrot, M., Gislason, S.R., Oelkers, E.H. (2013) Experimental determination of rhyolitic glass dissolution rates at 40-200°C and 2<pH<10.1. Geochimica et Cosmochimica Acta 100. 251-263.

Dessert, C., Dupré, B., François, L.M., Schott, J., Gaillardet, J., Chakrapani, G.J., Bajpai, S., (2001). Erosion of Deccan Traps determined by river

geochemistry: impact on the global climate and the 87Sr/86Sr ratio of seawater. Earth Planet. Sci. Lett. 188. 459– 474.

Dessert, C., Dupré, B., Gaillardet, J., François, L.M., Allègre, C.J. (2003) Basalt weathering laws and the impact of basalt weathering on the global carbon cycle. Chem Geol 202. 257-273.

Devidal, J.L., Schott, J., Dandurand, J.-L. (1997) An experimental study of kaolinite dissolution and precipitation kinetics as a function of chemical affinity and solution composition at 150°C, 40 bars, and pH 2, 6.8, and 7.8. Geochimica et Cosmochimica Acta 61 (24): 5165-5186.

Dove, P.M. (1994) The dissolution kinetics of quartz in sodium chloride solutions at 25 °C to 300 °C. Am. J. Sci. 294. 665-712.

Drever, J.I. (1997) The Geochemistry of Natural Waters. Prentice Hall, Upper Saddle River, New Yersey 07458.

Dürr, H.H., Meybeck, M., Hartmann, J., Laurelle, G.G., Roubeix, V. (2011) Global spatial distribution of natural riverine silica inputs to the coastal zone. Biogeosciences. 8. 597-620.

Eyring, H. (1935) The activated complex in chemical reactions. J. Chem. Phys. 3. 107-115.

Fekete, B.M., Vörösmarty C.J. and Grabs, W. (2000) Global, Composite Runoff Fields Based on Observed River Discharge and Simulated Water Balance. http://www.grdc.sr.unh.edu/

Frölicher, T.L., Joos, F., Raible, C.C. (2011) Sensitivity of atmospheric CO_2 and climate to explosive volcanic eruptions. Biogeosciences 8. 2317-2339.

Gaillardet, J., Dupré, B., Louvat, P., Allègre, C.J. (1999) Global silicate weathering and CO_2 consumption rates deduced from the chemistry of large rivers. Chemical Geology 159. 3-30.

Goddéris, Y., François, L.M., Probst, A., Schott, J., Moncoulon, D., Labat, D. and Viville, D. (2006) Modelling weathering process at the catchment scale: The WITCH numerical model. Geochimica et Cosmochimica Acta 70. 1128-1147.

Goddéris Y., I., Roelandt, C., Schott, J., Pierret M. and François, L.M. (2009) Towards an Integrated Model of Weathering, Climate, and Biospheric Processes. In Oelkers, E.H and Schott, J. (Eds) Reviews in Mineralogy & Geochemistry. Vol 70 pp. 411-434.

Goddéris, Y., Williams, J.Z., Schott, J., Pollard, D., Brantley, S.L. (2010) Time evolution of the mineralogical composition of Mississippi Valley loess over the last 10 kyr: Climate and geochemical modelling. Geochmica et Cosmochmica Acta 74. 6357-6374.

Goddéris, Y., Brantley, S.L., François, L.M., Schott, J., Pollard, D., Déqué, M., Dury, M. (2012) Rates of consumption of atmospheric CO_2 through the weathering of loess during the next 100 yr of climate change. Biogeosciences 10. 135-148.

Goddéris, Y., Brantley, S.L., François, L.M., Schott, J., Pollard, D., Déqué, M., Dury, M. (2013) Rates of consumption of atmospheric CO_2 through the weathering of loess during the next 100 yr of climate change. Biogeosciences, 10. 135-148.

Goldsmith, S.T., Carey, A.E., Lyons, W.B., Hicks, D.M (2008) Geochemical fluxes and weathering of volcanic terrains on high standing islands: Taranaki and Manawatu-Wanganui regions of New Zealand. Geochimica et Cosmochimica Acta 72. 2248-2267.

Gudbrandsson S., Wolff-Boenisch D., Gislason S.R. and Oelkers E.H. (2014) Experimental determination of plagioclase dissolution rates as a function of its composition and pH at 22°C. Geochimica et Cosmochimica Acta 139. 154–172.

Harmon et al., (2013) Surface water geochemistry and chemical weathering across Panama. Procedia Earth and Planetary Science 7. 342-345.

Harsh, J. (2012) Poorly Crystalline Aluminosilicate Clay Minerals. In Handbook of Soil Sciences Properties and Processes. Second edition. Huang, P.M., Li, Y. & Sumner, M.E (eds.). CRC Press. Boca Raton. USA. pp 23-1 23-13.

Kump, L.R., Brantley, S.L. and Arthur, M.A. (2000) Chemical weathering, atmospheric CO_2 and climate. Annu. Rev. Earth Planet. Sci. 28. 611-667.

Lasaga, A.C. (1981) Transition State Theory. Rev Mineral 8. 135-169.
Lauerwald, R., Hartmann, J., Moosdorf, N., Dürr, H.H., Kempe, S. (2013) Retention of dissolved silica within the fluvial system of the conterminous USA. Biogeochemistry 112. 637-659.

Le Hir, G., Donnadieu, Y., Goddéris, Y., Pierrehumbert, R.T., Halverson, G.P., Macouin, M., Nédélec, A., Ramstein, G. (2009) The snowball Earth

aftermath: Exploring the limits of continental weathering. Earth and Planetary Science Letters 277. 453-463.

Maher, K., Steefel C.I., White, A.F., Stonestrom, D.A. (2009) The role of reaction affinity and secondary minerals in regulating chemical weathering rates at the Santa Cruz Soil Chronosequence, California. Geochimica et Cosmochimica Acta 73. 2804-2831

Maher, K. (2010) The dependence of chemical weathering rates on fluid residence time. Earth and Planetary Science Letters 294. pp.101-110.

Mastin, L.G., Van Eaton, A.R. and Lowenstern, J.B. (2014) Modeling ash fall distribution from a Yellowstone supereruption. Geochem. Geophys. Geosyst., 15, 3459–3475.

Mitchell, T. and Jones, P. (2005) An improved method of constructing a database of monthly climate observations and associated high-resolution grid. International Journal of climatology. Int.J. Climatol. 25: 693-712.

Moosdorf, N., Hartmann, J., Lauerwald, R., Hagedorn, B., Kempe, S. (2011) Atmospheric CO_2 consumption by chemical weathering in North America. Geochimica et Cosmochimica Acta 75. 7829-7854.

Moon, S., Chamberlain, C.P., Hilley, G.E. (2014) New estimates of silica weathering rates and their uncertainties in global rivers. Geochimica et Cosmochimica Acta 134. 257-274.

Oelkers, E.H. and Schott, J. (1995) Experimental study of anorthite dissolution and the relative mechanism of feldspar hydroloysis. Geochimica et Cosmochimica Acta 59 (24): 5039-5053.

Oelkers, E.H., Schott, J., Devidal, J.L. (1994). The effect of aluminum, pH, and chemical affinity on the rates of aluminosilicate dissolution reactions. Geochim. Cosmochim. Acta, 58 (9), 2011-2024.

Oliva, P., Viers, J., Dupré, B. (2003) Chemical weathering in granitic environments. Chemi. Geolo. 202 (1-2). 134-147.

Palfy, J., Kocsis, A. (2014) Volcanism of the Central Atlantic magmatic province as the trigger of environmental and biotic changes aroung the Triassic-Jurassic boundary. In Keller, G., and Kerr, A.C., eds., Volcanism, Impacts, and Mass Extinctions: Causes and Effects The Geological Society of America Special Paper 505. 245-261.

Rimstidt, J.D. and Barnes, H.L. (1980) The kinetics of silica-water reactions. Geochimica et Cosmochimica Acta. Vol 44. 1638-1699.

Roeland, C., Goddéris, Y., Bonnet, M-P., Sondag, F. (2010) Coupled modeling of biospheric and chemical weathering processes at the continental scale. Global Biogeochem. Cycles. 24(2):18.

Rougier, J., Sparks, R.S.J., Cashman, K.V., Brown, S.K. (2018) The global magnitude–frequency relationship for large explosive volcanic eruptions. Earth and Planetary Science Letters 482. 621-629.

Self, S. (2006) The effects and consequences of very large explosive volcanic eruptions. Philosophical Transactions of the Royal Society, A. 364. 2073-2097.

Self, S., Widdowson, M., Thordarson, T., Jay, A.E. (2006) Volatile fluxes during flood basalt eruptions and potential effects on the global environment: A Deccan perspective. Earth And Planetary Science Letters 248. 518-532.
Schopka, H.H., Derry, L.A., Arcilla, C.A. (2011) Chemical weathering, river geochemistry and atmospheric carbon fluxes from volcanic and ultramafic regions on Luzon Island, the Philippines. Geochimica et Cosmochimia Acta 75. pp. 978-1002.

Schott, J., Pokrovsky, O.S. and Oelkers, E.H. (2009) The link between mineral dissolution/precipitation kinetics and solution chemistry. Reviews in Mineralogy & Geochemistry. Vol 70 pp. 207-258, 2009.

Shoji, S., Nanzyo, M., Dahlgren, R.A. (1993) Volcanic ash soils. Genesis, Properties and Utilization, Elsevier, Amsterdam, 288 pp.

Sparks, R.S, Bursik, M.I., Carey, S.N., Gilbert, J.S, Glaze, L.S., Sigurdsson, S., Woods, A.W. (1997) Volcanic Plumes. Wiley & Sons, London.

Sverdrup, H. and Warfinge, P. (1995) Estimating field weathering rates using laboratory kinetics. Rev. Mineral. 31, 485-541.

Walther, J.V., Hegelson, H.C. (1977) Calculation of the thermodynamic properties of aqueous silica and the solubility of quartz and its polymorphs at high pressures and temperatures. Am. J. Sci. 277. 1315-1351.

Wesolowski, D.J., Palmer, D.A. (1994) Aluminium speciation and equilibria in aqueous solution: V. Gibbsite solubility at 50°C and pH 3-9 in 0.1 molal NaCl solutions. Geochim. Cosmochim. Acta 58. 2947-2970.

White, A. F., Brantley, S. L., and Kubicki, J D. (2008) Quantitative approaches to characterizing natural chemical weathering rates: Springer: New York, p. 469-543.

White, A.F., Blum, A.E. (1995) Effect of climate on chemical weathering in watersheds. Geochim. Cosmochim. Acta 59(9); 1729-1747.

SUPPLEMENTARY MATERIAL

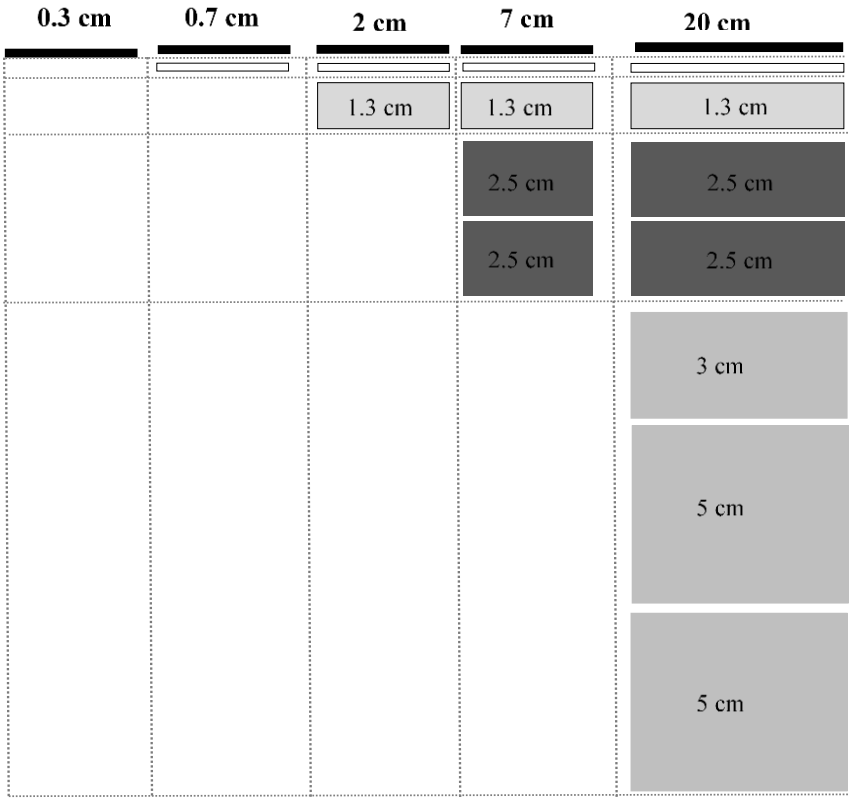

Figure S.7.1. Schematic representation of the deposit thickness.

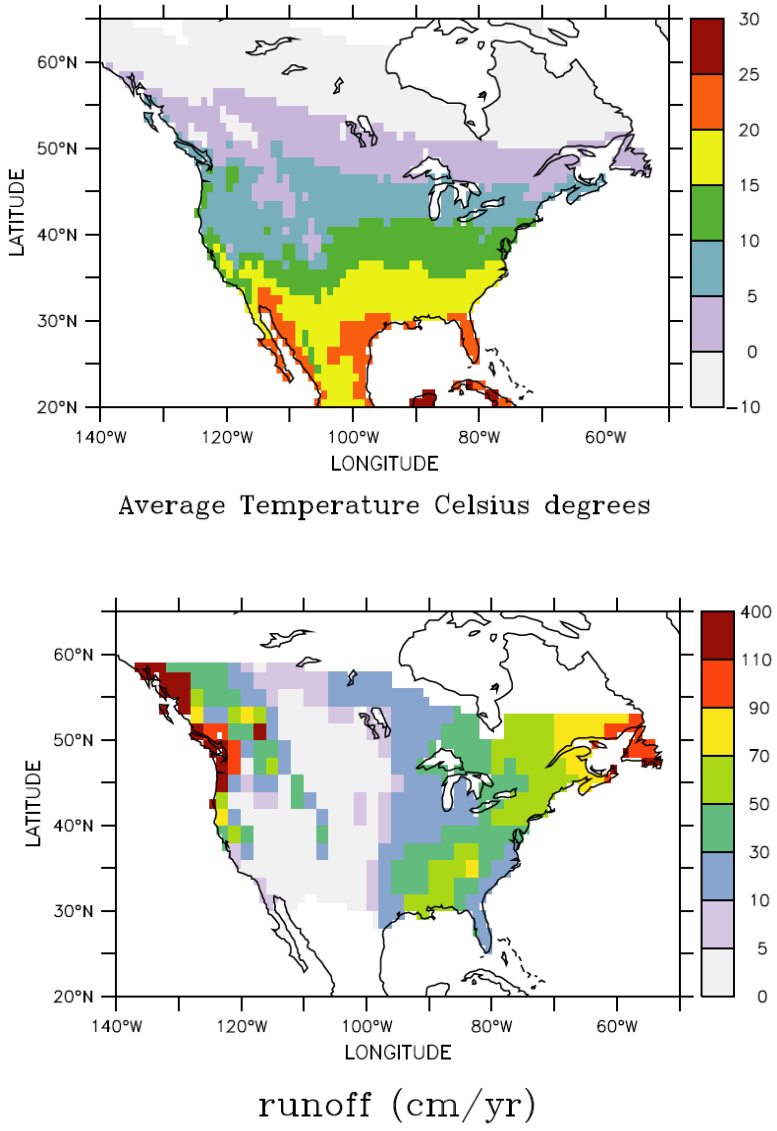

Figure S.7.2. Zone covered by the tephra deposit expressed as (a) average temperature (°C) and (b) runoff (cm yr^{-1}).

Rhyolitic glass

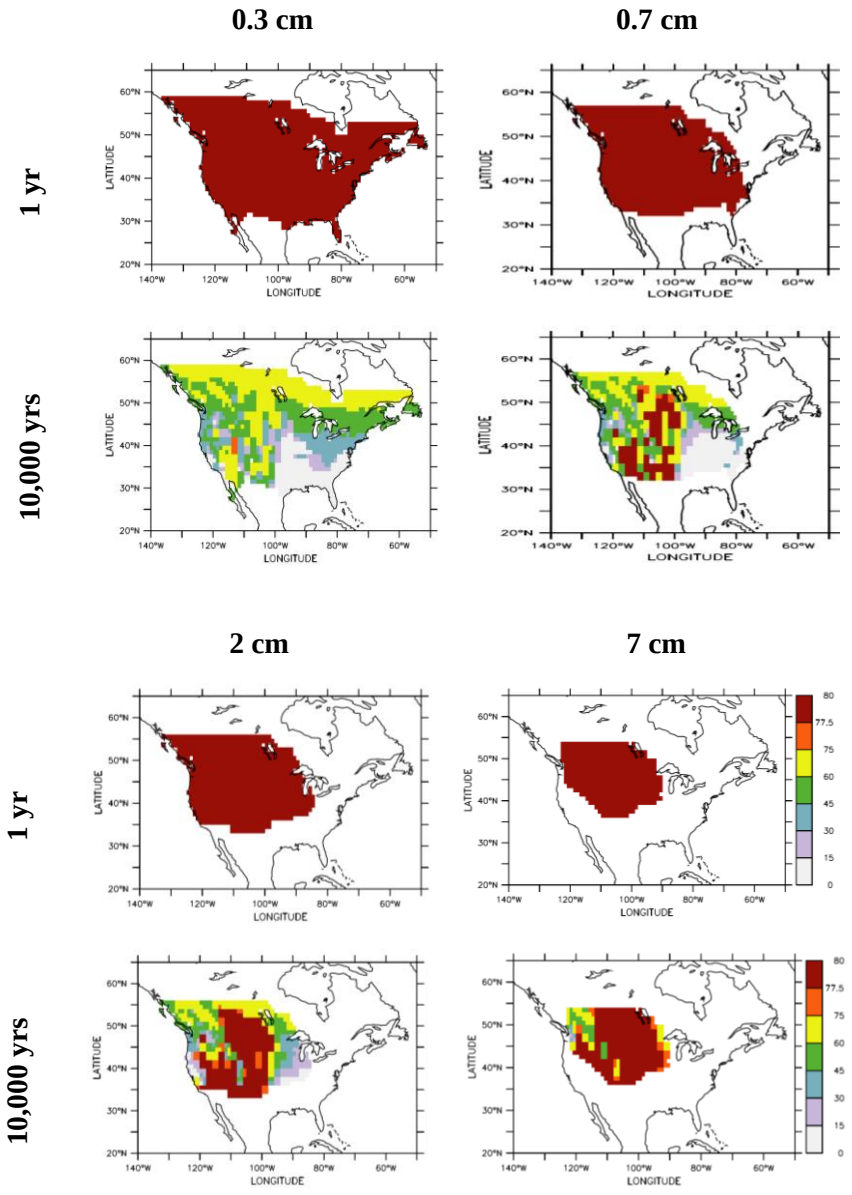

Figure S.7.3. (a) Distribution map of glass content at 0.3, 0.7, 2 and 7 cm after 1 and 10,000 years of weathering.

Albite

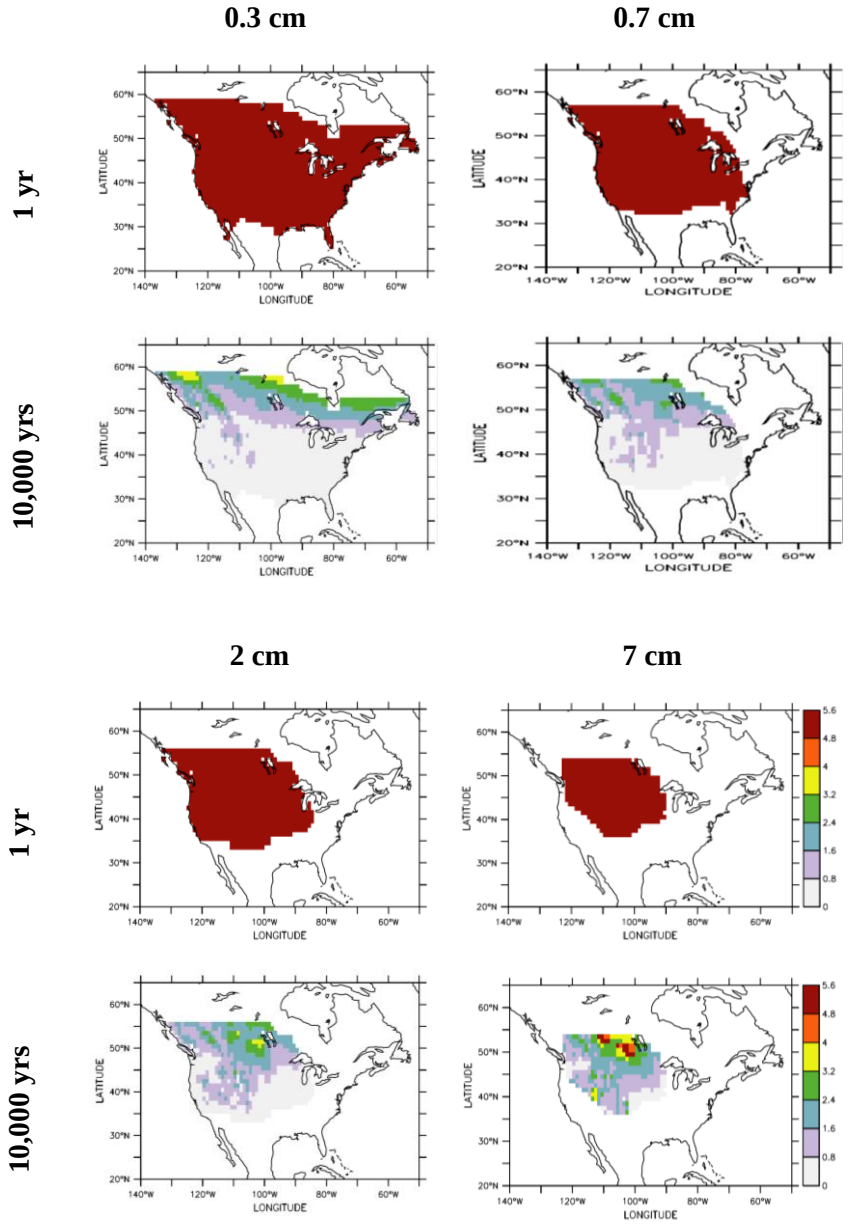

Figure S.7.3. (b) Distribution map of albite content at 0.3, 0.7, 2 and 7 cm after 1 and 10,000 years of weathering.

K-feldspar

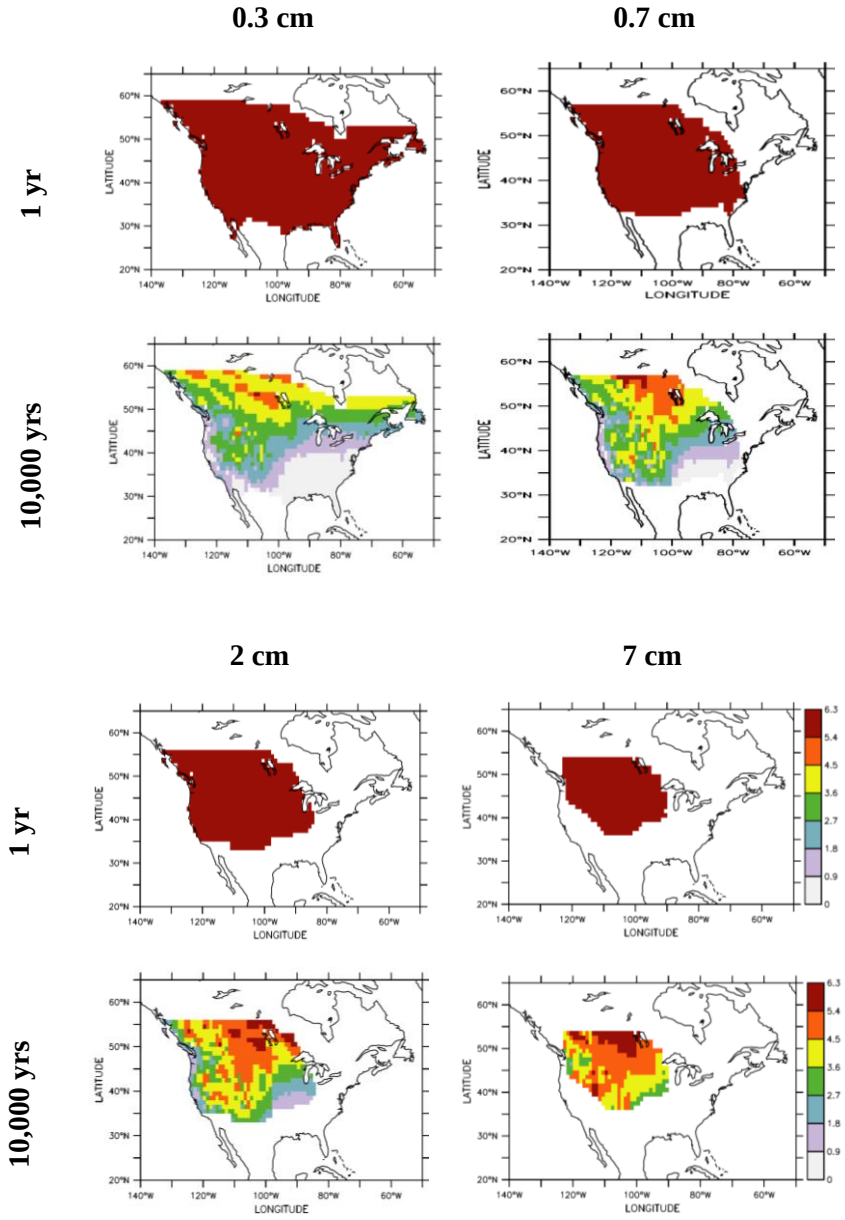

Figure S.7.3. (c) Distribution map of K-feldspar content at 0.3, 0.7, 2 and 7 cm after 1 and 10,000 years of weathering

Appendix 7.1. WITCH description adapted to our case study

The geochemical model WITCH has been applied to simulate the alteration of a volcanic ash deposit (rhyolitic glass 80%, quartz 7.34%, K-feldspar 6.26% and albite 5.54%), similar to those deposed by a super-eruption in Yellowstone (USA) but incorporating actual data of temperature and runoff. The model provides the fluxes of elements due to chemical weathering. The release of cations, which is promoted by water-mineral interactions, is controlled by the abundance of reactive components in the ash deposit (rhyolitic glass, K-feldspar and albite). Through dissolution kinetics laws of minerals and glasses, which have been coupled to the model, it is possible to quantify the concentration of cations exported from the ash deposit. Based on the budget of cations in solution, parameters as alkalinity and solution pH are estimated. Including as well, the eventual formation of secondary phases (allophanes and halloysite) based on the saturation index of the secondary phases. The difference in alkalinity in the output solution for the deepest layer is used to estimate the CO_2 consumption flux. In Figure A.7.1, a schema of the main inputs and outputs generated by the WITCH model are presented:

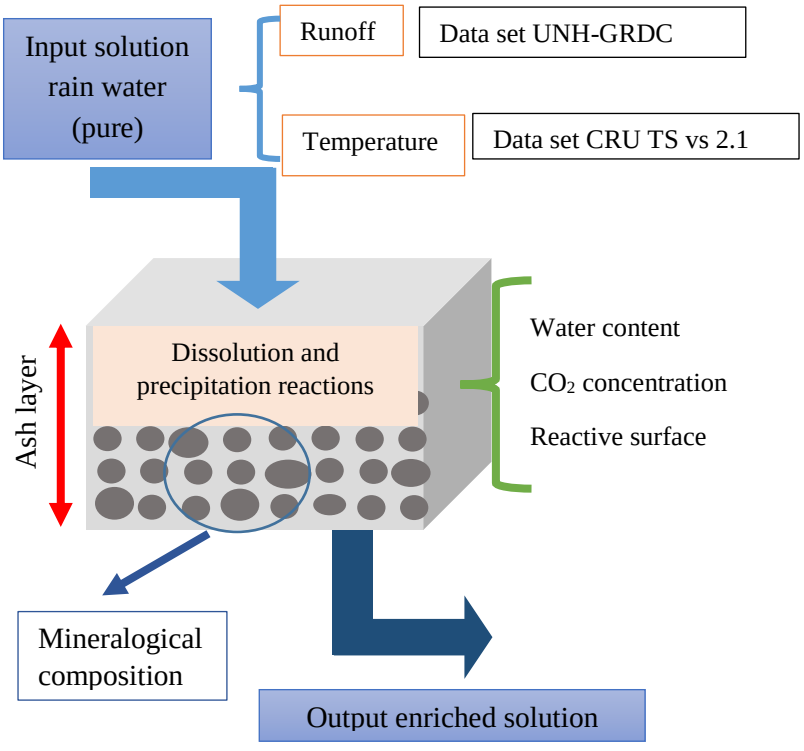

Figure A.7.1. Schematic representation of the main inputs required by the geochemical model WITCH.

The output is injected at each time step into the speciation module that calculates the complete speciation of the solution for some chemical species as H^+, OH^-, HCO_3^-, CO_3^{2-}, H_2CO_3, Al^{3+}, $AlOH_2^+$, $Al(OH)^{2+}$, $Al(OH)_4^-$, H_4SiO_4, $H_3SiO_4^-$, $H_2SiO_4^{2-}$. WITCH does not include a nucleation model, and precipitation rate is assumed to be proportional to the reactive surface area of the mineral, an input parameter calculated from the observed relative abundance of minerals in the ash layer. Reactive surface area is distributed among the various minerals according to their volume abundance; itself calculated form the weigh abundance reported for the ash layer (Goddéris et al., 2006).

A.7.1.1. General context for the main inputs used in our case study

A.7.1.1.1. Characterization of the rhyolitic ash deposit

The main characteristics of our simulated volcanic ash deposit were estimated from the geological registers documented for one of the biggest eruptions in Yellostone (Lava Creek Tuff 640 000 years ago) (Christiansen, 2001). The average chemical composition of the rhyolitic ash deposit was 77.07 ± 0.1 wt. % of SiO_2, 12.5 ± 0.36 wt. % of Al_2O_3, 1.44 ± 0.27 wt. % of FeO, 0.07 ± 0.06 wt. % of MgO, 0.36 ± 0.11 of wt. % Ca, 3.26 ± 0.4 of wt. % Na_2O and 5.15 ± 0.19 of wt. % K_2O. The average idealized mineralogy (CIPW norm) was 36.54 ± 3.53 wt. % of quartz, 30.44 ± 1.15 wt. % of K-feldspar, 27.57 ± 3.42 wt. % of albite and 1.58 ± 0.62 wt. % of anorthite. We considered that 80 vol% of the deposit corresponds to rhyolitic glass. The chemical formula estimated was $Al_{0.19}Ca_{0.005}Fe_{0.02}K_{0.09}Mg_{0.001}Na_{0.08}SiO_{2.40}$. In terms of petrology of the rhyolites of the Yellowstone Plateau volcanic field, Christiansen (2001) has signaled that the historical deposits coming from Lava Creek Tuff have phenocrysts of quartz, sanidine and subordinate sodic plagioclase. Minor phenocrysts include magnetite, ilmenite, ferroaugite, fayalite, iron-rich hornblende, zircon, chevkinite and allanite.

A.7.1.1.2. Surface coverage

The surface covered by the rhyolitic ash deposit was defined using the ashfall simulated maps presented by Mastin et al. (2014). They used the volcanic ash transport and dispersion model Ash3d to estimate the distribution of the ashfall from a modern-day super eruption at Yellowstone. Initially in our study we have selected the two extreme scenarios corresponding to the minimal and the maximal surface covered by volcanic ash reported by Mastin et al. (2014).

The briefest eruption (3 days) produces a relative narrow tephra deposit that extends toward the southwest. Instead, simulations with an umbrella cloud produce ash deposits that are much more widely dispersed. Without the umbrella cloud, the 10 mm isopach in the minimal scenario covers 1.2 million km^2, with the umbrella cloud, it covers 5.4 million, 4.5 times the area (Mastin et al., 2014). The maximal scenario corresponds to simulated fall thickness resulting from a week-long Yellowstone eruption. The minimal scenario corresponds to an eruption with no umbrella cloud that happened during 3 days (21-27 January) (see Figure A.7.2.).

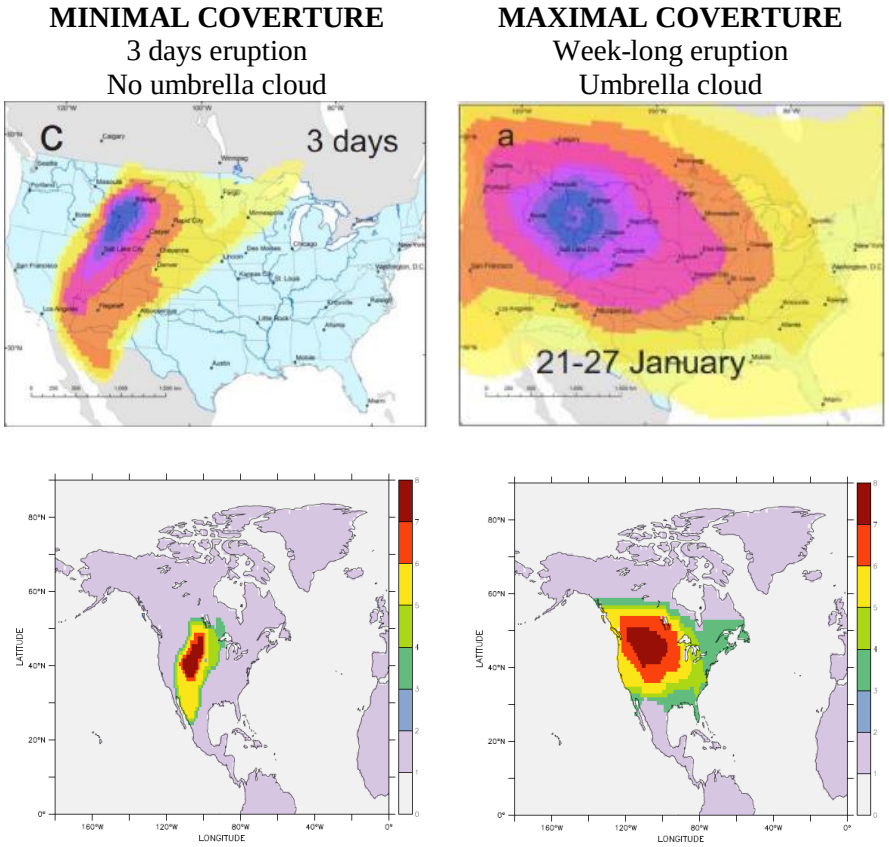

Figure A.7.2. Maximal and minimal surface covered by Yellowstone super eruption, presented by Mastin et al. (2014) and compared to the maps used in our study.

However, the first scenario (minimal surface covered) was not included in the final version of the study due to the low probability of occurrence of this kind of eruption in nature.

A.7.1.1.3. Erupted volume

In our study, the total amount of buoyant ash deposited by the super-eruption was already given by the ashfall maps of Mastin et al. (2014), which considered that only a fraction of the total erupted volume rouse in buoyant ash during a super-eruption. Mastin et al. (2014) fixed a value of 330 km^3 dense-rock equivalent (DRE) of magma. Sparks et al. (2005) mentioned that in terms of a super-eruption, the total volume of material erupted is around 1000 km^3 bulk or 400 km^3 dense-rock equivalent (DRE). Comparing with the geological records, the three major caldera-forming eruptions from Yellowstone that produced the Huckleberry Ridge Tuff, Messa Falls Tuff, and Lava Creek Tuff expelled about 2450, 280 and 1000 km^3 DRE of magma (Cristiansen, 2001). Therefore, the 330 km^3 volume, used in our study, represents about one third of a 1000 km^3 DRE eruption, which is above the threshold for a super-eruption (1000 km^3 bulk or 400 km^3 DRE) (Sparks et al., 2005).

A.7.1.1.4. Thickness of the volcanic ash deposit

The tephra deposit was divided in five isopatches of increasing thickness (3, 7, 20, 70 and 200 mm) surrounding the Yellowstone formed caldera. According to Mastin et al. (2014), the radially symmetric isopachs produced are only secondarily modified by ambient wind. In order to keep the same residence time of water for same depths independently of the isopatch, each isopatch was subdivided into layers keeping the same resolution. Thus, the 3mm isopatch has one layer of 3 mm, the 7 mm isopatch has two layers (3 and 4 mm), the 20 mm isopatch has three layers (3, 4 and 1.3 mm), the 70 mm isopatch has five layers (3-4-13-25-25 mm) and the 200 mm isopatch has 8 layers (3-4-13-25-25-30-50-50 mm).

A.7.1.1.5. Temperature

Average temperature values are extracted from the database CRU TS vs.2.1 (Mitchell and Jones, 2005). This data set comprises 1224 monthly grids of observed climate, for the period 1901-2002, and covering the global land (excluding Antarctica) surface at 0.5 degree resolution. This database has been developed by the Climatic Research Unit at the University of East Anglia and the Tyndall Centre for Climate Change Research.

The set of grids provides estimates of month by month variations in nine climate variables: daily mean, minimum and maximum temperature, diurnal temperature range, precipitation, wet day frequency, vapour pressure and cloud cover. (Mitchell and Jones, 2005).

A.7.1.1.6. Runoff

The data set used for quantifying the runoff was the UNH-GRDC Composite Runoff Fields V1.0. It has been developed by the Water Systems Analysis Group (WSAG) at CSRC at the University of New Hampshire (UNH) and the Global Runoff Data Centre (GRDC) (Fekete et al., 2000).

The data set combines observed river discharge information with a climate-driven water balance model in order to develop composite runoff fields which are consistent with observed discharges. The method applied utilized a gridded river network at 30-minutes spatial resolution to represent the riverine flow pathways and to link the continental land mass to oceans through river channels (Fekete et al., 2000).

A.7.1.2. Simulation code features

The WITCH model turns over the whole planet divided into regions of 1° lat. x 1° long., which were assigned with a number. Number 1 has been assigned for oceans, 2 for terrestrial crust not covered, 3 to 7 corresponds to covered regions increasing the thickness as its increase the value, ranging from 0.3 cm to 20 cm respectively (see figures 3.16 and 3.17). The simulation code stops in each cell (1° lat. x 1° long), and calculates the output parameters for the corresponding covered cells (3-7) for each box, passing through the whole set of layers before moving to the contiguous cell.

Due to the huge quantity of data generated by the model, it is not practical to print the results every single path of time, obtaining only the final simulated values at the end of the simulation. Thus in order to evaluate the evolution of

the parameters (geochemical fluxes, CO_2 consumption, etc.), we proposed six individual runs ranging from 0.1 years, 1 year, 10 years, 100 years, 1000 years and 10000 years. For longer time scales (> 10 years), an acceleration factor for the simulation has been included in order to diminish the simulation time. Being for 10 years (1 year x 10 times), 100 years (10 years x 10 times), 1000 years (10 years x 100 times) and 10 000 years (10 years x 1000 times). The initial conditions for all the simulated runs were obtained from a previous run (0.01 years).

References

Christiansen R.L (2001) The Quaternary and Pliocene Yellowstone Plateau Volcanic Field of Wyoming, Idaho, and Montana. Geology of Yellowstone National Park. Professional Paper 729-G. U.S. Geological Survey.

Fekete, B.M., Vörösmarty C.J. and Grabs, W. (2000) Global, Composite Runoff Fields Based on Observed River Discharge and Simulated Water Balance. http://www.grdc.sr.unh.edu/

Godderis Y., François L., Probst A., Schott J., Moncoulon D., et al. (2006) Modelling weathering processes at the catchment scale: The WITCH numerical model. Geochimica et Cosmochimica Acta, Elsevier, 70, pp.1128-1147. <10.1016/j.gca.2005.11.018>. <hal-00665423>

Mastin, L.G, Van Eaton, A. R. and Lowenstern, J.B. (2014) Modeling ash fall distribution from a Yellowstone supereruption. Geochem. Geophys.Geosyst., 15, pp. 3459–3475.

Mitchell, T. and Jones, P. (2005) An improved method of constructing a database of monthly climate observations and associated high-resolution grid. International Journal of climatology. Int.J. Climatol. 25. pp. 693-712.

Sparks, S., Self, S., Gratten, J., Oppenheimer, C., Pyle, D. and Rymer, H. (2005), Supereruptions: Global Effects and Future Threats, Report of a Geological Society Working Group, 25 pp., Geological Society of London, London, U. K.

PART III
CONCLUSION

CHAPTER 8 Conclusions and Outlook

8.1. SUMMARY OF MAIN FINDINGS

The importance of continental chemical weathering on the Si and C global cycles is being continuously highlighted with the arrival of new geochemical studies (e.g., Oelkers et al., 2012; Jones et al., 2014; Eiriksdottir et al., 2015; Raymond, 2017). Mechanistic modelling is a useful tool for describing water-rock interactions in natural systems. A critical requirement in such approach is a sound understanding of the weathering processes. In the case of polycrystalline volcanic rock weathering, it is necessary to buildup knowledge on the dissolution kinetics and thermodynamics of primary silicate minerals and glass and their secondary weathering products. These data can then be coupled to hydrological processes.

The experimental work undertaken in this PhD contributes to this effort by providing new insight into the dissolution rates of volcanic rocks differing in composition and crystallinity. Further, we apply for the first time a mechanistic model to predict the mineralogical evolution of a tephra deposit subjected to weathering over multimillennial timescales. This allowed the computation of the associated weathering fluxes and atmospheric CO_2 consumption.

8.2. SUMMARY OF EXPERIMENTAL DETERMINATION OF DISSOLUTION RATES OF PARTICULATE VOLCANIC ROCKS USING A FLUIDIZED BED REACTOR

We performed a series of dissolution experiments (**Chapters 4, 5 and 6**) of volcanic rocks in the laboratory using a homemade fluidized-bed reactor. A fluidized bed reactor offers some advantages over other devices such as the flow through reactor. For example, the former allows better agitation while diminishing the sample wear.

In chapter 4, we investigated the continuous dissolution of a volcanic ash sample (i.e. a pyroclastic rock) of basaltic composition at acidic (pH 2, 3 and 5) and alkaline (pH 8, 10, 11) conditions. Dissolution was carried out at a given pH value for 100 h, and then a new solution pH was introduced while keeping the same sample in suspension in the fluidized bed reactor.

Based on the temporal changes in the concentration of Si, Al, Fe, Ca, Mg, Na and K, we highlighted incongruent dissolution of the basaltic ash in both acidic and alkaline conditions. Further, we inferred the formation of a residual layer on the ash surface. The residual layer is Si-rich when dissolution takes

place at acidic pH values, and Al-rich in alkaline conditions. The thickness of the layer was on the order of a few micrometres, which is in good accordance with previous observations from several dissolution studies in silicate glasses. Besides, the calculation of the diffusivities of the alkali (Na and K) and alkaline earth (Ca and Mg) cations through the residual layer produces values that are comparable to those reported in other studies. Finally, we showed that dissolution of the ash decreased with increasing pH in the acid pH zone, and increased with increasing pH in the alkaline pH zone. The two dissolution behaviours could be described by fitting two equations that account for changing a_{H+} and a_{Al3+}.

In chapter 5, we studied the effect of crystallinity on the dissolution rates of volcanic rocks. In contrast to previous works, we compared natural rocks (a basalt, a dacite and a rhyolite) with their actual glassy counterparts obtained through melting and rapid quenching. The dissolution experiments were conducted at pH 4 and room temperature in a fluidized bed reactor. The dissolution rates were found to decrease with the rock/glass SiO_2 content ($r_{basalt} > r_{dacite} > r_{rhyolite}$). The basaltic rock and the basaltic glass exhibited significantly higher r_{Si} values than the dacitic and rhyolitic samples, in accordance with previous studies. However, discrepancies between the Si-based dissolution rate of the crystalline material and that of its glassy equivalent were noticed. The Si and Al-based rates were comparable, suggesting stoichiometric dissolution of the rock/glass. Only the basaltic glass sample (low Si:O ratio) agreed with the dissolution behaviour proposed in a previous study and which quantifies the dependence of r on the silica content of the solid. The discrepancy may arise from different particle size distributions. Alternatively, it may point to the important but unknown role of Fe content in increasing the susceptibility of Si-rich volcanic rocks to dissolution reactions. Comparable dissolution rates were obtained for the rock and glass with basaltic composition, in accordance with earlier findings. In contrast, differences were noticed for the silicic compositions. We suspected that the rapid dissolution of labradorite present in the dacite rock drove the high r values. This result invalidates the hypothesis that crystalline rocks will always dissolve at a slower pace than their glassy equivalents. Interestingly, the rhyolitic rock behaved like its glass. We interpreted this finding in terms of similar cooling rates, i.e. in the natural environment and in the laboratory.

Chapter 6 tested the hypothesis that the dissolution rate of a polycrystalline volcanic rock can be approximated from the dissolution rates of its individual silicate glass and mineral constituents. We determined the dissolution rates of a basalt, andesite, dacite and rhyolite rock at pH 2, 3 and 5 in our fluidized bed reactor (20 °C). The experimentally-derived rate values did not compare well with those calculated for the major rock's silicate constituents from kinetics rate laws available in the scientific literature. We posited that the

discrepancy originated from the surface areas of the rock constituents actually available for dissolution. By adjusting the relative surface areas of the rock constituents iteratively, we improved the agreement between the experimental and theoretical dissolution rates considerably, except in the case of the basalt. Overall, and unsurprisingly, we conclude that the dissolution rates of intermediate and silicic volcanic rocks mostly reflect the dissolution behaviour of their glass and major mineral constituents. Relatively minor mineral phases can, in first approximation be ignored. Further, we suggest that the dissolution behaviour of the rock increasingly approaches that of its glass constituent as the rock SiO_2 content increases.

8.3. SUMMARY OF WEATHERING OF CONTINENT-SCALE VOLCANIC ASH DEPOSIT USING THE MECHANISTIC MODEL WITCH

In **chapter 7**, we simulated the weathering of a continent-size tephra (rhyolite) deposit using the mechanistic model WITCH. The simulations were run for weathering periods of 0.1, 10, 100, 1000 and 10,000 yr. The model results emphasized the importance of tephra deposit thickness and drainage conditions in dictating the spatial distribution of the Si and base cation fluxes generated through weathering. We also found that weathering is transport-limited and that mineral solubility exerted a key control on the development of the weathering front in the deposit. The key finding of our study is that weathering of a continent-size tephra deposit such as those produced by supereruptions is likely to enhance the transfer of dissolved Si to the ocean significantly and over timescales of thousands of years. However, this effect will not lead to a sizeable consumption of atmospheric CO_2 if the tephra deposit that is being weathered is devoid of Ca- and Mg-silicate minerals. The mechanistic simulation of tephra weathering would benefit from a better knowledge of the thermodynamics and kinetics of precipitation/dissolution of short-range order allophane minerals that typically form in tephra-derived volcanic soils. Additionally, it would be useful to assess the impact of vegetation recovery on weathering dynamics. Finally, one could simulate with WITCH the weathering of supereruption tephra deposit in a different climate zone, i.e. characterized by high runoffs. For example, the eruption of Toba volcano (74 ka ago) produced an extensive deposit that blanketed large portions of Southeast Asia, including the entire subcontinent of India (Chesner, 2011).

8.4. INSIGHTS ACROSS CHAPTERS

8.4.1. Comparison of the experimentally-derived dissolution rates of basaltic samples (Chapters 4, 5 and 6)

In Chapters 4, 5 and 6, we measured the dissolution of basaltic materials (ash-rock-glass) with low SiO_2 content (~45-47%) in different pH conditions (2, 3, 4, 5, 8, 10 and 11) at 20-25 °C. Figure 8.1 summarizes the main findings.

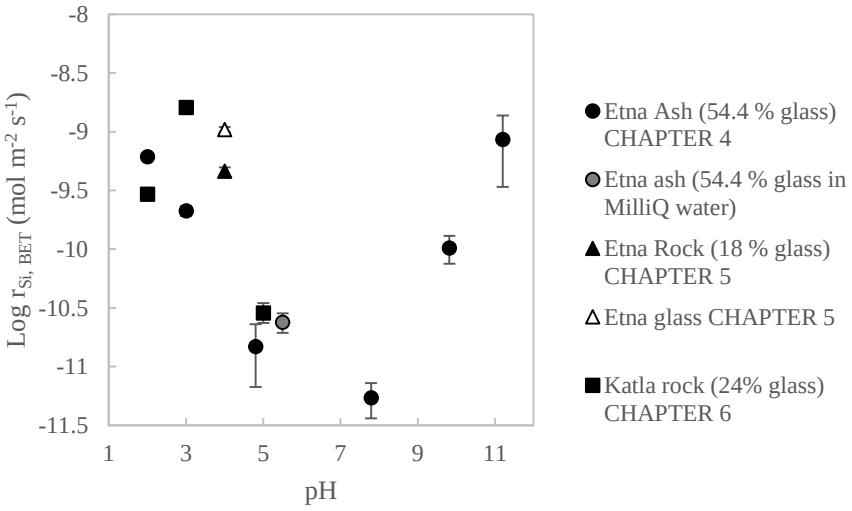

Figure 8.1. Dissolution rate of the basaltic rock/glass samples collected as a function of pH as measured in Chapters 4, 5 and 6.

The comparison focuses only on the dissolution rate values of the basaltic material as determined in the acidic zone (pH: 2, 3, 4 and 5), since dissolution rate values in the alkaline zone (pH: 8, 10 and 11) were measured exclusively for one sample, i.e. the Etna ash (Chapter 4). At acidic conditions (pH 5 and 5.5), the dissolution rates of the Katla rock (24 % glass, Chapter 6) and Etna ash (54% glass, Chapter 4) converge (Log $r_{Si,BET}$ ~ -10.5). At pH 4, the dissolution rate values corresponded to those of the Etna rock (18% glass) (Log $r_{Si,BET}$ = -9.33) and its glassy counterpart (Chapter 5) (Log $r_{Si,BET}$ = -8.98). At pH 3 the dissolution rate of the Katla rock (24% glass, Chapter 6) (Log $r_{Si,BET}$ = -8.79) was eight times higher than that found for the Etna ash (54% glass, Chapter 4) (Log $r_{Si,BET}$ = -9.68). In contrast, at pH 2, the dissolution rate of the Etna ash (54 % glass, Chapter 4) (Log $r_{Si,BET}$ = -9.21) is twice the dissolution rate of the Katla rock (24% glass, Chapter 6) (Log $r_{Si,BET}$ = -9.53). Clearly, a trend that would describe the dissolution behaviour of a basaltic composition at acidic pH does not emerge.

Using the experimental data from Chapter 4, we can derive an equation (Log $r_{Si, BET} = 0.29 \log (a^3_{H+} / a_{Al3+}) - 8.83$ Eq. [8.1]; $R^2=0.97$; see Figure 4.3) relating the dissolution rate of the Etna ash to the activity of H^+ and Al^{3+} in the acidic pH zone (pH 2, 3 and 5). This equation was used to estimate the corresponding dissolution rates of the basaltic rock (Katla, Chapter 6) based on the calculated activities of H^+ and Al^{3+} derived from the experimental concentrations of cations (see Appendix 6.5), using the geochemical model PHREEQC 2.6 (Parkhust and Appelo, 1999). The calculated dissolution rates of the Katla rock are plotted in Figure 8.2.

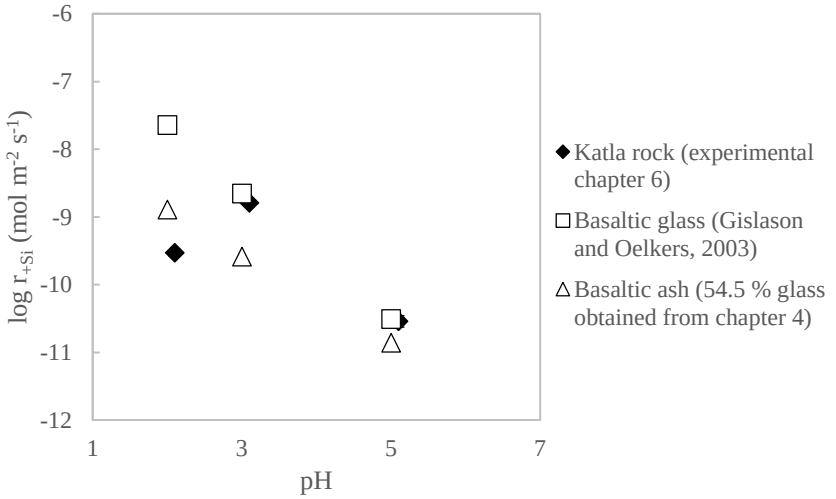

Figure 8.2. Comparison between the experimental dissolution rates obtained for the Katla rock (Chapter 6) and the dissolution rates calculated using the equation derived based on the dissolution of the Etna ash (Eq. [8.1], Chapter 4). The theoretical dissolution rates computed by applying Eq. [4.2] for the dissolution of basaltic glass (Gislason and Oelkers, 2003) are also shown.

According to Figure 8.2, the dissolution rate values obtained by applying Eq. [8.1], also described in Chapter 4) are smaller than those produced based on Eq. [4.2] from Gislason and Oelkers (2003). The match between the estimated and the measured dissolution rate values measured for the basaltic rock in Chapter 6 did not improve significantly, except at pH 2. At pH 3 and 5, the dissolution rates of the basaltic rock are closer to those corresponding to the dissolution of basaltic glass at the same pH using Eq. [4.2], as already mentioned earlier (section 6.4.3).

8.4.2. Comparison between the experimentally-derived dissolution rates of a rhyolitic rock (Chapters 6) and the dissolution rates of the Yellowstone rhyolitic ash inferred from the weathering model (Chapter 7)

We estimated the dissolution rates (r_{+Si} mol m^{-2} s^{-1}) of the Yellowstone rhyolitic ash using the Si exported from the deposit predicted by WITCH at different locations across North America (Chapter 7). These locations corresponded variable deposit thicknesses (see Figure 7.1). By considering the Si concentration maps (mol L^{-1}) produced by the weathering model, the flow of water passing through a 1-km^2 deposit (L s^{-1}) (*runoff (mm yr^{-1}) x surface (km^2)*), the corresponding mass of ash (*average bulk density of 1.30 g cm^{-3} based on the range of bulk densities reported for natural ash deposits, Leavesley et al. 1989; Spence et al., 2005*) and the specific surface area of the ash (*1 m^2 g^{-1}*), we estimated dissolution rate values ranging from 2.9 x 10^{-12} to 9.8 x 10^{-10} mol m^{-2} s^{-1} (log= -9.01 and -11.5) (Table 8.1).

Table 8.1. Inferred dissolution rates for different locations along North America after 0.1 yr and 10,000 yrs of simulation (pH =5.5-6.9 and T= 5-20 °C) (density 1.3 g cm^{-3} field ash deposit).

Location	**Florida**	**Virginia**	**North California**	**Lake Winnipeg**	**Yellowstone Caldera**
Thickness (mm)	3	7	20	70	200
0.1 yr					
Dissolution rate (mol m^{-2} s^{-1})	9.77×10^{-10}	2.79×10^{-10}	1.83×10^{-10}	7.67×10^{-11}	3.41×10^{-12}
Log r_{+Si}	-9.01	-9.55	-9.74	-10.11	-11.47
10,000 yrs					
Dissolution rate (mol m^{-2} s^{-1})	2.44×10^{-10}	6.97×10^{-11}	7.32×10^{-11}	7.67×10^{-11}	2.93×10^{-12}
Log r_{+Si}	-9.61	-10.16	-10.14	-10.11	-11.53

Based on our experimental study (see Table 6.2), the dissolution rates (at 20 °C and pH 2, 3 and 5) of a Si-rich polycrystalline rocks (dacite: Guagua Pichincha and rhyolite: Puyehue) are comprised between 4×10^{-12} and 1×10^{-10} mol m^{-2} s^{-1} (log = -11.4 and -9.9). These values are comparable with those derived from the weathering model (2.9×10^{-12} and 9.8×10^{-10}; log = -11.5 and -9.01).

Previous studies have repeatedly highlighted that weathering rates measured in the field are typically lower (one to five orders of magnitude) than the dissolution rates determined in laboratory experiments (e.g., Paces, 1983; Velbel, 1986; Sverdrup, 1990; Swoboda-Colberg and Drever, 1993; White and Brantley, 2003; Navarre-Sitchler and Branley, 2007; Salehikhoo et al., 2013). Several authors (Sverdrup and Warfvinge, 1988; Velbel, 1989; Hochella and Banfield, 1995; White et al., 1996; Harley and Gilkes, 2000; Li et al., 2006, 2010; Maher et al., 2006, 2009; Song and Seagren, 2008; Zhu, 2009; Moore et al., 2012) pointed such discrepancies probably reflect an inability to characterize and account for various inhibitory effects that occur in natural systems. There are several factors that may limit weathering rates in natural conditions, such as limitations on flow and transport into low permeability zones in heterogeneous material; limited diffusion of ions (affected by diffusion distance, residence time, tortuosity and soil water content); the effect of reaction affinity; changes in reactive surface with time (due to mineral coatings, secondary mineral-clay precipitation, and aging of reacting minerals), limitations of reactive surface area in natural porous media, and inhibitory-enhancing effects of (micro) biological activity. In contrast, in laboratory experiments involving continuously stirred or flushed systems, surface reactions and not diffusion processes are likely to be the rate limiting steps. The WITCH model, does not fully reproduce the natural conditions under which dissolution occurs. This may explain why, for the rhyolitic ash, there is a good agreement between the modelled dissolution rates and the experimental values.

8.5. FUTURE PROSPECTS FOR STUDYING CHEMICAL WEATHERING OF POWDERED VOLCANIC ROCKS USING A FLUIDIZED BED REACTOR

8.5.1. Dissolution behaviour of crystalline and glassy volcanic rocks

In **Chapter 4**, we highlighted the formation of a micrometric leached layer at the surface of the Etna ash subjected to dissolution. A detailed analysis of the leached layer using scanning and transmission electron microscopy would give more insights into its chemical composition and structure (Valle et al., 2010; Arab et al., 2008).

In **Chapter 5**, we compared the dissolution rates of a natural and synthetic rhyolitic glass samples. Our results depart from Wolff-Boenisch et al. (2006)'s findings, who predicted that the dissolution rate of a natural glass is higher than that of its synthetic counterpart (similar Si:O ratios). It would be interesting to expand the dataset to other glass compositions. Additionally, the influence of Fe content and quenching rate on the dissolution rate of glasses with similar SiO_2 content deserves further attention.

In **Chapter 6**, we argued that the relative surface areas of the main rock glass and silicate mineral constituents available for dissolution reactions may differ from those inferred based on their volumetric proportions. This hypothesis requires more investigations. In particular, detailed surface studies involving techniques such as scanning electron microscopy and X-ray photoelectron spectroscopy would help to describe more quantitatively the mineralogical and chemical evolution of the surface of the weathered samples. For example, one should confirm that the adjustment of the reactive surface area as applied in Chapter 6 is compatible with a selective weathering mechanism (e.g., Lai et al., 2015; Beckigham et al. 2017; Jung and Navarre-Sitchler, 2018).

8.5.2. Further applications using the fluidized bed reactor

The dissolution experiments carried out in this study were performed at room temperature (20-25 °C). The fluidized bed reactor could be used to derive temperature-dependent dissolution rate laws (Lowe, 1986). The results of dissolution experiments at different temperatures would provide new insights into the dissolution behaviour of polycrystalline rocks.

We measured the dissolution rates of volcanic rock/ash/glass materials using reactive solutions with different pH values (2, 3, 5, 8, 10, and 11) and constant ionic strength (0.01 M). The effect of ionic strength on dissolution rate is worth studying. A significant amount of silicate particles eroded from

extrusive magmatic rocks or ash deposits emplaced on the continents reaches the ocean (Jeandel and Oelkers (2015). The dissolution of these particles may constitute a significant, but largely overlooked, contribution to the dissolved chemical load of the ocean.

Finally, there is a lack of knowledge regarding the thermodynamics and kinetics of dissolution/precipitation of secondary minerals generated during the weathering of volcanic rocks. In particular, new studies should focus on allophanic minerals, which dominate the mineralogy of many soils derived from volcanic products (Lowe 1986; Parfitt 2009).

8.6. SIMULATION OF ASH WEATHERING USING THE MECHANISTIC MODEL WITCH

In **Chapter 7**, we modelled the weathering of a continent-size ash deposit that would be generated by a modern-day super-eruption of a hot-spot volcano, i.e. Yellowstone caldera in the United States. Similarly, other super-eruptions in the past which involved subduction-zone volcanoes produced voluminous ash deposits. For example, along the Pacific Ring of Fire, the eruption of Toba, Indonesia, expelled 2800 km^3 of magma in a single event 74,000 years ago. An extensive ash deposit blanketed large portions of Southeast Asia, including the entire subcontinent of India (Chesner, 2011). Climate in these equatorial latitudes differs from that found in the mid latitude region covered by the Yellowstone ash deposit. In South East Asia and parts of India, a high runoff regime may prevail, potentially enhancing weathering rates (Hartman et al., 2009). Thus, using the mechanistic model WITCH, it would be interesting to assess the impact of weathering of a Toba-like ash deposit (in equatorial latitudes) on the Si weathering flux and atmospheric CO_2 consumption, and to compare the results with the Yellowstone case study.

References

Arab, M., Cailleteau, C, Angeli, F., Devreux, F., Girard, L., Spalla, O. (2008) Aqueous alteration of five-oxide silicate glasses: Experimental approach and Monte Carlo modeling. Journal of Non-Crystalline Solids 354. 155-161.

Beckingham, L.E., Steefel, C.I., Swift, A.M., Voltolini, M., Yang, L., Sheets, J.M., Cole, D.R., Kneafsey, T.J., Mitnick, E.H., Zhang, S., Gautier, L., Ajo-Franklin, J.B., DePaolo, D.J., Mito, S. and Xue, Z. (2017) Evaluation of accessible mineral surface areas for improved prediction of mineral reaction rates in porous media. Geochimica et Cosmochimica Acta 205: 31-49.

Chesner, C.A. (2011) The Toba Caldera Complex. Quaternary International: 1-14.

Eirksdottir, E.S., Gislason, S.R., Oelkers, E.H. (2015) Direct evidence of the feedback between climate and nutrient, major, and trace element transport to the oceans. Geochimica et Cosmochimica Acta 166: 249-266.

Gislason S. and Oelkers E.H. (2003) Mechanism, rates, and consequences of basaltic glass dissolution: II. An experimental study of the dissolution rates of basaltic glass as a function of pH and temperature. Geochimica et Cosmochmica Acta, Vol. 67, No. 20, pp. 3817-3832.

Harley, A.D. and Gilkes, R.J. (2000) Factors influencing the release of plant nutrient elements from silicate rock powders: a geochemical review. Nutrient Cycling in Agroecosystems 56: 11-36.

Hartmann, J., Jansen, N., Dürr, H.H., Kempe, S., Köhler, P. (2009) Global CO_2- consumption by chemical weathering: What is the contribution of highly active weathering regions? Global and Planetary Change 69. Pp. 185-194.

Hochella, M.F. and Banfield, J.F. (1995) Chemical weathering of silicates in nature: a microscopic perspective with theoretical considerations. In: White, A.F. and Brantley, S.L. (eds.) Chemical Weathering Rates of Silicate Minerals. Rev Min 31, pp 353-406. Mineralogical Society of America, Washington.

Jeandel, C., Oelkers, E.H. (2015) The influence of terrigenous particulate material dissolution on ocean chemistry and global element cycles. Chemical Geology 395: 50-66.

Jones, M.T., Gislason, S.R., Burton, K.W., Pearce, C.R., Mavromatis, V., Pogge von Strandmann, P.A.E., Oelkers, E.H. (2014) Quantifying the impact

of riverine particulate dissolution in seawater on ocean chemistry. Earth and Planetary Sciences Letters 395: 91-100.

Jung, H., Navarre-Sitchler, A. (2018) Physical heterogeneity control on effective mineral dissolution rates. Geochimica et Cosmochimica Acta 227. 246-263.

Lai, P., Moulton, K. and Krevor, S. (2015) Pore-scale heterogeneity in the mineral distribution and reactive surface area of porous rocks. Chem. Geol. 411, 260-273.

Leavesley, G.H., Lusby, G.C., and Lichty, R., W. (1989) Infiltration and erosion characterisitics of selected tephra deposits from the 1980 eruption of Mount St. Helens, Washington, USA. In Hydrologycal sciences journal 34.3, pp. 339-353.

Li, L., Steefel, C.I., Kowalksy, M.B., Englert, A., and Hubbard, S.S. (2010) Effects of physical and geochemical heterogeneities on mineral transformation and biomass accumulation during a biostimulation experiment at Rifle, Colorado. J. Contam. Hydrol. 112: 45-63.

Li, L., Peters, C.A. and Celia, M.A. (2006) Upscaling geochemical reaction rates using pore-scale network modelling. Adv. Water Resour. 29: 1351-1370.

Lowe, D.J. (1986) Control on the Rates of Weathering and Clay Mineral Genesis in Airfall Tephras: a Review and New Zealand Case Study. In Rates of Chemical Weathering of Rocks and Mineral. Colman, S. M. and Dethier, D.P. (eds). pp. 265-330.

Maher, K., Steefel, C.I., White, A.F. and Stonestrom, D.A. (2009) The role of reaction affinity and secondary minerals in regulating chemical weathering rates at the Santa Cruz Soil Chronosequence, California. Geochim. Cosmochim. Acta 73: 2804-2831.

Maher, K., Steefel, C.I., DePaolo, D.J. and Viani, B.E. (2006) The mineral dissolution rate conundrum: insight from reactive transport modelling of U isotopes and pore fluid chemistry in marine sediments. Geochim. Cosmochim. Acta 70, 337-363.

Moore, J., Lichtner, P.C., White, A.F. and Brantley, S.L. (2012) Using a reactive transport model to elucidate differences between laboratory and field dissolution rates in regolith. Geochim. Cosmochim. Acta 93: 235-261.

Navarre-Sitchler, A. and Brantley, S. (2007) Basalt weathering across schales; Earth Planet. Sci. Lett. 261: 321-334.

Oelkers, E.H., Jones, M.T., Pearce, C.R., Jeandel, C., Eiriksdottir, E.S., Gislason, S.R. (2012) Riverine particulate material dissolution in seawater and its implicatios for the global cycles of the elements. C.R. Geoscience 344: 646-651.

Paces, T. (1983) Rate constants of dissolution derived from the measurements of mass balance in hydrological catchments. Geochim Cosmochim Acta 47: 1855-186.

Parfitt, R.L. (2009) Allophane and imogolite: role in soil biogeochemical processes. Clay Minerals 44: 135-155.

Parkhurst D.L. and Appelo C.A.J. (1999) User's guide to PHREEQC (Version 2) – a computer program for speciation, bacth reaction, one-dimensional transport, and inverse geochemical calculations. In USGS, Restin, VA, USA, pp. 99-4259.

Raymond, P.A. (2017) Temperature versus hydrologic controls of chemical weathering fluxes from United States forest. Chemical Geology 458:1-13.

Salehikhoo, F., Li, L., Brantley, S.L. (2013) Magnesite dissolution rates at different spatial scales: The role of mineral spatial distribution and flow velocity. Geochimica et Cosmochimica Acta 108: 91-106.

Song, X. and Seagren, E.A. (2008) In situ bioremediation in heterogeneous porous media: dispersion-limited scenario. Environ. Sci. Technol. 42: 63131-6140.

Spence, R., J., S., Kelman, I., Baxter, P.J., Zuccaro, G., and Petrazzuoli, S. (2005) Residential building and occupant vulnerability to tephra fall. In Natural Hazards and Earth System Science 5.4. pp. 477-494.

Svedrup, H. (1990) The Kinetics of Base Cation Release due to Chemical Weathering. Lund University Press: Lund, Sweden.

Svedrup, H. and Warfvinge, P. (1988) Weathering of primary silicate minerals in the natural soil environment in relation to a chemical weathering model. Water Air Soil Pollut 38: 387-408.

Swoboda-Colberg, N.G. and Drever, J.I. (1993) Mineral dissolution rates in plot-scale field and laboratory experiments. Chem. Geol. 105:51-69.

Valle N., Verney-Carron A., Sterpenich J., Libourel G., Deloule E., Jollivet P. (2010) Elemental and isotopic (^{29}Si and ^{18}O) tracing of glass alteration

mechanisms. Geochimica et Cosmochimica Acta, Vol. 74 (12), pp. 3412-3431.

Velbel, M.A. (1989) Effect of chemical affinity on feldspar hydrolysis rates in two natural weathering systems. Chem Geol 78: 245-253.

Velbel, M.A. (1986) The mathematical basis for determining rates of geochemical and geomorphic processes in small forested watersheds by mass balance: examples and implications. In: Colman S.M. and Dethier, D.P. (eds.) Rates of Chemical Weathering of Rocks and Minerals, pp 439-451. Academic Press, Orlando, Fl.

White, A.F. and Brantley, S.L. (2003) The effect of time on the weathering of silicate minerals: why do weathering rates differ in the laboratory and field, Chem. Geol. 202: 479-506.

White, A.F., Blum, A.E., Schulz, M.S., Bullen, T.D., Harden, J.W., Petersen, M.L. (1996) Chemical weathering rates of a soil chronosequence of granitic alluvium: I. Quantification of mineralogical and surface area changes and calculation of primary silicate reaction rates. Geochim Cosmochim Acta 60: 2533-2550.

Wolff-Boenisch, D., Gislason, S.R., Oelkers, E.H. (2006) The effect of crystallinity on dissolution rates and CO2 consumption capacity of silicates. Geochimica et Cosmochimica Acta 70. 858-870.

Zhu, C. (2009) Geochemical modelling of reaction paths and networks. In Thermodynamics and Kinetics of Water-Rock Interactions. Oelkers E.H. and Schott, J. (eds.). Mineralgoical Society of America. Reviews in Mineralogy & Geochemistry. Vol. 70: 533-569.

Appendix. List of Publications

Publications in conference proceedings

•**Aragón-Tobar C. F.**, Schott, J. and Delmelle P. (2017) Dissolution rates of a silicate rock: A case study with andesite at acidic pH values and 20°C. Goldschmidt 2017, Oral Presentation , August 14-18 th, Paris, FR

•**Aragón-Tobar C. F.** , Godéris Y. and Delmelle P. (2016) Altération d'un dépôt de cendres volcaniques à l'échelle continentale : implications géochimiques et climatiques. 13es Journées d'Etude des Sols, July 5-8 th, Louvain-la-Neuve, Belgium.

•**Aragón-Tobar C. F**. , Godéris Y., Delmelle P. and Opfergelt S. (2015) Weathering of Continental-Scale Volcanic Ash Deposit: Geochemical and Climatic Implications. Goldschmidt 2015, August 16-21 th, Prague Czech Republic.

• Guevara A., **Aragón C**., De la Torre E. (2013) Remediation of mining soils contaminated with heavy metals using electrokinetic treatment, 3rd International Seminar on Mining Environmental Affairs Enviromine December 2013, Santiago, Chile.

Other publications

• **Aragón C**., De la Torre E., Guevara A. (2014) Designing an electrokinetic remediation system (laboratory and pilot scale) for heavy metal contaminated soils. REVISTA POLITECNICA Vol 34, No 1 (2014) .

• Haro C., **Aragón C**., Guevara A., De la Torre E. (2014) Regeneration of bleaching clays used in the discoloration of Edible Vegetable Oils. REVISTA POLITECNICA Vol 34, No 1 (2014).

• **Aragón C.** (2013) Designing an electrokinetic remediation system for heavy metal contaminated soils. Thesis, Chemical Engineering, EPN,Quito, Ecuador.